

KINEMATICS AND STRUCTURE OF MASSIVE STAR FORMATION IN NGC6334 V



**KINEMATICS AND STRUCTURE OF
MASSIVE STAR FORMATION IN NGC6334 V**

INAUGURAL-DISSERTATION

zur

Erlangung des Doktorgrades
der Mathematisch-Naturwissenschaftlichen Fakultät
der Universität zu Köln



vorgelegt von

Atefeh (Mitra) Aghababaei

aus Teheran, Iran
August, 2023

Berichterstatter (Gutachter):

Prof. Dr. Peter Schilke University of Cologne

Prof. Dr. Gary Fuller University of Manchester

Vorsitzender der Kommission:

Prof. Dr. Andreas Zilges University of Cologne

Tag der mündlichen Prüfung:

October 2023

*Dedicated to my mom and dad,
For all their sacrifices and unwavering support.*

تقدیم بہ ماں و پدرم،
برای تمام از خودگذشتگی و حمایت بی دریغ شما

For Women, Life, Freedom



*Photo taken during an observation trip at IRAM Observatory,
Winter 2018.*

ABSTRACT

HOW filamentary molecular clouds fragment into star-forming hub clusters remains an unresolved issue. This thesis focuses on the observational studies of the massive hub protocluster NGC 6334-V, which is embedded within the filamentary cloud NGC 6334. It delves deeply into the mechanisms operating at three distinct scales: compact structures present within the hub cluster, the sub-pc scales characterizing the filamentary accretions toward the cluster, and the pc scales dynamics defining the relationship between the cluster and the entire molecular cloud. The primary observational data used in this work consist of spectral-line ALMA observations with a spatial resolution of 1800 au, sensitive to both the 3 mm continuum emission and various molecular species. Moreover, low-resolution ancillary observations at larger scales and different wavelengths are also utilized to compare and connect the sub-pc and pc scale filamentary structures, as well as to search for ionized gas.

High resolution ALMA observations reveal 28 compact cores in the central hub cluster NGC 6334-V of which four shows a detection of IR compact source counterparts. The existence of young high-mass cores suggests that cluster NGC 6334-V is in an early stage, and the observed segregation among the cores suggests that primordial segregation could be a potential formation scenario. The rotational temperature of CH_3CCH varies widely, ranging from a few tens of kelvin up to 252 K at the position of the hot core, with a measurement error of $\approx 20\text{--}50$ K.

Utilizing dense gas tracers, particularly H^{13}CO^+ , six prominent filaments were identified. These filaments have masses ranging from 90 to 150 M_\odot and lengths between 0.5 to 0.9 pc, resulting in a mass per length of approximately 150 to 280 $M_\odot \text{pc}^{-1}$. The central cluster exhibits a distinctive widespread SiO emission, with an exceptionally narrow linewidth of less than 1.8 km s^{-1} . The analysis of the SiO (2-1) line profile and spatial distribution reveals that 99.8% of SiO emission has a width of less than 10 km s^{-1} and 57% has a width of less than 1.8 km s^{-1} . This emission reveals a tail-like structure along three filaments and suggests that the SiO emission in NGC 6334-V primarily results from low-velocity shocks. These shocks could originate from the encounter of filaments with the high-density central hub or from the confluence of an H II region behind the cluster.

The morphological analysis of cluster NGC 6334-V on a large scale suggests a formation scenario based on the ionization injection process from cavities behind the cloud. In this scenario, ionized gas ejected from an unknown source behind the cloud hits the cloud from one side, effectively isolating source V from the rest of the NGC 6334 cloud and pushing the filaments to the opposite side while the accretion continues toward the center.

CONTENTS

Abstract	ix
List of Figures	xvii
List of Tables	xix
1. Introduction	1
1.1. Composition of the Interstellar Medium	2
1.2. Molecular Clouds	4
1.3. Filaments	5
1.3.1. Filament Formation	6
1.3.2. Filament Scales	7
1.3.3. Accretion onto Filaments	7
1.3.4. Fragmentation	8
1.4. Star Cluster	8
1.5. Star Formation	9
1.5.1. Low-Mass Star Formation	10
1.5.2. High-Mass Star Formation	11
1.5.3. Theoretical Models for the Formation of Massive Stars	14
1.6. NGC 6334 Complex	16
1.7. NGC 6334 V	18
1.8. About this work	19
2. Emission Mechanisms & Radio Interferometry	21
2.1. Radiative Transfer	22
2.2. Continuum Emission from Dust	24
2.2.1. Ionized gas and HII regions	25
2.3. Molecular Emission	26
2.4. Radio Astronomy	28
2.4.1. Single-dish Observations	29

2.4.2.	Radio Interferometry	32
3.	Observations & data analysis	35
3.1.	ALMA	36
3.1.1.	Observational setups	36
3.1.2.	Calibration	38
3.1.3.	Imaging	39
3.1.4.	Combination	40
3.2.	Ancillary data	43
4.	Continuum Emission Results	45
4.1.	Morphology	46
4.2.	Source Identification	46
4.3.	Counterparts in infrared and X-ray wavelengths	52
4.4.	Physical properties of continuum cores	52
4.5.	Core Structures in the NGC6334 V	55
4.5.1.	Minimum Spanning Tree (MST)	55
4.5.2.	Clump fragmentation and Jeans instability	58
4.5.3.	Core Mass Function (CMF)	61
4.5.4.	Mass Segregation in NGC6334 V	63
4.6.	Discussion	68
4.6.1.	Hierarchical Structures in NGC6334 Star Clusters	69
4.6.2.	Comparative Analysis of Time Evolution in NGC6334 Star Clusters	70
5.	Molecular Line Results - I	75
5.1.	Molecular Line Emissions: Moment Maps	76
5.2.	CH ₃ CCH: Temperature Tracer	78
5.2.1.	Details of XCLASS modeling analysis	79
5.2.2.	Unveiling Core Temperatures and Fluctuations through XCLASS Fits	80
5.3.	H ¹³ CO ⁺ : Filament Tracer	83
5.3.1.	Prior to Identifying Filaments: H ¹³ CO ⁺ and CCH Relationship	83
5.3.2.	Filament identification	85
5.3.3.	Velocity gradients	87
5.3.4.	Mass accretion rates	91

5.4. Discussion	95
5.4.1. On the nature and origin of NGC 6334-V	95
5.4.2. Association between the hub cluster and filaments	99
6. Molecular Line Results - II	101
6.1. SiO: Shock Tracer	102
6.2. SiO: moment maps	104
6.3. SiO Spectra Decomposition	106
6.4. Discussion	117
6.4.1. Origin of the extended SiO emission	117
6.4.2. Numerical Predictions for low-velocity shocks	120
7. Summary and outlook	129
7.1. Summary	130
7.2. Outlook	135
A. XCLASS: The eXtended CASA Line Analysis Software Suite	139
B. Error estimation for CH₃CCH	143
C. DisPerSE	147
D. Behind the Spectrum (BTS)	151
E. Example Grid of shock models in PDSM	157
F. Supplementary Figures	163
List of Abbreviations	168
Bibliography	169
Bibliography	186
Acknowledgements	187
Curriculum Vitæ	191

LIST OF FIGURES

1.1.	Herschel view of NGC 6357 and NGC 6334	6
1.2.	Fragmentation of molecular clouds into filaments and hubs	8
1.3.	Hierarchical fragmentation of a large cloud into small fragments. . .	10
1.4.	Evolution of forming single star from a prestellar core.	12
1.5.	Evolution of forming high stars from a clump.	14
2.1.	A view of absorption, spontaneous, and stimulated emission	26
2.2.	Energy levels of a diatomic molecule.	27
2.3.	Radio frequency band designations	29
2.4.	Components of a Radio Telescope.	29
2.5.	A schematic view of lobes in single-dish telescope	30
2.6.	Interferometric array of two antennas.	32
3.1.	The Atacama Large Millimeter/submillimeter Array.	37
3.2.	Comparing methods of ALMA 12-m and ACA data combination. . .	42
3.3.	NGC 6334 complex observed by <i>Herschel</i> and <i>APEX</i>	44
4.1.	Continuum 3 mm emission map and cores	47
4.2.	3 mm ALMA cores in comparison to infrared Spitzer map	53
4.3.	The histogram and KDE analysis of core properties	56
4.4.	MST and KDE distribution of core separations	57
4.5.	Gaussian fit uncertainty in Q parameter.	58
4.6.	CMF comparison of core masses	62
4.7.	Core mass vs. distance from cluster center.	66
4.8.	The evolution of Λ_{MSR} with different number of sources.	68
4.9.	CMF comparison: cluster V vs. other clusters in NGC 6334.	71
4.10.	The evolution of Λ_{MSR} in different clusters.	72
5.1.	Comparison of H^{13}CO^+ moment maps with other dense gas tracers.	77
5.2.	Maps of XCLASS analysis of CH_3CCH emission.	81

5.3. temperature dispersion comparison: CH ₃ CCH fit vs. Herschel map.	82
5.4. Comparative analysis of H ¹³ CO ⁺ and CCH.	84
5.5. Filaments in NGC 6334-V and velocity trends for H ¹³ CO ⁺ species.	88
5.6. P-V Analysis of H ¹³ CO ⁺ and velocity gradient in filaments.	90
5.7. Total mass accretion rates: NGC 6334-V vs. other clusters.	94
5.8. Large scale view of cluster V in ancillary observations	97
5.9. Distribution of ionized gas in NGC 6334-V.	98
5.10. Schematic of ionization injection behind the cloud.	99
6.1. Three moment maps of SiO (2–1) emission.	105
6.2. BTS Fit Analysis for SiO (2–1) Emission	108
6.3. Extracted SiO spectra over the selected regions	109
6.4. KDE of linewidths: narrow vs. broad regimes boundaries.	110
6.5. Linewidth of BTS spectra under three different constraints.	112
6.6. Velocity of BTS spectra under three different constraints.	113
6.7. KDE of linewidth from BTS spectra: analysis under three constraints.	115
6.8. KDE velocity from BTS spectra: analysis under three constraints.	116
6.9. SiO and EGO counterparts	119
6.10. SiO emission map with P-V cuts along filaments	121
6.11. H ¹³ CO ⁺ velocity map with SiO BTS spectra, overlaid with filaments and cores	122
6.12. Schematic view of different zones in a planer C-type shocks.	123
6.13. PDSM results: temperature and SiO abundances vs. shock velocity.	126
6.14. 2-D KDE of SiO (2–1) column density versus velocity.	128
B.1. MCMC: first run	144
B.2. MCMC: second run	145
B.3. MCMC: third run	146
C.1. An example of a persistence diagram	149
D.1. Comparison of different Gaussian line profiles with derivatives.	152
E.1. PDSM analysis for n _H = 10 ⁵ cm ⁻³ in (-G) scenario	159
E.2. PDSM analysis for n _H = 10 ⁵ cm ⁻³ in (-M) scenario	160
E.3. PDSM analysis for n _H = 10 ⁶ cm ⁻³ in (-G) scenario	161
E.4. PDSM analysis for n _H = 10 ⁶ cm ⁻³ in (-M) scenario	162

F.1. SiO channel map	164
F.2. SiO column density map	165
F.3. SiO column density and velocity map in region B	166

LIST OF TABLES

3.1. ALMA spectral windows: molecular transitions and continuum band.	37
4.2. Properties of the 3 mm ALMA continuum cores	50
5.1. Kinematic and physical properties of the filaments	87

1

INTRODUCTION

The universe is a vast, complex, and interconnected network of components. Everything is connected in some way, from the tiniest particles to the largest structures. How does the universe work as an interconnected network? One of the most intriguing aspects of the universe is star formation. In order to understand star formation, we must understand the complex relationship between the interstellar medium and the stars that form inside it. Can we find a relationship between the observed components inside the interstellar medium to understand the evolution of stars?

In this chapter, I will introduce the composition of the interstellar medium and provide an overview of the current understanding of each component, as well as their relationships with other components.

1.1. COMPOSITION OF THE INTERSTELLAR MEDIUM

The space between stars is not as empty as it may seem. Stars form from infalling gas and dust between the stars that we named as the Interstellar Medium (ISM). The ISM is a broad term for anything between stars within galaxies and is thus an essential component of galaxies. The predominant constituents of the ISM are defined as follows:

Interstellar gas: Interstellar gas mainly refers to atoms, molecules, and ions in the gas phase, with velocity distributions near thermal equilibrium. The ISM gas is primarily composed of the two most abundant elements in the universe, hydrogen, and helium. Hydrogen counts for 70% of the gas mass, which can be found in a neutral (H I), molecular (H₂), and ionized (H II) state. In addition, 28% of the mass is in helium and 2% in heavier elements such as oxygen, carbon, and nitrogen (Klessen and Glover, 2016).

Interstellar dust: In addition to the gaseous material that accounts for 99% of the matter in the ISM, 1% of the mass of interstellar matter is inferred to be in a particulate component commonly referred to as dust grains (Klessen and Glover, 2016). The size of the dust grains are less than a micron and are primarily composed of silicates and carbon compounds (Weingartner and Draine, 2001). The interstellar dust absorbs light over a wide range of frequencies.

Interstellar Radiation Field: The interaction of gas and dust with the interstellar radiation field (ISRF) determines the leading chemical and thermal states of

the interstellar gas. Draine, 2011 and Klessen and Glover, 2016 summarized six radiation components that dominate ISRF: galactic synchrotron emission from relativistic electrons, the cosmic microwave background (CMB), infrared and far-infrared emission from dust grains heated by starlight, bound-bound (bb), bound-free (bf) and free-free (ff) emission from 10^4 K ionized plasma, starlight, and finally X-rays from hot ($10^5 - 10^8$ K) plasma. Among all, most of the energy density of the ISRF is in the infrared, where thermal dust emission dominates, and in the optical and UV, where starlight dominates.

Cosmic rays: Most of the electrons and ions in interstellar space have velocities derived from the local thermal distribution. Cosmic rays are a subset of high-energy particles that include nonthermal electrons and ions with energies greater than those of thermal particles. Cosmic rays are extremely relativistic particles, with energies spanning from 100 MeV to more than 1 TeV (Klessen and Glover, 2016). They comprise primarily of energetic protons, $\sim 10\%$ alpha particles, $\sim 1\%$ relativistic electrons, $\sim 1\%$ metal nuclei, and smaller fractions of positrons and antiprotons (Blandford and Eichler, 1987). Galactic cosmic rays originate either in unevolved late-type stars and are injected into the surrounding ISM via flares out of their corona (Meyer, 1985) or, in evolved early-type stars, with a release into the ISM upon a supernova explosion (Simpson, 1983). Regardless of their exact origin, the injected cosmic rays are accelerated upon traveling in the ISM through repeated scattering off moving irregularities in the interstellar magnetic field.

Most of the baryons in the ISM are found with a temperature and density falling close to various characteristic states or distinct "phases" (Draine, 2011). These phases were classified by Draine, 2011 and recent review of Klessen and Glover, 2016 as follows:

- *Molecular Gas* refers to the coldest and densest phase of the ISM. The gas in this phase is gravitationally bound and structured in Giant Molecular Clouds (GMCs) with temperatures of 10–20 K and densities larger than 10^2 cm^{-3} (Ferrière, 2001).
- *Cold Neutral Medium (CNM)* Refers to cold and dense atomic gas with $T \sim 100$ K and densities of $\sim 30 \text{ cm}^{-3}$ (Field, Goldsmith, and Habing, 1969)
- *Warm Neutral Medium (WNM)* refers to warm and diffuse atomic gas with kinetic temperatures in the range 5000–8000 K and densities of $0.01 - 0.1 \text{ cm}^{-3}$ (Field, Goldsmith, and Habing, 1969).

- *Warm Ionized Medium (WIM)* refers to ionized gases with temperatures ranging from 6000 to 10 000 K and a density of 0.2 cm^{-3} , similar to WNM. WIM is a fundamental gas phase component of the Milky Way that represents more than 90% of the total ionized gas in the ISM (Haffner et al., 2009).
- *Hot Ionised Medium (HIM)* refers to a hot, low-density ionized gas created through stellar winds and blast waves from novae and supernovae. The HIM temperatures reach $T \sim 10^6 \text{ K}$, with densities of 0.004 cm^{-3} (McKee and Ostriker, 1977).

1.2. MOLECULAR CLOUDS

Molecular clouds are vast, cold, and dense regions of interstellar gas and dust where the conditions are suitable for forming stars. Among the five phases of the ISM described in § 1.1, molecular clouds appear in the coldest and densest phase: molecular gas. Molecular clouds also appear to have a hierarchical structure, indicating that the density of gas within these clouds is not uniform, and turbulence has a role in forming these clouds. These clouds are primarily composed of molecular hydrogen (H_2). However, they also contain other molecules, including carbon monoxide (CO), ammonia (NH_3), and water (H_2O), that can be used as tracers of clouds. Molecular clouds are extended regions with a hierarchical structure that are thought to be formed due to the turbulent nature of the ISM and the galactic potential. Molecular clouds have characteristic masses between 10^2 – $10^6 M_\odot$ and diameters ranging from 1 pc to 100 pc. They often have a cold environment of 10–20 K, and their typical densities are about 50 – 500 cm^{-3} . Clouds with masses greater than $10^4 M_\odot$ are classified as GMCs (Blitz, 1993). Following Dobbs et al., 2014, I here summarize the three most important mechanisms of GMCs formation:

Localized Converging flows are driven by stellar feedback processes such as the expansion of H II discussed in Section 1.5.2 (e.g., Bania and Lyon, 1980; Vazquez-Semadeni, Passot, and Pouquet, 1995) and supernova blast waves (e.g., McCray and Kafatos, 1987; Ntormousi et al., 2011). The converging streams of gas accumulate either in the galactic plane or above it to become molecular clouds. Alternatively, stars or supernovae may fall back into the disk plane and eject material vertically due to a local excess of pressure, which can also contribute to the formation of molecular clouds.

Spiral-Arm Induced Collisions are a mechanism to induce smaller clouds to agglomerate into larger ones in the presence of spiral arms. The timescale required to build a 10^5 – $10^6 M_{\odot}$ cloud through the accumulation of smaller clouds would be very slow (> 100 Myr, Blitz and Shu (1980)) in low-density environments. Therefore, collisions between small clouds in spiral arms and high surface density galaxies become much more frequent, and the formation time scale shrinks significantly (e.g., Casoli and Combes, 1982; Dobbs, 2008).

Gravitational Instability in single-phase gas disks is a potential mechanism for forming massive clouds on large scales. Single-phase infinitesimally thin gas disks become unstable and undergo fragmentation when their Toomre parameter $Q < 1$. The Toomre parameter is a dimensionless quantity used for determining the stability of a rotating disk of gas or stars against self-gravity and the potential for forming gravitational instabilities. Gas flowing through the spiral pattern encounters a shock, which raises the density and can trigger a gravitational collapse (Roberts, 1969). Cosmological simulations also reveal that self-gravitating, pressureless matter shrinks into filamentary structures (Springel et al., 2005).

Apart from the mentioned mechanisms, observations of various molecules also help to characterize the physical properties of the individual GMCs. The ^{12}CO molecule is the second most abundant molecule in molecular clouds and is an ideal tool to probe the characteristics of GMCs. Observations of CO and other dense gas tracers reveal that the density distribution in molecular clouds is not uniform and homogeneous. Molecular clouds harbor elongated, over-dense regions known as filaments that become gravitationally unstable and hierarchically fragment into clumps.

1.3. FILAMENTS

The recent observations by the Herschel Space Observatory revealed that filaments are abundant within molecular clouds and play a role as an intermediate step between molecular clouds, star-forming clusters, and down to the cores, see Figure 1.1 (Motte et al., 2010a; André et al., 2010; Könyves et al., 2015; Marsh et al., 2016). The clouds actively accrete from their diffuse environment and quickly exceed their thermal Jeans mass (Krause et al., 2020). The Jeans mass in the dense, cold gas is $\sim 10^4$ times smaller than in the diffuse, warm gas (Gómez and Vázquez-Semadeni, 2014). In multi-Jeans mass molecular clouds, the gravitational energy

overwhelms the cloud's internal energy and behaves as a pressureless collapse. This condition implies that first, the pressureless collapse contracts a 3-dimensional ellipsoid along its shortest dimension to form a sheet, and then the elliptical sheet contracts again along its shortest dimension to form filaments (Lin, Mestel, and Shu, 1965). Filaments have been known structures in nearby star-forming clouds for quite a long time (e.g., Lin, Mestel, and Shu, 1965; Schneider and Elmegreen, 1979).

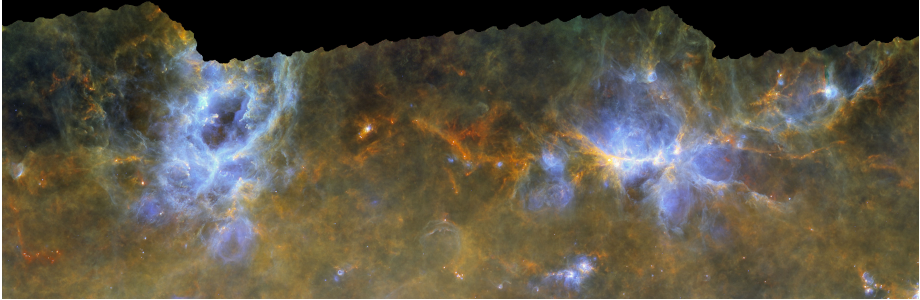


Figure 1.1.: The War and Peace Nebula, also known as NGC 6357 (left), and the Cats Paw Nebula, also known as NGC 6334 (right), are seen by the ESAs Herschel space telescope as part of the HOBY project (Motte et al., 2010a). The three-color image is a composite of the wavelengths of 70 microns (blue), 160 microns (green), and 350 microns (red). The RGB image was improved later by Causi et al., 2016. Significant filamentary substructures in the cloud indicate the ubiquitousness of filaments in star-forming regions.

1.3.1. FILAMENT FORMATION

Many mechanisms could contribute to the evolution of filaments, and in this subsection, I will briefly address the most important mechanisms based on Hacar et al., 2022.

Sheet interactions: According to the classical hypothesis of filament formation, due to gravitational instabilities, elongated sheets will collapse and fragment into filamentary structures with density enhancements toward their ends (e.g., Miyama, Narita, and Hayashi, 1987; Burkert and Hartmann, 2004).

Turbulence: A natural mechanism for forming networks of filaments in the absence of gravity is turbulence. The turbulence traces the underlying gas ve-

locity field and also generates an internal hierarchy of filaments (e.g., Tafalla and Hacar, 2015; Federrath, 2016; Clarke et al., 2017).

Magnetic field: The presence of a magnetic field amplifies filament formation via different events, such as: compressing of magnetized clouds by shock waves (Inoue and Fukui, 2013), stretching of over-densities in the diffuse gas (Hennebelle, 2013), and finally, converging flows caused by the transition of magnetic field orientation (Soler and Hennebelle, 2017).

Feedback: The mechanical and radiation feedback pressures can compress the cloud surfaces and shape the filaments. The filaments that are usually enhanced by the effects of radiation or wind have a low mass and are on parsec scales (e.g., Peretto et al., 2012; Suri et al., 2019).

Galactic dynamics: Giant filaments of >100 pc could be influenced by galactic rotation (Wada, Meurer, and Norman, 2002), galactic shear (Duarte-Cabral and Dobbs, 2017), and instabilities such as Parker or thermal instabilities that rapidly change the gas phases (Kim, 2002).

1.3.2. FILAMENT SCALES

Observations report that filaments are found in a vast range of masses and lengths. The mass of the filaments ranges from ~ 0.01 to $5 \times 10^6 M_{\odot}$, and their lengths span from ~ 0.03 to 300 pc from fibers to the giant galactic filaments (Hacar et al., 2022). Filaments show different stability and dynamical properties based on their mass and length. For instance, large filaments (> 1 pc) show high masses that mostly exceed critical line masses (up to $> 100 M_{\odot}$ pc), while short filaments (< 1 pc) indicate sub-critical line masses (e.g., Schisano et al., 2020; Arzoumanian et al., 2019). The critical line mass in filaments describes the minimum mass per unit length at which the filament becomes gravitationally unstable and collapses to form dense structures.

1.3.3. ACCRETION ONTO FILAMENTS

The velocity gradients around the filaments are usually perpendicular to the filament path and suggest coherent gas accreting onto the filaments. The accretion rate of filaments tends to be a few 10 to more than $100 M_{\odot} \text{ Myr}^{-1} \text{ pc}^{-1}$ (Kirk et al., 2013; Palmeirim et al., 2013). Accretion does not contribute to the stability of the filament, but it may generate fragmentation.

1.3.4. FRAGMENTATION

Accretion and turbulence onto and along filaments directly influence the supersonic compression to exceed their critical line mass, either locally or globally, and seed fragmentation (Mac Low, 1999). The fragmentation process appears in hierarchical and complex structures that could form hubs or cores at the intersections of filaments. Continued accretion along the filaments toward the hub creates an environment for star formation. Cluster formation in filamentary hub systems is one of the main topics of this thesis, which I further explore in more detail.

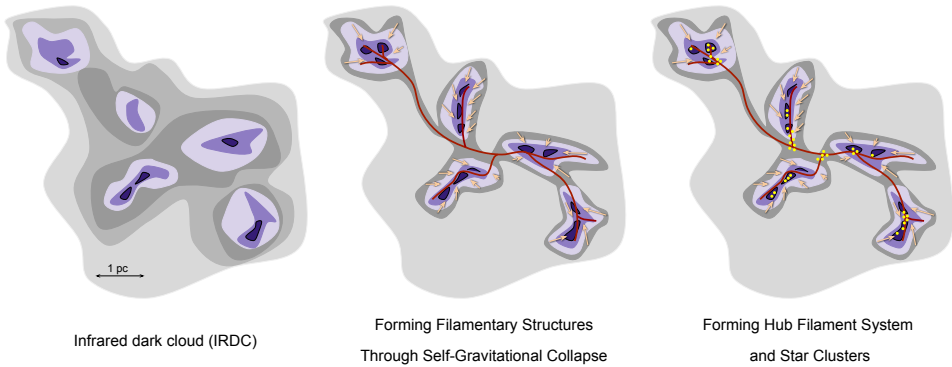


Figure 1.2.: Evolutionary sequence of forming filaments and hub clusters from a fragmented infrared dark cloud. from Left to right: Infrared dark clouds (IRDCs) are cold and dense molecular gas and dust regions. IRDCs are known to form filaments through gravitational fragmentation. As the cloud collapses under self-gravity, it begins to flatten out and form a disk-like structure. As the disk becomes dense, it becomes unstable and breaks into smaller pieces, forming filaments. These filaments can be elongated structures that are several light-years long and a few light-years wide. The denser regions of the filaments are where new stars and planets are likely to form.

1.4. STAR CLUSTER

Krause et al., 2020 defined a star cluster as a gravitationally bound system or group of stars inside a closed tidal volume that satisfy two conditions: not dark matter-dominated, which distinguishes star clusters from galaxies and contains at least 12 stars. Star clusters can be gravitationally bound or unbound. Unbound groups are named associations (Gouliermis, 2018), and bound clusters can be subdivided into Open Clusters (OCs) or Global Clusters (GCs). OCs have low mass ($10^5 M_{\odot}$) and

are young, with an age less than 1 Gyr, and generally exist in the disc of the Milky Way. GCs, on the other hand, are older and more massive than OCs associated with the Milky Way's bulge and halo (Krause et al., 2020) (Figure 1.2).

1.5. STAR FORMATION

Stars are believed to be formed inside dense clumps embedded within molecular clouds. Theoretically, the road to forming stars begins with the collapse of an isothermal gas condensation in a free fall time without considering rotation or magnetic fields. Whenever clumps exceed their Jeans mass, they become unstable and collapse gravitationally. Also, because of gravitational instabilities, massive bound clumps experience supersonic turbulence until they form self-gravitating cores. Because of non-uniform density distributions, denser parts exceed the Jean mass faster than outer and less dense parts, and hierarchy fragments clump into several dense cores (Figure 1.3).

The distribution of masses of dense, gravitationally bound objects known as cores within molecular clouds called Core Mass Function (CMF). Cores are thought to be the precursors of individual stars and play a crucial role in the star formation process. The CMF provides information about the distribution of core masses in a molecular cloud, which can in turn be used to study the process of star formation and the conditions that lead to the formation of cores and stars. As the collapse increases, heat cannot radiate away, traps, and breaks down isothermality. The radiation pressure raises the internal energy of the central part until a balance is created between radiation pressure and gravitational collapse. The core collapse creates a rotating disk within an accretion shock. At this stage, the core is in the earliest phase of stellar evolution and is called a protostar. The protocluster becomes a star by continuing accretion from its parent molecular cloud.

A statistical description of the distribution of masses of stars formed in a particular region or cluster is the Initial Mass Function (IMF). It represents the number of stars per unit mass interval in a given region and provides information about the relative proportions of stars of different masses that are formed. The IMF is a crucial ingredient in star formation and evolution models, and its shape and form reveal crucial information about the conditions in which stars are formed.

The evolution of stars is not unique; the evolution of low-mass stars and high-mass stars follows distinct processes that result in the formation of stars with different masses. While there are similarities in the overall process, there are also significant differences. Low-mass stars have a longer lifetime than high mass stars, evolve

slowly, and spend most of their lives in the main sequence (Stahler, 1983). They are also less luminous and have weaker radiation fields, meaning they have a less significant impact on the surrounding environment than high-mass stars. I will define low-mass and high-mass stars and take a closer look to their formation at the following sections. More information about this section and the following sections on star formations can be found in "Theory of Star Formation" by (McKee and Ostriker, 2007), " Note on Star Formation" by Krumholz, 2015, and "An Introduction to Radio Astronomy" written by (Ward-Thompson and Whitworth, 2015).

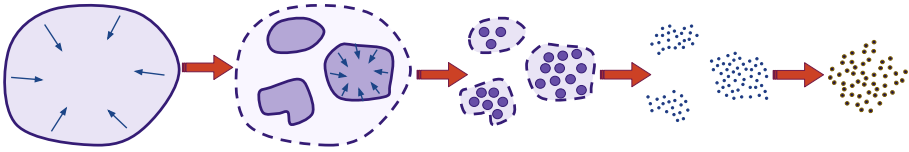


Figure 1.3.: Hierarchical fragmentation causes a large cloud to break into smaller fragments. From left to right, the sketch shows an interstellar cloud that becomes gravitationally unstable ($M_0 > M_J$) and starts to contract but remains isothermal. Because the density of the cloud is not uniform everywhere, parts of the original cloud become gravitationally unstable in their own right and start to contract on themselves. The process can continuously repeat as long as the gas remains isothermal and causes the original cloud to fragment.

1.5.1. LOW-MASS STAR FORMATION

Low-mass star formation typically refers to the formation of stars with masses up to less than eight solar masses (McKee and Ostriker, 2007) in a time short compared to the Kelvin-Helmholtz time-scale, $t_{\text{KH}} = Gm_*^2/RL$ (Kahn, 1974) where G is the gravitational constant, m_* is the mass of the object, R is the radius of the object, and L is the luminosity or rate at which energy is radiated away from the object. Kelvin-Helmholtz times is the time it takes for a protostar to contract and heat up by releasing gravitational potential energy and radiating away a significant fraction of the thermal energy of a star. This process starts with collapsing a core with masses in a range of thermal Jeans mass. As the core collapses, it begins to heat up and form a protostar at its center. As the protostar becomes more massive, it also becomes more luminous, emitting a significant amount of radiation. The luminosities of protostars are dominated by accretion.

Observations of the mass distribution surrounding protostars, the velocity distribution of circumstellar gas, and the non-stellar radiative flux can provide insights

into protostar growth. Modeling the Spectral Energy Distribution (SED) of the continuum, mass and temperature distributions will help us to identify the evolutionary phase of the object. Young stellar objects (YSOs) are classified into four main groups based on the slope $\alpha_{\text{IR}} = d\log(\lambda F_{\lambda})/d\log(\lambda)$ of their SED, which traces their evolutionary stages from the onset of accretion onto a protostellar core to the main sequence. To calculate the spectral index (or the slopes in the infrared SED), the fluxes are measured with data from the Infrared Astronomical Satellite (IRAS) (Krumholz, 2015).

Class 0: The earliest stage of YSOs evolution characterized by a SED which shows dominant submillimeter luminosity ($L_{\text{sum}}/L_{\text{bol}} > 0.5\%$; André, 2002) but little or no contribution from infrared emission. The class 0 objects often reveal a cold SED with bolometric temperature $T_{\text{bol}} < 70$ K (Chen et al., 1995)

Class I: The intermediate stage of YSOs evolution characterized by a SED with $\alpha_{\text{IR}} > 0$, also have a peak in the infrared and strong submillimeter emission. The class I objects are evolved protostars with both circumstellar disks and envelopes.

Class II: The later stage of YSOs evolution characterized by a SED with $-1.5 < \alpha_{\text{IR}} < 0$ that has a peak in the near-infrared and weaker submillimeter emission. Such sources are believed to be in pre-main sequence stars with significant circumstellar disks, also become visual as classical T Tauri stars.

Class III: The final stage of YSOs evolution characterized by a SED with $\alpha_{\text{IR}} < -1.6$ that has a peak in the near-infrared and no submillimeter emission. These objects are considered "pre-main-sequence" stars just about to reach the main sequence.

Figure 1.4 shows the SEDs of the different protostellar evolutionary stages via SEDs spectrum, schematic views of YSOs in each stage and parameters. This classification scheme is based on the YSOs SEDs, which provide information about the temperature and density of the dust and gas surrounding the young star and its disk. It allows us to infer the evolutionary stage of the YSOs

1.5.2. HIGH-MASS STAR FORMATION

High-mass star formation typically refers to the formation of stars with masses greater than eight solar masses. These stars are formed in Kelvin-Helmholtz time-scale less than the accretion time (McKee and Ostriker, 2007). It means they begin to

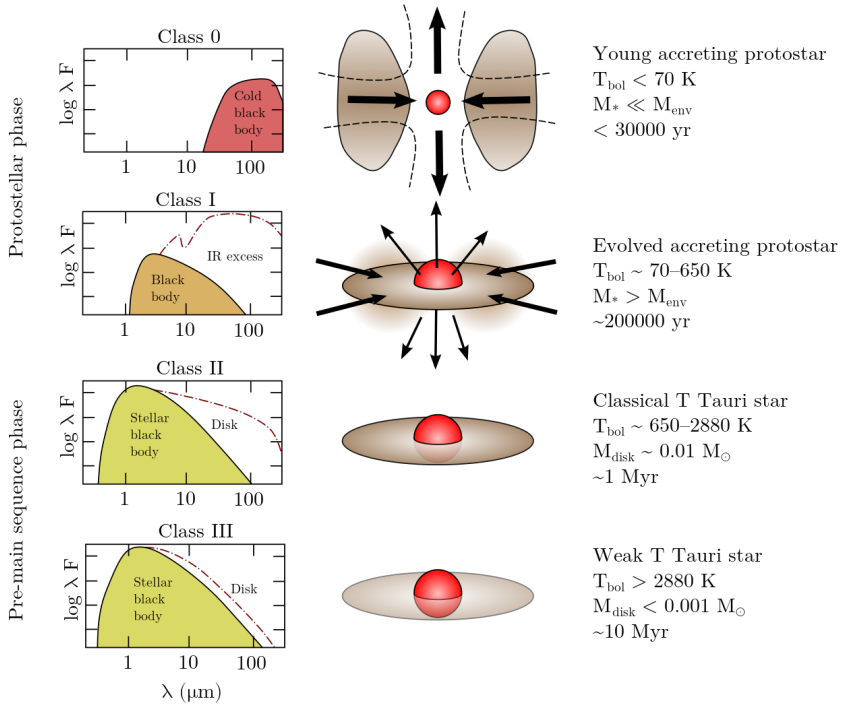


Figure 1.4.: The evolutionary sequence of forming a single star from a prestellar core at class 0 to class III YSOs. From left to right: The first column shows the shape of the SEDs, the second column shows a visual schematic of the YSOs, and the third column indicates the bolometric temperature and the circumstellar mass adopted from (André, 2002) review.

Image source: <https://commons.wikimedia.org/wiki/User:Vallastro>

undergo nuclear burning while still accreting to radiate away a significant fraction of their thermal energy (Figure 1.5). Entering to a Zero Age Main Sequence (ZAMS) causes two main feedback effects, radiation pressure, and photoionization, which do not significantly affect the formation of low-mass stars (Larson and Starrfield, 1971). High-mass stars also significantly impact the interstellar medium through their strong radiation, powerful stellar winds, and explosive deaths as supernovae. The evolution of high-mass stars is also challenging to study since their formation and subsequent development occurs while they are still embedded within molecular clouds. Furthermore, most high-mass star-forming clouds are located at considerable distances from us, which makes resolving inside the star-forming sites difficult compared to low-mass star-forming regions. Thus, they make the evo-

lution process of a high-mass star much more complex than that of a low-mass star formation, and it is still not fully understood. The formation of high-mass stars from large molecular clouds is a complex process that involves several stages of fragmentation and collapse. The following classification is a general overview summarized from (Zinnecker and Yorke, 2007; McKee and Ostriker, 2007).

IR dark clouds: Infrared dark clouds (IRDCs) are GMCs with high visual extinction, which means there are many materials and a lack of embedded bright IR sources, implying that IRDCs present the earliest stage of star formation. IRDCs are on the order of ~ 10 pc in size and pervaded by filamentary structures on the order of 1 parsec. Because of their high internal density and low temperature, they were thought to be the birthplace of high-mass stars.

Hot molecular cores: The highly dense clumps and condensations ($n > 10^7 \text{ cm}^{-3}$) within the fragmented cloud with sizes of 0.1-0.01 pc are thought to be the precursors to high-mass stars and stellar clusters. The turbulent core model argues that the central densities in these clumps are much greater than the mean densities and the time scale for gravitational collapse is also shorter. As the cores continue to collapse and heat up to >100 K, they become very compact and form hot molecular cores or protostars. These protostars are surrounded by a thick envelope of gas and dust, which continues to feed the protostar as it grows. These envelopes contain many complex organic molecules, evaporate off dust grains, and generate methanol maser emission (e.g., Menten, 1991; Walsh et al., 1998; Hill et al., 2005). As the temperature and pressure in the core of the protostar increase, nuclear fusion ignites, and the protostar enters the short-lived phase of the hot core, which is a more evolved stage in the formation of stars. If the protostars are massive enough, they will become high-mass O or B-type stars. The high-mass stars also heat the surrounding gas and generate a "protostellar outflow."

Hypercompact and ultracompact H II regions: The newly formed star is massive and hot enough to emit high-energy ultraviolet radiation. That ionizes the surrounding hydrogen gas and creates a quasi-spherical H II region. Depending on the size, formation origin, electron density, and mass of the enclosed star or stars, the H II region is either hyper- or ultra-compact. HCHII regions are believed to be the precursors to UCHII regions. They are formed first when the young forming massive star is still deeply embedded in dense gas, and can evolve into UCHII regions over time through expansion and a de-

crease in density. HCHII is optically thick at the cm wavelength, while UCHII is optically thin at the wavelength. Hypercompact H II regions are believed to have individual photoevaporating disks (Keto, 2007; Nielbock et al., 2007), and ultracompact H II regions are believed to represent disk-less stars photoionizing their cocoons and envelopes. Finally, the compact and classical HII regions expand hydrodynamically and disrupt the parent molecular cloud.

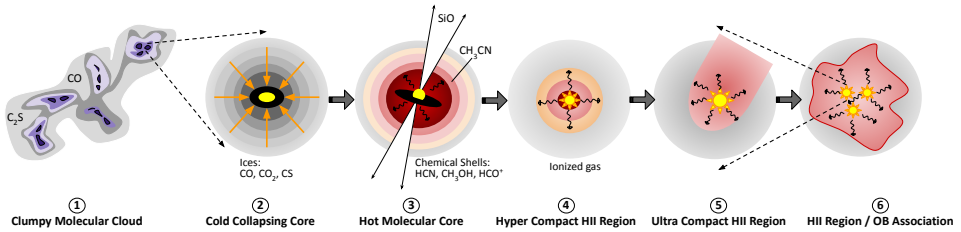


Figure 1.5.: The evolutionary sequence of forming high stars from a clumpy molecular core. From left to right: The clumpy molecular cloud begins to collapse under gravity (1), forming a dense, cold collapsing core called "prestellar core" (2). As the cores continue to collapse, they heat up and form protostars. These protostars are still surrounded by a thick chemical shell of gas and dust, which continues to feed the protostar. As the protostar grows, it begins to heat up and ionize the surrounding gas, creating a "hot core" (3). As the high-mass star continues to form, it heats up the surrounding gas and causes a "protostellar outflow" to occur. The high-mass stars typically are part of an OB association or a cluster and continue to evolve within an H II region environment (5 and 6).

Credit: The image was recreated based on Cormac Purcell's work.

1.5.3. THEORETICAL MODELS FOR THE FORMATION OF MASSIVE STARS

In the previous section, we learned about the observational phase of high-mass star formation. However, the formation of high-mass stars has yet to be fully understood. Depending on the initial and environmental conditions of the parent molecular clouds, several theories have been proposed to explain the process. This section reviews two competitive models for forming high-mass stars: (1) turbulent fragmentation and monolithic core collapse, (2) competitive accretion and runaway growth. The turbulent fragmentation model emphasizes the role of fragmentation in breaking down the initial core into smaller components that then collapse to

form stars, while the competitive accretion model emphasizes the role of accretion in building up the mass of a star.

Monolithic core collapse The theory proposes that high mass stars form through the collapse of a massive molecular cloud, without fragmentation, into a single star. This theory was proposed by Yorke and Sonnhalter, 2002. They used numerical simulations to study the collapse of isolated, rotating, non-magnetic, massive molecular cores with various masses. McKee and Tan, 2002 investigated the effects of supersonic turbulence and high pressures observed in regions of massive star formation. Zinnecker and Yorke, 2007 later expanded on the monolithic collapse model to incorporate the effects of magnetic fields and outflows, suggesting that these factors play a crucial role in shaping the final mass of the star.

Competitive accretion Compared to core accretion, competitive accretion is characterized by different initial conditions and physical processes that gather the mass of the most massive stars and form several massive stars within clusters (see e.g., Klessen, Burkert, and Bate, 1998; Bonnell, Bate, and Vine, 2003; Lada and Lada, 2003; Bate, Bonnell, and Bromm, 2003). Massive turbulent cloud fragments into several condensations of approximately M_{Jean} mass, and the individual fragments collapse in the cloud at a distance of approximately Jean's length ~ 0.05 pc (Larson, 1984). In this hierarchical picture of fragmentation, high-mass stars form from the accretion of gas and dust within the individual fragments onto smaller, lower-mass protostars. The accretion process is thought to be competitive, meaning that the most massive protostars accrete the most material, leading to the formation of the highest-mass stars. Although it caused the entire process to be inefficient because only a small fraction of the initial mass of clouds is converted into cores, and a fraction of the cores are converted to stars.

While the monolithic core-collapse theory and competitive accretion model have been popular explanations for forming high-mass stars, their limitations suggest they may need to provide a complete and accurate picture of the process. The recent work by Pelkonen et al., 2021 uses high dynamic range star-formation simulations to investigate the relationship between the final mass of a star and its prestellar core. The results showed that the CMF peak converged to a position close to the IMF peak, which is contrary to the core-collapse model. The similarities between the observed CMF (core mass function) and the stellar IMF (initial mass function)

from the same simulation lead to the conclusion that there is no direct relation between progenitor core masses and final stellar masses. Pelkonen et al., 2021 also found that a significant fraction of the mass reservoir of stars was outside of their progenitor cores and that the inflow region was much larger than the core. The competitive accretion model was also ruled out as the accretion rate was found to be a decreasing function of mass, contrary to the model. The study suggests that observed CMFs may not accurately represent the true cores due to resolution effects and potential fragmentation. The study concludes that larger computational resources and more efficient methods, such as non-ideal MHD and realistic cooling and heating with diffuse and point source radiative energy transfer, may benefit future works explaining star formation theories.

Throughout this chapter, I have explored the physics of the ISM and its dense molecular component, the molecular clouds, clusters, cores, stars and focusing on their formation and evolution. The present thesis aims to understand the early stages of cluster evolution in a massive filamentary cloud using observational data. In the following chapter, I introduce the NGC 6334-V as a sample cluster of our study and the observational data used.

1.6. NGC 6334 COMPLEX

NGC 6334 also known as the Cat's Paw Nebula, is a large and active star-forming region located in the Carina-Sagittarius arm of the Milky Way. It is located at a distance of 1.76 kpc (Russeil et al., 2020) and is one of the nearby largest and brightest HII regions known. The dense molecular gas is dominated by a ~ 20 pc long filamentary structure oriented along the northeast-southwest direction and along the direction of the galactic plane. The region is hot enough to emit emissions in a broad spectrum range, from radio to X-ray bands (e.g., Persi and Tapia, 2008; Russeil et al., 2010; Russeil et al., 2013). The nebula contains several massive, dense clumps with masses larger than $100 M_{\odot}$ and 150 O- to B3-type luminous stars (Neckel, 1978; Bica et al., 2003; Feigelson et al., 2009). The massive stars emit intense ultraviolet radiation, which ionizes the surrounding hydrogen gas and causes it to emit light in the visible and infrared parts of the spectrum. The central region of NGC 6334, consisting of a 12 pc long filament, comprises six main sources of star formation, assigned as Sources I to V and NGC 6334 I(N). These were identified using far-infrared/sub-mm/mm observations (e.g., Cheung et al., 1978; McBreen et al., 1979; Gezari, 1982). Source I is the most massive and luminous source and is thought to be responsible for much of the overall emission from the nebula. Sources

II to V and I(N) are also significant sites of star formation but are less massive and luminous than Source I. NGC 6334-V is a newly discovered source located at the intersection of the main filament and a smaller filament that extends toward the northwest-southeast direction (André et al., 2016), and is thought to be a site of ongoing star formation.

Many observations in recent years have focused on the effect of magnetic field structures on cloud formations at different scales (e.g., Zhang et al., 2014; Li et al., 2015; Juárez et al., 2017b; Palau et al., 2021; Arzoumanian et al., 2021; Cortés et al., 2021). Arzoumanian et al., 2021 reported a change in the orientation of the magnetic field in sub-filaments. The magnetic field shifted from being perpendicularly aligned with the outer portion of the sub-filament to parallel with the inner part as it merged into the main filament. They suggested that this change in the magnetic field direction may signal that gas flows inward from the sub-filaments towards the main filament. Tahani et al., 2022 used JCMT BISTRO $850 \mu\text{m}$ dust polarization observations and studied the magnetic field morphology of H II regions in association with NGC 6334. They investigated the role of H II regions on the morphology of magnetic fields in their parental cloud to determine the initial magnetic field morphology of the parental cloud prior to its evolution. They concluded that the magnetic field morphology of the NGC 6334 cloud was initially coherent and perpendicular but altered during cloud evolution due to internal feedback mechanisms or gas flow. The researchers also found that an increased polarization fraction accompanied the presence of radial polarization. Following that work, another study by Liu et al., 2022 used 1.3mm dust polarization and molecular line ALMA observations to study the multi-scale (from ~ 30 pc to 0.003 pc) physical properties of four dense clumps N6334I(N), I, IV, and V toward the central part of the NGC6334 cloud. They investigated the relationship between magnetic fields, column density gradients, local gravity, and velocity gradients and proposed that local gravity influenced magnetic field orientation in high column densities.

Another direction of recent studies focuses on the velocity distribution, the analysis of filamentary structures, and the effect of accretion along filaments in feeding star formation activities. Arzoumanian et al., 2022, studied the velocity structure along and across NGC 6334 central cloud and toward filaments using APEX observations $^{13}\text{CO}(2-1)$ and $\text{C}^{18}\text{O}(2-1)$ and NANTEN2 $^{12}\text{CO}(2-1)$. They showed a coherency in the velocity structure along the filamentary structure over the entire cloud and measured the properties of the 75 filaments identified in this study. The qualitative similarities between the observational results and numerical simula-

tions suggested that repeated HI compression trigger the formation and evolution of filamentary molecular clouds from expanding shells. We continue to study velocity structures in a zoomed-in region NGC 6334-V located at the end of the main central filamentary cloud NGC 6334. In the next section, we will learn about the general properties of this cluster and review recent studies.

1.7. NGC 6334 V

NGC 6334-V is located in the southernmost active star-forming site along the large-scale NGC 6334 dense gas filament. NGC 6334-V is placed at the intersection of the main filament and a smaller filament that extends toward the northwest-southeast direction (e.g., André et al. 2016).

NGC 6334-V is exhibiting signs of recent and ongoing star formation. It is a luminous far-infrared source, with a $L_{bol} \sim 10^4 L_{odot}$ (Harvey and Gatley, 1983). Furthermore, the presence of a CO molecular outflow (Fischer et al., 1982) and an NH_3 maser (Kraemer and Jackson, 1995), and H_2O and OH masers (Raimond and Eliasson, 1969) imply that energetic processes are active in the region (Zhang et al., 2014). These masers are commonly associated with high-mass star-forming regions and serve as tracers of ongoing star formation (Forster and Caswell, 1989; Brooks and Whiteoak, 2001). Furthermore, several infrared sources have been detected in the region that are believed to be associated with young stellar objects (Harvey and Gatley, 1983; Harvey, Wilking, and Joy, 1984; Simon et al., 1985; Kraemer et al., 1999). These sources are indicative of ongoing star formation and suggest that NGC 6334-V is a highly active region where new stars are being formed.

In addition to the above-mentioned signposts of star formation, NGC 6334-V is also characterized by three faint associated radio sources (Rengarajan and Ho, 1996). These sources may be associated with young, energetic stars and can provide valuable insights into the physical processes at work in the region.

Previous studies (Hashimoto et al., 2007; Simpson et al., 2009) have suggested the existence of two independent outflows in NGC 6334-V each potentially powered by one of the two infrared sources (KDJ3 and KDJ4) identified in the region (Kraemer et al., 1999). One of the outflows is oriented east-west along the line of sight, while the other has a north-south orientation almost in the plane of the sky.

One of the most recent studies by Juárez et al., 2017a used Submillimeter Array (SMA) molecular observations at 345 GHz to study magnetized filamentary structures toward a detected hot core in the center of cluster V. They showed the gas infall from the larger-scale extended dense core (~ 0.1 pc) of NGC 6334-V toward

the higher density hot core region (~ 0.02 pc) through two distinctive converging flows dragging the magnetic field, whose strength seems to have been overcome by gravity. Part of this thesis will study the connection of gas flows from large scale (≤ 1 pc) to small scale (≤ 0.1 pc).

1.8. ABOUT THIS WORK

The main goal of this thesis is to characterize the kinematics and structure of the massive star-forming cluster NGC 6334-V, embedded in the filamentary cloud NGC 6334. Through continuum and spectral line high spatial resolution ALMA observations, along with multi wavelength ancillary observations, I will identify the continuum cores embedded in the central hub and investigate the stages of an evolutionary sequence. Moreover, I will utilize different molecular line tracers to characterize the mass accretion process and investigate the effects of accretion in creating both high- and low-velocity shocks. This thesis is organized as follows:

Chapter 1 presents an overview of star formation, beginning with large-scale molecular clouds and proceeding to hierarchical fragmentation through filaments, leading to the birth of star clusters that serve as a harbor for star-forming regions. The chapter then briefly explains both low and high-mass star formation and introduces the theoretical models for massive star formation. In the end, it introduces the NGC 6334 complex and, specifically, source V as the target of this research.

Chapter 2 introduces the underlying theories of radiative transfer, emission mechanisms and provides a brief overview of both single-dish observation and radio interferometry.

Chapter 3 presents the details of the observations targeted at the high-mass protocluster NGC 6334-V, and explains the data reduction process that yielded the maps and data cubes essential for scientific analysis.

Chapter 4 presents the detailed analysis performed on the continuum data to study the physical properties within the observed protocluster NGC 6334-V.

Chapter 5 and 6 delve into the detailed analysis of molecular line emissions. Chapter 5 focuses on the study of temperature determination and filamentary accretion towards the central cluster. Chapter 6 is dedicated to characterizing the shocked gas and investigating the origin of extended SiO emissions.

1

Chapter 7 summarizes the results of the previous chapters and provides an outlook on potential next steps in high mass star formation research.

2

EMISSION MECHANISMS & RADIO INTERFEROMETRY

2.1. RADIATIVE TRANSFER

Radiative transfer refers to the transport of electromagnetic radiation through a medium in a complex process involving the interaction of radiation with matter, including absorption, scattering, and emission (Chandrasekhar, 1960). The intensity and direction of radiation can change as it interacts with the medium. The basic equation for radiative transfer while neglecting the scattering part is

$$dI_\nu = -I_\nu \kappa_\nu ds + j_\nu ds, \quad (2.1)$$

which describes the rate of change of radiation intensity with respect to distance along a thickness ds in a medium (Draine, 2011). This equation takes into account the attenuation of the intensity due to the effective absorption (the difference between true absorption and stimulated emission) $(-I_\nu \kappa_\nu ds)$ and the increase in intensity due to spontaneous emission $(j_\nu ds)$ by sources within the medium. The κ_ν is the attenuation coefficient at frequency ν , with dimensions of 1/length, and j_ν is the emissivity at frequency ν , with dimensions of power per unit volume per unit frequency per unit solid angle. By defining the optical depth as $d\tau = \kappa_\nu ds$ and the source function as $S_\nu = \frac{j_\nu}{\kappa_\nu}$, we can simplify the radiative transfer equation as

$$\frac{dI_\nu}{d\tau_\nu} = -I_\nu + S_\nu. \quad (2.2)$$

The intensity in Thermodynamic Equilibrium (TE) is uniform $I_\nu/d\tau_\nu = 0$, and given by the Planck function $B_\nu(T)$, thus

$$I_\nu = S_\nu = B_\nu(T) = \frac{j_\nu}{\kappa_\nu} \quad (\text{in TE}). \quad (2.3)$$

The general solution of the radiative transfer equation is obtained by integrating Eq. 2.2 by invoking the integrating factor $e^{-\tau_\nu}$:

$$I_\nu(\tau_\nu) = I_\nu(0)e^{-\tau_\nu} + \int_0^{\tau_\nu} e^{-(\tau_\nu - \tau')} S_\nu d\tau'. \quad (2.4)$$

The right-hand side of the equation above consists of two terms. The first term corresponds to the background intensity attenuated by the optical depth. The second term represents the radiation emitted by the medium. In the case of uniform medium, the emission coefficient and source function are also uniform and the Eq. 2.4 simplify into

$$I_\nu(\tau_\nu) = I_\nu(0)e^{-\tau_\nu} + S_\nu^0(1 - e^{-\tau_\nu}) \quad (2.5)$$

that has two solutions: If the background intensity dominates over emission from the medium, then the observed intensity is given by

$$I_\nu(\tau_\nu) \simeq I_\nu(0)e^{-\tau_\nu} \quad (2.6)$$

and if the emission from the medium dominates and the background intensity becomes negligible, then the observed intensity is given by

$$I_\nu(\tau_\nu) \simeq S_\nu^0(1 - e^{-\tau_\nu}) \quad (2.7)$$

In this case, if the medium is optically thin ($\tau_\nu \ll 1$), the observer will receive the emission that passes through the medium (Ward-Thompson and Whitworth, 2011) and the Eq. 2.7 becomes

$$I_\nu(\tau_\nu) \approx S_\nu^0 \tau_\nu. \quad (2.8)$$

and in an optically thick medium ($\tau_\nu \gg 1$), the observer will receive the emission from a thin layer at the front of the medium and the Eq. 2.7 simplifies to

$$I_\nu(\tau_\nu) \approx S_\nu^0. \quad (2.9)$$

There are two types of radiation: continuum and line radiation. Continuum radiation comes from interstellar dust, free-free radiation (Bremsstrahlung), and synchrotron radiation from ionized plasma distributed over a wide range of frequencies (Marr, Snell, and Kurtz, 2015). Two mechanisms can produce radio continuum radiation in star forming regions: thermal and nonthermal radiation. Thermal radiation is any electromagnetic radiation emitted by matter due to its thermal energy, which is measured through the temperature of the matter. Thermal radiation is produced either from the dust grains due to the heating by the absorbed surrounding radiation, or from free electrons interacting with the Coulomb field of a charged particle (ionization), or when electrons move from one orbit in an atom to another (excitation). In contrast, line radiation comes from molecular spectral lines that peak at specific frequencies. The study of continuum radiation is known as photometry, and the study of line radiation is named spectroscopy. In order to further studies, the books of Ward-Thompson and Whitworth, 2015; Draine, 2011 provided a more detailed overview of radiative transfer.

2.2. CONTINUUM EMISSION FROM DUST

In star forming regions, young stellar objects are surrounded by abundant gas and dust. Interstellar dust consists of tiny grains, less than a micron, mostly silicates and carbon components. The dust grains absorb the radiation emitted by the protostar, causing high extinction at optical wavelengths in star-forming regions. Due to the low dust temperature, the absorbed radiation is re-emitted at longer wavelengths, mainly at infrared (IR) and millimeter (mm) wavelengths. The radiation from the dust can be studied by observing it at specific wavelengths. The background intensity is usually negligible when studying the continuum emission from dust. We also assume a black body radiation field, which is a uniform and isotropic radiation field in thermodynamic equilibrium. If the emitting dust is at a single temperature, we can substitute S_ν^0 with the Planck function $B_\nu(T_{\text{dust}})$ in Eq. 2.7

$$I_\nu(\tau_\nu) = B_\nu(T_{\text{dust}})(1 - e^{-\tau_\nu}) \quad (2.10)$$

where τ_ν is the optical depth as a function of frequency and $B_\nu(T_{\text{dust}})$ is the Planck function:

$$B_\nu(T_{\text{dust}}) = \frac{2h\nu^3}{c^2} \frac{1}{e^{h\nu/kT_{\text{dust}}} - 1} \quad (2.11)$$

By obtaining enough measurements of I_ν in Eq. 2.10 across various frequencies, we can use this equation to calculate the temperature and optical depth of the dust being observed. We can calculate the flux density by integrating the specific intensity over the angular size as

$$S_\nu = \int_{\Omega_{\text{source}}} B_\nu(T_{\text{dust}})(1 - e^{-\tau_\nu}) d\Omega \quad (2.12)$$

Where the angular size of the source, Ω_{source} , can be determined observationally from the angular diameter as $\Omega_{\text{source}} = (\pi/4ln2)\theta_S$ and the optical depth, τ_ν , is proportional to the column mass density along the line of sight l and absorption coefficient κ_ν as $\tau_\nu = \int \kappa_\nu \rho dl$.

The observed flux density can be used to estimate the mass of gas and dust in optically thin emissions as

$$M_{\text{d+g}} = \frac{S_\nu D^2}{B_\nu(T_{\text{dust}})\kappa_\nu}, \quad (2.13)$$

where D is the distance to the source.

We can estimate the volume density and column density of dust and gas from the total mass. Since the molecular hydrogen H_2 has a major contribution to gas, it is common to refer to these variables as n_{H_2} and N_{H_2} , respectively. The volume density in a spherical cloud is given by

$$n_{H_2} = \frac{1}{\mu m_H} \frac{M_{d+g}}{(4/3)\pi R^3}, \quad (2.14)$$

where μ is the mean molecular mass per Hydrogen atom, m_H is the Hydrogen mass, and R is the radius of the cloud. Finally, the column density can be determined by integrating over volume density along the line of sight as

$$N_{H_2} = \int_{\text{line of sight}} n_{H_2} dl. \quad (2.15)$$

2.2.1. IONIZED GAS AND H II REGIONS

Generally, the gas associated with star-forming locations can be ionized through different mechanisms, including photoionization, ionization through shocks, and ionization in accretion flows. Ionized gas is the common state of matter in the interstellar medium (ISM), where ultraviolet radiation from young, massive stars can ionize the surrounding gas. Regions of ionized gas are known as H II regions, where ionized hydrogen atoms (H^+) are the most abundant particle in these regions. H II regions can be observed through their emission at centimeter wavelengths, which come from the interaction of free electrons with charged particles such as protons or ionized hydrogen nuclei. This type of emission is known as "free-free" emission or Bremsstrahlung. Additionally, H II regions can be observed in the (far) infrared and submillimeter regimes, mainly due to the thermal emission from dust grains in associated clouds. Thus, the continuum radiation from H II regions mainly contains a mixture of thermal emission from dust grains and free-free emission from unbounded particles.

The morphology of the H II region depends on the initial distribution of the surrounding medium, and the size depends on the total energy radiated by the source. In the homogeneous H II regions, electrons from ionized atoms are free particles and unbounded, so the radiation produced will have a continuum spectrum known as thermal Bremsstrahlung or free-free emission. The fundamental equation of flux density in H II region is given by

$$S_\nu = \int_{\Omega_{\text{source}}} B_\nu(T_e)(1 - e^{-\tau_{ff}(\nu)})d\Omega \quad (2.16)$$

where $\tau_{ff}(\nu)$ is the optical depth of the free-free emission expressed as

$$\tau_{ff}(\nu) = 0.08235 \left[\frac{EM}{\text{cm}^{-6} \text{pc}} \right] \left[\frac{T_e}{\text{K}} \right]^{-1.35} \left[\frac{\nu}{\text{GHz}} \right]^{-2.1} \quad (2.17)$$

where EM is the emission measure defined as $EM = \int_0^l n_e^2 dl$ with the electron density n_e of the ionized gas. For a homogeneous H II region with constant density, Equation 2.16 is become as

$$S_\nu = S_\nu (1 - e^{-\tau_{ff}(\nu)}) \Omega_{\text{source}} \quad (2.18)$$

2.3. MOLECULAR EMISSION

Atoms, ions, and molecules typically have discrete, quantized energy levels that transition from one level to another by emitting or absorbing a photon. Three different processes of absorption, spontaneous emission, and stimulated emission would happen between an upper energy level (E_u) and a lower energy level (E_l) to change the energy state of electrons among levels (Figure 2.1).

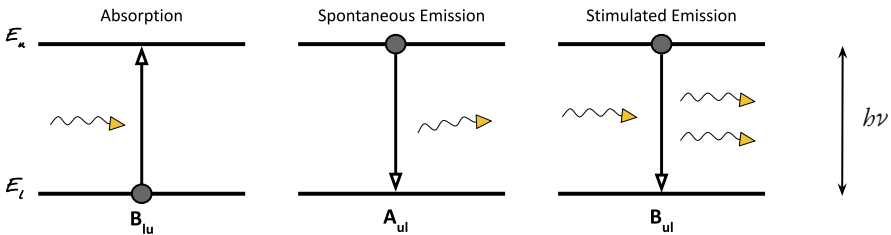


Figure 2.1.: Three possible processes between an upper energy level (E_u) and a lower energy level (E_l)

The energy difference between transition states determines the frequency of the observed photon. Nevertheless, the precise frequency ν of the absorbed or emitted photon may not be observed due to line-broadening and Doppler effects. To account for this, a line profile $\phi(\nu)$ is introduced to describe the susceptibility of the transition to photons of frequency ν . Furthermore, molecular spectra are more complex than most atomic spectra because molecules have additional degrees of freedom associated with vibration and rotation. In particular, each electronic state of a molecule comprises a range of vibrational levels, each with a corresponding ladder of rotational levels. Therefore, electronic transitions occur in molecules be-

tween certain vibrational and rotational levels within each electronic state (Figure 2.2).

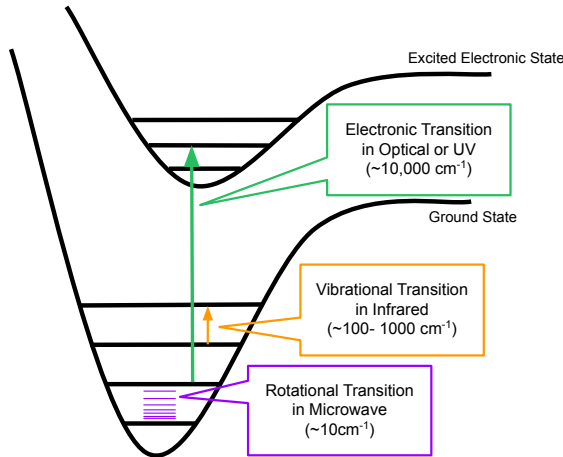


Figure 2.2.: The energy levels of a diatomic molecule are classified into three levels electronic, vibrational, and rotational.

In electronic transition, an electron changes molecular orbitals with large energy differences and relatively high-energy photons in the optical and ultraviolet regimes. In vibrational transitions, the energy of photons is observed in the infrared region, and rotational transitions yield photons in the millimeter and sub-millimeter radio regimes. In the interstellar medium, temperatures are $\sim 10\text{--}20$ K, and molecules are mostly rotationally excited. Molecular transitions may also occur between specific rotational states of vibrational states, named rovibrational transitions.

The density populations of transitions between two energy levels with density populations N_u and N_l for the upper and lower states are usually described by the excitation temperature, T_{ex} , through the Boltzmanns equation

$$\frac{N_l}{N_u} = \frac{g_l}{g_u} e^{-\Delta E_{lu}/k_B T_{\text{ex}}}, \quad (2.19)$$

where g_u and g_l are the degeneracies of the upper and lower levels, and ΔE_{lu} is the energy difference between both states. The total molecular column density can be calculated from the sum of all the i -level column densities as follow

$$N_{\text{mol}} = \sum_{\text{all levels}} N_l = N_u \sum_{\text{all levels}} \frac{g_l}{g_u} e^{-\Delta E_{lu}/k_B T_{\text{ex}}}. \quad (2.20)$$

by defining partition function as $Q \equiv \sum g_l e^{-\Delta E_l/k_B T_{\text{ex}}}$, the molecular column density, N_{mol} can be written as

$$N_{\text{mol}} = N_u \frac{Q}{g_u} e^{-\Delta E_u/k_B T_{\text{ex}}}. \quad (2.21)$$

Three observational parameters are needed to calculate the column density: the excitation temperature, the observed linewidth, and the optical depth at the center of the line; we also need to distinguish between single rotational transitions and transitions with hyperfine structure. The total partition function is a coupling between transitional and internal functions, where the transitional component is unnecessary in calculating column density (Araya et al., 2005). The internal partition function also contains rotation, electronic, and electronic modes. If the electronic and vibrational modes are assumed to be negligible, we can write $Q \simeq Q_{\text{rot}}$. It is worth noting that in the case of collisional excitation in high gas density under the Local Thermodynamic Equilibrium (LTE) conditions, T_{ex} equals the kinetic temperature T_{kin} .

2.4. RADIO ASTRONOMY

Radio waves are a form of electromagnetic (EM) radiation with wavelengths ranging from about 1 mm to 100 km, corresponding to frequencies ranging from 300 GHz to 3 kHz (Marr, Snell, and Kurtz, 2015) that penetrates through interstellar dust and gas to detect the thermal continuum and spectral line emission from objects too cold to produce visible light (Figure 2.3). Radio observations can commonly be carried out using single-dish antennas or interferometers that are employing multiple antennas. A simple radio telescope is composed of three main parts: an antenna that includes a dish or reflector to collect radio lights, a mounting structure that holds and moves the dish to track the object, and a group of feed that collects the reflected radio waves from the dish and converts the EM waves in free space into confined EM waves in transmission lines. The second part is the receivers, which contain two parts: front-end and back-end receivers. The front-end receiver attaches to the telescope and is very close to the feeds to amplify and convert the input signal and restrict unnecessary frequency ranges. The amplified signal is sent to the back-end receiver, which measures its power and converts it to a digital sig-

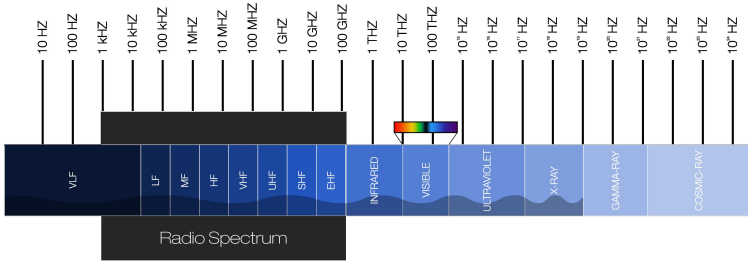


Figure 2.3.: Radio frequency band designations
 credit: <https://www.nasa.gov>

nal. Finally, in the third part, the digital signal is stored on a computer for further analysis(Figure 2.4).

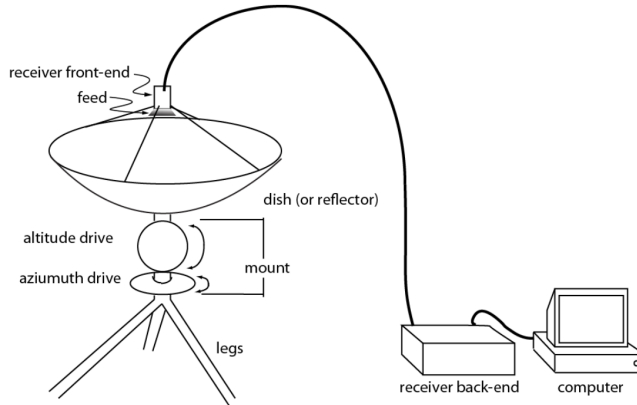


Figure 2.4.: A prime focus radio telescope and its three main parts: antenna, receivers and computer.
 Credit: Marr, Snell, and Kurtz, 2015

This thesis is focused on the study of star-forming regions in the (sub-)millimeter wavelength range. The following sections will discuss the techniques used in radio astronomy observations and the fundamental principles of radio observations using single-dish telescopes and radio interferometers.

2.4.1. SINGLE-DISH OBSERVATIONS

In a single-dish observation, we use one antenna to observe the astronomical source. The primary parabolic reflector collects and focuses radiation, making faint sources

detectable. The effective area (A_{eff}) of a telescope determines how much radiation is captured, and the amount of power a telescope collects from a source of given flux density (F_ν), is given by (Marr, Snell, and Kurtz, 2015)

$$P = F_\nu A_{\text{eff}} \Delta\nu, \quad (2.22)$$

where $\Delta\nu$ is the frequency range bandwidth. The power measured from the source is equivalent to the antenna temperature (T_A) with different contamination from the receiver noise and other sources of unwanted radiation. In order to determine antenna temperature in single-dish observations, telescopes observe a nearby patch of the sky, known as the off-position, which contains no signal from the radio sources, and subtract the measured voltage when the telescope is pointed at the source (V_{on}) from the measurement when it is pointed away from the source (V_{off}).

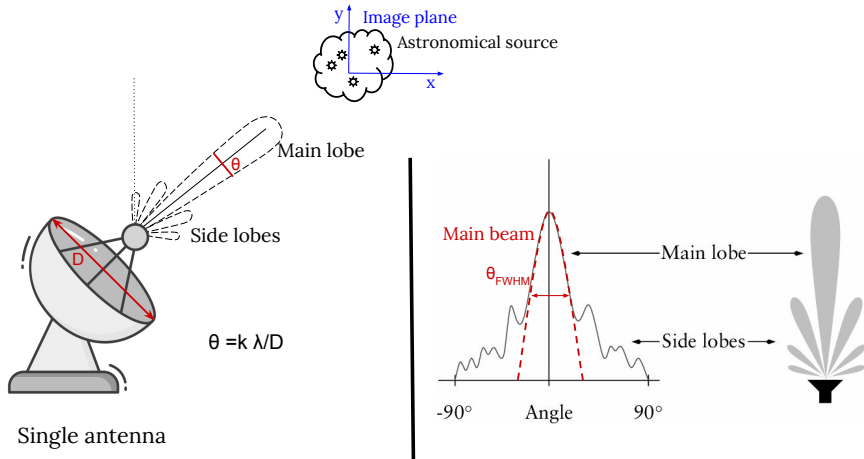


Figure 2.5.: A schematic view of main lobe and side lobe in single-dish telescope

The primary reflector also provides the ability to differentiate the emission from objects close to each other in angular position on the sky, which determines the resolutions on the map. Every dish has a beam pattern that measures the sensitivity of the telescope to incoming radio signals as a function of the angle. The beam pattern contains a large central part named the main beam, which peaks toward the pointing direction of the antenna and oscillates between zero and ever-decreasing (but non-zero) values. The zero points on either side of the main lobe are called the first nulls, and the non-zero responses outside the first nulls are called side-

lobes (Figure 2.5). The main beam is approximated as a Gaussian function of the form

$$P_{\text{main}}(\theta) = \exp\left[-4\ln 2 \left(\frac{\theta}{\theta_{\text{FWHM}}}\right)^2\right] \quad (2.23)$$

Where θ_{FWHM} is the Full Width at Half-Maximum (FWHM) of the main beam. As shown in Figure 2.5, the angular resolution of the telescope in the FWHM of the main beam as a function of the wavelength of the observation (λ) and is the diameter of the primary reflector (D) as

$$\theta_{\text{FWHM}} = 1.022\lambda / D. \quad (2.24)$$

Astronomical sources are commonly classified as resolved or unresolved. An extended or resolved source has a much larger angular size than the main beam of the telescope. However, an unresolved source (also called a point source) has an angular size much smaller than the main beam. In the point source observations, the antenna temperature is given by

$$T_A = \frac{A_{\text{eff}}}{2k} F_\nu. \quad (2.25)$$

And finally, we can directly measure the source flux density if the astronomical source is a point source via

$$F_\nu = \frac{2k}{A_{\text{eff}}} T_A. \quad (2.26)$$

Unlike an unresolved source, we do not observe the flux density of a resolved source. Instead, the antenna temperature measures intensity averaged over the main beam as

$$I_\nu = \frac{2k}{A_{\text{eff}}\Omega_{\text{main}}} T_A, \quad (2.27)$$

Where Ω_{main} is the solid angle of the main beam and determined by integrating the main beam power pattern (Equation 2.23) over all angles and is defined as

$$\Omega_{\text{main}} = \frac{\pi}{-4\ln 2} \theta_{\text{FWHM}}^2 \quad (2.28)$$

2.4.2. RADIO INTERFEROMETRY

Long wavelengths of radio waves set some limitations in terms of spatial resolution in single-dish observations that are directly connected to the size of the dish. One solution to this problem is the aperture synthesis technique. Through this method, a large number of telescopes are arranged in an array, and each pair of telescopes is treated as an interferometer to synthesize a new telescope with a significantly larger diameter.

In its simplest form, an interferometer contains two pairs of telescopes that observe the same source. The outputs of telescopes are combined and mathematically processed to produce the equivalent resolution of a single, large telescope. By using this approach, we can achieve an effective resolution that is approximately equal to the diameter of a telescope, whose diameter equals the largest distance between antennas in the array (Figure 2.6). As shown in Figure 2.6, consider two identical

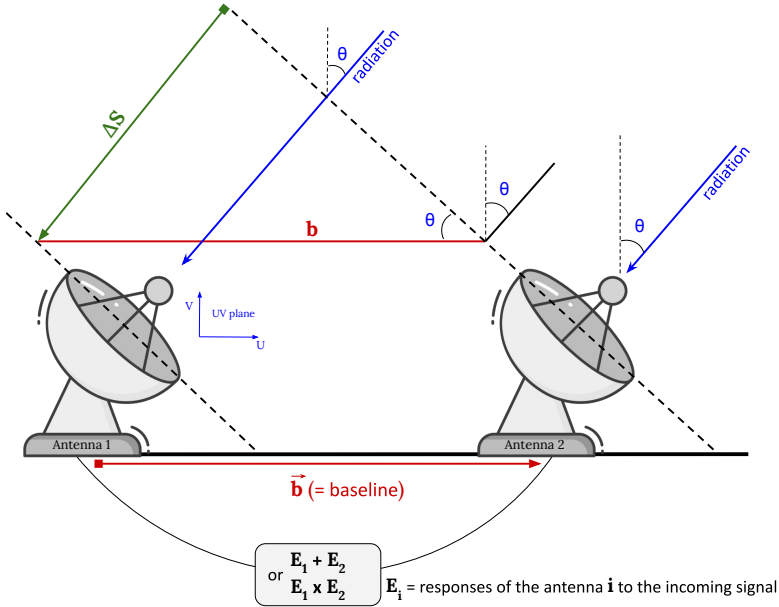


Figure 2.6.: A schematic view of two array of two antennas

antennas separated by b , along with a radio source with a minimal angular extent, which can be assumed to be a point. The signals from a point source are transmitted parallel to both antennas along directions θ relative to the zenith. The electric field E_1 and E_2 are the responses of the antennas to the incoming signal with a phase difference of $\Delta\phi = 2\pi\nu\tau$ and time delay $\tau = \Delta S/C$.

$$\begin{aligned} E_1 &= E_0 \cos(2\pi\nu\tau) \\ E_2 &= E_0 \cos(2\pi\nu\tau + \Delta\phi) \end{aligned} \quad (2.29)$$

In actual interferometer observations, the signals from the two antennas are processed by the receivers in every single antenna and could then be added or multiplied. Since the additive interferometer could contain contributions due to receiver noise, we consider the multiplicative approach. A more detailed description of noise in interferometry is discussed in Marr, Snell, and Kurtz, 2015. The power as a function of time is obtained by multiplying and averaging the electric fields (Equations 2.29) in the correlator and considering $\nu = 1/\lambda$ and $\Delta S = b \sin\theta$, allowing us to write

$$\begin{aligned} P_\theta &= \langle E_1 \cdot E_2 \rangle = \frac{E_0^2}{2} \cos(2\pi\nu\tau) \\ &= \frac{E_0^2}{2} \cos\left(2\pi \frac{b}{\lambda} \sin\theta\right) \end{aligned} \quad (2.30)$$

which is applied for multiplicative interferometer. Due to the Earth rotation, θ slowly varies with time, and the response of an interferometer is quasi-sinusoidal. This oscillating response is often referred to as fringes. The multiplicative interferometer can be calibrated by observing a point source with a known flux density F_ν and fitting the fringe oscillations to the expected time dependence. The calibrated response of a multiplicative interferometer is given by

$$R = F_\nu \cos\left(2\pi \frac{b}{\lambda} \sin(\omega_E t)\right) \quad (2.31)$$

where $\theta = \omega_E t$ is the source position relative to the baseline zenith.

3

OBSERVATIONS & DATA ANALYSIS

This chapter presents a comprehensive overview of the observations utilized in this thesis, emphasizing the essential role of the Atacama Large Millimeter/sub-millimeter Array (*ALMA*) data in our research. Our analyses mainly rely on the *ALMA* data. Furthermore, I also examined archival data obtained at submillimeter and infrared wavelengths to explore the connection between the larger structures detected through ancillary data and the small scale structures observed through *ALMA*.

3.1. *ALMA*

The *ALMA* is the largest ground-based aperture synthesis telescope operating in the frequency band ranging from 84 GHz to ~ 950 GHz, corresponding to wavelengths of 0.32 mm to 3.6 mm. *ALMA* contains 66 high-precision antennas located at the 5000-m high plateau at Chajnantor and divided into two groups: the 12-meter array and the Atacama Compact Array (*ACA*).

The 12-meter array is composed of 50 antennas, each with a diameter of 12 meters, which are arranged in different extended configurations. In the most compact 12-m array configurations (~ 160 m), resolutions range from 0.5 arcsec at 950 GHz to 4.8 arcsec at 110 GHz. In the most extended 12-m array configuration (~ 16 km), the resolutions range from 20 mas at 230 GHz to 43 mas at 110 GHz. These numbers refer to the FWHM of the synthesized beam (point spread function), which is the inverse Fourier transform of a (weighted) *u-v* sampling distribution.

The Atacama Compact Array (*ACA*) is composed of 16 antennas located in a compact configuration. Twelve 7-m antennas were designed for interferometry (the 7-m array) and four 12-m antennas for single-dish observations (*TP Array*). The four single-dish antennas provide spatial information samples equivalent from 0 m up to 12 m spacing as auto-correlations. The 7-m array samples baselines from 9 m to 30 m, bridging the baseline sampling gap between the 12-m array and the *TP Array*. The *ACA* array in a compact configuration with a maximum baseline of 160 m observes shorter wavelengths and reaches a resolution of 4.8 arcsec at 110 GHz. The maximum baseline of the *ACA* is 0.6 km, providing a wide field of view for surveying the sky.

3.1.1. OBSERVATIONAL SETUPS

The region NGC 6334-V was observed with the *ALMA* during its Cycle 3, between April and September 2016 (Project ID: 2015.1.00230.S). The observations



Figure 3.1.: The compact array and a part of the 12-meter array in the aerial image of the ALMA interferometer
Credit: Clem & Adri Bacri-Normier

Table 3.1.: Spectral windows used in the ALMA observations centered at eleven transitions and one broad continuum band

Transition	Freq. (GHz)	Δv_{res} (km s ⁻¹)	Beam size $\theta''_{\text{maj}} \times \theta''_{\text{min}} ; \text{PA}^\circ$
CH ₃ CCH (5 _K -4 _K)	85.449	0.495	1.7 × 1.3 ; -43.0
H42 α	85.688	0.494	1.7 × 1.3 ; -44.1
NH ₂ D (1-0)	85.926	0.492	1.7 × 1.3 ; -44.5
HC ¹⁵ N (1-0)	86.054	0.492	1.7 × 1.3 ; -44.0
H ¹³ CN (1-0)	86.340	0.424	1.7 × 1.3 ; -43.9
H ¹³ CO ⁺ (1-0)	86.754	0.488	1.8 × 1.4 ; -47.0
SiO (2-1)	86.847	0.487	1.8 × 1.4 ; -47.2
HN ¹³ C (1-0)	87.090	0.486	1.7 × 1.3 ; -43.9
CCH (1-0)	87.316	0.484	1.6 × 1.3 ; -44.3
HCN (1-0)	88.631	0.413	1.7 × 1.3 ; -47.3
H ¹⁵ NC (1-0)	88.865	0.476	1.6 × 1.1 ; -42.2
Continuum	87.600	106.9	1.5 × 1.1 ; -57.4

were carried out using the 12 m array consisting of 40–43 antennas and the 7 m

Atacama Compact Array (ACA) with up to 8–9 antennas. I mapped an area of $2' \times 2'$ with phase center coordinates of R.A. (J2000) = $17^{\text{h}}19^{\text{m}}57^{\text{s}}$ and Dec. (J2000) = $-35^{\circ}57'52''$, and reached an angular resolution of $\approx 1''.4$ (corresponding to ≈ 2400 au). The black square in Figure 3.3 shows the coverage of ALMA observation. The 12-m array has minimum and maximum baselines of 14–626 m, corresponding to 1.4arcsec–25arcsec in angular scales, with the main array at 88 GHz. Both compact and extended configurations are selected to overlap the observed angular scales. The combined data sets obtained from the main arrays and compact arrays give a final scale coverage of 1.4arcsec to 40arcsec.

The observations were conducted in Band 3 of ALMA at a frequency of about 87.6 GHz. The spectral setup consists of a broad spectral window (with a total bandwidth of 1875 MHz) used to characterize the continuum emission and twelve high-resolution spectral units targeting specific spectral lines (see Table 3.1). The high-resolution units provide a bandwidth of 58.59 MHz each, a spectral resolution of 141 kHz (equivalent to $\approx 0.5 \text{ km s}^{-1}$), and cover frequencies of specific molecular transitions as a tracer of studying dense (e.g., HCN, H^{13}CO^+ , and CH_3CCH), ionized (e.g., H42ff) and shocked gas (e.g., SiO).

3.1.2. CALIBRATION

The effects of ionospheric, atmospheric, or instrumental variations can distort the raw data observed by the interferometer. Calibration is the process of correcting the measured visibilities and obtaining the true visibilities. In interferometric observations, three primary calibrations are commonly used: flux, gain/phase, and bandpass.

Flux calibration is the process of correcting the conversion factor between the instrumental response and the true flux density of the observed object. Flux calibration is done by observing a bright point-like source with a known flux density. The ideal source for this calibration is a point source located at the phase center of the field, where all baselines in the interferometer measure the same amplitude equal to the flux density of the source and zero phase. The flux was calibrated by observing the bright quasar J1733–1304 (with a flux of 3.63 Jy at 91.5 GHz, and a spectral index of -0.53) and Neptune.

Gain/phase calibration is the process of correcting the visibility amplitudes and phases for the remainder of the observation. The response of the instrument can vary in time and frequency, and is a function of the electronic components of the instrument. This response can be corrected by observing a known calibrator source

with a known position and flux density and using its measured visibilities to determine the gain and phase corrections for each antenna. These corrections can then be applied to the visibilities of the target object. The gain calibrator was the quasar J1717–3342 (flux of 0.64 Jy at 91.5 GHz, with a spectral index of -0.32). The phase calibrator was observed every eight minutes to correct for the variations in the atmosphere during the observations.

Bandpass calibration is the process of correcting for the frequency response across the bandpass, especially in spectral line observations. This response can be corrected by observing a known bright continuum source with a known spectral shape and using its measured visibilities to determine the frequency-dependent response of the interferometer. This response can then be applied to the visibilities of the target object. The bandpass response was calibrated through observations of the bright quasars J1617–5848 and J1924–2914.

The data calibration was performed using the ALMA calibration pipeline available in Common Astronomical Software Application (CASA) version 4.7.2. The calibrated dataset contains all spectral lines and saved in the form of CASA MeasurementSets. Following calibration, I identified line-free channels within the wide band of 1875 MHz centered at the frequency of 87.6 GHz. I utilized the CASA task `uvcontsub` to subtract the continuum level using line-free channels.

3.1.3. IMAGING

In interferometric observations, the Fourier transform of the measured visibilities represents the intensity distribution map of the source in the uv -plane. The baseline vectors u and v (measured in wavelengths $u = \frac{b_x}{\lambda}$ and $v = \frac{b_y}{\lambda}$), form the axes of the uv -plane. The uv -plane contains information about the spatial frequencies of the source, which correspond to the size and shape of the emission region. However, the observed visibility distribution does not entirely cover the uv -plane due to practical limitations. During interferometer observations, in addition to the primary beam of each telescope, a synthesized beam of the interferometer also exists. This synthesized beam is calculated through the Fourier transform of the points in the uv -plane for measuring visibilities. Cleaning continuum emission and molecular spectra datasets were performed using CASA task `tclean`. I set the deconvolver to multiscale synthesis, and used the auto-multithresh masking method. As a compromise between resolution and sensitivity, the robust parameter of Briggs was set to $+0.5$. Finally, I used the ‘model-assisted’ method (see Sadaghiani et al. 2020 for details) to combine datasets taken with the 12 m array and 7 m ACA for both line

and continuum maps. In this method, the *ACA* image is used as a source model in the cleaning process of the 12 m array dataset. This process improves convergence and produces an image with fewer artifacts (e.g., negative values due to missing fluxes, side lobe effects, and so on). Using the ‘model-assisted’ method, I generated final combined images of the 12 m array and 7 m *ACA* datasets using the feather task in *CASA*.

The final continuum image has a synthesized beam of $1''.5 \times 1''.1$, with position angle $-57^\circ.4$, while the line data cubes have a beam of about $1''.7 \times 1''.3$. The root-mean-square (rms) noise level for the continuum image is about $0.04 \text{ mJy beam}^{-1}$, which results in a dynamic range of ≈ 600 measured as the peak brightness of the map to the mean rms value throughout the map. For the spectral line images, the rms noise level per a 0.5 km s^{-1} channel width ranges from $1.0 \text{ mJy beam}^{-1}$ (in emission-free channels) to about $5.0 \text{ mJy beam}^{-1}$.

3.1.4. COMBINATION

One limitation of observing nearby sources with an interferometer is that the array misses some of the extended emissions from the source due to the non-zero shortest baseline. One solution for recovering the missing flux is to combine high-resolution observations from the interferometric array with lower-resolution observations of the same source obtained using a single-dish or compact telescope.

Among the different configurations of the *ALMA* array, the extended 12-m configuration can provide a highly detailed and high-resolution view of fine structures. In contrast, compact 7-m configurations or single-dish observations can recover the emission of the extended structures in the observed region. Combining data from the 12-m and 7-m arrays could enhance the sensitivity and resolution of *ALMA* observations. There are several approaches to combining data from two arrays or an array and single-dish observations. There are several approaches for combining data from two arrays or an array and single-dish observations. In this work, I tested three different approaches using *ALMA* data to determine which approach recovers the highest emission:

Joint deconvolution: The joint deconvolution method involves combining the visibilities of two calibrated data sets in the uv -plane. Each 12-m and *ACA* data set is first calibrated separately using the *ALMA* calibration pipeline. The visibilities are then combined in the uv -plane using the *CONCAT* task in *CASA*, with weights of 1 applied to each data set. Next, the combined data set is *CLEANed* using the auto-masking algorithm. The weighting scheme used in

the CLEANing process is also set to Briggs with a robust parameter of 0.5, similar to the 12-m data cubes. The exact number of iterations needed may vary depending on the configurations due to the large number of points in the combined data set. I set the iteration count to 100,000. The final image shows no success in recovering emission, and I had to move on to other approaches. The final combined image is restored with a synthesized beam of $1''.6 \times 1''.2$.

Feather: This approach combines observations from separate telescopes, particularly a single dish, with interferometric data in the image domain. This work assumes that *ACA* behaves similar to single-dish data. First, two distinct images were derived independently from the 12-m and *ACA* data sets. Once the imaging stage is complete, the two resulting images are combined utilizing the Fourier transform plane through the implementation of the Feather task in the *CASA* software package. Notably, the weights assigned to both the *ACA* and 12-m images during the process have an identical value of 1, similar to the joint deconvolution technique. The final combined image in feather method is restored with a synthesized beam of $1''.7 \times 1''.3$.

Model-assisted: In this method, the *ACA* image is used as a source model in the cleaning process of the 12 m array dataset. This process improves convergence and produces an image with fewer artifacts (e.g., negative values due to missing fluxes, side lobe effects, and so on). Using the ‘model-assisted’ method, I generated final combined images of the 12 m array and 7 m *ACA* datasets using the feather task in *CASA*. The final continuum image has a synthesized beam of $1''.5 \times 1''.1$, with position angle $-57^\circ.4$, while the line data cubes have a beam of about $1''.6 \times 1''.2$.

To evaluate the effectiveness of the different data combination methods, the amount of extended emission recovered in both continuum and molecular line maps was considered. In Figure 3.2, the left panel displays the combined peak intensity maps of H^{13}CO^+ towards NGC 6334-V generated using the three methods. Meanwhile, the right panel illustrates the spectrum of the marked regions on the maps. Table 3.2 lists the peak intensity, flux density, noise level, and signal-to-noise ratio in the marked regions. Based on the values presented in the table, all three methods yield similar results. However, the data combination using the model-assisted cleaning plus Feather method yielded the highest integrated intensity, with a better signal-to-noise ratio compared to the other two methods. Therefore, this ap-

proach was employed in the remaining molecular emission datasets observed with ALMA.

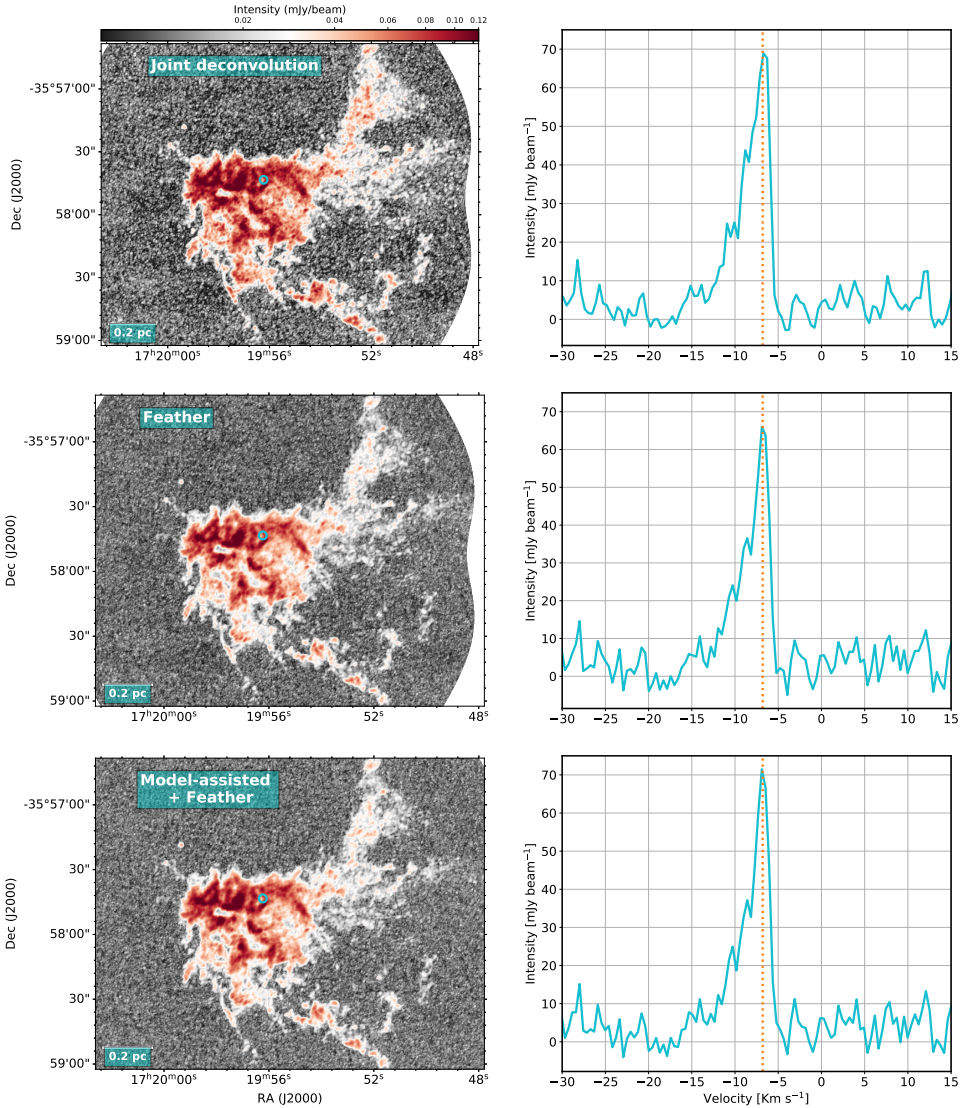


Figure 3.2.: *Left*: Peak intensity maps of H^{13}CO^+ toward NGC 6334-V were created using a combination of ALMA 12-m data and ACA data with three combination methods: Joint deconvolution, Feather, and Model-assisted. (*Right*): Extracted spectrum from the cyan circle in the maps. The model-assisted spectrum shows a higher peak intensity.

Table 3.2.: Specifics of the data combination methods based on the position indicated towards H¹³CO⁺ peak intensity maps (see Fig. 3.2).

Method	Peak intensity [mJy/beam]	Flux density [10 ⁻² Jy]	rms noise level [mJy/beam]	SNR
Joint deconvolution	68.9	1.71	10.5	6.5
Feather	66.0	1.76	9.5	6.9
Model-assisted cleaning	71.5	2.03	10.0	7.1

3.2. ANCILLARY DATA

I explored archival data observed at submillimeter and infrared wavelengths to investigate the association between large structures traced by the ancillary data and the small scale structures observed with ALMA. I use ¹³CO (2–1) line data taken with the SHeFI receiver¹ (see Zernickel, Schilke, and Smith, 2013) and 350 μm continuum data (André et al., 2016) obtained with the ArTéMiS² bolometer camera, at the Atacama Pathfinder EXperiment (APEX) 12 m telescope. The ¹³CO (2–1) data covers the whole giant molecular cloud of NGC6334, over a spatial extent of 29'4 × 13'8 with an angular resolution of 30''/2. In the top panel of Fig. 3.3, the contours show the distribution of the ¹³CO velocity-integrated emission overlapped on the hydrogen column density N(H₂) map in color scale. The hydrogen column density N(H₂) and dust temperature maps were derived by Russeil et al., 2013 who used the 160 μm, 250 μm, 350 μm, and 500 μm wavebands of the *Herschel* observations from the HOBYS project (Motte et al., 2010a). The field of view targeted in the ALMA observations presented here is shown as a square box on the temperature map in the bottom panel of Fig. 3.3. The 350 μm continuum data observed with the APEX telescope mapped the central region of NGC 6334 with an angular resolution of 8 arcsec, corresponding to 0.07 pc at a distance of 1.76 kpc (Russeil et al., 2020).

I use the infrared images at 3.6, 4.5, 5.8, and 8.0 μm from the *Spitzer* Space Telescope's Infrared Array Camera (IRAC) and the catalogue of young stellar objects (Willis et al., 2013) to identify infrared counterparts in the NGC 6334-V region. In addition, I use Hα (at 6562 Å) data observed with the ESO 36 cm telescope located at La Silla Observatory. The observations cover a field of view of 38' × 38' around the NGC 6334 and NGC 6357 star-forming complexes (see Russeil et al. 2016 for details).

¹<https://www.apex-telescope.org/ns/instruments/shefi/>

²<https://www.apex-telescope.org/ns/artemis/>

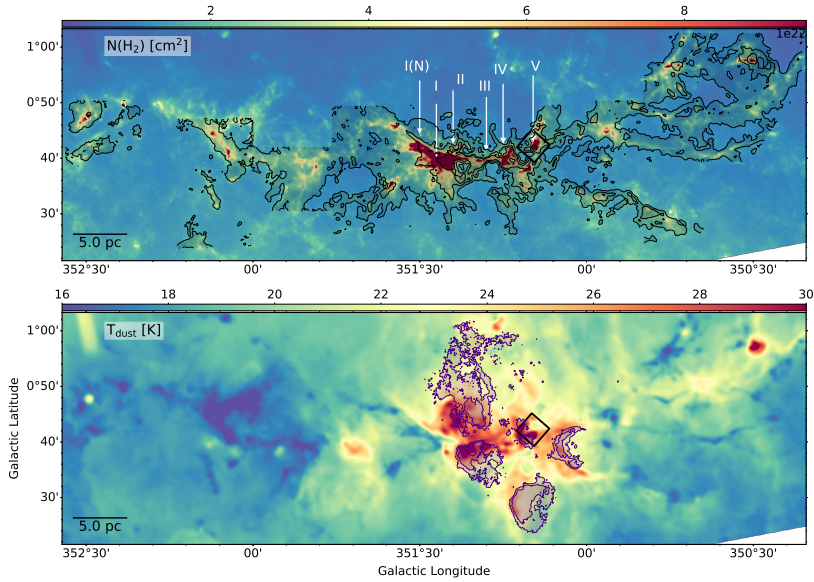


Figure 3.3.: NGC 6334 star-forming complex. The color images correspond to the hydrogen column density $N(\text{H}_2)$ (top panel) and dust temperature (bottom panel) derived from the *Herschel* HOBYS data (Motte et al., 2010b) at a resolution of $18''/2$. The contours in the top panel show the APEX ^{13}CO peak intensity map (see Zernickel, 2015; Arzoumanian et al., 2022), while the contours in the bottom panel correspond to the $\text{H}\alpha$ emission at 6562 \AA (Russeil et al., 2016) which traces the presence of H II regions. The area mapped with ALMA around NGC 6334 source V is highlighted with a black box in the bottom panel. Its central coordinates are R.A.(J2000) = $17^{\text{h}}19^{\text{m}}57^{\text{s}}$ and Dec.(J2000) = $-35^{\circ}57'52''$.

4

CONTINUUM EMISSION: SOURCE ANALYSIS IN NGC 6334-V

In Section 2.2, I introduced the concept of continuum emission and discussed the physical properties that can be extracted from such observations. This chapter presents a detailed study of the physical properties of the NGC 6334-V protocluster through *ALMA* continuum observations. I begin this chapter by presenting the morphology of the continuum emission toward the observed region, identifying compact sources and their counterparts in radio, infrared, and X-ray wavelengths, and measuring the physical properties of these sources. Subsequently, the distribution of dense cores and the physical properties of protoclusters, such as core mass function and the level of mass segregation, are studied.

4

4.1. MORPHOLOGY

Figure 4.1 shows the 3 mm *ALMA* (or 87.6 GHz) continuum emission towards NGC 6334-V. The map reveals a bright central region of about 0.3 pc in size with a clumpy morphology, surrounded by a fainter component that extends to 0.4-0.5 pc, mainly towards the west. The emission also extends in the form of elongated features toward the northwest. The high angular resolution observations of $1''.4$ allow us to gain insight into the mass condensations within the cluster, and it appears that most of the compact sources are located within the center of the cluster. All sources are marked on the map shown in Figure 4.1. In Section 4.2, I will explain the identification method for these continuum sources, determine their physical properties, and indicate the counterparts of the detected *ALMA* sources at various wavelengths.

4.2. SOURCE IDENTIFICATION

I used the Source Extractors (*SExtractor*) package (Bertin and Arnouts, 1996) to identify compact continuum sources. *SExtractor* is a software package for extracting sources and measuring their photometric properties from astronomical images to build a catalog. The software identifies pixels in a basic FITS cube likely to be associated with a objects, then groups these pixels to form discrete sources. The software then measures the total flux, size, and orientation angle of the selected sources. Several steps in the *SExtractor* control how it performs source detection and measurement. Here are brief explanations of the four key steps:

1. Determination of the background level of images by dividing the image into subregions and calculating the median pixel value over each mesh grid.

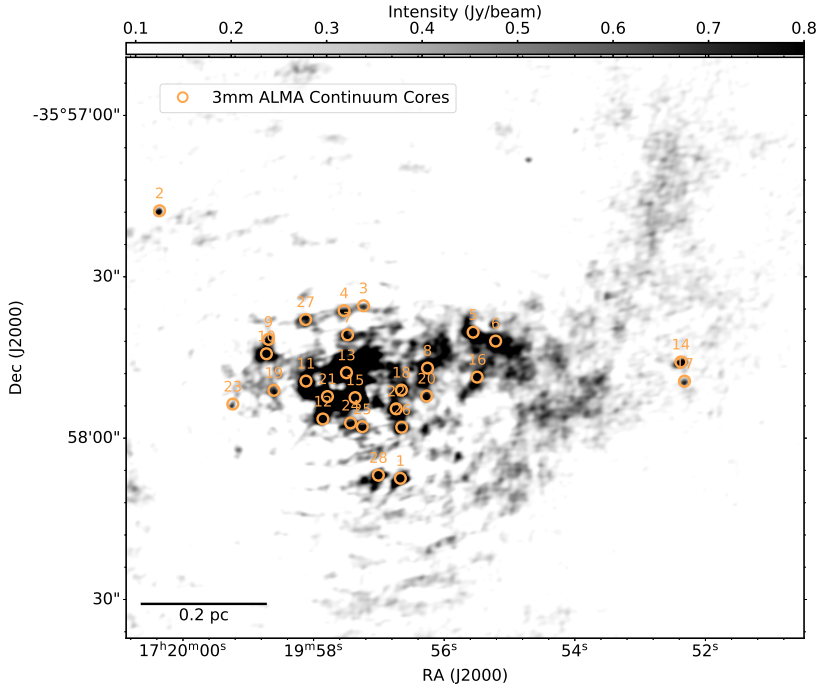


Figure 4.1.: Continuum 3 mm intensity image in gray scale. Compact continuum cores identified by SExtractor are marked with orange circles.

2. Smoothing of the estimated background level to suppress noise and minimize the impact of bright extended features.
3. Application of weight maps to account for the variations in noise level in the background. This ensures that sources are detected and measured accurately across the entire image.
4. Flagging pixels in the image that are affected by the unreliable background or have unphysical properties that could affect source detection and measurement. For this, the parameter `BACK_SIZE` used by SExtractor controls the size of the background mesh to estimate the local background level in the image.
5. Finally, source deblending occurs by discarding the most deviant values and then computing the mean and standard deviation again. At a given rms threshold, SExtractor executes several steps to determine a background level in a given area. This procedure is iterated until all pixel values within a mesh

grid fall within the range of the mean rms noise $\pm\sigma$. Then, if the area is not classified as background, it is split into separate sources.

The algorithm eventually merges adjacent identified sources if their intensity difference is smaller than an intensity threshold decided by the user. The sources overlapping in the image can not be detected separately with a single threshold. Therefore, the algorithm deblends them by searching for intensity variations based on multiple thresholds. The parameter `DEBLEND_NTHRESH` given by the user sets the number of deblending thresholds used by the `SExtractor` when attempting to separate overlapping sources. The parameter `DEBLEND_MINCOUNT` sets the minimum number of pixels required for the `SExtractor` to consider two sources as separate objects during the deblending process. Finally, the parameter `DETECT_MINAREA` sets the minimum number of connected pixels required for the `SExtractor` to consider a region as a potential source detection.

I used a detection threshold of 8σ and a deblending threshold of 8σ for each source, where σ is the rms noise. Because the noise level is not uniform across the continuum map, σ is calculated locally for a region around each source using the standard deviation of the pixel values in a background mesh across different regions of the map. A detection must have at least 5 pixels with a pixel size of $0''.2$ to be recognized as a source. The `SExtractor` output includes the central position, the major and minor axes, together with the position angle of the ellipse that describes the spatial extent and the integrated flux of each detected source. All configuration parameters are listed in the Table 4.1.

Table 4.1.: List of configuration parameters in the `SExtractor` software package

Parameter	Description	Value
<code>DETECT_MINAREA</code>	Minimum number of connected pixels above threshold required for an object to be considered a detection.	5
<code>DETECT_THRESH</code>	Detection threshold in standard deviations above background noise for object detection.	8
<code>THRESH_TYPE</code>	Type of thresholding method used for object detection.	RELATIVE
<code>PIXEL_SCALE</code>	Physical size of each pixel in the image, typically in units of arcseconds.	0.2
<code>DEBLEND_MINCOUNT</code>	Minimum number of pixels required for an object to be considered for deblending.	0.001
<code>DEBLEND_NTHRESH</code>	Number of thresholds used in the deblending process to separate overlapping objects.	24

I carefully inspected the identified sources and manually removed those associated with `CLEANING` artifacts produced in the imaging process. The final catalog,

listed in Table 4.2, includes 28 compact sources. Among the identified objects, the three brightest sources at the center were already reported by Juárez et al., 2017b in their SMA observations at 870 μm . The remaining 25 sources are newly identified objects with these ALMA observations at 3 mm.

Table 4.2.: Properties of the ALMA continuum sources detected towards NGC 6334-V

#	ALMA 87.6 GHz continuum source parameters ^(a)						Derived physical properties ^(b)								Other ^(c)
	R.A.	Dec.	I_{peak}	S_{int}	θ_S , PA	R	$M(T_{\text{rot}})$	$M(T_{\text{est}})$	$n_{\text{H}_2}(T_{\text{rot}})$	$n_{\text{H}_2}(T_{\text{est}})$	$N_{\text{H}_2}(T_{\text{rot}})$	$N_{\text{H}_2}(T_{\text{est}})$	T_{rot}		
(1)	(2)	(3)	(4)	(5)	(6)	(7)	(8)	(9)	(10)	(11)	(12)	(13)	(14)	(15)	
1 ^a	17:19:56.686	-35:58:07.70	2.96	4.31	1.6×0.94 , +32	0.61	6.738	11.003	39.8	32.6	47.6	104.9	31		
2 ^{c,d}	17:20:00.370	-35:57:17.94	1.10	0.43	0.64×0.5 , +41	0.28	-	0.483	-	14.2	-	21.3	50 ^{est}	604077(ICII)	
3 ^a	17:19:57.250	-35:57:35.61	0.78	0.43	0.88×0.48 , -3	0.32	0.25	1.236	8.9	23.7	5.6	40.9	91		
4 ^a	17:19:57.546	-35:57:36.52	0.92	1.29	1.42×0.74 , +8	0.51	1.313	3.349	13.1	16.8	13.1	45.3	48		
5	17:19:55.571	-35:57:40.53	2.03	7.55	3.04×1.56 , -40	1.09	12.141	19.218	12.8	10.0	27.3	57.7	31		
6	17:19:55.227	-35:57:42.17	1.55	7.98	2.48×1.72 , -12	1.03	11.322	20.249	14.1	12.4	28.4	67.3	34		
7	17:19:57.493	-35:57:41.02	0.91	1.94	1.84×0.92 , -8	0.65	2.719	4.727	14.1	11.5	17.9	39.6	33		
8 ^a	17:19:56.270	-35:57:47.21	1.37	8.19	3.86×1.62 , +67	1.25	10.373	7.713	7.4	2.6	17.9	17.4	38	326819(ICI)	
9	17:19:58.704	-35:57:41.86	1.03	1.08	1.24×0.6 , +60	0.43	1.755	2.915	28.1	23.6	23.7	54.4	32		
10	17:19:58.736	-35:57:44.53	1.23	6.47	2.32×1.78 , 0	1.02	8.835	16.291	11.6	10.4	23.0	56.0	35		
11 ^a	17:19:58.130	-35:57:49.61	1.59	9.92	2.66×1.9 , -78	1.12	7.948	25.131	7.7	11.9	16.8	70.7	59		
12	17:19:57.871	-35:57:56.66	1.69	2.80	1.52×1.14 , +5	0.66	1.764	7.352	8.2	17.3	10.5	60.2	77		
13 ^d	17:19:57.511	-35:57:48.06	4.22	57.13	6.0×3.38 , +17	2.25	30.847	54.074	3.7	3.2	16.3	37.7	86	N	
14	17:19:52.391	-35:57:46.05	1.20	1.08	1.08×0.6 , +20	0.4	-	2.651	-	27.2	-	57.9	20 ^{est}		
15 ^e	17:19:57.378	-35:57:52.69	32.54	76.53	2.58×1.74 , +19	1.06	13.903	35.457	16.1	20.0	33.3	111.7	252	HC	
16 ^a	17:19:55.510	-35:57:48.88	0.96	0.86	1.84×0.46 , +67	0.46	1.134	2.249	15.5	15.1	13.9	36.9	38		
17	17:19:52.335	-35:57:49.62	0.71	0.22	0.34×0.28 , +44	0.15	-	0.286	-	53.8	-	43.4	20 ^{est}		
18 ^a	17:19:56.670	-35:57:51.29	1.13	1.08	1.38×0.74 , +38	0.51	1.225	1.115	12.0	6.0	11.8	15.8	46	335150(NIRCI)	
19 ^b	17:19:58.621	-35:57:51.33	0.84	1.29	1.16×0.88 , -54	0.51	1.727	3.339	18.1	17.3	17.8	46.3	37		
20 ^a	17:19:56.282	-35:57:52.40	1.19	0.43	0.6×0.44 , +32	0.26	0.396	0.331	39.6	13.6	19.8	18.2	42	326819(NIRCI)	
21 ^f	17:19:57.802	-35:57:52.49	9.85	31.69	3.74×1.96 , +51	1.35	18.645	79.903	10.4	21.4	27.4	153.6	79	SE	
22	17:19:56.749	-35:57:54.77	1.68	3.45	1.74×1.14 , -72	0.7	2.368	8.75	9.3	16.9	12.8	62.7	69		
23	17:19:59.250	-35:57:53.88	0.85	0.22	0.52×0.38 , +45	0.22	-	0.614	-	38.0	-	44.4	20 ^{est}		
24	17:19:57.448	-35:57:57.40	0.93	0.86	1.64×0.48 , +17	0.44	0.41	2.321	6.1	17.7	5.2	41.5	104		
25	17:19:57.267	-35:57:58.09	0.98	0.65	0.96×0.62 , -1	0.39	0.175	1.753	3.9	21.1	2.9	42.6	182		
26	17:19:56.665	-35:57:58.20	1.13	1.08	1.2×0.64 , +10	0.44	1.013	2.505	18.0	19.9	15.4	46.1	47		
27	17:19:58.135	-35:57:38.17	0.89	2.16	1.58×1.1 , +9	0.66	2.615	5.33	12.8	12.6	16.5	43.7	39		
28	17:19:57.022	-35:58:07.12	1.26	3.02	1.76×1.06 , +44	0.68	4.047	7.845	17.0	16.6	22.6	59.7	37		

^{1(a)} Observed parameters of the ALMA compact sources identified as explained in Sect. 4.2. Each column contains: R.A. (right ascension, Col. 2) in ^h.^m.^s; Dec. (declination, Col. 3) in ^o.['].^{''}; I_{peak} (peak intensity at 87.6 GHz, Col. 4) in mJy beam⁻¹; S_{int} (integrated flux density, Col. 5) in mJy; θ_S (observed size as major and minor axis of the ellipse defined by SExtractor) in arcsec and PA (position angle, Col. 6) in degrees. ^(b) Physical properties of the ALMA compact sources. Each column contains: R (radius, Col. 7) determined as the equivalent deconvolved radius of the observed size after taking into account the synthesized beam; M (gas and dust mass based on rotational temperature, Col. 8) in M_{\odot} ; $M(T_{\text{est}})$ (gas and dust mass based on estimated temperature, Col. 9) in M_{\odot} ; $n_{\text{H}_2}(T_{\text{rot}})$ (volume density based on rotational temperature, Col. 10) in 10^7 cm⁻³; $n_{\text{H}_2}(T_{\text{est}})$ (volume density based on estimated temperature, Col. 11) in 10^7 cm⁻³; $N_{\text{H}_2}(T_{\text{rot}})$ (column density based on rotational temperature, Col. 12) in 10^{23} cm⁻²; $N_{\text{H}_2}(T_{\text{est}})$ (column density based on estimated temperature, Col. 13) in 10^{23} cm⁻²; T (gas temperature, Col. 14) in K, from the CH₃CCH fit. ^(c) Counterparts at

other wavelengths. Symbols HC, N and SE denote the millimeter sources reported by Juárez et al. (2017b) at 870 μm with the SMA; while the digits correspond to the catalog number of Willis et al. (2013) based on infrared data from 2 μm up to 24 μm .

[†] θ_a and θ_b are the major and minor observed sizes of a compact source.

^a Continuum sources with detection of IR compact source counterparts.

^b A continuum source classified as a Class I YSO.

^c A continuum source classified as a Class II YSO.

^d A continuum source identified by Juárez et al. 2017b and notated as N (North).

^e A continuum source identified by Juárez et al. 2017b and notated as HC (Hot Core).

^f A continuum source identified by Jiménez-Serra et al. 2010 and notated as SE (South-East).

^g A continuum source identified by Feigelson et al. 2009 as X-ray source.

4.3. COUNTERPARTS IN INFRARED AND X-RAY WAVELENGTHS

I compare the compact objects detected in the 3 mm *ALMA* continuum map with the infrared point sources listed in the catalog published by Willis et al. (2013). The catalog contains sources distributed throughout the entire NGC 6334 cloud, ranging from $2\mu\text{m}$ up to $24\mu\text{m}$, which are also categorized into class I, II, and III YSOs based on their spectral index and near-infrared colors. If an infrared object is located within the range of an *ALMA* continuum source (typically less than $2''$), I consider both sources to be related. Only three of the 28 *ALMA* continuum sources have infrared counterparts (refer to Col.12 of Table 4.2). These three sources comprise of two class I objects and one class II object according to the classification in Willis et al., 2013. The most prominent and central *ALMA* sources, identified as sources N, HC, and SE, are associated with extended infrared emission that appears brighter at $4.5\mu\text{m}$, indicating the possible existence of Extended Green Objects (EGOs) and shocked gases (Cyganowski et al., 2008; Chambers et al., 2009).

Apart from the infrared counterparts, I investigate whether the *ALMA* continuum cores overlap with objects detected at other wavelengths. Our investigation reveals that the class II core is also coincident with an X-ray source (Feigelson et al., 2009). This X-ray source (CXOU J172000.3–355710) is located near the ionized bipolar region and in the outer part of the cluster. All the sources and their corresponding counterparts are listed in Col.12 of Table 4.2.

4.4. PHYSICAL PROPERTIES OF CONTINUUM CORES

Following the source identification obtained with *SExtractor*, I list the photometric properties of the compact sources in NGC 6334-V in Cols. 4–6 of Table 4.2. The peak intensities (I_{peak}) of the detected sources range from 0.7 to 10 mJy/beam, except for the source associated with the hot molecular core, which has a peak intensity of ~ 32.5 mJy/beam. The integrated flux densities are in the range 0.2 to 57 mJy, with ~ 76.5 mJy for the hot core. The mean observed source size, determined directly from *SExtractor* and corresponding approximately to the size at half intensity, is $1''.8 \times 1''.1$, with variations of about a factor 2 between the different sources. I determine the equivalent deconvolved radius of each source, after taking into account the contribution from the synthesized beam. The compact sources have radii ≈ 1250 au, typical of dense cores.

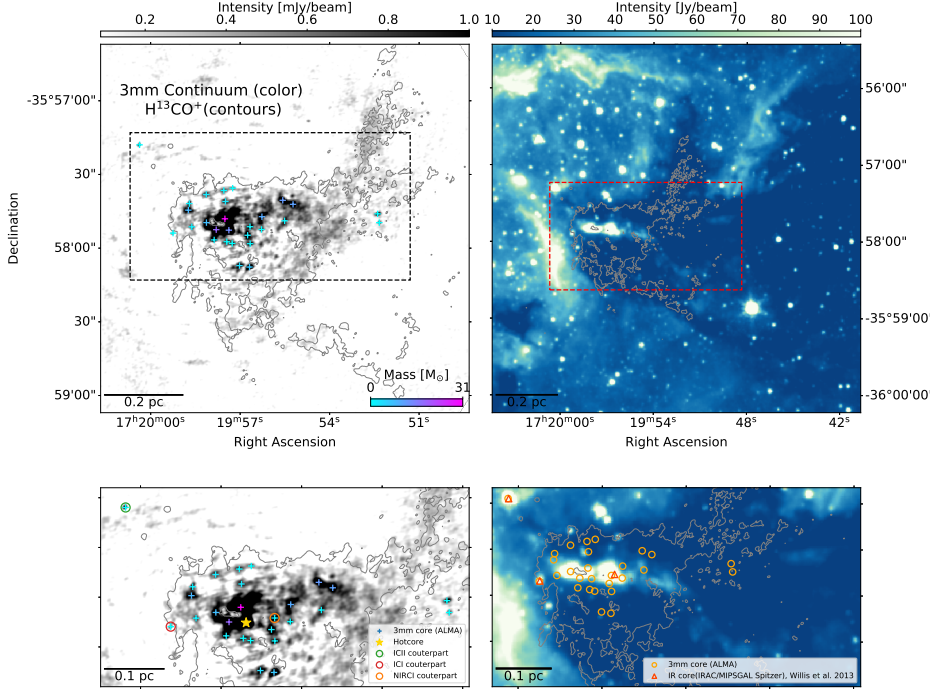


Figure 4.2.: The top left panel shows the continuum emission map in grayscale, with the 3 mm ALMA continuum core marked by a plus indicator and colored by the mass number. The bottom left panel is a zoomed-in view of the upper map with markers for the infrared source counterparts. The top right panel displays the Spitzer 3.6 μm map in color scale, with H^{13}CO^+ contours overlaid. The bottom right panel is a zoomed-in view of the upper map, with 3 mm ALMA continuum cores marked by orange circles and their infrared counterparts marked by red triangles.

Based on the flux and source size, I determine the gas and dust mass and density of each core assuming that the ALMA continuum emission at 3 mm is dominated by dust. The low correlation between millimeter continuum sources and radio continuum counterparts confirms that there is likely only a small contribution from ionised gas in the 3 mm ALMA emission, with a small contribution from ionized gas. I use equation 2.13 from Section 2.2 and determine the gas and dust mass (M) as

$$M = R \frac{S_{\text{int}} d^2}{B_\nu(T_d) \kappa_\nu}, \quad (4.1)$$

where S_{int} is the integrated flux density at a frequency ν of 87.6 GHz, d is the distance to the source (1.76 kpc for NGC 6334; Russeil et al. 2020), $B_\nu(T_d)$ is the Planck function at the isothermal dust temperature T_d , and κ_ν is the absorption coefficient per unit of total mass density at a frequency ν . I adopt a dust mass opacity coefficient at 87.6 GHz of 0.1385 g cm^{-2} (Ossenkopf and Henning, 1994), optically thin dust emission and a gas to dust factor R of 100 (Hildebrand, 1983; Lis et al., 1998).

For T_d determination, I used two methods: In the first approach, I assume a strong coupling between gas and dust grains in NGC 6334 due to the high densities throughout the cloud ($N_{\text{H}_2} 10^{22} \text{ cm}^{-2}$, see Figure 3.3), and use the rotational temperatures (T_{rot}) derived from CH_3CCH emission lines (see Chapter 5.2). The adopted² T_{rot} is listed in Col. 11 of Table 4.2 and varies from 30 K to 250 K at the position of the hot core. In the second approach, I assumed temperatures based on theoretical values and other publications (e.g., Sadaghiani et al., 2020). I adopted 20 K if the core is detected only in the ALMA maps, 50 K if it has an infrared counterpart, and 100 K for the only hot molecular core with a chemically-rich spectrum. I derive masses for the dense cores using rotational gas temperature in the range 0.1 to $31 M_\odot$, with a mean and median mass of $\sim 5.2 M_\odot$ and $\sim 1.8 M_\odot$, respectively (see Col. 8 of Table 4.2). For masses calculated based on assumed temperatures T_{est} , the masses show higher values and range from ~ 0.5 to $80 M_\odot$, with a mean and median mass of $\sim 11.7 M_\odot$ and $\sim 4.0 M_\odot$, respectively (see Col. 9 of Table 4.2).

Assuming that the cores are spherical with a radius R , I can use the equation 2.14 to calculate the volume density of molecular hydrogen, n_{H_2} as

$$n_{\text{H}_2} = \frac{1}{\mu m_{\text{H}}} \frac{M}{\frac{4}{3}\pi R^3}, \quad (4.2)$$

where μ is the mean molecular mass per hydrogen atom (equal to 2.3), m_{H} is the mass of hydrogen, and R is the equivalent deconvolved radius listed in Col. 7 of Table 4.2. The derived volume density based on gas temperature (n_{H_2}) ranges from 2×10^7 to $20 \times 10^7 \text{ cm}^{-3}$, with mean and median values of $7 \times 10^7 \text{ cm}^{-3}$ and $6 \times 10^7 \text{ cm}^{-3}$ respectively (see Col. 10). For the case where we consider the assumed temperatures, the volume density (n_{H_2}) changes to higher values from 3×10^7 to

²I use the XCLASS-derived temperature from CH_3CCH (see Chapter 5.2) to determine the temperature of the compact continuum sources. The gas temperature derived from the CH_3CCH lines was used as the dust temperature under the presumption that the dust temperature was equal to the gas temperature. For each source, I average the CH_3CCH temperature for the pixels included in the SExtractor-defined ellipse that defines each continuum sources.

$53 \times 10^7 \text{ cm}^{-3}$, with mean and median values of $18 \times 10^7 \text{ cm}^{-3}$ and $16 \times 10^7 \text{ cm}^{-3}$ respectively (see Col. 11).

As discussed in Section 2.2, I can also calculate the column density of molecular hydrogen, N_{H_2} , using Equation 2.15, which is repeated here for convenience:

$$N_{\text{H}_2} = \int_{\text{line of sight}} n_{\text{H}_2} dl, \quad (4.3)$$

where l is the size of the source, corresponding to twice the radius R . I obtained similar column densities for all the cores with a mean value of $22 \times 10^{23} \text{ cm}^{-2}$ (see Col. 10) in the case of T_{rot} and $22 \times 10^{23} \text{ cm}^{-2}$ (see Col. 10) in the case of T_{est} .

In Figure 4.3, the top plots depict the histogram and Kernel Density Estimation (KDE) of the observed peak intensity, flux density, and deconvolved radius properties for the 28 ALMA continuum sources in NGC 6334-V. The middle row shows the determined properties of dust and gas mass, H_2 volume density, and H_2 column density based on the gas temperature, while the bottom plots display the same properties but based on an assumed temperature.

4.5. CORE STRUCTURES IN THE NGC6334 V

4.5.1. MINIMUM SPANNING TREE (MST)

The ALMA continuum map toward NGC 6334-V has revealed the presence of a cluster of dense cores, richer than originally known. The total mass of all the dense cores together adds up to $\approx 144 M_{\odot}$. The identified dense cores are preferentially distributed in the central $\approx 0.3 \text{ pc}$ of the region, with the two most massive ones, with masses $\gtrsim 15 M_{\odot}$, located at the very center.

In order to study the spatial distribution of cores in the cluster, I determined the Minimum Spanning Tree (MST) of the continuum cores. The MST is a subgraph of straight lines connecting data points with the minimum total edge weighted distance and without closed loops. I used the python package `NetworkX`³ to generate the MST for the ALMA cores in NGC 6334-V. This package is based on Kruskal's algorithm (Kruskal, 1956) to find the MST for a connected weighted graph. `NetworkX` provides the `minimum_spanning_tree` function, which takes a connected, weighted graph as an input and returns the MST of the graph as a subgraph.

The left panel of Figure 4.4 shows the MST of continuum cores overlaid on the continuum emission map. The other massive cores, with masses $\gtrsim 8 M_{\odot}$ (less than

³Available at <https://networkx.github.io/>

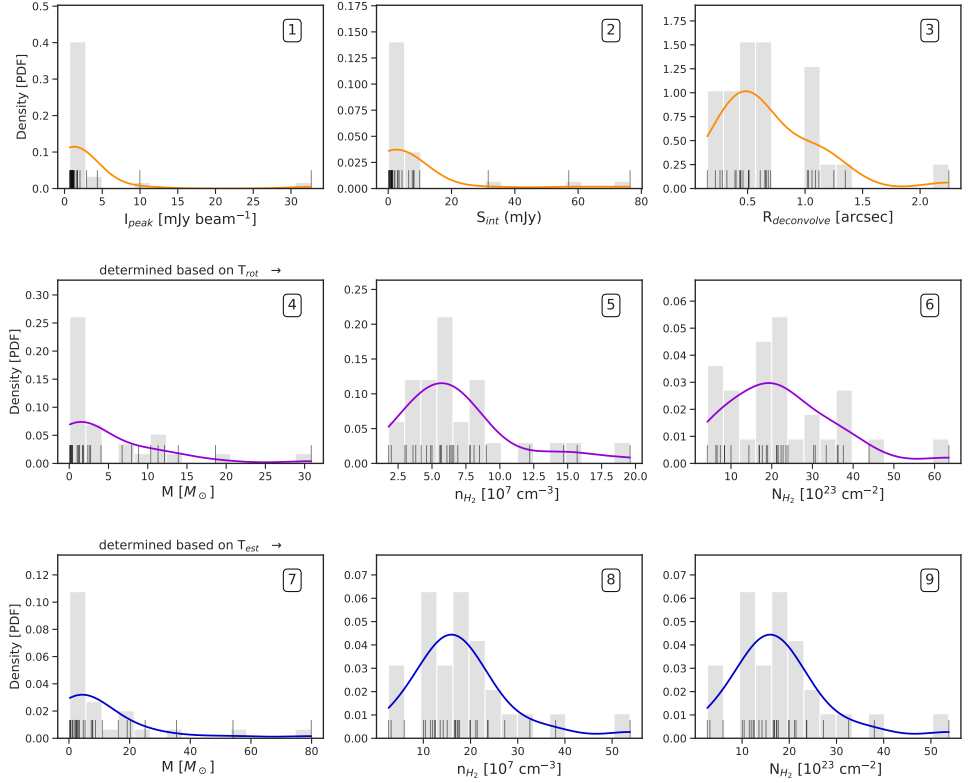


Figure 4.3.: The histogram and KDE of various properties for the 28 ALMA continuum sources in NGC 6334-V. The properties include peak intensity (1), flux density(2), and deconvolved observed radius (3). The properties in the second row are calculated based on the rotational temperature of CH_3CCH : dust and gas mass (4), H_2 volume density (5), and H_2 column density (6). The third row shows the same properties as the second row but based on the estimated temperature: dust and gas mass (7), H_2 volume density (8), and H_2 column density (9). Finally, the rug-style solid black lines show the values of the values marked at the bottom of each panel just above the x-axis.

$15 M_{\odot}$), appear distributed throughout the cluster, although preferentially along the north-west, south-west and north-east directions, likely matching the elongated structures seen in molecular gas (see Chapter 5.3).

The outcome of MST also indicates that continuum cores are clustered in the center and are not randomly distributed throughout the observed region. Based on the MST results, I evaluate the internal structure of the cluster NGC 6334-V by measur-

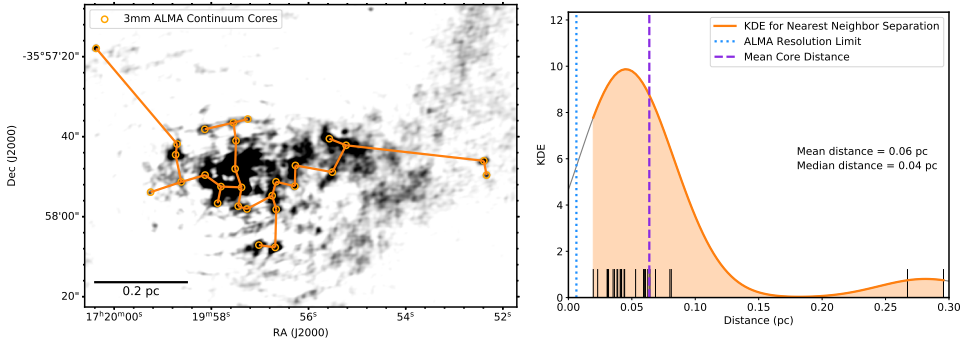


Figure 4.4.: *Left:* The minimum spanning tree (MST) created for the ALMA continuum sources in NGC6334V. The plot includes continuum emission in the grey background, the position of cores in orange circles, and tree structures in orange lines. *Right:* The KDE plot shows the distribution of projected separations between the nearest neighbors in NGC6334-V. The plot includes a blue dotted line indicating the 1300 au resolution limit of the ALMA observations, a vertical purple dashed line representing the mean distance between the cores in the cluster, and short vertical lines at the bottom depicting observed separations among the members of the cluster.

ing the Q parameter. The Q parameter introduced by Cartwright and Whitworth (2004), is a dimensionless quantity to quantify and differentiate between radially concentrated structures and fractal-like distributions. The Q parameter is defined as the ratio of the normalized mean length of line segments in the MST, denoted as \bar{m} , to the mean separation between the cores normalized by the cluster radius as \bar{s} . The equation to calculate the Q parameter is:

$$Q = \frac{\bar{m}}{\bar{s}} = \frac{\frac{\bar{m}}{\sqrt{N\pi R^2}}}{\frac{\bar{s}}{R}}, \quad (4.4)$$

where N is the total number of cores in a cluster and R is the radius of the cluster, defined as the distance between the mean position of all cores and the furthest core. A high value of Q ($Q > 0.8$) implies a large-scale radial density gradient or centrally concentrated clusters. In contrast, a low value of Q ($Q < 0.8$) indicates that the distribution is more uniform or has fractal subclustering.

I measured the normalized mean length to be $\bar{m} = 0.376''$ (~ 0.003 pc) and the normalized mean separation to be $\bar{s} = 0.461''$ (~ 0.004 pc). Using these values, I calculated the Q parameter to be 0.82. To estimate the uncertainty of the Q param-

eter, I used the approach described in Sadaghiani et al., 2020. I randomly removed approximately 20% (= 6 cores) of the cores available in the sample and measured the Q parameter for the remaining sample. Repeating this process for 100 realisations gives a distribution of the Q parameter. Fitting a Gaussian to this distribution resulted in a standard deviation $\sigma = 0.005$, which corresponds to the uncertainty of the Q parameter (see Figure 4.5). The Q value of 0.82, although close to the limit threshold between uniform and centrally concentrated distribution, slightly favors a centrally concentrated cluster, and the cores within the cluster tend to be closer to the center of the cluster, rather than being spread out evenly or having a fractal sub-clustering distribution. While the MST algorithm provides practical insights into the networks of cores and their spatial distribution within the cluster, it should be noted that it only considers pairwise distances between points and may not fully capture the complexity of the cluster, where there are multiple substructures or hierarchies. In Section 4.5.2, when I introduce other physical structures, I will study how cores correlate with filamentary structures and velocity distributions.

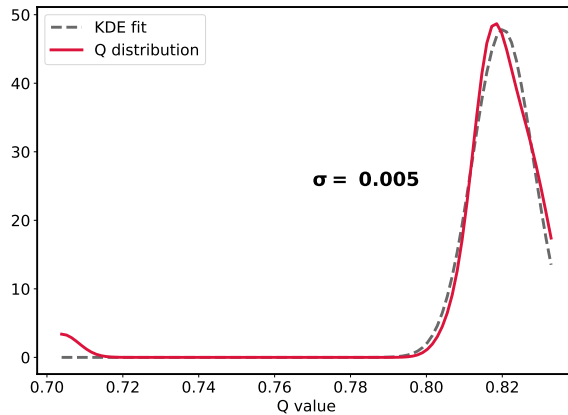


Figure 4.5.: KDE of the Q parameter values generated during the iterative process of removing $\sim 20\%$ of the cores. The grey dashed line represents a Gaussian fit to the Q distribution. The standard deviation of the fitted Gaussian is taken as the uncertainty of the Q parameter.

4.5.2. CLUMP FRAGMENTATION AND JEANS INSTABILITY

In this section, I discuss the formation process of continuum cores and how fragmentation processes can influence the formation of compact sources in the proto-cluster NGC 6334-V. The typical depiction of the formation of stars involves the

breaking up of clouds due to the balancing of gravity and thermal pressure following Jeans instability.

In an isothermal, uniform medium with the volume density of molecular hydrogen n_{H_2} and kinetic temperature of T , the minimum length scale at which gravitational perturbations are in excess of the critical mass collapse and fragment is the Jeans length and is defined as:

$$\lambda_J = c_{\text{eff}} \left(\frac{\pi}{G\rho} \right)^{1/2}, \quad (4.5)$$

where c_{eff} is the 'effective' sound speed which is a parameter that takes the thermal motions of the gas into account. ρ is the density and G is the gravitational constant.

The minimum mass required for a perturbation to collapse and form a gravitationally bound object is Jeans mass, which is derived by assuming that the spherical gas cloud with diameter λ_J has a uniform density ρ using

$$M_J = \frac{\pi^{5/2}}{6 G^{3/2}} c_{\text{eff}}^3 \rho^{-1/2}, \quad (4.6)$$

Based on the thermal or non thermal contributions, I can determine the thermal and non thermal jeans mass. In the case of pure thermal support, the effective speed of sound is equivalent to the thermal sound speed and can be calculated using the equation:

$$c_s = \sqrt{\frac{\gamma k_B T}{\mu_{\text{H}_2} m_{\text{H}}}}, \quad (4.7)$$

where γ is the adiabatic constant, and for the isothermal medium is 1, k_B is the Boltzmann constant, T is the average temperature of the clump, μ_{H_2} is the mean molecular weight per hydrogen molecule, and m_{H} is the mass of hydrogen.

Assuming the thermal pressure dominates the fragmentation process, I can calculate the thermal contribution of Jeans mass by

$$\frac{M_{\text{Jeans}}^{\text{th}}}{M_{\odot}} = 0.6285 \left(\frac{T}{10 \text{ K}} \right)^{3/2} \left(\frac{n_{\text{H}_2}}{10^5 \text{ cm}^{-3}} \right)^{-1/2}. \quad (4.8)$$

In the case of the non-thermal pressure only, it is necessary to first determine the non-thermal component of the lines by subtracting out the thermal velocity dispersion (Palau et al., 2015) using

$$\sigma^{\text{nth}} = \sqrt{(\sigma^{\text{obs}})^2 - (\sigma^{\text{th}})^2}, \quad (4.9)$$

where the thermal velocity dispersion (σ^{th}) is equivalent to the thermal sound speed (c_s). In order to estimate the observed velocity dispersion, σ^{obs} , I used the second-moment map of H^{13}CO^+ molecular line observed with ALMA and took the mean velocity dispersion over the central region of the cluster. Finally, the turbulent Jeans mass is calculated (Palau et al., 2015) as

$$\frac{M_{\text{Jeans}}^{\text{nth}}}{M_{\odot}} = 0.8255 \left(\frac{\sigma^{\text{nth}}}{0.188 \text{ km s}^{-1}} \right)^3 \left(\frac{n_{\text{H}_2}}{10^5 \text{ cm}^{-3}} \right)^{-1/2}. \quad (4.10)$$

I assumed a spherical, symmetric clump with a radius of 0.6 pc, determined from the average distances between all pairs of cores, and a temperature of 20 K, estimated from the average temperature across the cluster. The total mass M_{total} of $144 M_{\odot}$ calculated based on the sum of all observed cores. In this case, the thermal Jeans length is given as $\lambda_J \sim 0.03$ pc and the non-thermal jeans length is given as $\lambda_J \sim 0.17$ pc. From the KDE plot shown in Figure 4.4, the median distance is estimated to be 0.04 pc, which is similar and within the same order of magnitude as the thermal Jeans length.

Using the Jeans length, I also calculate the thermal Jeans mass of $0.01 M_{\odot}$ and non-thermal jeans mass of $1.4 M_{\odot}$. The mean mass of the observed core is $\sim 5 M_{\odot}$, which is significantly larger than the thermal Jeans mass but within the same order of magnitude as the non-thermal Jeans mass. I also observe cores with masses between the thermal and non-thermal Jeans mass (see the core mass of 2, 3, 17, 18, 20, and 23 in Table 4.2). The smaller cores indicate that while thermal Jeans fragmentation might still occur, other factors may prevent these smaller fragments from undergoing further fragmentation. Moreover, the non-thermal Jeans mass falls within the range of common masses for diffuse, clumpy interstellar clouds, suggesting that the cloud is unstable against gravitational collapse.

The wide range of core masses also suggest a critical interplay between thermal and turbulent pressures in star formation, with turbulent pressures potentially playing a more dominant role in regulating the fragmentation process. The initial conditions, which are likely influenced by large-scale processes, seem to influence the fragmentation process and subsequent star formation significantly. While our results agree with the non-thermal Jeans mass, they also emphasize the complexity of the fragmentation process and the likely influence of other factors such as

magnetic fields, angular momentum, clump collisions, and feedback from star formation in addition to the thermal and non-thermal Jeans instability.

4.5.3. CORE MASS FUNCTION (CMF)

Figure 4.6 shows the CMF of the NGC 6334-V cluster. The CMFs are compared to the Kroupa initial mass function (Kroupa, 2001), as shown with the dark gray dashed line. To facilitate comparison to higher masses, the IMF has also been shifted by a factor of 15. The dashed black line shows the theoretical completeness level of mass based on the mass sensitivity limit of ALMA observations at 3 mm. It measures the observational sensitivity of the data and represents the minimum mass that the telescope can reliably detect.

To calculate the completeness limit at 3 mm ALMA observations in the CMF plot, I consider a threshold of 0.3 mJy/beam for the rms noise level, measured by the random noise in the data and calculated by selecting a region of the data without any sources. To measure the resolution of the observations, I estimate the beam size based on the restoring beam used during the imaging as $1''.5 \times 1''.1$. I also adopt the dust mass opacity coefficient at 87.6 GHz of 0.1385 g cm^{-2} as in the mass calculation and assume the minimum temperature of 30 K if the core detected from ALMA data. I find 82% for objects with masses larger than the completeness level of $0.4 M_{\odot}$. Our analysis shows that 82% of the objects have masses larger than the completeness level of $0.4 M_{\odot}$.

Figure 4.6 shows the CMF of the core masses calculated based on two sets of masses that are either calculated by gas temperatures or estimated temperatures. The observed slope of the CMF in the low mass regimes ($0.8 < M < 5 M_{\odot}$) for T_{rot} assumption is -0.57 which is smaller but similar to the CMF of T_{est} which is -0.42 , but the major difference rises in the high mass regimes ($M > 5 M_{\odot}$) where the measured slope of -2.12 for T_{rot} is much steeper than CMF of T_{est} with the slope of -1.03 and also the power-law index of the IMF (-1.3). The steeper slope of the observed CMF compared to the IMF may challenge the assumption that the shape of the IMF is inherited from the CMF since there is not a direct correspondence between these two functions.

The CMF of cores in low mass regimes shows similar trends with steeper slopes than the -0.3 Kroupa IMF power-law index. However, the main difference lies in the high-mass regimes. The CMF of cores, whose masses were calculated based on the rotational temperature of CH_3CCH shows a steep slope, indicating a deficit in the distribution of high-mass cores. The CMF of the cores, whose masses were

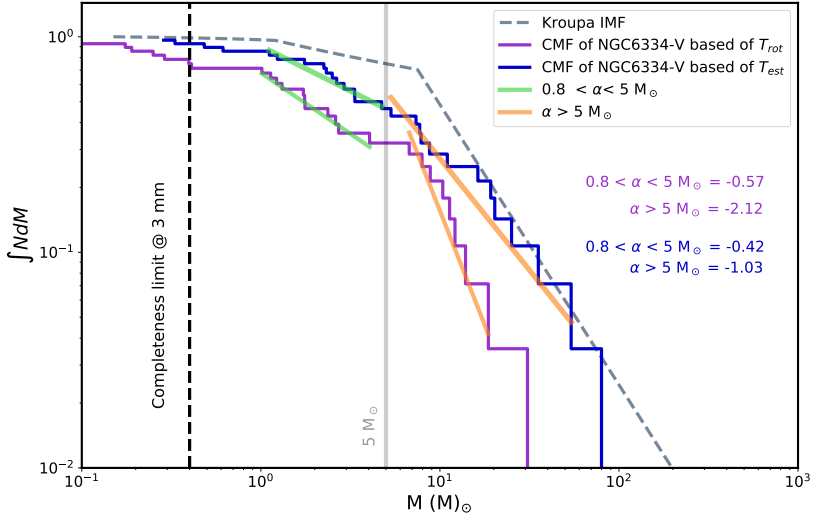


Figure 4.6.: Comparison of CMF for ALMA Core Masses with Two Different Temperature Assumptions in NGC 6334-V. The gray dashed line shows the Kroupa initial mass function shifted by a factor of 15 to the higher masses. The orange lines indicate the slope of cores with masses higher than $5 M_{\odot}$ and the green lines show masses between 0.8 and $5 M_{\odot}$ for both CMFs.

calculated based on the estimated temperature, shows a flatter slope similar to the Kroupa IMF, indicating a top-heavy distribution of high-mass cores. The choice between these two plots has significant implications for the physical process and evolution of the cores.

The deficit in the distribution of high-mass cores may suggest more evolved and smaller structures that have either lost their initial mass or fragmented into smaller cores. However, in this scenario, we would expect to observe more low-mass cores than what we observed. On the other hand, the top-heavy distribution of high-mass cores would suggest the presence of younger high-mass cores, indicating an early-stage cluster.

It is worth noting that the measured slope in high mass cores could be biased towards steeper slopes due to the uncertainty in the resolution limit of the observations and temperature measurement. Resolution bias is related to the limited angular resolution of the observations. The resolution of the ALMA observations could be insufficient to resolve small-scale fragmentation. Unresolved multiplicity

at small scales leads to overestimating core masses, consequently biasing the CMF towards flatter slopes.

TEMPERATURE BIAS IN THE CMF

In Section 4.4, I discussed two approaches for estimating core temperatures for mass calculations. The first approach is based on the assumption that cores detected only in the ALMA image have a temperature of 20 K, cores with an infrared counterpart have a temperature of 50 K, and the central hot molecular core has a temperature of 100 K. The second approach considers the spectral line fits of the molecular CH₃CCH emission map and assumes the rotational temperature. In the first approach, the accuracy of the chosen temperature values for calculating the mass of cores could be the source of error in mass and, in the second approach, the assumption of considering CH₃CCH rotational temperature to be the same as the gas temperature is not an accurate assumption since the CH₃CCH emission does not necessarily trace the gas temperature due to the projection effect.

These types of systematic errors in temperature determination affect the observed CMF. One way to determine this error is to employ simulations. Sadaghiani, 2021 discussed this error with the other clusters within the same ALMA observations. They used Monte-Carlo simulation and, for 100,000 runs, generated a group of temperatures uniformly distributed between 20 and 100 K. The new temperatures are assigned the observed sources, and a synthetic CMF is built by recalculating the masses. The slope of the synthetic CMFs shows a standard deviation of 0.10, and most synthetic CMFs are flatter than the slope of Kroupa IMF. In summary, one reason for inconsistencies between the CMF and the IMF is the uncertainty in temperature determination.

4.5.4. MASS SEGREGATION IN NGC6334 V

In this section, I study the effect of mass segregation in the young stellar cluster NGC 6334-V. Mass segregation is a phenomenon observed in star clusters where more massive stars tend to concentrate toward the center of the cluster, while low-mass stars are distributed randomly all over the cluster. This segregation can have significant implications for the evolution and dynamics of star clusters (e.g., Chandrasekhar, 1942; Spitzer, 1969; Zinnecker, McCaughrean, and Wilking, 1993; Bonnell and Davies, 1998a; Liu et al., 2015; Moeckel and Bonnell, 2009; Plunkett et al., 2018; Busquet et al., 2019).

The physical origins and causes of this effect remain unclear. This uncertainty arises from intrinsic difficulties in observation, such as the short process of mass segregation or early-phase protostars, and a lack of clear understanding of the structures and dynamics of the large-scale motions that govern cloud dynamics (Plunkett et al., 2018).

Two possible scenarios are discussed to explain mass segregation: it can be primordial, meaning clusters form with the most massive stars near the center of the gravitational potential (e.g., Chandrasekhar, 1942; Spitzer, 1969; Hillenbrand and Hartmann, 1998), or it can be dynamical, implying the most massive stars migrate to the center post-formation due to two- and multi-body dynamical interactions between stars over time (e.g., Murray and Lin, 1996; Allison et al., 2009b). Primordial mass segregation can be the result from the initial conditions of star formation based on competitive accretion theory (Bonnell and Bate, 2006). However, dynamical segregation can occur if star clusters are born in a dynamically cool and fractal state with a Q value approximately equal to zero (Allison et al., 2009a). Therefore, understanding the origin of mass segregation may provide insights into the processes of clustered star formation and help differentiate models of massive star formation.

In order to search for evidence of mass segregation in cluster NGC 6334-V I followed the three different methods: spatial distribution of the low and high-mass cores, core position relative to the center, and measuring the degree of segregation using the Λ_{MSR} parameter, as used in the recent publication (Sadaghiani et al., 2020) on other clusters in NGC 6334.

- In the first method, I partition the members of each cluster into two groups: high-mass cores ($M > 25 M_{\odot}$) and low-mass cores ($M < 25 M_{\odot}$). The reason for selecting the threshold of $25 M_{\odot}$ is our assumption of a star formation efficiency of 30% (Alves, Lombardi, and Lada, 2007) to categorize the potential high-mass and low-mass stars. A compact source with a mass of approximately $25 M_{\odot}$ will yield a B-type star. Afterwards, derive the MST individually for each group of cores and calculate the mean distance of each group. The average distance of high-mass cores from each other is 0.0426 ± 0.001 pc, which is lower than the average distance of low-mass cores at 0.0697 ± 0.007 pc. This means the distribution of high-mass cores is more compact than low-mass cores.

It is also worth noting that while the result proves the segregation within the cluster, they still suffer from the lack of statistics, and higher-resolution ob-

servations could improve the results. Furthermore, our analysis only applies to those cores whose masses have been calculated based on assumed temperature since the masses derived using gas temperature do not include high mass cores exceeding $25 M_{\odot}$. In the following method, I will investigate the location of the high-mass core from the center of cluster NGC 6334-V.

- According to the first method, I discovered that high-mass stars are nearer to each other than their low-mass partners. However, the compact configuration of massive cores alone is not sufficient to declare that a cluster is segregated. The distance of massive stars from the center of the cluster comprises another crucial factor in the study of segregation.

The main challenge with the second method lies in defining the center of the cluster. I used three strategies to specify the central point in NGC 6334-V: first, assuming that the physical center of mass of the cores is the center of the cluster; second, determining the geometrical center or the mean position of the cluster members; and third, presuming the location of the most massive core to be the cluster center. The difference between the coordinates of the three defined centers is negligible, indicating a mean relative offset of 2.7 mas. Figure 4.7 shows the relationship between the mass of the cores and their relative distance to the center. I again repeat the analysis for two sets of masses. The masses calculated based on the gas temperature are shown in the top row plots in purple, and the masses determined using the assumed temperature are shown in the bottom rows of the plot in blue. In each panel, two dashed lines divide the panels into four quadrants. The vertical dashed line shows the mass threshold of $25 M_{\odot}$, while the horizontal dashed line shows the distance threshold of one-third of the cluster radius. The utilization of these thresholds for assessing mass segregation implies that the proportion of massive cores located near the center reflects the level of segregation within the cluster. Although a suggestion of segregation is observed in both datasets, it is essential to mention that due to the limited resolution, the small core population, and the inaccuracies in temperature determination, we cannot conclusively confirm the level of mass segregation.

- The third method involves detecting and quantifying mass segregation by comparing the *MST* of stars within a cluster with the *MST* of the most massive stars. This approach, introduced by Allison et al., 2009b allows the quantitative measurement of segregation using the Λ_{MSR} parameter. The Λ_{MSR} pa-

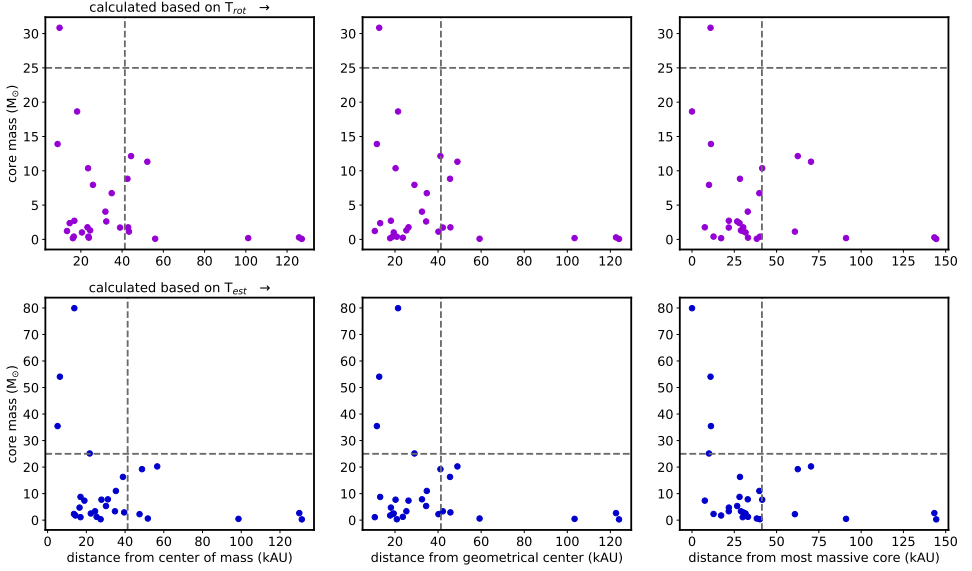


Figure 4.7.: The mass of cores versus their distance from the center of cluster NGC 6334-V. Each row represents different masses calculated based on either the gas temperature (top panels) or the estimated temperature (bottom panels). Each column corresponds to distances from different reference points: the center of mass (left panels), the geometrical center (middle panels), and the location of the most massive core (right panels). The vertical and horizontal dashed lines partition each panel into four quadrants, with a mass threshold of $25 M_{\odot}$ and a distance threshold of one-third of the cluster radius.

parameter compares the 2D spatial distribution of N most massive cores with a spatial distribution of N randomly selected cores using the MST method. If the length of the MST of the most massive stars is significantly shorter than the average length of the MSTs of the random stars, then the massive stars exhibit a distinct and more concentrated distribution, and the cluster is called mass segregated. In this method, the mass segregation ratio (Λ_{MSR}) define as the ratio between the average random path length and that of the massive stars as:

$$\Lambda_{\text{MSR}} = \frac{\langle l_{\text{random}} \rangle}{l_{\text{massive}}} \pm \frac{\sigma_{\text{random}}}{\sigma_{\text{massive}}}, \quad (4.11)$$

where $\langle l_{\text{random}} \rangle$ is the average length of the MST of sets of N_{MST} random cores, l_{massive} is the mean MST length of the N most massive sources and σ_{massive} and σ_{random} display the standard deviation associated with the aver-

age length of the massive and random MSTs, respectively.

I follow the strategy mentioned in Allison et al., 2009b to calculate the Λ_{MSR} parameters. In the first step, I determine the $\langle l_{\text{random}} \rangle$ by generating a large sample of 10000 clusters and N cores that are uniformly distributed over a circle area similar to the actual size of the cluster. The positions of each core within the two-dimensional disk-like cluster are obtained as follows:

$$\begin{aligned} r &= (2 - \alpha)R_r/2^{1/(2-\alpha)}, \\ \phi &= 2\pi R_\phi, \\ x &= r \cos(\phi), \\ y &= r \sin(\phi), \end{aligned} \tag{4.12}$$

where R_r and R_ϕ are random numbers ranging from 0 to 1, and $\alpha = 1$. For a disk with a radius of R_{disk} centered at (X_c, Y_c) , the r parameter and randomly generated coordinates are scaled as follows:

$$\begin{aligned} r &= R_{\text{disk}}((2 - \alpha)R_r/2^{1/(2-\alpha)}), \\ x &= X_c + r \cos(\phi), \\ y &= Y_c + r \sin(\phi). \end{aligned} \tag{4.13}$$

For a given values of most massive cores (N_{MST}), I generate the random sample of N cores where the $N = N_{\text{MST}}$. I started with the 3 most massive cores in our observed ALMA continuum cores and increased this value up to the 25 most massive cores. Then, I determine the average length of the MST of sets of N random cores as well as the length of the MST of the N_{MST} most massive cores to calculate the Λ_{MSR} parameter. I repeat the above steps a thousand times to determine how the degree of mass segregation changes with masses. As in the previous steps, I repeated the test for the two sets of masses to compare the differences.

A $\Lambda_{\text{MSR}} \approx 1$ implies that the distribution of massive sources is similar to other cores in a uniform cluster. On the other hand, $\Lambda_{\text{MSR}} > 1$ implies the presence of mass segregation, with the massive objects being more concentrated toward the center of the cluster. Conversely, $\Lambda_{\text{MSR}} < 1$ implies massive objects are broadly distributed within the entire cluster. Figure 4.8 shows the variation of Λ_{MSR} with N_{MST} for two sets of masses based on the gas temperature (left panels) or the estimated temperature (right panels). With increasing

N_{MST} , each point represents a cumulative mass range, decreasing from the most massive core with the σ error in Λ_{MSR} shown in grey vertical line. Both sets of mass estimates show similar results. The Λ_{MSR} is around 8.5 for $N_{\text{MST}} < 5$ for both, and then drops sharply towards three and smoothly reduces to 2 when $N_{\text{MST}} > 5$. Although we do not have a rich sample due to the lack of statistics, only a few of the most massive stars still show clear evidence of mass segregation.

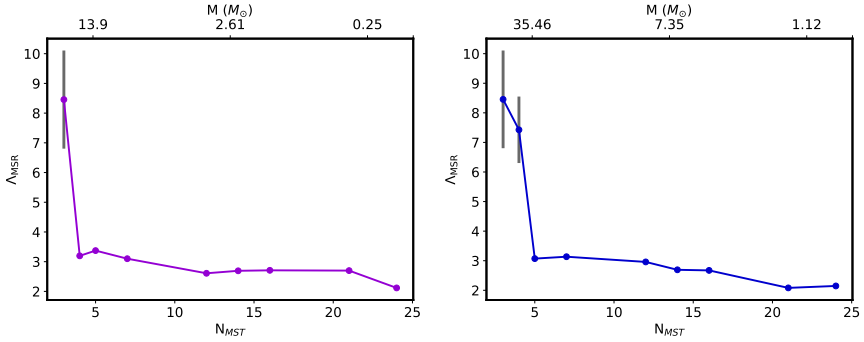


Figure 4.8.: The evolution of Λ_{MSR} with N_{MST} for two masses calculated based on the gas temperature (left panels) or the estimated temperature (right panels). Each point of the figure corresponds to all cores with the mass greater than N_{MST} . The mass which corresponds to a sharp drop of Λ_{MSR} determines the segregation threshold.

The present analysis obtained from the three different methodologies reveals indications of mass segregation in NGC 6334-V. However, it is essential to acknowledge that possible bias may affect the results because of the large uncertainties in temperature measurements and the unresolved multiplicity that leads to the absence of many low-mass cores. Therefore, higher-angular observations, along with accurate temperature determination, become necessary to characterize mass segregation comprehensively. Later in Section 4.6, I discuss the origin of segregation and compare our findings on source V with other sources in the NGC 6334.

4.6. DISCUSSION

As discussed in previous sections, through ALMA observations towards NGC 6334-V, I identified the presence of 28 cores in the cluster and revealed clear evidence of star formation. I presented the distributions of core temperature, mass, column

density, and volume for all identified cores (Section 4.4). Additionally, I determined various physical properties of the cluster, such as fragmentation and instability (Section 1.3.4), separations between the members (Section 4.5.1), mass distribution among the members (Section 4.5.3), and mass segregation (Section 4.5.4). In this section, I focus on two subjects: hierarchical structures and time evolution in NGC 6334-V as a member of NGC 6334 filamentary cloud.

4.6.1. HIERARCHICAL STRUCTURES IN NGC6334 STAR CLUSTERS

One of the initial subjects that can be considered in the NGC 6334 cloud and its known sites is the investigation of hierarchical structures and the fragmentation process. The NGC 6334 cloud is a filamentary cloud aligned with the Galactic disk, with an extent of about 50 pc (Persi and Tapia, 2008; Russeil et al., 2013; Sánchez-Monge et al., 2015). It exhibits hierarchical structures down to scales of 1000 au (Sadaghiani et al., 2020). The central part of the cloud, where all five mentioned clusters are located, comprises a 10 pc long filament characterized by an average density of approximately 10^6 cm^{-3} . The filament undergoes fragmentation itself into several star-forming clumps with extents of 1 pc and masses up a few hundred solar masses. Sub-millimeter observations using *Herschel* have identified many compact sources within these clumps, typically separated by tens to hundreds of thousands of au. A study of the velocity field of HCO^+ towards the central part of the filament by Zernickel, Schilke, and Smith, 2013 revealed a significant velocity gradient that suggests a gravitational collapse and contraction in this region.

The 3 mm *ALMA* observations reveal additional levels of fragmentation within the massive protoclusters, appearing at a scale of approximately 0.1 pc. Protocluster NGC 6334-V, as well as four other observed protoclusters, shows several smaller dense cores with a size of 100 to 1000 au that indicate the presence of fragmentation on the smaller scale. In Section 4.5.1, I report that the mean separation of cores in NGC 6334-V is 12.4 kau, which is most similar to cluster NGC 6334-I(NW) with a mean core separation of 11.7 kau.

In terms of Jeans instability, cluster NGC 6334-V reveals similarity to values for other clusters NGC 6334-E, NGC 6334-I, and NGC 6334-I(N) within the same cloud, NGC 6334 reported by Sadaghiani, 2021. These clusters have a mean mass of the observed cores considerably larger than the thermal Jeans mass. Furthermore, cluster NGC 6334-V, similar to NGC 6334-I and NGC 6334-I(N), displays some hints that there could be an excess of massive cores, but this evidence is not dominant. If the excess of massive cores proves true, it could suggest that turbulent pressure is

more dominant than thermal pressure in regulating the fragmentation process in these clusters. While turbulent fragmentation has also been observed in the massive star-forming region G28.34-P1 (Wang et al., 2011), this is not always the case since other studies (see, for example, Palau et al., 2015) have suggested thermal Jeans fragmentation in various high-mass star-forming clouds of scales 0.1 pc.

4.6.2. COMPARATIVE ANALYSIS OF TIME EVOLUTION IN NGC6334 STAR CLUSTERS

The 3 mm ALMA observation of NGC 6334-V used in our project is part of a larger project that includes four other clusters: NGC 6334-I, NGC 6334-I(N), NGC 6334-I(NW), and NGC 6334-E in the NGC 6334 cloud. A recent study by Sadaghiani et al., 2020 revealed a trend of evolution for these four clusters, suggesting an evolutionary order based on the number of young stellar objects and infrared counterparts. Cluster NGC 6334-V is part of the filamentary cloud NGC 6334, which contains many sites of star-forming regions similar to NGC 6334-V but at different evolutionary stages. One aspect of studying cluster NGC 6334-V is to examine its evolution in relation to other clusters within the cloud. In the following, I will investigate the correlation between the time evolution and the properties of CMF and mass segregation of the cluster based on the observed evolutionary trend among the star-forming regions in NGC 6334.

COMPARATIVE ANALYSIS OF CMF IN NGC6334 STAR CLUSTERS

In Section 4.5.3, I defined low mass regimes ($0.8 < M < 5 M_{\odot}$) and high mass regimes ($M > 5 M_{\odot}$) and generated two CMF based on the masses, taking the assumed temperature (T_{assume}) and rotational temperature (T_{rot}) respectively. In Figure 4.9, I show the CMFs of NGC 6334-V compared with four other clusters in NGC 6334 cloud that were introduced in Sadaghiani, 2021.

The CMF of cluster NGC 6334-V for cores with masses less than $5 M_{\odot}$ shows a deficit relative to the IMF in both cases NGC 6334-V (T_{rot}) with the slope of -0.57 and NGC 6334-V (T_{assume}) is -0.42 , where the IMF slope is -0.3 . However, both cases of the CMF in source V show a comparable slope to NGC 6334-I(NW) (see violet and red lines in Figure 4.9) and very close behavior to NGC 6334-IN (see blue and cyan lines in Figure 4.9), respectively.

For cores with masses larger than cutoff masses of $5 M_{\odot}$, the CMF of the NGC 6334-V (T_{rot}) with a slope of -2.12 shows a large deficit from the IMF slope ($= -1.1$). This behavior is more similar to the CMF of the NGC 6334-I(NW) ($\alpha = -1.32$ for

$M > 2 M_{\odot}$) and NGC 6334-E ($\alpha = -3.17$ for $M > 2 M_{\odot}$) clusters, which also show a deficit in high mass regimes and exhibit a steep behavior, likely attributed to the limited number of sources. On the other hand, the CMF of the NGC 6334-V (T_{assume}) with the slope -1.03 shows an excess with respect to the IMF slope ($\alpha = -1.1$). This behavior is more similar to the CMF of the NGC 6334-I ($\alpha = -0.71$ for $M > 2M_{\odot}$) and NGC 6334-I(N) ($\alpha = -0.99$ for $M > 2 M_{\odot}$) that are more evolved clusters (Sadaghiani et al., 2020). The excess of massive cores is also comparable to other high-mass star-forming regions, such as G28.34+0.06 (Zhang et al., 2015), Sagittarius B2 (Sánchez-Monge et al., 2017), and W43-MM1 (Motte, Bontemps, and Louvet, 2018).

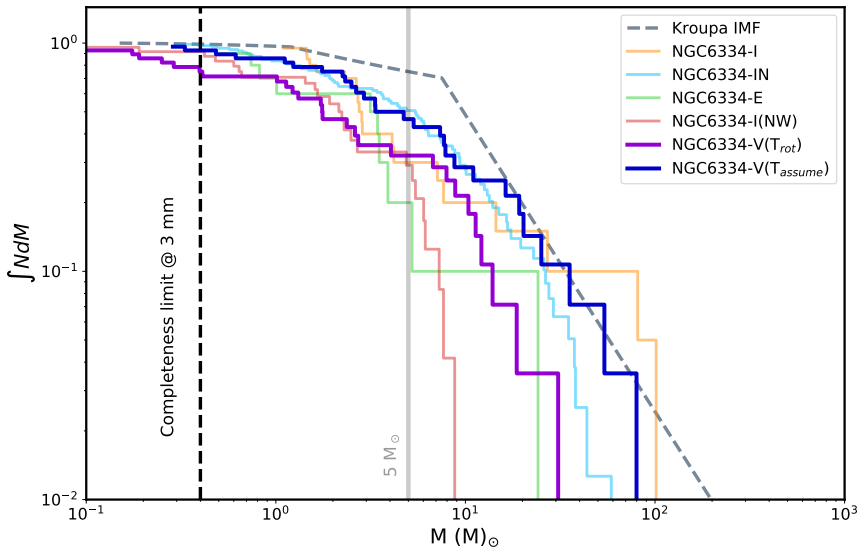


Figure 4.9.: The cumulative core mass function of continuum sources identified in NGC6334-V (violet for masses calculated based on CH_3CCH rotational temperature and blue for masses calculated based on assumed temperatures.) compared with other clusters in NGC 6334, NGC6334-I (orange), NGC6334-I(N) (cyan), NGC6334-I(NW) (red), NGC6334-E (grey) from Sadaghiani et al., 2020. The grey dashed line shows the Kroupa initial mass function shifted by a factor of 15 to the higher masses.

COMPARATIVE ANALYSIS OF MASS SEGREGATION IN NGC6334 STAR CLUSTERS

In Section 4.5.4, I present evidence suggesting mass segregation within cluster NGC 6334-V. However, due to the limited number of detected cores, it would be challenging to trace the origin of segregation solely within cluster NGC 6334-V. A

comparative analysis with the other clusters within the NGC 6334 cloud is worth considering since the cloud harbors numerous clusters in different evolutionary stages, providing an opportunity for a broader insight into similar clusters to NGC 6334-V.

Figure 4.10 represents the evolution of Λ_{MSR} in cluster NGC 6334-V in comparison to four other clusters: NGC 6334-E, NGC 6334-I, NGC 6334-(N), and NGC 6334-I(NW). Our comparison with clusters studied by (Sadaghiani et al., 2020) reveals that the behavior of cluster NGC 6334-V has a close similarity to cluster NGC 6334-I. Apart from that, cluster NGC 6334-I(N) also reveals a less significant evidence of mass segregation. I compare the free fall and dynamical time scales of the cluster

4

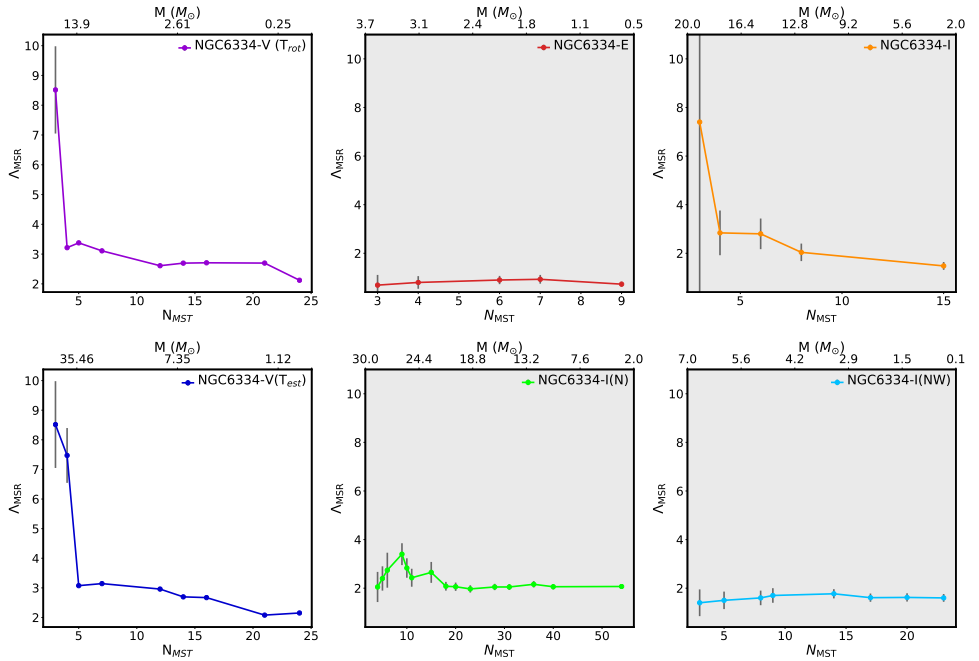


Figure 4.10.: The evolution of Λ_{MSR} with N_{MST} for the two mass distributions in cluster V, calculated based on the gas temperature (left panels) or the estimated temperature (right panels). Each point of the figure corresponds to a arbitrary mass range relative to the most massive cores. The mass which corresponds to a sharp drop of Λ_{MSR} determines the segregation threshold.

NGC 6334-V with two other clusters, NGC 6334-I and NGC 6334-I(N), to investigate the origin of mass segregation. This comparison is meaningful as free fall time and relaxation time are interconnected in the context of mass segregation in grav-

itational systems. The free fall time is the characteristic timescale for an object or a system to collapse under its gravity and undergo gravitational collapse. It represents the time for an initially unbound system to collapse into a more compact configuration. The free fall time t_{ff} (Shu, Adams, and Lizano, 1987) is given by the equation:

$$t_{\text{ff}} = \sqrt{\frac{3\pi}{32G\rho}}, \quad (4.14)$$

where G is the gravitational constant, and ρ is the average H_2 density of the cluster. The relaxation time is a timescale that characterizes the evolution of a system towards a more relaxed or equilibrium state because of gravitational interactions between its constituent members. The time relaxation requires the number of fragments within the cluster and its crossing time (Bonnell and Davies, 1998b). In other words, it represents the time it takes for a system to achieve a statistical equilibrium, where the effects of interactions, collisions, and gravitational interactions have equilibrated and are given by the equation:

$$t_{\text{relax}} = \frac{N}{8\log(N)} t_{\text{cross}} \simeq \frac{N}{16\log(N)} \frac{1}{\sqrt{G\rho}} \quad (4.15)$$

where N is the number of cluster members. Therefore, the relationship between free fall time and relaxation time determines the extent to which mass segregation can occur in a gravitational system.

If $t_{\text{relax}} < t_{\text{ff}}$, the system has sufficient time for interactions to occur and for mass segregation to take place. In such cases, the system can reach a more relaxed state where more massive objects sink towards the center because of gravitational interactions and sufficient dynamical interactions, leading to more pronounced mass segregation.

If $t_{\text{relax}} > t_{\text{ff}}$, the system has not yet had enough time to relax and achieve significant mass segregation. In this scenario, the effects of dynamical interactions might be limited, and the system may exhibit less pronounced mass segregation.

I determine the t_{relax} of 8×10^7 and t_{ff} of 6×10^5 yrs showing two order of magnitude larger relaxation time than free fall time. This indicates that the timescale for the system to reach a relaxed state because of gravitational interactions is significantly longer than the timescale for collapse under its gravity. Both times are also consistent with values reported by Sadaghiani et al., 2020. The supporting evidence for mass segregation in Section 4.5.4 and the high value of relaxation time challenge the dynamical segregation scenario in this cluster. In such case, primordial mass

segregation suggests that the mass differences were present from the initial stages of the formation rather than arising solely from dynamical interactions over time.

5

MOLECULAR LINES - I: TEMPERATURE AND FILAMENT ANALYSIS IN NGC 6334-V

This chapter presents 3mm ALMA observations toward molecules with extended emissions and explores the properties of molecular tracers, including CH_3CCH as a temperature tracer and H^{13}CO^+ as a filament identifier. By investigating temperature, mass, and velocity distributions, I aim to gain insights into temperature characteristics, filamentary structures, and the impact of large scale filaments and HII regions on the formation of the hub cluster NGC 6334-V.

5.1. MOLECULAR LINE EMISSIONS: MOMENT MAPS

Figure 5.1 show the moment maps of all molecules that reveal extended emissions. The top panels show the velocity-integrated emission (0^{th} -order moment), velocity (1^{st} -order moment), and linewidths (FWHM, obtained from the 2^{nd} -order moment) maps of the H^{13}CO^+ (1–0) line emission. The integrated emission map reveals a structure similar to the continuum emission (cf. Figure 4.1). I find clumpy emission features in the central region, with several elongated structures stretching toward the north-west and south-west. These elongated structures, which might be considered as filaments (see Section 5.3.2), are associated with coherent velocity gradients along them (see velocity map in Figure 5.1) similar to what is found in regions with mass-accreting filaments (e.g. Peretto et al., 2013; Treviño-Morales et al., 2019; Schwörer et al., 2019). The H^{13}CO^+ line velocity map shows that the dense gas is at velocities within -4 and -8 km s^{-1} . The 2^{nd} -order moment map shows low values of linewidths (≈ 1 km s^{-1}) in the outer parts of NGC 6334-V, while they increase up to 30 km s^{-1} in the central region, where the continuum dense cores concentrate. I note that the velocity dispersion image is saturated to a maximum of 4 km s^{-1} in Figure 5.1. The H^{13}CO^+ emission line is optically thin, and is a proper candidate of tracing molecular gas along filaments.

The lower panels in Figure 5.1 display the velocity-integrated emission (0^{th} -order moment) maps for the molecular lines HCN (1–0), H^{13}CN (1–0), HN^{13}C (1–0), CCH (1–0), and CH_3CCH (5_k-4_k), all of which are considered as dense gas tracers, together with the shock gas tracer SiO (2–1). The spatial structure of all the dense gas tracers is similar to that of the H^{13}CO^+ emission, although some species exhibit an additional elongated feature extending towards the north-east.

The middle panels show the velocity-integrated emission (0^{th} -order moment) of the HCN, H^{13}CN , and HN^{13}C emission lines. The HCN intensity map shows the most extended emission among all molecular lines, while its isotopologue H^{13}CN is mainly found toward the central region. The isomer HN^{13}C has a much more

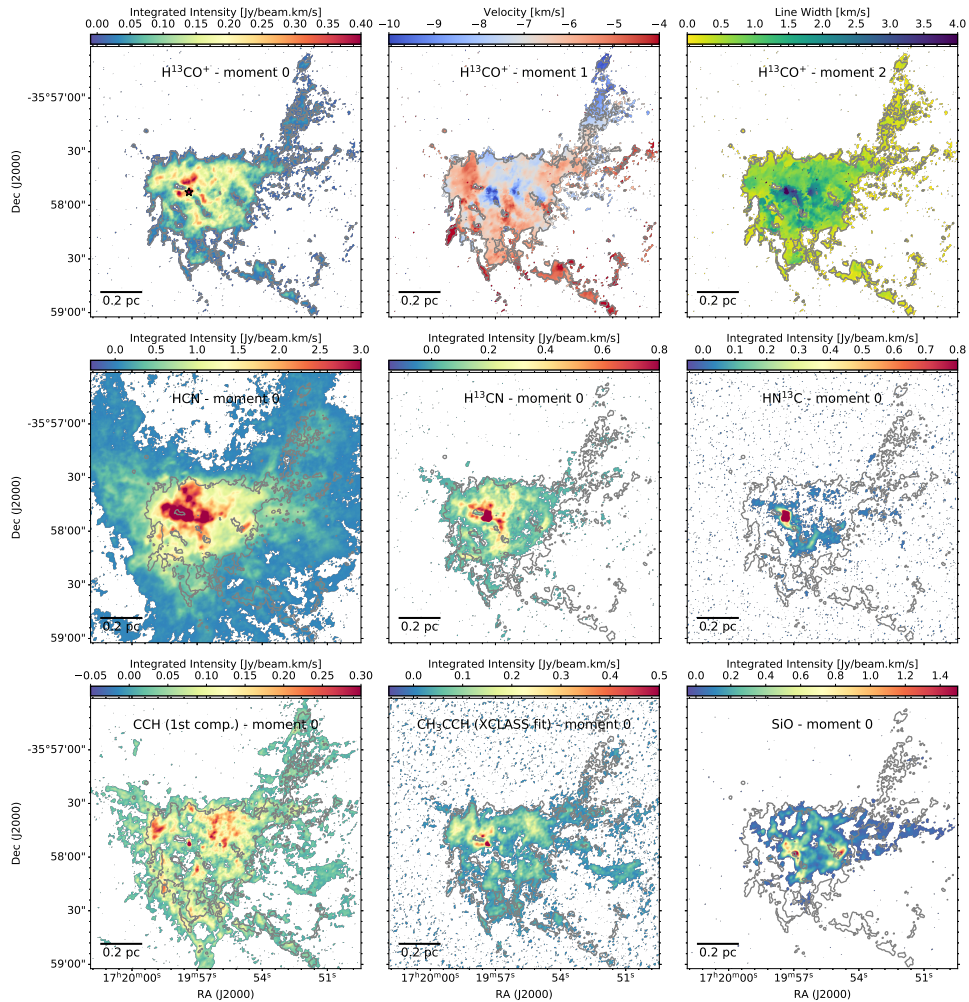


Figure 5.1.: (Top): Velocity integrated intensity (0th-order moment), velocity offset (1st-order moment), and velocity (2nd-order moment) maps of the H^{13}CO^+ (1-0) line emission. In all panels, the gray contour marks the H^{13}CO^+ (1-0) integrated intensity at a level of $0.025 \text{ Jy beam}^{-1} \text{ km s}^{-1}$. The star symbol in the top-left panel marks the position of the hot core (core #15 in Table 4.2). (Middle and Bottom): Integrated intensity (0th-order moment) maps of HCN (1-0), H^{13}CN (1-0), HN^{13}C (1-0), CCH (1-0), CH_3CCH (5_k-4_k) and SiO (2-1), with the gray contours as in the top panels.

concentrated structure resembling the brightest parts of HCN and H¹³CN and is the least abundant one which is also absent in the most of the central regions.

The bottom panels show the velocity-integrated emission (0th-order moment) of the CCH, CH₃CCH (1st component of the spectrum) and SiO emission lines. The intensity map of CCH is similar to H¹³CO⁺ in terms of morphology of elongated features although it traces more elongated branches, including the filamentary-like features towards the north-east. The emission in the central region, however, appears different compared to the other dense gas tracers, with no clear emission peaks. This might be due to chemical effects, since CCH is highly affected by ultraviolet radiation (e.g., increasing its abundance; Cuadrado et al., 2015; Tiwari et al., 2019; Kim et al., 2020; Barnes et al., 2020), and NGC 6334-V is surrounded by a number of H II regions (see Section 5.4.1). The integrated emission of CH₃CCH shows a spatial distribution similar in extent to the other dense gas tracers, although with a deficit of emission to the south-west of the central region. The shock tracer SiO shows a different spatial structure compared to the dense gas tracers (see Section 6.1 for more details). There are two bright areas, one close to the center of the cluster and the other about 0.2 pc to the west, while the fainter SiO emission appears to preferentially extend to the west, likely following the elongated features seen in the dense gas.

In the following, I start with CH₃CCH to characterize the temperature of the gas in NGC 6334-V (see Section 5.2), then focus on the analysis of the H¹³CO⁺ as a dense gas tracer to identify filamentary structures (see Section 5.3). In chapter 6, I present the analysis on SiO emission to understand the presence of shocked-gas in the region.

5.2. CH₃CCH: TEMPERATURE TRACER

CH₃CCH, known as methyl acetylene, is a prolate symmetric top molecule with a carbon chain backbone (Townes and Schawlow, 1975). The rotational energy levels can be expressed by the formula $E = hBJ(J + 1) + h(A - B)K^2$, where J and K are quantum numbers representing the rotational states of the molecule. The K quantum number is a quantized projection of the angular momentum along the symmetry axis of the molecule. In CH₃CCH molecule, the radiative transitions between the K-ladders are forbidden. The relative populations of the K-ladders depend primarily on the kinetic temperature of the colliding particles, which means that for a given J quantum number, there is a K-ladder that has a wide range of energy levels emitting over a narrow frequency range. So, each K component of a

given rotational transition represents a different excitation energy spanning over a narrow frequency range that can be observed simultaneously (Askne et al., 1984; Bergin et al., 1994).

I use the molecule CH₃CCH to determine the excitation temperature toward NGC 6334-V. In our ALMA data, we have observations of the CH₃CCH (5_K-4_K) transition with K ranging from 0 to 4, and with energy levels of the upper states ranging from 12 to 128 K. I use the eXtended CASA Line Analysis Software Suite (XCLASS¹, Möller, Endres, and Schilke 2017) to determine the excitation temperature together with the molecular column density in NGC 6334-V. For this, I use continuum subtracted CH₃CCH spectral data cube and fit the five K -ladder components of CH₃CCH (5_K-4_K) molecular transition, simultaneously. In Appendix A, I present the theoretical framework for using the XCLASS application. Also, I explain the background of the parameters and the function myXCLASSMapFit for fitting spectra across the entire emission map.

5.2.1. DETAILS OF XCLASS MODELING ANALYSIS

I use the myXCLASSMapFit function, with the Trust Region Reflective algorithm (`trf`)² to fit a spectral data cube with 480 frequency channels, and 1280×1280 pixels. The `trf` algorithm is a fast local optimization algorithm that guarantees that the fitting parameters remain within the user-defined parameter limits. The fit parameter set for each CH₃CCH component consists of the source size in arcsec, the rotational temperature (T_{rot}) in K, the column density (N_{tot}) in cm⁻², the velocity width (V_{width}) in km s⁻¹, and the velocity offset (V_{off}) in km s⁻¹ from the systemic velocity (V_{LSR}).

Figure 5.2 shows the results from the XCLASS analysis, corresponding to the CH₃CCH column density (top-left), rotational temperature (top-right), velocity offset (bottom-left) and velocity width (bottom-right). The column density and rotational temperature increase toward the central region, where the dense cores are located. The higher temperatures in this central region are likely due to the star-formation activity within the dense cores. Towards the hot molecular core, the gas temperature increases up to ≈ 250 K, the highest in the NGC 6334-V region.

The offset velocity ranges from -4.0 to -7.5 km s⁻¹ with respect to the systemic velocity of the source V . I determine a systemic velocity of -6.2 km s⁻¹ in

¹<https://xclass.astro.uni-koeln.de>

²https://docs.scipy.org/doc/scipy/reference/generated/scipy.optimize.least_squares.html

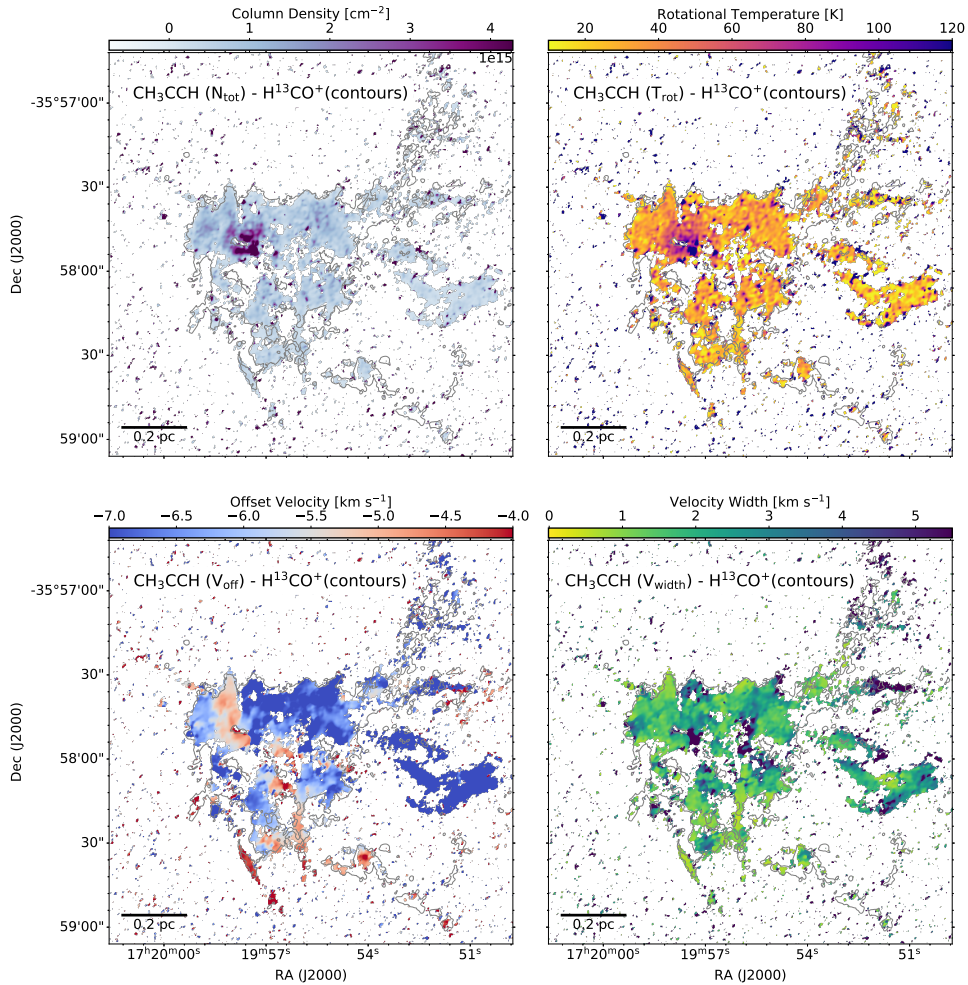
NGC 6334-V by fitting a Gaussian to the averaged spectrum of the H^{13}CO^+ (1–0) emission. This value is consistent with the value of -5.7 km s^{-1} reported by Juárez et al. (2017b). The velocity width map shows an homogeneous distribution over the entire region with typical values of 2 to 3 km s^{-1} , and the broadest velocity width is $\approx 10 \text{ km s}^{-1}$ at the position of the hot core. A comparison between the XCLASS-derived maps for the offset velocity and velocity width based on CH_3CCH (see Figure 5.2) with the 1st and 2nd-order moment maps derived from H^{13}CO^+ (see Figure 5.1) reveals a similar velocity structure for both dense gas tracers. The gas is blue-shifted towards the north-western direction, and red-shifted in the southern and north-eastern regions.

5.2.2. UNVEILING CORE TEMPERATURES AND FLUCTUATIONS THROUGH XCLASS FITS

5

One use of XCLASS results is in the temperature estimation of detected cores through 3mm ALMA observation. In Chapter 4, I employed the CH_3CCH temperature map from the XCLASS results to estimate the temperature of the identified cores. The top-left panel of Figure 5.3 displays the 3mm ALMA continuum cores overlaid on the XCLASS fit temperature map. To measure the temperature of each core, I calculate the mean value over the area of a deconvolved radius. In the top-right panel of Figure 5.3, I again overlay the same cores, but this time I colorized them based on the range of rotational temperature. It is worth noting that the Herschel observation with 8 arcsecs angular resolution (0.07 pc) is the only temperature map available for tracing NGC 6334-V so far, but it suffers from low resolution for accurately tracing core temperatures. Thus, the resolution of Herschel data is insufficient to ensure the accuracy of rotational temperature measurements. The bottom-left panel of Figure 5.3 shows continuum cores with the color code representing the rotational temperature of CH_3CCH overlaid on the 3mm ALMA continuum map. Finally, the bottom-right panel of Figure 5.3 displays continuum cores with the color code representing the dust mass overlaid on the 3mm ALMA continuum map

All cores except four were traced by the XCLASS fitted temperature map of CH_3CCH molecular emission. For the four cores that did not show any fitted rotational temperatures, I made assumptions based on old publications (e.g., Sadaghiani et al., 2020). For the cores observed for the first time within the ALMA observations (core numbers 14, 17, and 23 in Table 4.2), I assumed a temperature of



5

Figure 5.2.: Physical parameters derived from the XCLASS analysis of the CH₃CCH emission: (*Top-Left*) CH₃CCH molecular column density, (*Top-Right*) rotational temperature, (*Bottom-Left*) offset velocity, and (*Bottom-Right*) velocity width. The grey contours in all maps show the H¹³CO⁺ (1–0) integrated intensity at a level of 0.025 Jy beam⁻¹ km s⁻¹ (see Figure 5.1). I note that the velocity linewidth (Δv) shown in the bottom-right panel relates to the velocity dispersion σ corresponding to the 2nd-order moment by $\Delta v = \sqrt{8 \ln 2} \sigma$.

20 K, and for core number 2 in Table 4.2, which had class II infrared counterparts (604077(ICII)), I assumed a temperature of 50 K.

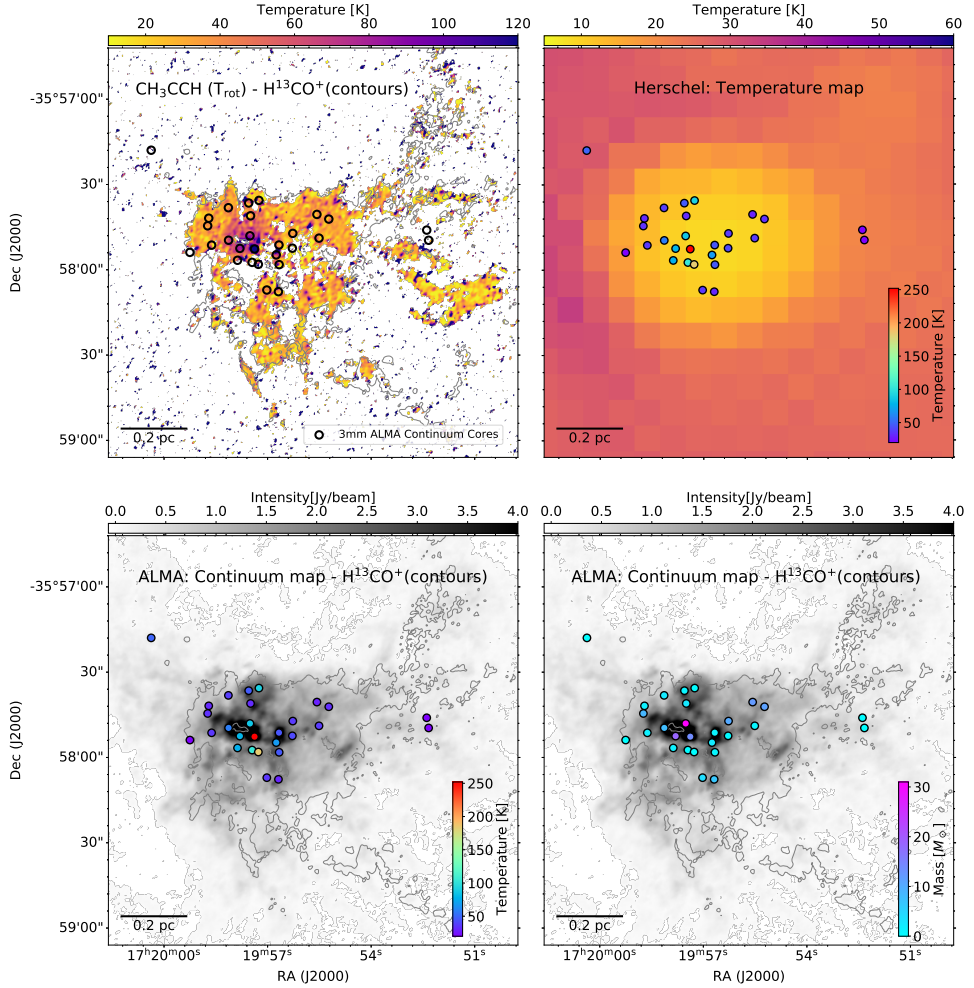


Figure 5.3.: Comparison of temperature dispersion for CH₃CCH temperature fit and Herschel temperature map, as well as the mass and temperature of continuum cores. (*Top-Left*) Rotational temperature from CH₃CCH XCLASS fits and the position of continuum cores. (*Top-Right*) Herschel temperature map and ALMA continuum cores, with the color code representing the rotational temperature of CH₃CCH. (*Bottom-Left*) Continuum cores with the color code representing the rotational temperature of CH₃CCH overlaid on the 3mm ALMA continuum map. (*Bottom-Right*) Continuum cores with the color code representing the dust mass (see Sect. 4.4) overlaid on the 3mm ALMA continuum map.

It is important to note that the temperature derived from CH₃CCH does not directly measure the core temperature; rather, it represents the embedded gas de-

tected along the line of sight of the identified core. Although these measured values are not directly observed from the cores, they can still provide a rough estimate of the temperature in that particular region.

The temperature map obtained through XCLASS fitting reveals widespread fluctuations across the map, ranging from 10 K to 100 K. These fluctuations could originate from disruptions in the flow of accretion gas. In order to verify the accuracy of these fluctuations, it is necessary to measure the errors associated with the fitted values. I use the Markov chain Monte Carlo (MCMC)³ package to derive the error values.

In Appendix B, I present the typical errors obtained for the derived values in the XCLASS fitting procedure. Based on the MCMC algorithm implemented within XCLASS, I derive typical errors of ≈ 0.3 – 0.5 dex, for the logarithm of the column density, ≈ 20 – 50 K for the temperature, ≈ 0.2 – 0.4 km s⁻¹ for the velocity offset and ≈ 0.3 – 0.8 km s⁻¹ for the velocity width. In the case of temperature, the estimated error associated with temperature measurements is relatively large. Large error values suggest a considerable degree of uncertainty in the temperature estimation process, which makes it challenging to confidently interpret and draw conclusions based solely on these temperature fluctuations.

5.3. H^{13}CO^+ : FILAMENT TRACER

As seen in Figure 5.1, the dense gas tracers in NGC 6334-V show elongated features that are reminiscent of filaments as found in other star-forming regions (e.g. Peretto et al., 2013; Treviño-Morales et al., 2019; Schwörer et al., 2019). These elongated features appear to converge in the center where the dense cores are located. Based on this, I aim at identifying filaments in NGC 6334-V. But before identifying the filament paths, I first look at the relation of H^{13}CO^+ to CCH as one of the molecular emissions with the nearest filamentary features as the ones in H^{13}CO^+ .

5.3.1. PRIOR TO IDENTIFYING FILAMENTS: H^{13}CO^+ AND CCH RELATIONSHIP

Among all the extended emission maps shown in Figure 5.1, CCH exhibits filamentary features that closely match those observed in H^{13}CO^+ . The moment 0, 1, and 2 maps of H^{13}CO^+ and CCH, displayed in Figure 5.4, offer additional in-

³The MCMC algorithm uses the emcee package available at <https://emcee.readthedocs.io/en/stable/>

sights into their relationship. CCH can be found widely in various astronomical environments. The CCH molecule is commonly considered tracing molecular gas in a partially ionized state, mainly C^+ , in association with Photodissociation Regions (PDRs), since its abundance suddenly enhanced in the PDRs region (e.g. Wootten et al., 1980; Meier and Turner, 2005); The gas-phase chemistry of CCH proceeds via two main pathways: the dissociative recombination with hydrocarbon ions, and the direct photodissociation of acetylene (C_2H_2) (Meier and Turner, 2005). The moment maps of CCH and $H^{13}CO^+$, as shown in Figure 5.4, exhibit similar emissions at first glance, raising the question of whether both trace the same cold, dense gas. However, distinguishing CCH associated with Photodissociation Regions (PDRs) from cold, dense gas would be challenging.

5

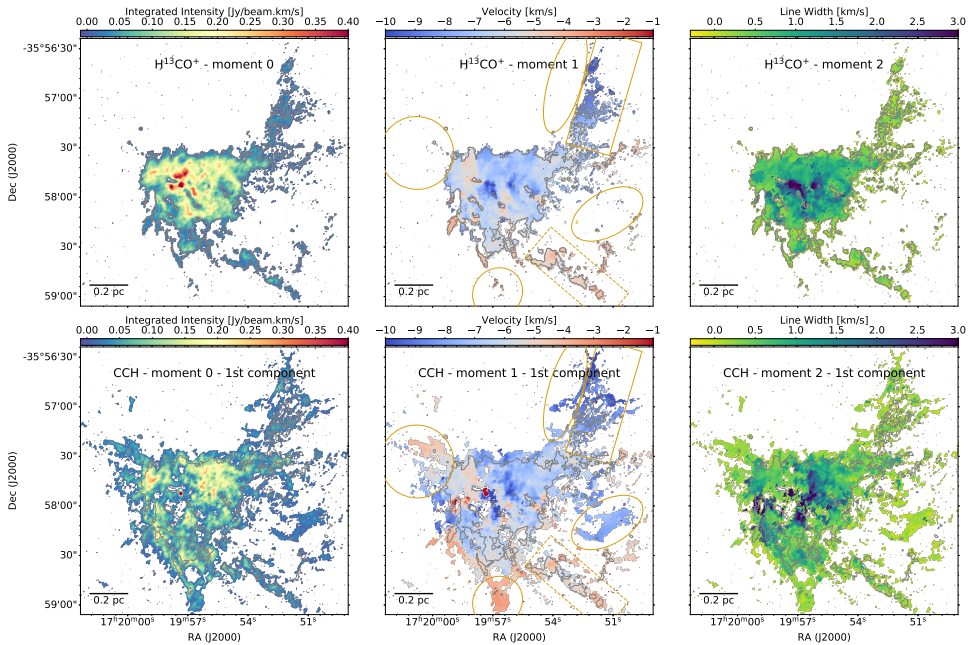


Figure 5.4.: Comparative extended emission maps of $H^{13}CO^+$ and CCH. The first row shows the $H^{13}CO^+$ moment 0, 1, and 2 maps, representing the integrated intensity, intensity-weighted velocity, and line width, respectively. The second row shows the corresponding moment 0, 1, and 2 maps for CCH. These maps provide insights into the relationship between the filamentary features traced by $H^{13}CO^+$ and CCH in the molecular cloud.

The first challenge concerns the exact spatial location of cluster NGC 6334-V, as this location may influence the observations and analyses. It is plausible that all the structures are aligned along the line of sight. In Section 5.4.1, I show that an HII region could be situated behind the cloud, potentially creating a layer comprising both Photodissociation Regions (PDRs) and dense gas. The presence of the HII region in the background induces dissociative-related chemistry, thereby increasing the formation of CCH. The gold ellipses marked in Figure 5.4 show regions within the map where cold materials traced by H^{13}CO^+ is absent and where CCH is most likely tracing the PDRs.

One way to check the origin of CCH emission is to compare the velocity ratio of CCH and H^{13}CO^+ in the first-moment map of both molecules and test it with the velocity gradient of recombination line data. If I assume that H^{13}CO^+ and CCH both are optically thin, then the velocity ratio of CCH and H^{13}CO^+ could give more information about the origin of CCH. I selected two rectangles along the elongated features I expect to see filaments. The solid-line rectangle shows a velocity separation of 2.0 km s^{-1} between CCH and H^{13}CO^+ , while the rectangle with a dashed line shows data points with less than 1.0 km s^{-1} separation, suggesting that both may trace similar gas. A definitive separation remains difficult due to the lack of recombination line observations and limited data points. However, both H^{13}CO^+ and CCH in the rectangular areas effectively trace the same underlying phenomena and confirm the presence of filaments in this cluster. In section 5.3.2, I will determine the path of these filaments.

5.3.2. FILAMENT IDENTIFICATION

I use the emission of the H^{13}CO^+ (1–0) line since it is not affected by the presence of detectable hyperfine spectral lines in this region, since it is expected to be optically thin, and since it is found to trace well the dense gas features observed in the other dense gas tracers (cf. Figure 5.1). Additionally, I also make use of a stacked image that includes the peak intensity emission map of other molecular species associated with extended emission in NGC 6334-V (i.e., HCN, CCH, H^{13}CO^+ , H^{13}CN , HN^{13}C , and CH_3CCH). Although this second dataset does not have velocity information, it can be used to identify some structures that appear enhanced in other species compared to H^{13}CO^+ . By stacking multiple molecular species together I also avoid possible biases due to chemical effects. The stacked map was used as a guide to finalize the filament path in the H^{13}CO^+ emission map. I also stacked the spectrum along each path to guarantee that filaments trace accretion accurately.

I applied the Discrete Persistent Structures Extractor (**DisPerSE**) software (Sousbie, 2011) to the H^{13}CO^+ spectral cube and to the stacked intensity peak image in order to identify filamentary features. **DisPerSE** is a structure finding algorithm that can handle both position-position and position-position-velocity datasets, and has been commonly used to characterize filaments in star-forming regions (e.g., Treviño-Morales et al., 2019; Suri et al., 2019). The main function of **DisPerSE** is `mse` which calculates Morse-Smale Complex (**MSC**) and extracts filamentary structures from a given data set. The main input parameter of the `mse` function is the persistence level, which we define interactively using a persistence diagram where all critical point pairs are plotted. The function `upSk1` is used to connect maxima to saddle points, and to generate the so-called skeleton file, which contains the information (position and velocity) of the identified filaments. The skeleton file can be improved by adjusting various parameters, including smoothing, angle restrictions, and detection threshold. Finally, the output can be saved in the workable format of `.fits`, `.vtp`, or `.ASCII`. Additional information regarding the theory and application of the **DisPerSE** approach can be found in Appendix C.

I identified a total of six common filamentary structures in both datasets (i.e., the H^{13}CO^+ data cube and the stacked image. See Figure 5.5). I define these common structures as the main filaments in NGC 6334-V. The merged skeleton file has been created manually after cross-checking the location of the skeletons defined for each one of the two datasets with the images and cubes of the different spectral lines. It is worth noting that these filaments are identified either as one large segment or as several small segments⁴ that I have manually connected to reproduce the final skeleton structure of filaments in NGC 6334-V. Moreover, towards the center of the region and in the interface region between molecular gas and ionized gas from extended H II regions (see Section 5.3.2, and Russeil et al. 2016), the velocity structure of the gas is complex likely due to the interaction of forming dense cores and feedback. For example, multiple velocity components are detected in the central part of the region, hampering identification of velocity-coherent filamentary structures. Therefore, I do not extend the filament paths toward the central region of the cluster.

Figure 5.5 shows the six identified filaments. The north-west feature identified previously by eye seems to be formed by three filaments (F1, F2 and F3). Two additional filaments are found towards the south-west direction (F4 and F5), with

⁴These small segments likely belong to larger-scale filamentary structures that **DisPerSE** artificially separates. Once connected, these small segments show a coherent structure both spatially and in velocity, further supporting that they belong to one single larger structure.

the final filament (F6) pointing towards the north-east. The paths of the filaments, identified based on molecular emission, fit well with the infrared dark features seen in the *Spitzer* infrared images (see the bottom plot of Figure 5.8).

In Table 5.1, I list the main properties of the filaments. Their lengths range from about 0.3 to 0.9 pc, although this can be limited by sensitivity effects, since the selected molecules may not be bright in lower-density regions towards the outskirts of the cloud. This seems to be the case for F6 which is only detected in some molecular species. Most of the filaments extend west, with the exception of filament F6, which is elongated in the opposite direction, being also the shortest in length. Filament F5 is significantly bent and seems to merge with filament F4 in the south. This might be due to the presence of H II region bubbles located in the northern and southeastern directions (see discussion in Section 5.4.1). Filaments F2 and F3 seem to change their direction abruptly around the position of detected dense cores lying between these filaments. This might be caused by star formation activity affecting the gas around these dense cores.

Table 5.1.: Kinematic and physical properties of the filaments

Filament ID ^(a)	V_{grad} (km s ⁻¹ pc ⁻¹)	T (K)	M (M _⊙)	L (pc)	M/L (M _⊙ pc ⁻¹)	(M/L) _{crit, th} (M _⊙ pc ⁻¹)	(M/L) _{crit, north} (M _⊙ pc ⁻¹)	\dot{M} (10 ⁻⁵ M _⊙ yr ⁻¹)
F1	-5.2	30.9	156.5	0.86	181.9	51.6	117.2	83.2
F2	+1.7	26.2	150.6	0.71	212.1	43.7	112.0	26.2
— inner	-5.2							
— outer	-1.7							
F3	-0.5	29.9	98.3	0.65	151.2	49.9	103.4	5.0
— inner	-1.7							
— outer	+6.5							
F4	+2.5	31.6	116.9	0.93	125.7	52.7	153.8	29.9
F5	+2.6	30.0	96.3	0.57	169.0	50.1	160.1	25.6
F6	+3.1	31.9	97.8	0.35	279.5	53.3	114.7	31.0
— inner	-8.7							
— outer	+9.7							

^(a) Filament IDs as shown in Figure 5.5. For filaments F2, F3 and F6, the position-velocity plots shown in Figure 5.6 suggest the presence of different velocity gradients. For each one of these filaments, I provide the global value obtained fitting the data throughout the whole extent of the filament, and the inner and outer values corresponding to the sub-datasets fitted in Figure 5.6.

5.3.3. VELOCITY GRADIENTS

In order to characterize the properties of the identified filaments, I start exploring their velocity structure. As seen in Section 5.3.2, the velocity map of H¹³CO⁺

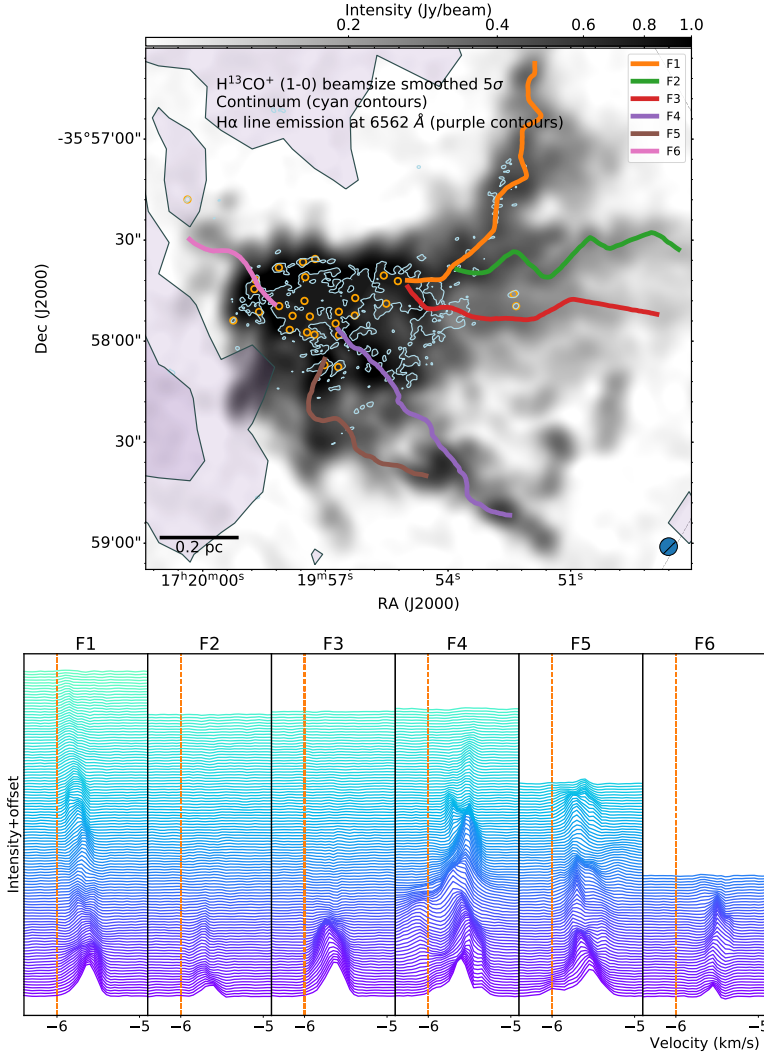


Figure 5.5.: *Top*: Filaments identified in the NGC 6334-V region using H^{13}CO^+ and PPV cube of the stacked intensity map. The six filaments (F1 to F6) are highlighted in different colors, and overlaid on an H^{13}CO^+ (1–0) intensity map smoothed to a resolution of five times the beam size. The cyan contours depict the ALMA 3 mm continuum emission (see Figure 4.1), while the orange circles mark the position of the compact dense cores (see Section 4.2). Purple-filled contours mark the $\text{H}\alpha$ line emission at 6562 Å (Russeau et al., 2016). *Bottom*: Velocity trend among filaments for the molecular species H^{13}CO^+ . The spectra are extracted by moving from the main hub outward onto the filaments paths indicated in the *Top* panel. Each spectrum corresponds to one position along the spine and is generated by averaging spectra over a circular region with a radius of 2σ (where σ represents the beam size). The dashed orange vertical lines indicate the systemic velocity at -6 km s^{-1} .

shows a velocity gradient in the dense gas and along the filaments. In particular, the H^{13}CO^+ velocities to the north-east, where filament F1 is located, are blue-shifted, whereas the velocities to the south, where filaments F4 and F5 are located, are red-shifted (see Figure 5.1). I have used the Python package `pvextractor`⁵ to characterize the velocity variation along the paths of the six identified filaments.

The left panels in Figure 5.6 show the position-velocity (PV) diagrams for the six filaments. I find a variety of velocity structures, with filament F1 having a clear velocity gradient from about -6 km s^{-1} close to the center of the cluster down to -10 km s^{-1} in the outskirts. Filaments F4 and F5, on the contrary, increase their velocity from -6 km s^{-1} in the center up to -4 km s^{-1} in the outer parts. The velocity of all the filaments close to the center is about -6 km s^{-1} , consistent with the estimated systemic velocity of the gas in NGC 6334-V. The PV diagrams of all filaments show a broader velocity distribution towards the center of the region, with emission covering several km s^{-1} , and much narrower (1 km s^{-1}) in the outer regions. This is in agreement with the velocity width maps shown in Figs. 5.1 and 5.2. The velocity structure along the filaments is, in some cases, complex with several velocity components. This is clearly seen in the PV plot of filament F4, where at least two different velocity components can be identified at the position of $\sim 0.1 \text{ pc}$.

In order to derive velocity gradients along the filaments, I have manually fitted Gaussian components to the spectra extracted at different positions along the filament paths. The positions have been selected to be evenly spaced with a separation of 2.5 times the beam size. The fitted velocity of the different Gaussian components are shown in the right panels of Figure 5.6, with the error bar depicting the width of the fitted Gaussian. To derive the velocity gradient, I fit a linear regression to the centroid velocities of the Gaussian fits, excluding those positions along the filament path with multiple Gaussian components (see blue and orange symbols in the right panels of Figure 5.6).

I obtain velocity gradients in the range $0.5\text{--}5.2 \text{ km s}^{-1} \text{ pc}^{-1}$ (in absolute magnitude, see Table 5.1). The velocity gradient for filament F1 is negative, suggesting that it may extend backwards with respect to the central hub that hosts the forming cluster, if we consider that the gas flows from the outer parts to the center. Filament F3, with a very small velocity gradient of about $-0.5 \text{ km s}^{-1} \text{ pc}^{-1}$, might be located close to the plane of the sky. The other filaments, with positive velocity gradients, would extend in the foreground direction.

⁵<https://pvextractor.readthedocs.io/en/latest/>

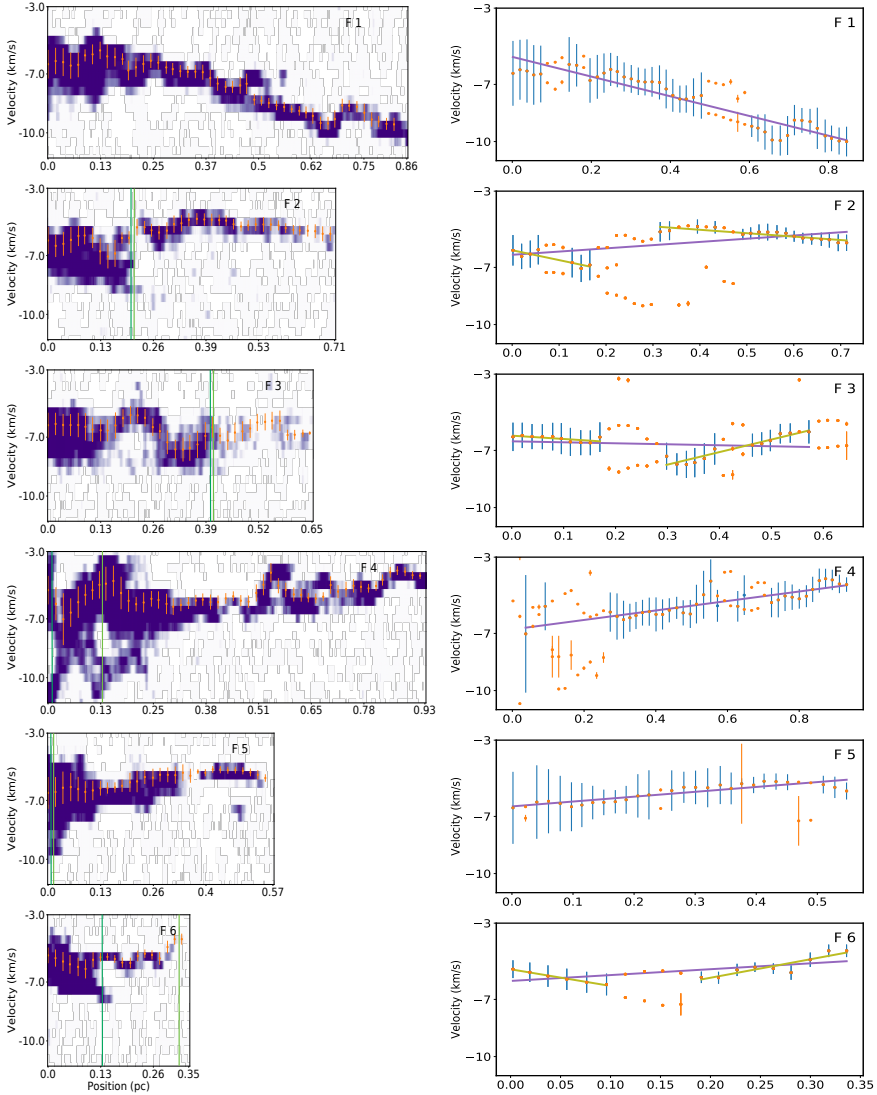


Figure 5.6.: *Left:* Position velocity cut along each filament from H^{13}CO^+ shown in Figure 5.5. The orange dots indicate the peak velocity constructed by extracting mean spectra over a beamsize area along the path of filaments, and the vertical bar shows the FWHM of each spectrum. *Right:* Plots demonstrate the process of calculating the velocity gradient. The orange dots represent each component's peak and the measured error. I only considered single components and removed multiple components from our calculations. The orange dots with blue vertical lines represent single-component spectra, and the blue lines represent the FWHM. Three filaments show wiggly shapes along the path of the filaments, and I fit multiple lines in olive color to indicate a change in slopes. However, I calculated the velocity gradient using the general regression line shown in purple.

The linear fits shown in Figure 5.6 reveal the complexity in the velocity structure of some of the filaments. Filaments F2, F3 and F6 show a change in the velocity slope that might be related to the 3-dimensional orientation of the filament with respect to the observer or to the presence and interaction of dense cores with the gas flowing along the filament. I have marked the location of those dense cores located in the vicinity of the filaments as vertical lines in the PV plots. The presence of core 17 and 14 may be responsible of the two velocity components seen in filament F2 at a position of 0.20 pc and F3 at a position of 0.40 pc; while cores 2 and 9 may affect filament F6, and cores 1 and 28 may affect filament F4 and F5. For completeness, I have also divided the three filaments with a change in the velocity part in two sub-regions corresponding to the inner and outer parts of the filament. Based on this, I determine velocity gradients for these parts and list them in Table 5.1.

5.3.4. MASS ACCRETION RATES

I calculate the mass accretion rate of each filament considering its mass, length and velocity gradient, following Kirk et al. (2013). The filaments are considered to be cylinders, and I assume that the gas flows along the filament. Under these assumptions, the mass accretion rate, \dot{M} , is given by

$$\dot{M} = V_{\parallel} \times \frac{M}{L}, \quad (5.1)$$

where M is the mass of the filament, L is its length, and V_{\parallel} the velocity of the gas along the filament. Due to projection effects, the filament may be inclined by an angle α with respect to the plane of the sky. In that case, the observed parameters are related to the actual length and velocity by

$$L_{\text{obs}} = L \cos(\alpha) \quad \text{and} \quad V_{\parallel, \text{obs}} = V_{\parallel} \sin(\alpha), \quad (5.2)$$

with $V_{\parallel, \text{obs}} = \nabla V_{\parallel, \text{obs}} L_{\text{obs}}$. Then the mass accretion rate can be derived as

$$\dot{M} = \frac{\nabla V_{\parallel, \text{obs}} M}{\tan(\alpha)}. \quad (5.3)$$

I consider a value of α equal to 45° , although the derived accretion rates may vary by a factor of ≈ 1.7 if the inclination angle is 30° or 60° . The mass of each filament is derived using Equation 4.1. The flux of each filament is obtained from the ArTeMIS dust continuum map at $350 \mu\text{m}$ (André et al., 2016), after integrating over a polygon

that we define along each filament path, while the temperature is derived from the CH₃CCH temperature map (see Figure 5.2). The masses and mass accretion rates of each filament are listed in Table 5.1. The masses of the filaments are in the range 90–150 M_{\odot} , which together with the lengths of ≈ 0.5 –0.9 pc, result in line masses of ≈ 150 –280 $M_{\odot} \text{ pc}^{-1}$. The total line mass of all six filaments is 1119 $M_{\odot} \text{ pc}^{-1}$, calculated by adding up all individual line masses.

To study the stability of filaments, I compare their line mass, M/L (mass per unit length), to the critical line mass. Measuring the critical line mass varies depending on whether the thermal gas pressure is the sole force opposing gravity or if turbulence within the gas also contributes to a supporting pressure. In the case of an isolated, infinitely long filament in which the thermal gas pressure is the only force opposing gravity, the critical line mass measure as (Ostriker, 1964)

$$(M/l)_{\text{crit, th}} = 2c_s^2/G = 16.7 \left(\frac{T}{10\text{K}} \right)^2 M_{\odot} \text{ pc}^{-1}, \quad (5.4)$$

where G is the gravitational constant, and c_s is the sound speed directly connected to the thermal velocity dispersion. Thus, the equation 5.4 depends on the gas temperatures and only considers thermal pressure as the opposing force to gravity. The measured line mass for filaments in the are presented in table 5.1. The mean value of thermal line mass is 50 $M_{\odot} \text{ pc}^{-1}$ and the total line mass of all filaments is 300 $M_{\odot} \text{ pc}^{-1}$ which is much smaller than observed line mass. The model commonly used in publications, assume that the turbulence within the gas also provides a supporting pressure as a force against gravity (Chandrasekhar, 1951; Wang et al., 2014). The critical mass per unit length (line mass) measures gravitational instability against collapse in an isothermal gas cylinder as (Wang et al., 2014)

$$(M/l)_{\text{crit}} = 2\sigma^2/G = 465 \left(\frac{\sigma}{1\text{km s}^{-1}} \right)^2 M_{\odot} \text{ pc}^{-1}. \quad (5.5)$$

When the cylinder is supported by thermal pressure, the parameter σ represents the sound speed, c_s . Conversely, if the cylinder relies predominantly on turbulent pressure, σ is substituted with the 1D velocity dispersion, with an associated factor of $\sqrt[3]{}$ when converting from a 3D velocity dispersion.

In section 4.5.2, I show that turbulence pressure has a dominant contribution compared to thermal contribution in NGC 6334-V; therefore, it is necessary to calculate the velocity dispersion and compare the observed line masses with the non-thermal critical line masses. The velocity dispersion can be calculated using either

2nd moment maps (M_2) or *FWHM*, as shown below:

$$\begin{aligned} \sigma &= \sqrt{M_2} \\ &\text{or} \\ \sigma &= \frac{\text{FWHM}}{\sqrt{8 \ln 2}} \end{aligned} \tag{5.6}$$

I measured the σ by analyzing the linewidths and second-moment map of the H^{13}CO^+ cube along the path of filaments. The calculated $(M/l)_{\text{crit, nonth}}$ for all filaments is displayed in table 5.1. If the M/L value is higher than the thermal $(M/l)_{\text{crit, th}}$, then these filaments are likely unstable due to Jeans-like fragmentation. On the contrary, if the M/L value is higher than the turbulent $(M/l)_{\text{crit, nonth}}$, they are likely susceptible to turbulent fragmentation. I find $(M/l)_{\text{crit, nonth}}$ larger than $(M/l)_{\text{crit, th}}$ with a factor of ~ 2 and 3 , indicating that contribution of non-thermal pressures are larger than thermal pressure. Although it is worth noting that both models mentioned above represent a simplified case of an isolated and highly idealized gas cylinder.

The values for the observed line mass of filaments 1, 2, 3, and 6 are about twice as large as the non-thermal critical M/L value. This indicates that these filaments are unstable and undergo collapse and fragmentation, which is also supported by the presence of dense cores found along some of them. On the other hand, filaments 4 and 5 have either similar or larger nonthermal critical line mass values compared to the observed values. This could be due to the chaotic environment near the HII regions where these filaments are located. In comparison to Mon R2 with close evolutionary stage, Treviño-Morales et al., 2019 found that thermal and non-thermal pressures are similar, agreeing within a factor of 2. They further compared this result to the work of Pokhrel et al., 2018, who found that thermal motions are less efficient at larger scales, such as whole clouds, but more efficient at smaller scales, like protostellar objects.

The derived mass accretion rates are in the range $0.5 - 8 \times 10^{-4} M_{\odot} \text{ yr}^{-1}$, adding up to a total of $\approx 2 \times 10^{-3} M_{\odot} \text{ yr}^{-1}$ for the six filaments. Figure 5.7 shows total mass accretion rates of different star-forming regions. The x-axis signifies the star-forming regions from other publications falling into different ranges of mass accretion rates, and the y-axis represents the total mass accretion rates over all filaments (in $M_{\odot} \text{ yr}^{-1}$). The plot contains vertical bars whose heights correspond to the value of total mass accretion rates within specified sources.

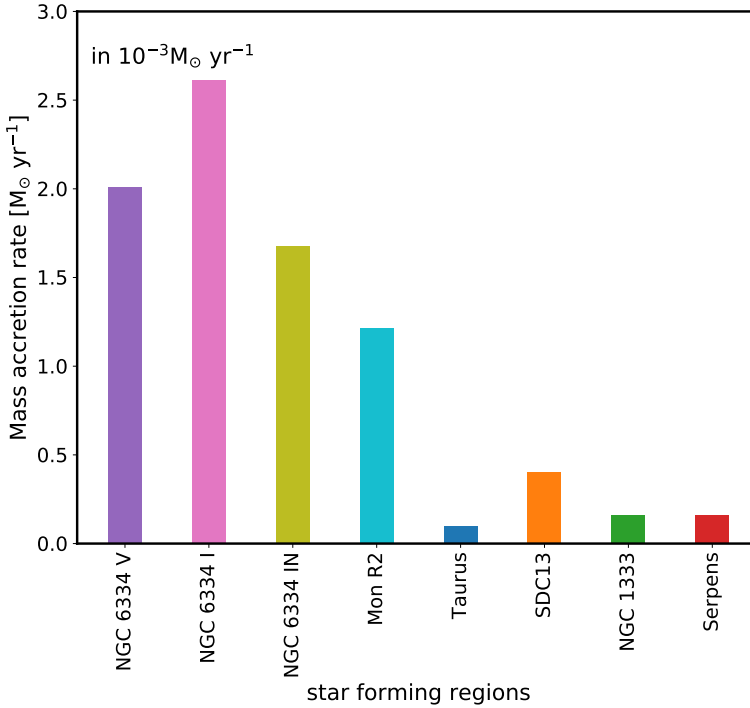


Figure 5.7.: Comparison of total mass accretion rates in NGC 6334-V with two other clusters source I and IN (Sadaghiani et al., 2020) and with different low-mass and high-mass star forming regions: Mon R2 (Treviño-Morales et al., 2019), Taurus (Hacar et al., 2013), SDC13 (Peretto et al., 2013), NGC 1333 (Peretto et al., 2014) and Serpens (Kirk et al., 2013).

The total mass accretion rate of NGC 6334-V is the second highest to compare with the other regions (e.g. Treviño-Morales et al., 2019; Hacar et al., 2013; Peretto et al., 2013; Peretto et al., 2014; Hacar, Tafalla, and Alves, 2017; Kirk et al., 2013), except for NGC 6334-I, which has the highest accretion rates. The first three bars show three sources V, I, and IN, in NGC 6334 cloud with similar mass accretion rates. NGC 6334-I is the most massive and evolved cluster with a hypercompact H II region (Sadaghiani, 2021). Slightly lower than NGC 6334-V, NGC 6334-IN still exhibits a relatively high mass accretion rate. Since all are part of the same complex, NGC 6334-V, NGC 6334-I, and NGC 6334-IN are likely influenced by similar environmental factors that promote filamentary accretion and exhibit similar physical conditions conducive to high mass accretion rates. Sadaghiani et al., 2020 introduced sources I, IN, and V as the most massive clumps in the filament and men-

tioned the similarities of mass accretion rates in sources I and IN. They suggest that competitive accretion is an alternative scenario not only for mass accretion inside a cluster but also as an accretion mechanism over larger scales between the clusters embedded in a filament.

There is a drop to Mon R2, which has mass accretion rates of $\approx 1 \times 10^{-3} M_{\odot} \text{ yr}^{-1}$. According to Treviño-Morales et al., 2019, Mon R2 is an active star-forming region with intense fragmentation in its filaments. The low mass accretion rate in Mon R2 might be attributed to different environmental conditions, such as the lower mean pressure.

The rest of the regions (Taurus (Hacar et al., 2013), SDC13 (Peretto et al., 2013), NGC 1333 (Peretto et al., 2014) and Serpens (Kirk et al., 2013)) have significantly lower mass accretion rates, with Taurus having the lowest among them. The low mass accretion rate in Taurus is consistent with its status as a nearby, relatively quiescent star-forming region. The low rate indicates a less active phase of star formation, which might be due to its more evolved state or different physical conditions. Similar to Taurus, NGC 1333 and Serpens also have a relatively low mass accretion rate among the regions. SDC13 is another region with a lower mass accretion rate than NGC 6334-V. It suggests that the filaments in SDC13 are either less efficient at accreting mass or are in a different evolutionary state compared to NGC 6334-V.

The comparisons reveal that NGC 6334-V is among the regions with high mass accretion rates, indicating active star-forming processes. The variations in total mass accretion rates across different regions can be attributed to factors such as age, dynamical state, ambient pressure, and external triggers affecting the filaments.

5.4. DISCUSSION

5.4.1. ON THE NATURE AND ORIGIN OF NGC 6334-V

As mentioned in previous sections, we identified 6 filaments with scales smaller than 1 pc. In this section, I explore existing archival data to see if these structures are connected to the main molecular clouds of NGC 6334 and whether there is a hierarchical structure for the filamentary shapes in the NGC 6334-V region. In Fig. 5.8, the top and middle images show the ^{13}CO peak intensity and $350 \mu\text{m}$ continuum maps covering the main NGC 6334 molecular cloud, respectively. The black box indicates the observed area covering NGC 6334-V. The ^{13}CO emission map shows at least three distinct ridges seemingly converging on the position of

NGC 6334-V. I overlaid the ^{13}CO intensity map as a contour on top of the $350\ \mu\text{m}$ continuum map. These two maps also reveal an excellent coincidence spatially of filamentary features appeared in large scale. However, the NGC 6334-V region is relatively separate from the main cloud of NGC 6334, and there is a cavity in between. As shown in the top image of Fig. 5.8, ionized gas, indicated by violet transparent contours of $\text{H}\alpha$ emission, fills the gaps between the main molecular complex NGC 6334 and NGC 6334-V. The bottom image presents the three color composite image using Spitzer/IRAC data at 3.6 (blue), 4.5 (green), and 8 (red) μm (Russeil et al., 2019). The H^{13}CO^+ velocity integrated emission maps is overlaid as a transparent gray contour. The H^{13}CO^+ emission distribution aligns perfectly with the $8\ \mu\text{m}$ dark area. In addition, a horizontally elongated $4.5\ \mu\text{m}$ emission feature can be observed at the center, which is known as a green extended object (EGO G351.16+0.69, Chen et al. 2013). The peak position of this object coincides with the position of the hot core where outflows have been detected (e.g., Juárez et al. 2017b).

From ancillary data, I show $\text{H}\alpha$ infrared with a pixel size of $9\ \text{arcsec} \times 9\ \text{arcsec}$ and ionized radio emission at $843\ \text{MHz}$ and a lower resolution of $45\ \text{arcsec}$ in Figure 5.9. The infrared $\text{H}\alpha$ emissions show two bubbles filling the cavities between cluster V and the rest of the cloud. The radio emission has a spherical shape, covering the hub in source V. Aside from resolution, radio emission and infrared $\text{H}\alpha$ emission are consistent and target the same source at different wavelengths. Infrared observations only show that the front emission cannot penetrate deep into the cloud. It means the infrared H II region could be a dominant emission of the cavities. However, radio observations reveal emissions from behind the cloud. In this case, the $843\ \text{MHz}$ data show emission from both cavities within the cloud and the hub cluster in source V. A schematic view of ionization injection process from cavities behind the cloud also showed in Figure 5.10. The ionized gas could be ejected as a lobe of outflow from an unknown star behind the cloud, slapping the cloud from one side and isolating source V from the rest of the cloud. The ionized gas and hub cluster encounter could also reshape the system and push filaments to the other side. Since no ionized gas is detected from the filaments, the accretion continues toward the central hub, and star-forming activities resume. Triggering star formation by expanding H II regions in neighboring filaments was also the subject of works by Fukuda and Hanawa, 2000; Deharveng et al., 2015.

Radio continuum emissions can generally have two origins of thermal emission from free–free or non-thermal emission mechanisms from high energetic events

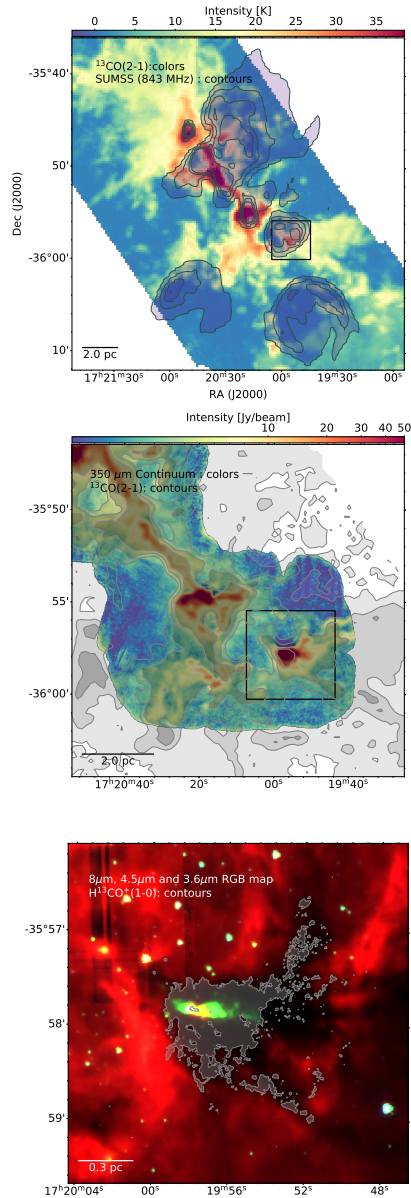


Figure 5.8.: From Top to Bottom, $^{13}\text{CO}(2-1)$ (*Top*) with 843 MHz ionized gas (Bock, Large, and Sadler, 1999) in purple contours, 350 μm continuum maps (*middle*) with overlapping ^{13}CO as contours, and the three-color composite image (*Bottom*) using Spitzer/IRAC data at 3.5 (blue), 4.5 (green), and 8 μm (red), and the H^{13}CO^+ velocity intensity map in gray contour. The $^{13}\text{CO}(2-1)$ and 350 μm continuum maps are obtained at the APEX 12m telescope, using with the SHeFI receiver and the ArTéMiS bolometer, respectively. The black box indicates the area observed with ALMA for this study.

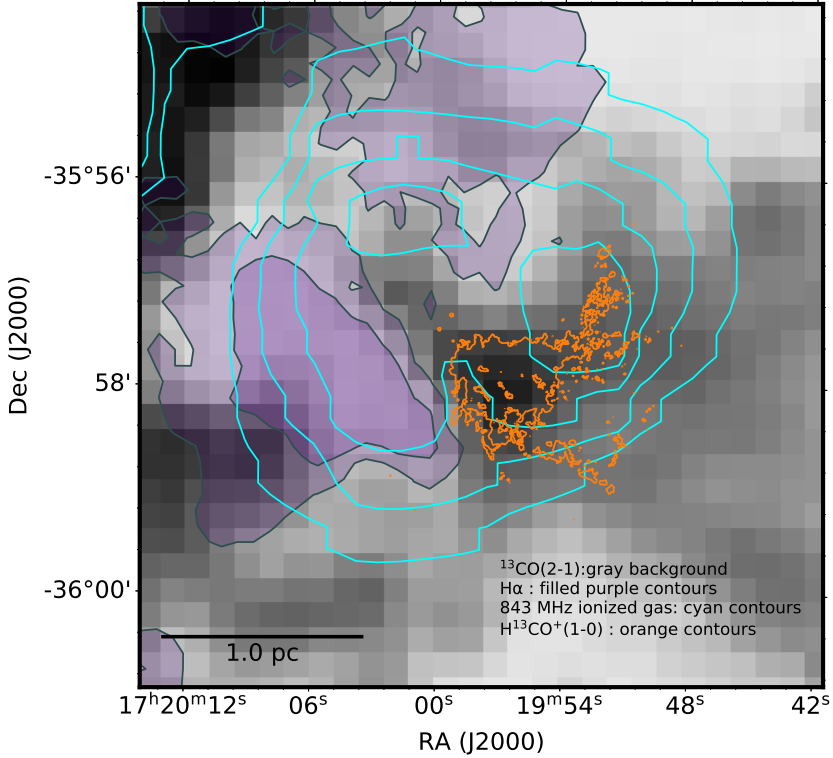


Figure 5.9.: Distribution of ionized gas in NGC 6334-V.

such as supernova remnants, AGNs, or outflows. Based on the H II region based on H α detection, the dominant mechanism of the continuum emission is free–free emission.

Apart from ionized radio emission, The 6 cm continuum emission observations at the Very Large Array (VLA) (Rodriguez, Canto, and Moran, 1982), and H α line surveys performed at the AAO/UKST (Parker et al., 2005) and at 36 cm telescope located at La Silla Observatory (Russeil et al., 2016) revealed a low resolution but large cavities of ionized gas toward in north-west and south-east of NGC 6334-V which is consistent with our results.

5.4.2. ASSOCIATION BETWEEN THE HUB CLUSTER AND FILAMENTS

In section 5.4.1, I consider the *ALMA* observation of cluster NGC 6334-V compared to other archival observations in different wavelengths and spatial scales. I show large-scale filaments in ^{13}CO peak intensity and $350\ \mu\text{m}$ continuum maps converge to the cluster NGC 6334-V through smaller filaments observed with *ALMA* observation. I also suggested that the ionized cavity observed in radio emission at 843 MHz could be located behind the cloud, smashing the cloud from one side and dis-

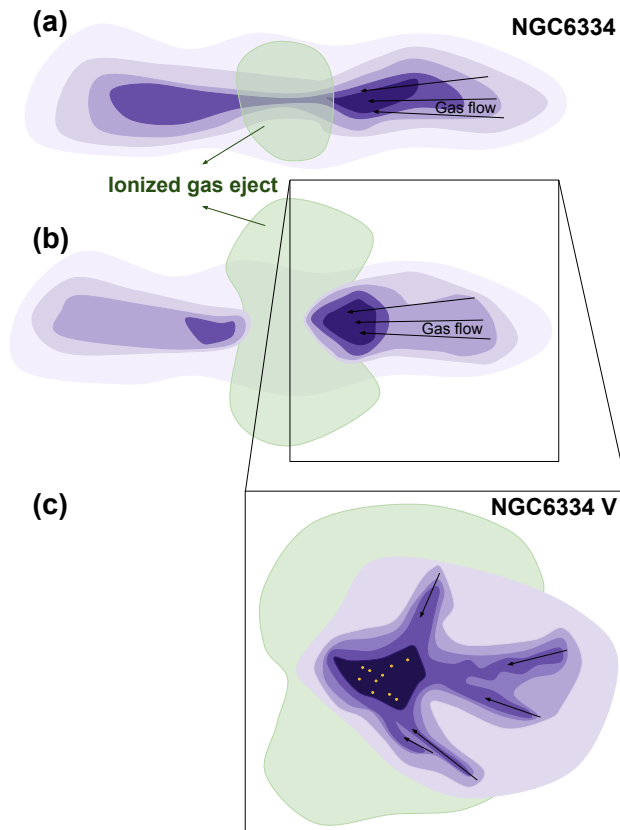


Figure 5.10.: A schematic view of the ionization injection process from cavities behind the cloud is presented. (a) Depicts an ejection of ionized gas from behind the cloud, complete with filamentary structure and accretion flows. (b) Illustrates the ionized gas colliding with the cloud and reshaping filaments to one side. (c) Demonstrates the continued accretion from the filament and the resumption of star-forming activities.

entangling the source V from the rest of cloud NGC 6334. In this section, I consider the role of filaments in forming hub cluster systems.

A hub/ridge filament arrangement can be described as a molecular cloud complex with gas flowing through the filaments into a central hub where massive dense cores (MDCs) form on a scale of 0.1 pc (e.g., Tigé et al., 2017; Motte, Bontemps, and Louvet, 2018). Hubs are reliable sites for massive star formation (e.g., Tigé et al., 2017; Motte, Bontemps, and Louvet, 2018; Kumar et al., 2020). A hub-filamentary system assumed to be more compact and dense in comparison to filaments (Busquet et al., 2013) and presenting a global non-isotropic collapse, the gas flows through the filaments to form the central hub.

Based on the “fray and fragment” scenario proposed by Tafalla and Hacar, 2015, in the beginning, large-scale supersonic collisions of two gas flows produce a filamentary density enhancement in the range of 10 pc long. These gas flows are in the scale of the cloud of NGC 6334. Then, a series of substructure filaments and fibers originated from residual turbulent motions and gravity. Finally, the velocity-coherent fibers accumulate and formulate a chain of dense regions similar to NGC 6334-V. The simulations presented in Lee and Hennebelle, 2018 describe a collapsing molecular cloud and summarize the main features of the process in a global collapse that forms stellar (hub) clusters, prominent filamentary structures, and stars forming along radial filaments feeding the core.

Later, Tokuda et al., 2019 discussed that cloud-cloud collision in a colliding between two massive filaments with a line mass of $100 M_{\odot} \text{ pc}^{-1}$, triggers the massive star formation in the center of collision and develops hub systems. This scenario also confirms the global hierarchical collapse Motte, Bontemps, and Louvet, 2018.

One of the important findings of high resolution ALMA observations are the identification of six radial filaments constituting hub-filament cluster NGC 6334-V. This is very similar to Mon R2 (Treviño-Morales et al., 2019) and can argue the global collapse proceeds forming stars in the central hub. I determine the physical properties of filaments (see Tabl 5.1) and show the total mass accretion rate toward the center of cluster is about $2.7 \times 10^{-3} M_{\odot} \text{ yr}^{-1}$ which is the sum of all mass accretion rates along each filaments. Comparing the total mass accretion rate of source V with other regions in NGC 6334 such as source I and I(N) shows lower accretion rates.

6

MOLECULAR LINES - II: SHOCK ANALYSIS IN NGC 6334-V

6.1. SiO: SHOCK TRACER

The interstellar shocks appear when the interstellar medium is disturbed by sudden energetic events, such as cloud-cloud collisions, the pressure of ionized gas, stellar winds, like those from supernova explosions or jet/outflow emissions from young stellar objects (cf. Draine and McKee, 1993; Guillet, Pineau Des Forêts, and Jones, 2007). In this situation, supersonic wind propagates through the surrounding ambient medium via shock waves. The shock wave propagates through the medium, compressing and heating the gas through an irreversible, pressure-driven fluid dynamical disturbance. In terms of the chemistry of the medium in shock environments, the transformation process through shock chemistry occurs on quick short time scales (between 10^2 to 10^4 years), which initially, high-temperature reactions are predominant, but as time passes, reactions at lower temperatures become more dominant. Two types of shocks are commonly studied in the interstellar medium: Fast shocks ($v \geq 40 \text{ km s}^{-1}$) and slow shocks ($v < 40 \text{ km s}^{-1}$) (Tielens, 2005).

6

Fast shocks, also known as J-shock, are violent fast events that heat gas to a high temperature with a discontinuity jump of the hydrodynamical variables on either side of the shock front (Gusdorf, 2008). In J-shocks, the shock front, which is much thinner than the post-relaxation layer, the kinetic energy of the gas is converted into thermal energy through elastic collision, and the postshock relaxation layer will use this thermal energy for further molecular dissociation and ionization processes (Tielens, 2005). The J-shocks happens in high-pressure regions, such as expanding supernovas, HII regions, or outflows.

Slow shocks, also known as C-shocks, are weak, low-velocity events that occur in a magnetized medium with low ionization and high density and molecular fraction. C-shocks exist when the shock velocity stays below magnetosonic velocity, which is the propagation speed of the magnetic precursor Lesaffre et al., 2013. Slow shocks generate continuous changes in the hydrodynamical variables on either side of the shock front (Tielens, 2005). The shock front in C-shocks is much thicker than the cooling length scale, with a typical temperature of 3000 K set by the balance between heating and cooling (Gusdorf, 2008). The C-shocks happens during cloud-cloud collisions or colliding flows.

The consequence of a shock around astronomical objects increases the abundance of many molecules such as CH_3OH , H_2CO , HCO^+ , NH_3 , HCN , HNC , CN , CS , SO , SO_2 (Gusdorf, 2008). The remarkable case is that of SiO, which is typically a minor component in molecular clouds, is mainly affected and enhanced in some

cases by a factor of 10^6 cm^{-3} (Martin-Pintado, Bachiller, and Fuente, 1992), and is the main subject of this section.

The gas phase of SiO is produced through the sputtering of Si-bearing material within grains, which is expelled during shocks, leading to the release of Si in the gas phase. Silicon is released either from the grain cores or mantles. Cores refer to the silicate/graphite grains (Draine, 1994) with high sputtering thresholds, and mantles refer to ices (Whittet, 1993) and require lower shock velocities for erosion. The released silicon in the gas phase is processed into SiO mostly through reactions with OH and O₂ (cf. Langer and Glassgold, 1990; Schilke et al., 1997) as:



In hot post-shock gas with a high abundance of OH, the SiO in the gas phase could be destroyed through a chemical reaction:



Shock waves are driven by various astronomical phenomena, which influence the shape of the observed SiO emission line profile. The kinematics of SiO, as observed through its spectral lines, can provide information about the dynamics of the gas in star-forming regions. For example, the linewidth and shape of the SiO lines can reveal the velocities and directions of gas flows, which can be influenced by the pressure and momentum of a shock event.

In a young, embedded cluster, molecular outflows possess a collimated structure and develop a bipolar shape due to the conservation of momentum during the collapse of a rotating core. The SiO observed from these outflows exhibits broad line profiles with linewidths of some tens of km s^{-1} (Martin-Pintado, Bachiller, and Fuente, 1992), and, depending on the angle of the reference points, one or two lobes can be detected. Stellar winds ejected from stars can also interact with the dust and gas in the surrounding interstellar medium. This interaction can produce shock waves that can lead to the compression and heating of the material around the star and trigger various chemical reactions, including SiO. The SiO produced by stellar winds is less collimated and shows non-symmetric spherical shapes. In more evolved stellar clusters, supernovae generate the most powerful shocks in the ISM. During the adiabatic phase of their evolution, the remnants of supernovae drive

shocks into the ISM at velocities up to 100 km s^{-1} (see e.g., McKee and Ostriker, 1977; Dopita, Mathewson, and Ford, 1977).

Apart from high-velocity SiO with broad line profiles, narrower SiO lines have also been observed in low-mass star-forming regions such as NGC 1333 (Lefloch et al., 1998) and L1448–mm (Jiménez-Serra et al., 2004). Lefloch et al., 1998 suggested that these lines might trace shocked material that deflected and slowed due to interactions with large-scale outflows or pre-existing clumps. Another publication by Jiménez-Serra et al., 2004 proposed that narrow SiO lines could come from gas affected by the magnetic fields in young magnetohydrodynamic (MHD) shocks. Recent high-spectral resolution observations have revealed widespread SiO emission characterized by a narrow line profile (less than $\sim 0.5 \text{ km s}^{-1}$) in colder environments. Some examples include the G035.39–00.33 infrared dark cloud (Jiménez-Serra et al., 2010), the W43–MM1 ridge (Louvet et al., 2016), three IRDCs, G028.37+00.07, G034.43+00.24, and G034.77–00.55 studied by Cosentino et al., 2018 which represent the line width of ($< 3 \text{ km s}^{-1}$). Many recent publications suggested that the extended emission of SiO originated in large scale interactions (Louvet et al., 2016; Nguyen-Luong et al., 2013) or a fossil record of a past large-scale interaction occurring nearby the cloud or cluster (Cosentino et al., 2018). The main subject of this chapter is to present the ALMA observations toward widespread SiO emission in NGC 6334-V and study the SiO production by investigating the origin of shocks.

6.2. SiO: MOMENT MAPS

Figure 6.1 shows the integrated intensity (0^{th} -order moment), velocity (1^{st} -order moment) and linewidth (2^{st} -order moment) maps of the SiO(2–1) emission. The SiO intensity map (top panel) shows a widespread distribution around the central region where the continuum cores are located, with an extension towards the west, in the same direction as the two main elongated, filamentary-like structures seen in the dense gas (see also Sect. 5.3.2). The SiO emission around the cluster of dense cores is clumpy and stronger than that in the outskirts, where the emission is fainter.

The velocity map (1^{st} -order moment map) in the middle panel of Fig. 6.1 shows velocities ranging from -20 km s^{-1} to 0 km s^{-1} . This reveals the presence of high velocity compact cores or clumps which is predominantly at $\approx -15 \text{ km s}^{-1}$, in particular towards the hot molecular core and dense cores at the center of the cluster.

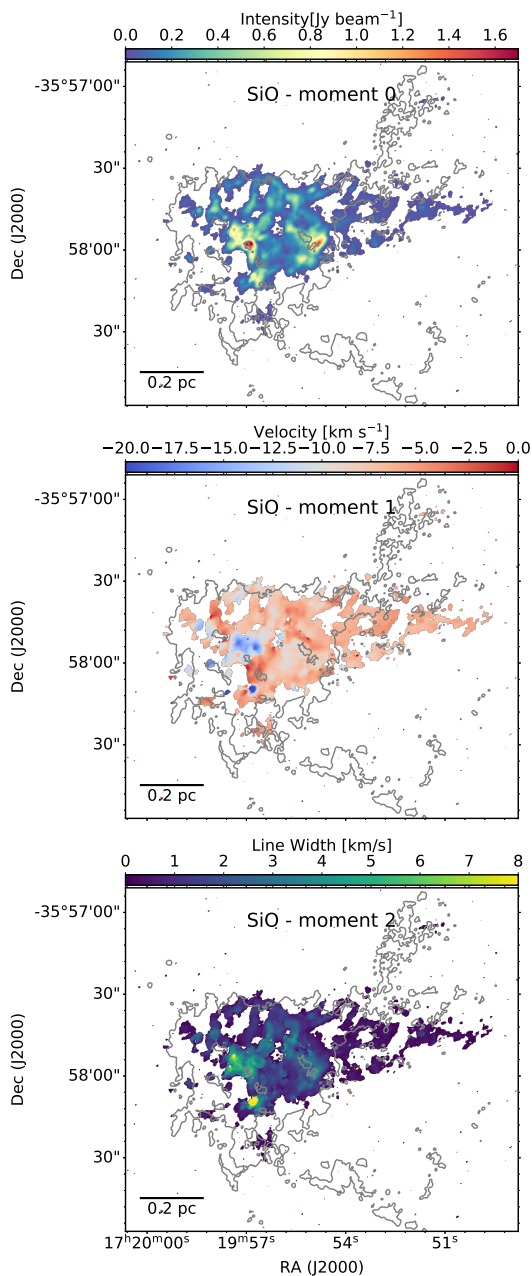


Figure 6.1.: From *Top* to *Bottom*, integrated intensity, velocity and velocity linewidth maps of SiO (2–1). The spectral data of all maps have been masked with a threshold of 3σ . Grey contours in all maps show the H¹³CO⁺ (1–0) integrated intensity at a level of $0.025 \text{ Jy beam}^{-1} \text{ km s}^{-1}$ (see Fig. 5.1).

The extended emission has velocities $\approx -6 \text{ km s}^{-1}$, similar to the dense gas and systemic velocity of the cluster.

The velocity linewidth (2^{st} -order moment) map in the bottom panel of Fig. 6.1 shows high values $> 8 \text{ km s}^{-1}$ in those regions where the velocity is clearly blue-shifted, suggesting extremely broad line profiles. However, the emission has relatively narrow line profiles ($\approx 1\text{--}2 \text{ km s}^{-1}$) in the regions where the extended and weak SiO emission dominates.

6.3. SiO SPECTRA DECOMPOSITION

I investigate the population of low- and high-velocity shocks through the SiO velocity width across the NGC 6334-V region to understand the properties of the shocked gas. In low-velocity shocks, SiO emission lines are often characterized by narrow linewidths, which indicate the relatively slower and more uniform gas motion in the shock. In high-velocity shocks, the change in velocity across the shock front is significantly higher, and SiO emission lines often show broad linewidths. In this section, first, I fit the spectra all over the SiO emission maps and then classify linewidth components based on narrow and broad widths thresholds and number of components.

For fitting the spectra, I use the Behind The Spectrum (BTS)¹ spectral fitting package (Clarke et al., 2018a). BTS is fully automated python routine for fitting multiple velocity components in optically thin lines. The algorithm does not make any initial assumptions about the number of components in the spectrum. Instead, it uses the first, second, and third derivatives of the spectrum to calculate the number and positions of velocity components. The least squares fitting is then used to determine the optimal number of components after evaluating the fit from overfitting and over-lapping velocity centroids. More information about the theory and usage of BTS is given in Appendix D.

The original version of the BTS source code fits multiple-component spectra, allowing up to six components. However, this number can be adjusted as needed. I modified the source code to adapt the BTS for our purposes and limit the maximum number of components. Since most of the positions in NGC 6334-V seem to have only one or two distinguished velocity components, I set a maximum of three Gaussian velocity components in BTS when fitting the SiO emission. I consider only emission features with an intensity higher than 5σ to obtain more robust re-

¹<https://github.com/SeamusClarke/BTS>

sults. With *BTS*, in total 10831 were fitted. Out of them, I find a total of 70.9% pixels fitted with one single velocity component, 24.7% pixels with two components, and 4.4% with three components. Moreover, 99.8% of the fitted velocity components in NGC 6334-V have linewidths less than 10 km s^{-1} , which may indicate that the SiO emission in NGC 6334-V is not dominated by high-velocity shocks. In fact, 57% of the fitted velocity components exhibited even narrower linewidths, less than 1.8 km s^{-1} , suggesting that the SiO emission in NGC 6334-V is predominantly influenced by low-velocity shocks.

The *BTS* fit maps are shown in Fig. 6.2. In case of multiple components, I only consider the first component. The top panel shows the integrated intensity (0^{th} -order moment map) SiO emission from the *BTS* SiO fitted data cube. The image is comparable to the actual 0^{th} -order moment map shown in Fig. 6.1. The middle panel shows the centroid velocity (1^{st} -order moment map) of fitted components, which exhibits good agreement with the 1^{st} -order moment map obtained from the observed velocity SiO emission map. Finally, the bottom panel shows the linewidth distribution of fitted spectra. The map reveals a wide range of linewidths, spanning from very narrow components of approximately 0.5 km s^{-1} to significantly broader components of around 30 km s^{-1} .

Figure 6.3 shows spectra extracted from selected positions all over the SiO emissions map. I define two regions: region A which shows the central hub emission and where most of the continuum cores are located and region B which shows the tail of SiO emission extended toward the filaments 2 and 3 and where only two continuum cores are located. In region A, a vast collection of narrow, broad, multi-component, and red-and blue-shifted spectra are seen. In contrast in region B the spectra mostly show single narrow features without any wings in spectra.

The study of narrow Gaussian profiles at systemic velocity has gained recent attention in research. However, a clear and universally accepted definition of the precise ranges of such profiles has yet to be determined. The definition of narrow and broad Gaussian profiles varies among publications, depending on the observation spatial resolution and the characteristics of the studied sources. Nguyen-Luong et al. (2013) consider linewidths exceeding 25 km s^{-1} as indicative of broad components to study spectra of single-dish IRAM 30 m telescope data. Louvet et al. (2016), also using single-dish data from the IRAM 30 m telescope, observe a range of low-velocity shock components spanning from 7 to 12 km s^{-1} . Similarly, Sadaghiani (2021) adopts a threshold of 12 km s^{-1} to differentiate narrow line profiles from

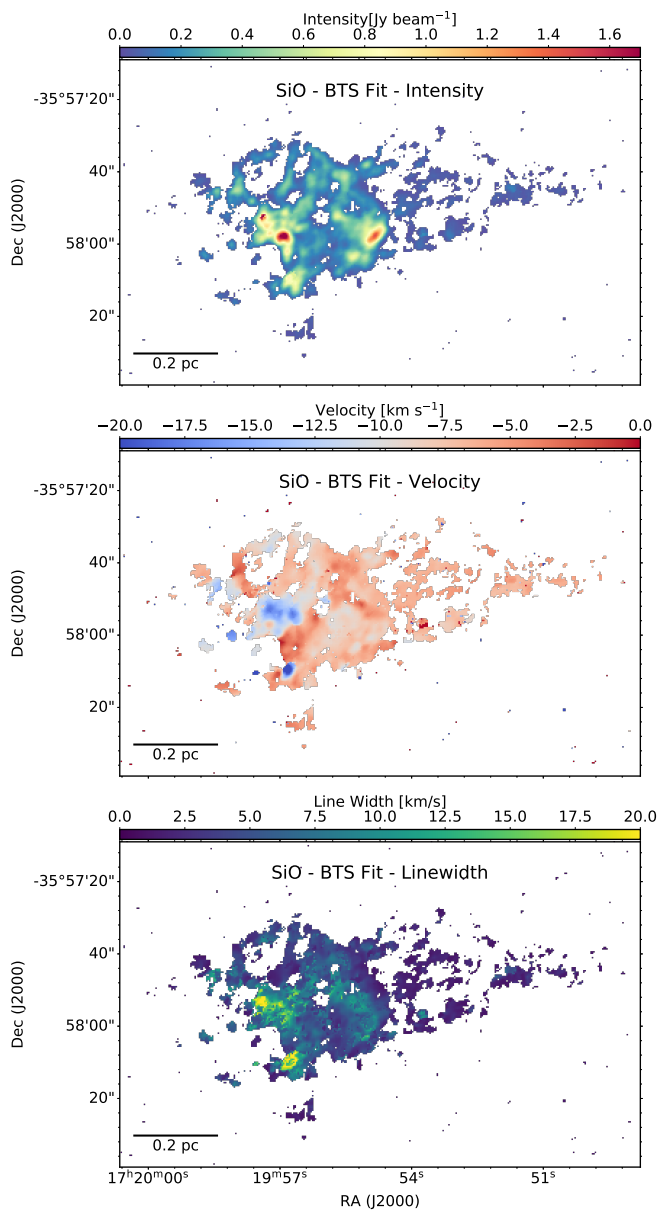


Figure 6.2.: BTS fitting results for SiO (2-1) emission are presented (refer to Section 6.3). The *Top* panel displays intensity, the *Middle* panel shows the velocity, and the bottom panel shows the linewidth of first component of SiO spectra.

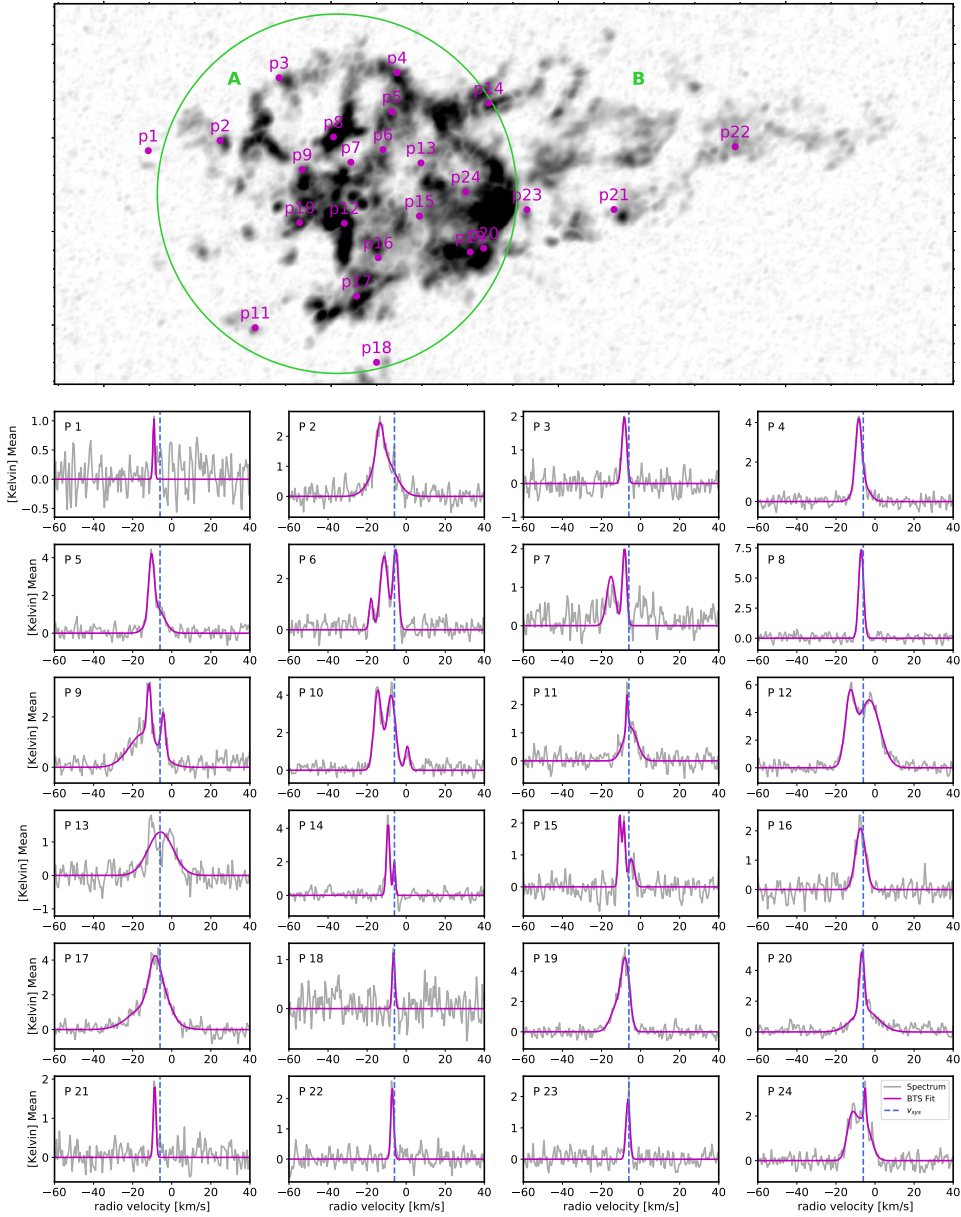


Figure 6.3.: Extracted SiO spectra over the selected regions A (inside the green circle) and B (outside the green circle). In region B, the spectra mostly show narrow features. In contrast, a vast collection of narrow / broad linewidth, multi-component, and red-and blue-shifted spectra appear in region A.

broad ones; however, their analysis employs high-resolution ALMA observations rather than single-dish data.

In contrast to the aforementioned studies, some investigations employ significantly lower limits for narrow Gaussian profiles. For instance, Jiménez-Serra et al. (2010) define two distinct ranges: linewidths up to 3 km s^{-1} for narrow profiles and linewidths between 4 and 7 km s^{-1} for high-velocity components. Duarte-Cabral et al. (2014) identify two regions in SiO line profiles, with a very broad emission characterized by line widths of approximately 17 km s^{-1} and a low-velocity emission with linewidths ranging from 3 to 6 km s^{-1} . Cosentino et al. (2018) consider narrow components to have linewidths below 3 to 5 km s^{-1} , depending on the sources, in using single-dish IRAM observations. In single-dish observations, where the spatial resolution is lower, the multiple components in the SiO Gaussian profile may not be separable, resulting in broader observed components. Therefore, using enhanced spatial resolution observations are expected to resolve complex velocity structures into distinct Gaussian profiles and enable a more precise characterization of the individual components within the SiO emission.

The present ALMA observations with high-resolution data allow more possibility to reduce the limit of narrow components. Figure 6.4 shows the KDE of linewidths with a decomposition limit for narrow and broad components. Based

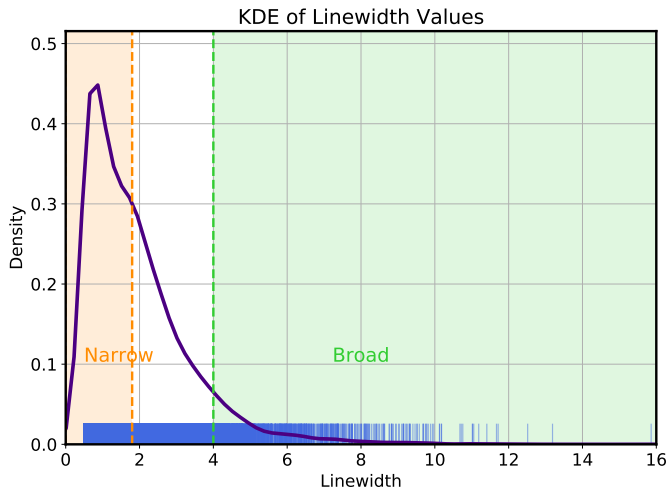


Figure 6.4.: The KDE of the distribution of linewidths with the shaded regions highlighting the boundaries of two categories: the "Narrow component" (orange) and the "Broad component" (green).

on the KDE distribution of linewidth and centroid velocity shifts, I adopt two distinct criteria of linewidth with less than 1.8 km s^{-1} for Gaussian profile and larger than 4 km s^{-1} threshold for broad profiles with a gap of 2.2 km s^{-1} for intermediate linewidth to statistically separate the low- and high-velocity components. The threshold of narrow components aligns with the second peak in the KDE. Also, it contains more than three channel widths, which is sufficient resolution to detect a spectrum. Also, the border between narrow, intermediate, and broad components shows clear separations in spectra accumulation within the emission map.

I show the linewidths maps in three different classifications. The maps of linewidths are shown in Figure 6.5, segregated into three different categories, and Figure 6.6 represents the centroid velocities based on the linewidth classifications defined by each criterion. I classify the BTS-fitted spectra into each group based on the extent of linewidth broadness or narrowness, along with the number of their components.

1. **Broad spectra:** Single or multiple components with at least one broad line profile larger than 4 km s^{-1} . The top panel of Figure 6.5 exhibits the broad components that exceed 4 km s^{-1} . The broad components are highly concentrated in the central hub where the hot core and other massive cores are located. All broad components accumulated in Region A, apart from few pixels with broad components were detected outside the hub in Region B. These features can be attributed to the outflows of two detected cores, labeled as 14 and 17 (see Figure 4.1), located nearby these spectra.
2. **Intermediate spectra:** Components with a linewidth between 1.8 and 4 km s^{-1} . The middle panel of Figure 6.5 shows intermediate linewidth components, which are primarily spread in the center and toward the border of regions A and B. The majority of the pixels under this criterion show a inhomogeneous distribution of linewidths where their centroid velocities shift from $\sim -2 \text{ km s}^{-1}$ to $\sim -8 \text{ km s}^{-1}$ where the systemic velocity of the source is about -6 km s^{-1} (see Figure 6.6). This neighbouring red shifted and blue shifted velocities could be due to the fact that the formation of SiO originates from different events such as outflows originated from various cores. I used this criterion as a gap to differentiate very broad and very narrow components. Similar to the very broad spectra very few detected spectra in region B can be connected to the outflows of two detected cores, labeled as 14 and 17, in nearby (see Figure 4.1). Therefore, the broad linewidths could suggest

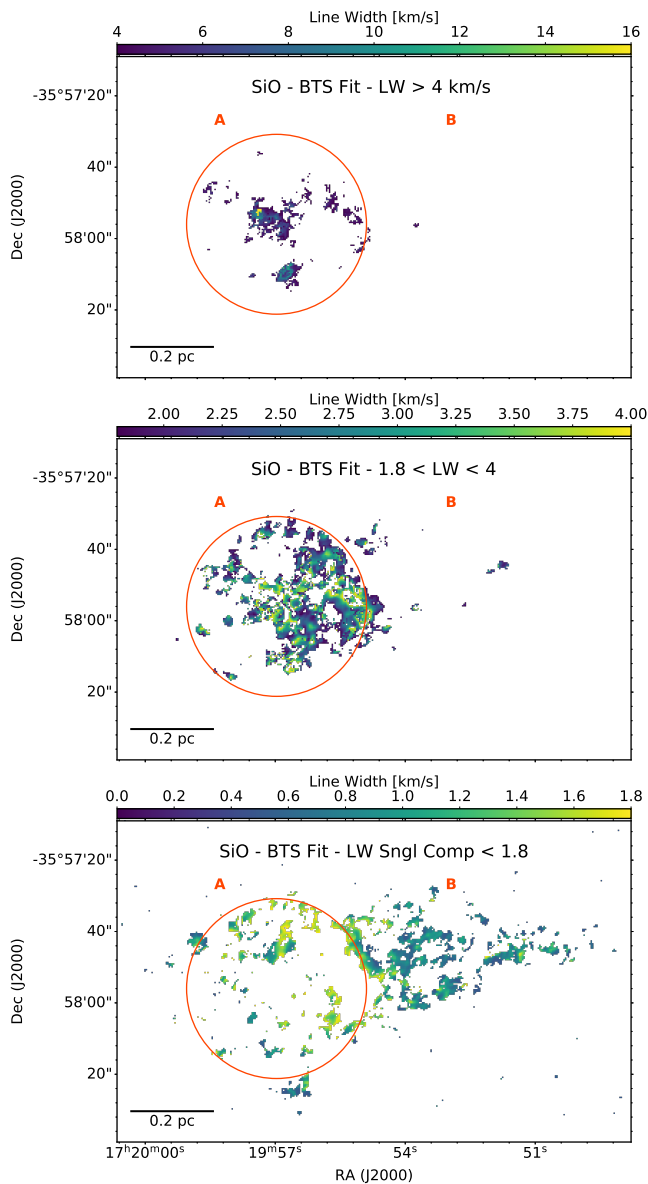


Figure 6.5.: Linewidth component of **BTS** fitted spectra under three different constraints: (*Top*) Linewidth of all broad components larger than 4 km s^{-1} . (*Middle*) Linewidth of intermediate components with linewidths between 1.8 and 4 km s^{-1} . (*Bottom*) Linewidth of single narrow components less than 1.8 km s^{-1} .

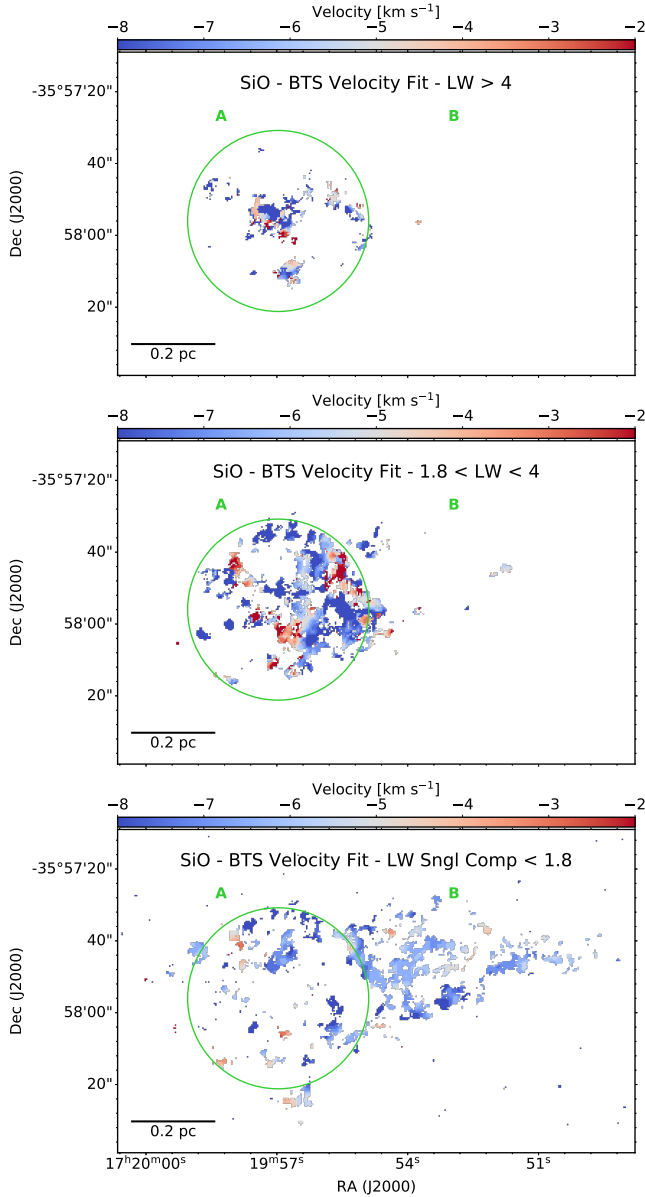


Figure 6.6.: Velocity component of *BTS* fitted spectra under three different constraints: (*Top*) Velocity of all broad components larger than 4 km s⁻¹. (*Middle*) Velocity of intermediate components with linewidths between 1.8 and 4 km s⁻¹. (*Bottom*) Velocity of single narrow components less than 1.8 km s⁻¹.

a possible connection between the presence of outflows and high-velocity shocks in NGC 6334-V.

3. **Single narrow spectra:** Single narrow components smaller than 1.8 km s^{-1} without any overlap. The limit of 1.8 km s^{-1} represents three times the resolution and contains three channels of ALMA observations. The bottom panel of Figure 6.5 displays the fitted velocity linewidths only for the pixels containing a single velocity component with a linewidth of less than 1.8 km s^{-1} . By doing this, I exclude those pixels that may be dominated by high-velocity outflows and shocks. I identify a total of $\approx 55\%$ SiO line profiles (corresponding to $\approx 75\%$ of all the pixels fitted with a single-velocity component) with narrow linewidths. The pixels with narrow SiO components are preferentially located in the more extended and diffuse emission around the central cluster, and along the three main elongated filamentary-like structures identified in the dense gas. In Sect. 6.4.1, I discuss the possible connection between the presence of filaments and slow-velocity shocks in NGC 6334-V.

6

Figure 6.7 and 6.8 show the KDE of the linewidths and velocity centroid of the three groups of broad, intermediate, narrow, and single narrow components respectively. The top plot in Figure 6.7 shows the KDE distribution of all linewidths larger than 4 km s^{-1} . The broadest width component is located at 43 km s^{-1} , and the mean value of all broad components is at $\sim 6 \text{ km s}^{-1}$. The broad linewidths observed in the SiO spectra can be attributed to ongoing star formation activities, particularly the influence of outflows originating from hot cores and young protostars in the central hub cluster. The middle plot in Figure 6.7 shows the KDE distribution of all linewidths between 1.8 and 4 km s^{-1} . The probability density of the linewidth decreases as their widths increase, with a mean of 1.58 km s^{-1} . Most of the multiple-component spectra also appear within this range of linewidths, which often accompany narrower or broader components.

The bottom plot shows narrow line profiles without the contribution of other components. The single narrow components show two peaks in their distribution, one at 0.8 km s^{-1} and the other at 1.6 km s^{-1} . The first peak could be related to the resolution limit of ALMA observations for resolving lower velocity components.

Figure 6.8 shows the distribution of centroid velocities for the aforementioned three groups: broad, intermediate, and single narrow components. The mean velocity for all three groups shows a shift toward the negative with respect to the systemic velocity of cluster NGC 6334-V. The $v_{\text{sys}} = -6 \text{ km s}^{-1}$ calculated based on

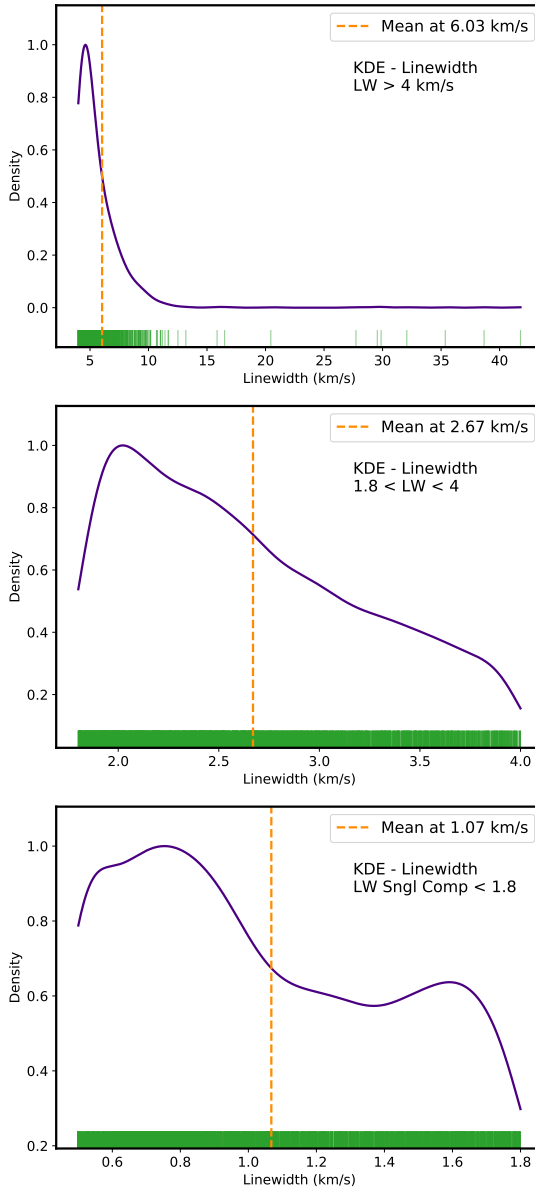


Figure 6.7.: KDE distribution of linewidth component of *BTS* fitted spectra under three different constraints: (*Top*) Distribution of linewidths of all Broad components larger than 4 km s^{-1} . (*Middle*) Distribution of linewidths of intermediate components with linewidth between 1.8 and 4 km s^{-1} . (*Bottom*) Distribution of linewidths of single narrow components less than 1.8 km s^{-1} .

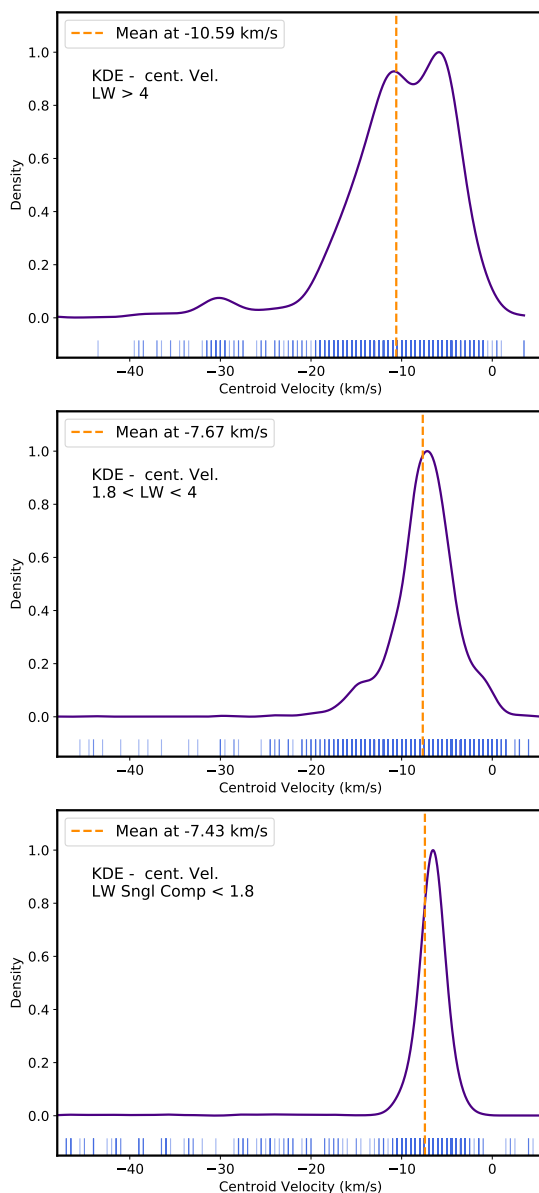


Figure 6.8.: KDE distribution of velocity component of BTS fitted spectra under three different constraints: (*Top*) Velocity probability distribution of all broad components larger than 4 km s^{-1} . (*Middle*) Velocity probability distribution of intermediate components with linewidths between 1.8 and 4 km s^{-1} . (*Bottom*) Velocity probability distribution of single narrow components less than 1.8 km s^{-1} .

the H^{13}CO^+ spectra. For the very broad velocities, the mean reaches -11 km s^{-1} ; however, for the narrow profiles, the mean is about -7 km s^{-1} .

6.4. DISCUSSION

6.4.1. ORIGIN OF THE EXTENDED SiO EMISSION

SiO is commonly observed in environments such as molecular outflows or where shocks propagate into molecular clouds. In such environments, shocks sputter or vaporize neutral silicon atoms from dust grains (Schilke et al., 1997), which then react with either OH or O_2 to form SiO. Previous studies described the SiO emission line profile as a composition of two Gaussian components at approximately the same central velocity, in which each component potentially traces different phenomena (e.g., Martin-Pintado, Bachiller, and Fuente, 1992; Schilke et al., 1997; Gusdorf et al., 2008; Jiménez-Serra et al., 2010). The broad Gaussian component is typically associated with high-velocity shocks. These shocks are often a sign of intense activity, such as the powerful outflows generated by protostars (e.g., Gusdorf et al., 2008; Gusdorf et al., 2015; Bally, 2016; Duarte-Cabral et al., 2014). In contrast, the narrow Gaussian component is typically associated with low-velocity shocks. These shocks could result from cloud-cloud collisions, gas inflows, or less intense outflows from protostars due to the limitations in the angular resolution observation (e.g., Jiménez-Serra et al., 2010; Nguyen-Luong et al., 2013; Louvet et al., 2016). In Cluster NGC 6334-V I observed widespread extended SiO(2–1) emission via 3 mm ALMA observations. In section 6.3, I fit the extracted spectra from SiO and classified their linewidths into three groups: broad, intermediate, and narrow components. The concentration of broad and intermediate components shows a clear separation from narrow components. The broadest linewidth is revealed in the central region of the hub cluster, and as one moves further to the edge of the hub, the linewidths become narrower. The narrow linewidths are primarily concentrated in tail features that extend toward filaments 1, 2, and 3. Based on this separation in linewidths, I summarize our findings regarding the origin of SiO in regions A and B.

Region A: High velocity shocks. Region A contains most of the 3mm ALMA continuum cores and the SiO emission shows broader linewidths which could suggest the high velocity shocks and production of SiO in the gas phase of molecular outflows. The top plot of Figure 6.9 shows the SiO emission overlaid on the $350\mu\text{m}$ continuum emission. Region A, which primarily contains

broad components (cf. section 6.3), also coincides with 350 μ m ARTEMIS continuum emission in a region that exhibits the highest column density. The 350 μ m ARTEMIS continuum emission often reveals cold dust in the regions of star formation, where young stars heat the surrounding dust and gas. This supports the evidence of ongoing star formation in the central hub. As mentioned in Section 4.3, the central hub region in NGC 6334-V is associated with an EGOs counterpart bright at 4.5 μ m (EGO G351.16+0.69, Chen et al. 2013) and likely associated with strong shocks, since the bright 4.5 μ m emission commonly originates from infrared H₂ transitions excited in shocks (e.g. De Buizer and Vacca, 2010). This region is also associated with broad SiO emission lines (cf. Figure 6.1, bottom plot) confirming the presence of high-velocity shocks. Figure 6.9 (bottom panel) compares the 4.5 μ m emission of the EGOs with the blue- and red-shifted high-velocity of the SiO (2–1) line. It is interesting to note that most of the SiO emission is observed almost perpendicular to EGOs direction and not along the EGOs emission.

Also, the blue- and red-shifted SiO emission contours as shown the bottom panel of Figure 6.9, traces outflows toward the hot core source, as reported in Juárez et al. 2017b. Apart from the outflow components, the other blue and red-shifted features which are adjacent to narrow SiO features (in gray areas) might trace interfaces between shocked and ambient gas as Class I CH₃OH masers known as a tracer of shocked interface regions are also detected (Chen et al., 2013). Although the SiO emission shows blue and red wings, the data resolution is insufficient to identify individual outflows in region A and requires higher resolution observations.

Region B: Low velocity shocks. The SiO spectrum from region B shows a narrow profile without broad line wings, unlike the spectrum from region A. The region B in the infrared image shows a lack of 4.5 μ m emission, and thus, it clearly implies that this SiO feature has a different origin. Such narrow SiO components have been found in the regions with the presence of a low-velocity shock originating by global infall, cloud-cloud collision, or less powerful outflows of low- or intermediate- mass YSOs (Louvet et al., 2016; Jiménez-Serra et al., 2010).

Figure 6.10 shows the position-velocity cut obtained from SiO emission, which was determined along the trajectory of filaments identified from the H¹³CO⁺ emission map. The purpose of this representation is to investigate whether

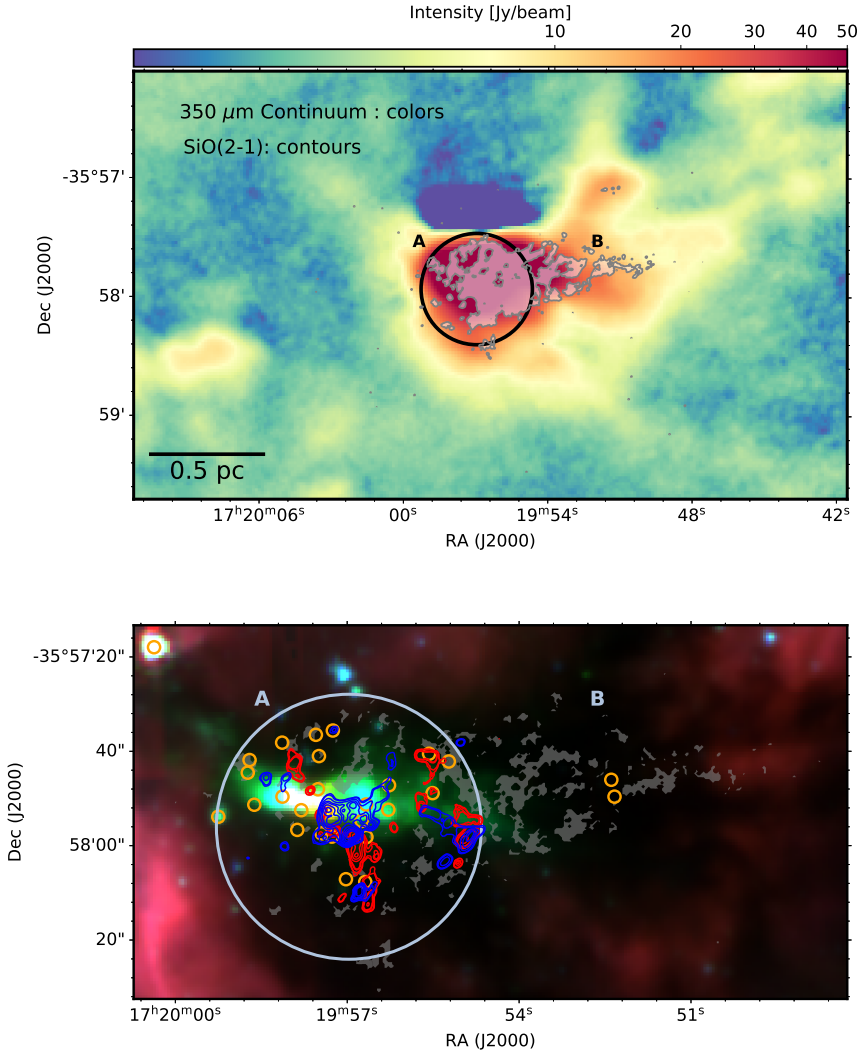


Figure 6.9.: *Top*: Large-scale view of NGC 6334-V with 350 μ m ARTEMIS continuum emission observed (colormap). The SiO(2-1) ALMA emission are specified by filled gray contours, and regions A and B overlay on top to indicate the fast and slow shocks compared to column densities of large-scale 350 μ m continuum emission. *Bottom*: Three-color composite image as same as the bottom image in Fig. 5.8 and velocity-integrated emission map only including narrow single Gaussian components ($\text{FWHM} \leq 1.8 \text{ km s}^{-1}$) in gray area. In the circle A, the blue and red contours are averaged emission from blue (from -40 km s^{-1} to -10 km s^{-1}) and red-shifted (from -4 km s^{-1} to 10.5 km s^{-1}) velocity channels of SiO (2-1).

there is an enhancement of SiO within the process of accretion onto the filaments. All PV cuts show velocity components close to the connecting point of the filaments to the central hub. Filaments 1, 2, 3, and 4 show velocity components around -7 km s^{-1} , extending from where filaments connect to the hub and continuing along the paths of filaments for about 0.25 pc. The filament F1 shows the highest accretion rate among the identified filaments in NGC 6334-V, and F2 and F3 show significant deviations in their PV diagrams (See Figure 6.10). Filament 4, on the other hand, shows two long and distinct emission features perpendicular to the filament path that could indicate outflows. The outflow could be the trail of nearby cores or other unidentified cores. In Figure 6.10, the extended SiO features, which are outside of the hub, are mostly distributed between filaments (F1, F2, and F3). The velocities of these extended SiO features align well with the velocities of these filaments, as shown in the channel plots covering velocities from -7 km s^{-1} to -5 km s^{-1} in Figure F.1 in the appendix.

Figure 6.11 shows the H^{13}CO^+ velocity gradient map and a SiO velocity integrated map only including SiO single Gaussian components with linewidths $\leq 1.8 \text{ km s}^{-1}$, as well as F1, F2, and F3 marked by solid lines. I detect prominent velocity differences at the interfaces between filaments and the presence of SiO narrow components in the interacting regions. The close correspondence between the distribution of filaments and SiO emissions suggests a possible association between the extended shocked gas and the filaments and/or the interactions between them. According to BTS fitting results, SiO emission exhibits narrow components near the edge of the hub and extends toward filaments 2 and 3. The presence of narrow SiO emission near the connecting point of filaments to the central hub may indicate a specific condition for producing accretion shocks. However, further investigations are needed in the following study to clarify the origin of the extended SiO emission.

6.4.2. NUMERICAL PREDICTIONS FOR LOW-VELOCITY SHOCKS

Extended SiO emission associated with narrow linewidths could suggest alternative explanations for the origin of shocks and SiO formation. In this section, I introduce ParisDurham shock model (PDSM) (Flower and Pineau des Forêts, 2003; Lesaffre et al., 2013; Flower and Pineau des Forêts, 2015) for the prediction of the properties of a diffuse shock. This is a public numerical tool for simulating and analyzing magnetized shock waves in interstellar environments that could handle

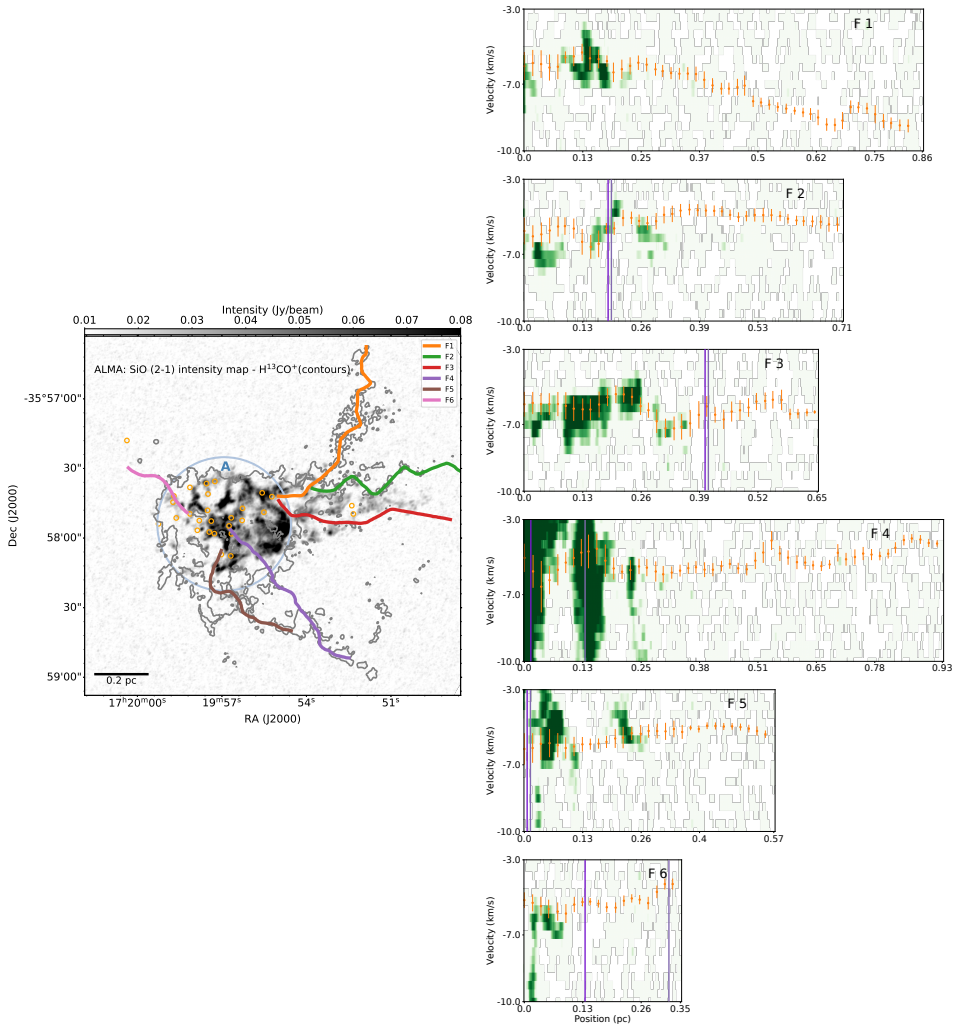


Figure 6.10.: *Left*: SiO peak intensity emission map overlaid by cores detected by ALMA continuum emission and identified filaments by H¹³CO⁺ emission map. *Right*: Position velocity cut along each filament from SiO emission map. The orange dots indicate the peak velocity constructed by extracting mean spectra over a beamsize area from H¹³CO⁺ along the path of filaments, and the vertical bar shows the FWHM of each spectrum.

different types of shocks, such as J-type and C-type. The code tracks the dynamical, thermal, and chemical evolution of a fluid particle in a steady-state plane parallel shock wave as it moves from the preshock medium to the post-shock medium (see Figure 6.12). The model simultaneously solves the dynamics and non-equilibrium chemistry, accounting for processes like ionization, which are crucial to understanding shock dynamics. There are three main ingredients in the *PDSM* code:

Dynamics: The *PDSM* code models the coupled evolution of velocity, density, temperature, and chemical composition in a 1D steady-state flow during the progression of a shock wave. It solves ordinary coupled differential equations by integrating as a function of z (see Figure 6.12) to ensure the conservation of particle number, mass, momentum, and energy for neutrals, ions, and electrons, and monitors changes in chemical species and hydrogen levels. The type of shock (J-type or C-type) depends on the shock velocity relative to the magneto-sonic speed. J-type shocks occur when the shock velocity exceeds the magneto-sonic speed, while C-type shocks occur if the velocity is

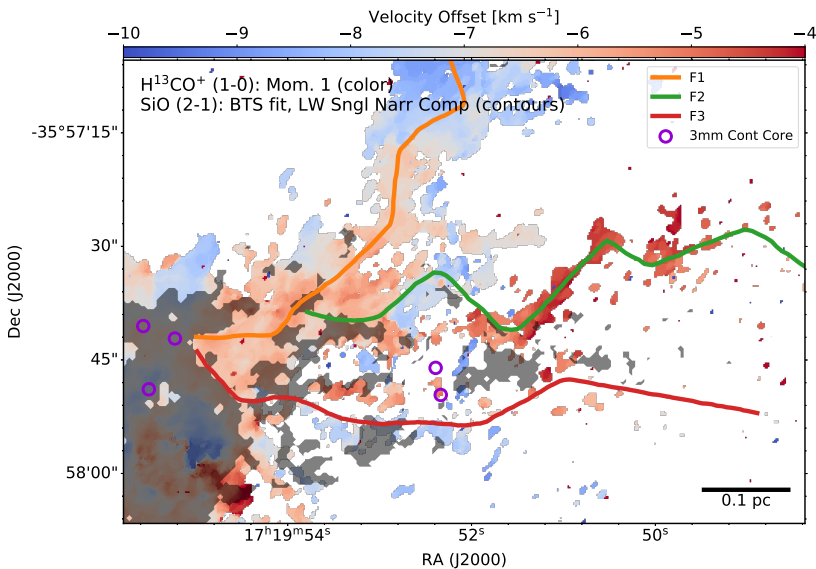


Figure 6.11.: H^{13}CO^+ (1-0) velocity map in color, and SiO (1-0) BTS fitted single spectra are shown in gray area. Furthermore, filaments and continuum cores are over-plotted. As filaments converge to the hub, the gradient of velocity in the H^{13}CO^+ map changes and the narrow SiO spectrum appears.

lower, leading to a broader dissipation of kinetic energy due to ion-neutral interactions. The code employs the DVODE integrator to solve the coupled equations.

Heating and cooling processes: The PDSM code incorporates various cooling and heating mechanisms to simulate shock waves accurately. For cooling, the code contains mechanisms such as H₂ line cooling due to collisional excitation, rotational and vibrational radiative cooling by molecules like CO and H₂O, pure rotational cooling by OH and NH₃, atomic cooling through fine-structure and metastable lines, inelastic scattering of electrons on H and H₂, and collisional dissociation and ionization. The heating mechanisms included in the code consist of viscous and compressive heating, ambipolar-diffusion heating through elastic scattering between neutrals and charged particles, heating due to cosmic rays, photoelectric effects on small grains and polycyclic aromatic hydrocarbons, photoionization and photodissociation heat-

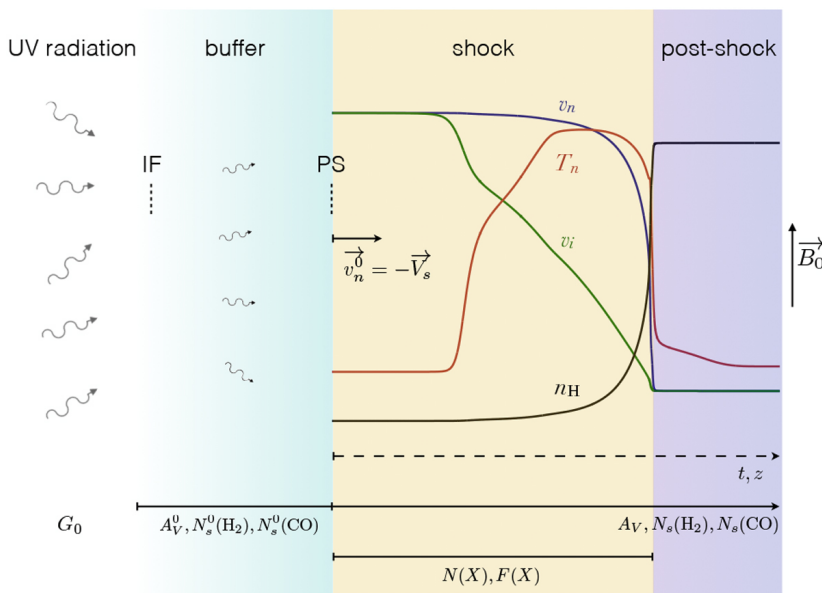


Figure 6.12.: Schematic view of the preshock zone (light-blue), shock layer (yellow) and post-shock region (purple) in a planer C-type shocks. The preshock buffer is initially determine to set the initial condition for the shock. As the shock process occurs, there is no further compression taking place in the post-shock region.

Credit: Godard et al., 2019

ing, and collisional de-excitation of H₂ levels. Additionally, the code considers mechanisms that can either heat or cool, such as energy transfer through gas-grain collisions, enthalpy transfer between neutral, ion, and electron fluids, and the exo-/endothermicity of chemical reactions.

Chemical species and grains: The *PDSM* code can model chemical species composed of elements such as H, D, He, C, N, O, Na, Mg, Si, S, and Fe, which can be neutral, singly ionized, or part of icy grain mantles or refractory cores. Users can modify the species list from an input file (*species.in*) to suit specific requirements. Typically, the standard models involve around 134–138 species. The code also includes a representative polycyclic aromatic hydrocarbon (PAH) species and a grain species to track grain charge. The number of grains is self-consistently determined based on initial conditions specified by the user. Additionally, the thickness of ice mantles on grains is computed based on total elemental abundances, ice bulk density, and the grain core size distribution at the current point in the simulation.

6

Chemical network: The *PDSM* code enables users to customize the list of chemical reactions for simulations. The standard configuration involves approximately 1000 reactions connecting around 130 species, but it can be expanded to include species, such as deuterated ones. The code supports various gas-phase chemical reactions, including neutral-neutral reactions, ion-neutral reactions (enhanced by ion-neutral drift), radiative and dissociative recombinations, charge exchange, ionization, and dissociation by secondary energetic electrons and photons. Some H₂-related reactions are treated at a detailed level for better accuracy, including H₂ reformation on grains, ortho-to-para conversion, and collisional dissociation. Additionally, the code simulates processes that transfer species between grains and gas, such as sputtering of icy mantles and refractory species from grain cores by drifting heavy neutrals, charge balance of grains and polycyclic aromatic hydrocarbons (PAHs), adsorption of species on ice mantles, and various desorption mechanisms from ice mantles.

The first step to execute the *PDSM* shock model is to specify all input parameters and initiate a preshock model. The user sets several initial values, including input files, shock parameters, environment parameters, grain properties, excitation and cooling options, numerical parameters, output specifications, and developer options, all within the *input_mhd.in* file. Then the *PDSM* code computes the initial

abundance of species involved, usually using values at chemical equilibrium in the preshock region. Depending on whether the model is irradiated or non-irradiated, different chemical networks and input files must be used. For non-irradiated models ($RAD=0$), grain surface processes should be excluded, while for irradiated models ($RAD \neq 0$), the grain surface processes should be included. Reaching chemical equilibrium can be time-consuming, requiring an adequately long `duration_max` parameter. The procedure for initiating a preshock model is further described in Appendix E.

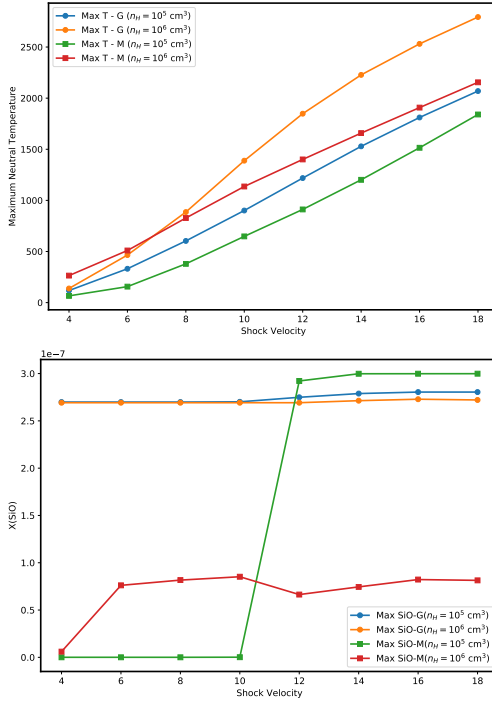
In the second step, the `input_mhd.in` file should be updated with the preshock conditions calculated earlier. The user also needs to define dynamical shock parameters such as shock speed, transverse magnetic field, initial shock type, number of fluids, and shock age. Finally, the shock model can be executed based on new input parameters. A series of shock models with the same preshock conditions can be run with varying dynamical parameters.

Generally, for every static model, the values of the preshock density `nH_init`, cosmic ray ionization rate `zeta`, and radiation field `RAD` remain unchanged. The model is repeatedly executed by changing one input parameter, such as shock velocities. The final output of the model tracks the abundances of different molecules, temperatures, and energies over time for each shock velocity. Additionally, one could track the changes of each shock model over the changes of free parameters, such as different velocities.

In this study, I am interested in SiO abundances in C-shocks. Apart from the initial condition of the preshock grid, the assumption of free silicon in the gas phase or grain mantles in the preshock model also affects the results. Louvet et al., 2016 defined two scenarios for free silicon: the gas phase scenario (-G) where 10% of free silicon exists in the form of neutral silicon in the gas phase, and 1% in the grain mantles. In the second scenario or the grain mantles phase scenario (-M), 10% of free silicon exists in grain mantles and the 1% in the gas phase. The remaining 89% is preserved in the core of other interstellar grains. Figure 6.13 shows a replication of the Louvet et al., 2016 model in C-shocks for these two scenarios but with higher number densities (10^5 and 10^6 cm^{-3} instead of 10^4 cm^{-3}). The parameters for the grid of shock models are explained in Appendix E.

Figure 6.13 shows two examples of free parameter tracking. Figure 6.13 (a) shows the maximum neutral temperatures for two shock densities of 10^5 and 10^6 cm^{-3} , repeated for the two aforementioned scenarios. The maximum neutral tempera-

ture rises almost linearly the shock velocities, and the (-G) scenario displays has a slightly higher temperature than the corresponding (-M) scenario.



(a) Maximum neutral temperature reached in each of the shock models versus the shock velocity based on two scenarios: the gas phase scenario and the mantle phase scenario. The preshock densities for each scenario are 10^5 and 10^6 cm^{-3} .

(b) The maximum local abundances of SiO ($X(\text{SiO}) = n_{\text{SiO}}/n_{\text{H}}$) reached in each of the shock models versus the shock velocity based on two scenarios: the gas phase scenario and the mantle phase scenario. The preshock densities for each scenario are 10^5 and 10^6 cm^{-3} .

Figure 6.13.: A example of PDSM output for maximum neutral temperature and local abundances of SiO in every shock model against the shock velocity. Each color correspond to different initial parameters.

Figure 6.13 (b) exhibits the peak local abundances of SiO over the entire shock region under the same conditions for column densities and the (-G) and (-M) scenarios for the same four models as in panel (a) of Figure 6.13. The maximum local abundance of each component, such as SiO, is defined as $X(\text{SiO}) = n_{\text{SiO}}/n_{\text{H}}$ where n_{H} is the preshock density which could be 10^5 and 10^6 cm^{-3} for each scenario. The maximum abundances of SiO-M exhibit a significant jump between velocities of 10 to 12 km s^{-1} , suggesting that in shock densities of 10^5 cm^{-3} and velocities of 12 km s^{-1} , assuming the initial free Si is in grain mantles, the SiO abundances increase in the gas phase for velocities $\leq 12 \text{ km s}^{-1}$. The jump between velocities of 10 to 12 km s^{-1} is similar with Louvet et al., 2016 findings for shock densities of 10^4 cm^{-3} . This could mean that the process of SiO formation in the gas phase will speed up at a velocity threshold of about 12 km s^{-1} . Louvet et al., 2016 also

declared that the evolution of the maximum SiO abundance in the gas phase is impacted by the shock velocity and indicates the presence of a velocity threshold associated with sputtering processes. These processes affect the mantles, directly releasing SiO into the gas phase.

It is important to note that the abundance I consider here is the local abundance, which differs from observations. The ratio of local densities determines this local abundance. In reality, observers do not have access to this information. When the shocks are placed on the plane of the sky, the width of the shock is too narrow to be resolved. In practice, observers cannot access the evolution of local abundances and only have access to integrated quantities i.e. the column density (ratios).

Another limiting factor is the lack of additional transitions to constrain the model better, as the SiO(2-1) line is not necessarily optically thin in the models compatible with observations. Observation of lines with smaller opacities, specifically the (5-4), (6-5), and (8-7) lines, and especially interferometric observations with higher angular resolution, would be beneficial in identifying distinct shock structures.

Despite these limitations, and based on the modeling results shown in Figure 6.13, I explore how the results predicted by the model compare with the observational data of NGC 6334-V. For this, I have generated Figure 6.14 showing the column density of SiO as a function of the velocity of the gas. The column density of SiO is derived assuming LTE conditions and the optically thin emission SiO(2-1) (see e.g., Csengeri et al., 2016). It also considers that the emission originated from the low-velocity component of the spectra and uses a single excitation temperature. I have estimated the column density of SiO to be in the range of 10^{-13} and 10^{-14} cm^{-2} (see Appendix F and Figure F.2). Similar to the modeling results, I see a change of a factor of three in the SiO column density, which is encouraging. However, I can not directly compare the results from the observations in Figure 6.14 with those from the modeling in Figure 6.13 because of different reasons. First, the model considers the shock velocity, while in the observations, I have a measurement of the velocity of the gas, which can differ from the actual shock velocity since pre-shock and post-shock gas may also emit in SiO at different velocities. Second, we do not have an actual measurement of the SiO abundance but just the SiO column density. To estimate the observational abundances of SiO, we need to determine both the column densities of SiO and those of either H₂, H, or, in the worst-case scenario, any molecular emission unaffected by shocks. However, I could not find high-resolution archival data for H or H₂ to determine SiO abundances accurately. Furthermore, the ALMA dust continuum emission or molecular

emission, such as H^{13}CO^+ , CCH , HC^{15}N , or H^{13}CN , does not cover the entire SiO emission, specifically region B, which holds our interest in terms of narrow components. This is one of the significant constraints when comparing SiO emission with models like PDSM. We also would need to have information on the H_2 content at the locations where SiO is located to determine the SiO abundance, but this is not possible with the current dataset, since the ALMA observations do not detect continuum emission that could be used to determine the H_2 column density across all the region where SiO is detected, and the larger-scale images of Herschel or APEX do not have enough spatial resolution to resolve the structure seen in SiO. Despite these limitations, we consider that the first attempt of comparison between Figures 6.14 and 6.13 is promising. Future observations of other transitions of SiO may help to characterize the SiO shock gas properties better, and this may help to establish a better connection between observations and modelling.

6

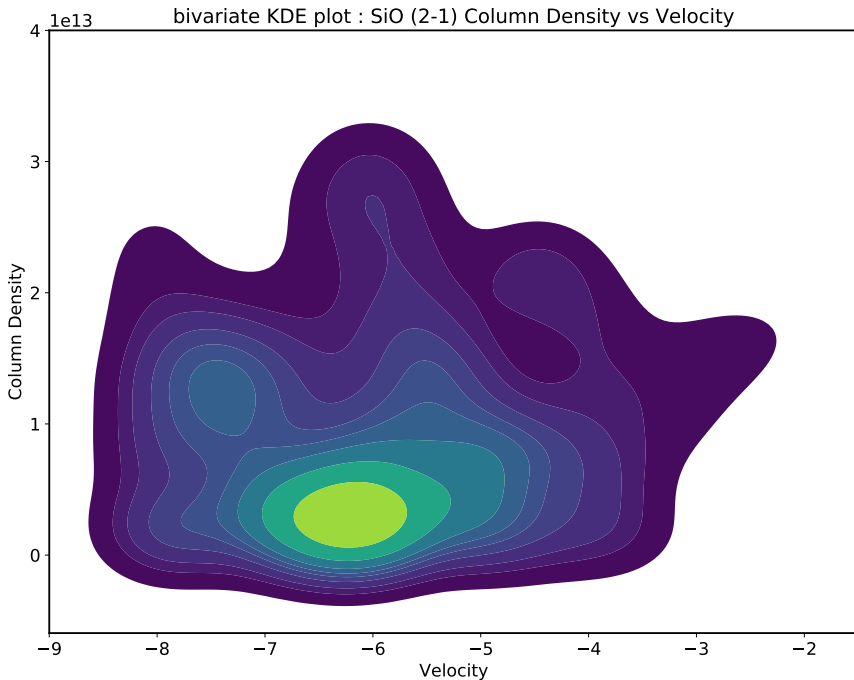


Figure 6.14.: For each pixel within region B, the offset velocity and column density are extracted (see Figure F.3) and the bivariate KDE of SiO (2–1) column density versus velocity is then plotted.

7

SUMMARY AND OUTLOOK

7.1. SUMMARY

I studied the kinematics and structure of accretion in the massive protocluster NGC 6334-V, embedded in a filamentary cloud NGC 6334. I used the ALMA interferometer telescopes to conduct observations in band 3 at a frequency of about 87.6 GHz, and collected data on twelve high-resolution spectral units targeting specific spectral lines, as well as a broad spectral window (with a total bandwidth of 1875 MHz) used for the continuum emission. I mapped an area of $2' \times 2'$, and reached an angular resolution of $\approx 1''.4$ (corresponding to ≈ 2400 au). I performed the data calibration using the ALMA calibration pipeline in CASA and identified line-free channels within the wide band of 1875 MHz centered at the frequency of 87.6 GHz. I cleaned the continuum emission and molecular spectra datasets individually using a model-assisted method, and for each dataset, I combined the final image of the 12m extended array and the 7m compact array using the CASA task, feather. The final continuum image has a synthesized beam of $1''.5 \times 1''.1$, and the line data cubes have a beam of about $1''.7 \times 1''.3$.

Apart from ALMA observations, I also used ancillary data at submillimeter and infrared wavelengths and studied the association between large structures traced by the ancillary data and the small scale structures observed with ALMA.

I utilized ALMA continuum emission, H^{13}CO^+ , CH_3CCH , and SiO to characterize the morphological and physical properties. The results are summarized into three categories of small scale (< 1 pc), intermediate scale (~ 1 pc), and large scale (> 1 pc) as follows:

Small scale (< 1 pc): I characterized the mass distribution on a small cluster scale and mapped the temperature over the cluster.

- I used CH_3CCH as a thermometer and calculated the accurate temperature within the cluster using “XCLASS”. The maximum temperature of 252 K belongs to the hot core, while it drops to tens of Kelvins in the surrounding areas. I also determined an error of ≈ 20 –50 K for the temperature measurement, which is quite large and suggests a considerable degree of uncertainty in the temperature estimation process.
- I used the continuum emission from ALMA observations to identify massive cores in the central region. I identified 28 sources and found that 4 have counterparts to previous infrared sources: 1 class I, 2 class II, and 2 NIRCI sources in the region. Additionally, my analysis confirmed the existence of one hot core (HC) and two other cores (N and SE), as pre-

viously reported by Juárez et al., 2017b. Further, I derived the masses of these dense cores, using rotational gas temperatures, ranging from 0.1 to $31 M_{\odot}$, with a mean mass of $\sim 5.2 M_{\odot}$. Since the rotational temperature tracers are not detected at the positions of all sources, I also calculated the masses based on an assumed temperature. I observed higher values ranging from ~ 0.5 to $80 M_{\odot}$, with a mean mass of $\sim 11.7 M_{\odot}$ and a total core mass of $\sim 144 M_{\odot}$. In addition, I determined the volume density (n_{H_2}) based on gas temperature with the mean values of $7 \times 10^7 \text{ cm}^{-3}$ and $18 \times 10^7 \text{ cm}^{-3}$ if considering the assumed temperatures. I also obtained column densities for all the cores with a mean value of $22 \times 10^{23} \text{ cm}^{-2}$ in the case of T_{rot} and $22 \times 10^{23} \text{ cm}^{-2}$ in the case of T_{est} .

I indicated that the spatial distribution of cores in the cluster is clustered in the center and is not randomly distributed throughout the observed region. I evaluated the internal structure of the cluster NGC 6334-V. I measured the Q parameter to be 0.82, which suggests a centrally concentrated cluster, and the cores within the cluster tend to be closer to the center of the cluster.

Discussing the formation process of continuum cores, I calculated the Jeans length and mass for thermal and non-thermal contributions. The thermal Jeans length is computed as $\lambda_J \sim 0.03 \text{ pc}$, and the non-thermal Jeans length is computed as $\lambda_J \sim 0.17 \text{ pc}$. This, in comparison to the observed median distance of 0.04 pc , shows the same order of magnitude as the thermal Jeans length. Using the Jeans length, I computed the thermal Jeans mass of $0.01 M_{\odot}$ and non-thermal jeans mass of $1.4 M_{\odot}$. The mean mass of the observed core is $\sim 5 M_{\odot}$, which is significantly larger than the thermal Jeans mass but within the same order of magnitude as the non-thermal Jeans mass.

The wide range of core masses also suggests a critical interplay between thermal and turbulent pressures in star formation, with turbulent pressures potentially playing a more dominant role in regulating the fragmentation process. Our observations suggest that fragmentation in star formation is significantly dominated not only by thermal and non-thermal Jeans instabilities but also by a complex interplay of factors such as magnetic fields, angular momentum, and star formation feedback.

I calculated the completeness limit at 3mm *ALMA* observations using a CMF plot and showed the significant difference in the high mass regimes ($M > 5M_{\odot}$) where the measured slope of -2.12 for T_{rot} is much steeper than the CMF of T_{est} with the slope of -1.03 and also the power-law index of the IMF (-1.3). I argued that the deficit in the distribution of high-mass cores might suggest more evolved and smaller structures that have either lost their initial mass or fragmented into smaller cores and the top-heavy distribution of high-mass cores would suggest the presence of younger high-mass cores, indicating an early-stage cluster. I also indicate that both results could be biased due to the uncertainty of temperature measurements and insufficient angular resolution to resolve small scale fragmentation. Finally, I showed mass segregation in NGC 6334-V. The relaxation time is one order of magnitude larger than free fall times, suggesting primordial segregation is a possible formation scenario in cluster NGC 6334-V.

Intermediate scale (~ 1 pc): I studied the two phenomena of accretion along filaments and the nature of widespread SiO in the central cluster, which is elongated toward the filaments on the intermediate scale (~ 1 pc).

- I identified six prominent filaments accumulating material toward the center through the *ALMA* observations of dense gas tracers. I used the $H^{13}CO^+$ emission map and the DisPerSe algorithm as guides to detect filaments. I calculated the properties of filaments, such as velocity gradients, mass, length, mass per length, and mass accretion rates.

I used PV plots to determine velocity gradients and calculate mass accretion rates in filaments. Derived velocity ranged from $+3.1$ to -5.2 $\text{km s}^{-1} \text{pc}^{-1}$, and two of these values were negative. The trajectories of the filaments were found to be non-linear, with wiggles appearing in filaments 2, 3, and 6. Additionally, the velocity gradient sign changed for filaments 3 and 6. These changes in values relate to the filament location and angle within the sky plane. A negative velocity gradient, indicating a redshift along the filament, suggests it might extend backward from the central hub hosting the forming cluster, assuming gas flows from the outer parts toward the center. Meanwhile, filaments with positive velocity gradients will likely extend in the foreground direction.

Our study revealed that the filament masses range from 90 to 150 M_{\odot} and lengths from approximately 0.5 to 0.9 pc, resulting in a mass per length of around 150 to 280 $M_{\odot} \text{ pc}^{-1}$. Comparisons with critical line mass values showed that filaments 1, 2, 3, and 6 have twice the non-thermal critical M/L value, suggesting instability, collapse, and fragmentation, further supported by dense cores along these filaments. In contrast, filaments 4 and 5 showed similar or larger non-thermal critical line mass values, which could be due to the chaotic environment near the HII regions.

- I detected a unique, widespread SiO emission with low-velocity components throughout the entire central hub of this cluster. The analysis of BTS line fitting revealed that 57% of the fitted velocity components exhibited even narrower linewidths, less than 1.8 km s^{-1} , suggesting that the SiO emission in NGC 6334-V was predominantly influenced by low-velocity shocks. I classified the fitted spectra of SiO emission with three boundaries: broad linewidth ($\text{LW} > 4 \text{ km s}^{-1}$), intermediate linewidth ($1.8 < \text{LW} < 4 \text{ km s}^{-1}$), and narrow linewidth ($\text{LW} < 1.8 \text{ km s}^{-1}$). Additionally, I divided the very central region, where most of the cores are located (region A), from the rest of the surrounding area (region B).

Our findings showed that the broad components were highly dominant in the central region of the hub cluster. These broad spectra also revealed the red- and blueshifted wings perpendicular to the direction of the EGO counterpart bright at $4.5 \mu\text{m}$ (EGO G351.16+0.69, Chen et al. 2013). I concluded that the SiO emission in region A was a product of high-velocity shocks and that shocks either originated from outflows or interfaces between shocked and ambient gas.

Our study also revealed that the narrow components mostly appeared in a single Gaussian line profile and the velocity distributions spread in a tail feature towards the direction of filaments 1, 2, and 3. Some segments were observed where the filaments joined the central hub, and no cores were detected. I also showed that SiO PV cuts followed the path of filaments 2 and 3 for about 0.25 pc. I detected prominent velocity differences at the interfaces between filaments and the presence of SiO narrow components in the interacting regions. Based on the close correspondence between the distribution of filaments and SiO emissions, I suggested a possible association between the extended shocked gas and

the filaments and/or the interactions between them, which may indicate a specific condition for the production of accretion shocks and the formation of gas phase SiO.

Large scale(> 1 pc): I showed a relationship between large-scale clouds and small-scale cluster filaments. Also, I suggest a formation scenario in NGC 6334-V on the large scale.

- I compared archival observations on source V at different scales and wavelengths to find a hierarchical relationship between the small scale filaments and the large-scale filaments in NGC 6334 cloud. I identified three large filaments in the ^{13}CO (2-1) emission map observed with APEX that converged at the center of source V. Similar trajectories of large filaments also detected 350 μm continuum maps and appear as dark features in Spitzer/IRAC data. The comparison of ALMA and large-scale archival data shows that the large-scale filaments split into smaller branches at the higher resolution of ALMA. Higher-resolution ALMA observations also show that accretion along one filament is followed by the number of branches that probably spread in an inhomogeneous dusty background.
- I showed a distinct separation between the cluster NGC 6334-V and the rest of the NGC 6334 cloud. I presented ionized data on both low-resolution radio emission (843 MHz) and infrared $\text{H}\alpha$ emission from Source V. These data sets revealed a common emission originating from the cavity. Moreover, the 843 MHz data displayed a spherical shape wrapping both cavities and the hub cluster. Based on the cluster morphology in the neighboring ionized cavity, I proposed a formation scenario based on the triggering of star formation by expanding HII regions in neighboring filaments. According to this scenario, a lobe of ionized gas was expelled from an unknown star behind the cloud, which struck the cloud and separated Source V from the rest of the cloud. This interaction between the ionized gas and the central cluster also had the potential to reshape Cluster V and push filaments toward the opposite side. Interestingly, despite the lack of ionized gas within the filaments, the accretion towards the central hub continued, allowing star formation to resume.

7.2. OUTLOOK

The research presented in this thesis provides significant insights into the structures and properties of the cluster NGC 6334-V. However, as with all research, it opens new avenues for further investigation and raises questions that can be the subject of future studies. In this section, I will mention potential future studies framed within the context of two observational scales.

INTERFEROMETRIC OBSERVATION WITHIN SMALL SCALE STRUCTURES (< 1 PC)

The limitations of low-resolution data have constrained our exploration of small-scale features. To investigate these features further and address the issues raised, higher-resolution observations would be significantly beneficial in the following topics:

Accurate determination of CMF: In Section 4.5.3, I showed the study of CMF of identified ALMA continuum cores. However, observational limitations such as resolution and temperature hindered the comparison of the CMF to the Initial Mass Function (IMF). With an improved spatial resolution and mass sensitivity, I could better resolve the fragmentation process in this cluster to understand spatial distribution and mass segregation. Moreover, the higher dust emissivity at shorter wavelengths would render high-spatial resolution observations more sensitive to dust emission than the current data. Such an improvement would be sufficient to probe the multiplicity in the cores and also lower mass end of the CMF in the high-mass star-forming cluster V.

Another challenge in studying the CMF was determining the temperature of cores. By observing molecular species such as CH₃CN, known to be a tracer of gas temperature in warm, dense environments, and different transitions of H₂CO, which can estimate the temperature of less dense cores with no detectable CH₃CN emission, I could derive the gas temperature for cores where the lines are detected. This approach could also provide a comprehensive comparison to rotational temperature computed from CH₃CCH emission.

Probing the origin of shock environments: In Chapter 6, I showed that the intensity map of the SiO (2-1) molecular emission towards NGC 6334-V reveals a complex and widespread morphology with different origins in the central hub (region A) and surrounding hub (region B) of the cluster NGC 6334-V. In the central hub, I suggested the SiO originated from high-velocity shocks or outflows, and I also identified red- and blue-shifted wings. However, the

ALMA data resolution was insufficient to identify outflow lobes individually. Higher-resolution observations toward SiO or other outflow tracers, such as CO and its isotopologues, would potentially offer a more detailed picture of outflows.

In Region B, or the area surrounding the central hub, where the SiO emission exhibits a widespread morphology with narrow linewidths, I suggested that the extended SiO emission originated from low-velocity shocks. These shocks might occur near the point where filaments connect to the central hub. I also introduced the PDSM as a numerical modeling code designed to simulate shock environments and estimate the probability of producing SiO under these conditions. However, observing additional SiO transitions with smaller opacities (e.g., 1–0, 3–2, 5–4, 6–5, 8–7) at a higher angular resolution is necessary to enrich the chemical network and provide better constraints for the model.

INTERFEROMETRIC OBSERVATION WITHIN LARGE SCALE STRUCTURES (> 1 PC)

Cluster NGC 6334-V is part of the filamentary cloud NGC 6334, and to better understand the evolution of a cluster, it is essential to study the connection of the cluster with other neighboring clusters and clumps in the cloud. The possible studies are listed as follows:

7

Statistical tracing of time evolution in NGC 6334: In Section 4.6.2 and 5.3.4, I compared the cluster NGC 6334-V with other clusters observed as part of this observation project and showed different physical properties, with different evolutionary stages of these clusters. Evolutionary differences among the various clusters in NGC 6334 are also published in other statistical studies (e.g., Russeil et al., 2010; Tigé et al., 2017), showing some are in a pre-stellar stage and others in a more advanced phase with active ongoing feedback. However, to study the correlation between time evolution and cluster properties, I require a larger sample of clusters in higher resolutions. Conducting statistical observations of diverse sources could target a range of topics, such as widespread SiO, H II regions, and distribution of properties such as mass, temperatures, column densities, accretion rates, etc. The outcome of such a study could yield a rich catalog of all sources at different evolutionary stages. This approach reduces the dispersion of initial conditions as they all form within the same molecular cloud, thereby allowing us to study the time evolution of the physical properties of the regions where clusters form.

Local and global filaments in mass assembly processes In Section 5.4.1, I showed that the local filaments in source V are merged into global filaments that span along the cloud NGC 6334. However, the ancillary observation resolution and current molecular tracers were insufficient to study the mass accretion of the larger filaments in detail and their connection with local filaments. Detecting infalling motions in the NGC 6334-V and also in other similar clusters in the cloud could provide an opportunity to study the mass assembly process in massive proto-clusters. The proof of accelerated velocity signatures would highlight the existence of extended collapsing modes at scales of about 1 pc and more within these clusters. Moreover, using other molecular line emissions such as N_2H^+ or HC_3N as a tracer of high-density material to quantify local velocity fields of dense gases or HNC to trace low-density material to characterize global dynamics and large-scale collapse would be beneficial in studying the time evolution of both local and large scale.

Impact of magnetic fields on the Structure of NGC 6334-V: One of the studies missing from this thesis is an investigation into the magnetic field, a gap that exists due to the lack of polarization observations. The presence and orientation of magnetic fields have shown a significant impact on the evolution of interstellar filaments (e.g., Seifried and Walch, 2015). Recent observations shed light on the role of the magnetic field in forming the hub-filament network NGC 6334. Arzoumanian et al., 2021 presented the B-field structure at a resolution of ~ 0.1 pc toward the long ridge and hub structure NGC 6334, where source V is also part of that observations. They revealed that the B-field generally exhibits a perpendicular or random orientation to the sub-filament in the outer part. However, the B-field aligns parallel to their spines in the inner region, where the sub-filaments merge with the clump-hub. The orientation of the B-field in source V is also parallel to the filaments. Another study by Liu et al., 2023 presented high-resolution (~ 900 au) ALMA dust polarization toward four clumps in cloud NGC 6334, where source V is one of them. They also presented the B-field nearly parallel to elongated streamers in a very central hub that connects the hot core to two other cores (core numbers (15), (13) and (21) in Figure 4.1). Therefore, another observation toward source V, aligned with the field of view of the current ALMA map, may enhance understanding of the magnetic field concerning the filaments and their connection to the large scale filaments identified through BISTRO observations (Arzoumanian et al., 2021) and could also integrate insights into

the fine-scale streamers that link the cores within the central hub (region A) with ALMA observations (Liu et al., 2023).



XCLASS: THE EXTENDED CASA LINE ANALYSIS SOFTWARE SUITE

XCLASS solves the radiative transfer equation, taking into account opacity effects, and uses the model optimizer package MAGIX (Möller et al., 2013) to determine a best fit to the observational data. Through XCLASS functions, one can model a spectrum with an arbitrary number of molecules, where the contribution of each molecule is described by an arbitrary number of components in a file called (.molfit). The model (or synthetic) spectrum is obtained by solving the radiative transfer equation under the local thermal equilibrium (LTE) assumption for an isothermal object in one dimension. The LTE assumption implies that the excitation temperature does not necessarily need to be the physical temperature but must be constant for all transitions. However, a non-LTE description requires collision rates which are available only for a few molecules. So, LTE is a reasonable approximation in this case. In XCLASS, the `myXCLASS` function models a spectrum by solving the radiative transfer equation in one dimension for an isothermal object, known as the detection equation (Stahler and Palla, 2004). The equation defined by the received brightness temperature T_{B0} at ($\nu = \nu_0$) as

$$T_{B0} = T_0[f(T_{ex}) - f(T_{bg})][1 - e^{-\Delta\tau_0}] \quad (\text{A.1})$$

T_0 is the equivalent temperature of transition, T_{ex} is excitation temperature, T_{bg} assumed here to be approximately Planckian in its energy distribution, $\Delta\tau_0$ is the cloud optical thickness at line center and the function $f(T) = [\exp(T_0/T) - 1]^{-1}$.

The myXCLASS function models a spectrum with arbitrary numbers of isolated or blended molecules. myXCLASS assumes all components are aligned in a user-defined stack along the line-of-sight, where the background and the observer are placed at the ends. The solution of the equation A.1 for the closest layer to the background is,

$$T_{mb}(\nu) = \sum_{m,c} [\eta(\theta^{m,c}) [S^{m,c}(\nu)(1 - e^{-\tau_{m,c}^{m,c}(\nu)}) + I_{bg}(\nu)(e^{-\tau_{tot}^{m,c}(\nu)} - 1)]] + (I_{bg}(\nu) - J_{CMB}). \quad (\text{A.2})$$

The sums in this equation go over the indices m for molecule and c for component, and following, $\eta(\theta^{m,c})$ is the beam filling factor, $S^{m,c}$ is the source function derived by Kirchhoff's law of thermal radiation, I_{bg} is the beam averaged continuum background temperature, and J_{CMB} is the radiation temperature of the cosmic background. Based on the user-input values of the excitation temperature (kinetic temperature in LTE) and column density, the program calculates the optical depth for a molecule m , transition t , and component c as,

$$\tau_t^{m,c}(\nu) = \left[\frac{c^2}{8\pi\nu^2} A_{ul}^t N_{tot}^{m,c} g_u^t e^{-E_l^t/k_B T_{ex}^{m,c}} \right] \frac{1 - e^{-h\nu^t/k_B T_{ex}^{m,c}}}{Q(m, T_{ex}^{m,c})} \cdot \phi^{m,c,t}(\nu), \quad (\text{A.3})$$

where the Einstein A_{ul} coefficient, the energy of lower state E_l , the upper state degeneracy g_u , the partition function $Q(m, T_{ex}^{m,c})$ and the rest frequency of transition ν^t are taken from the SQLite3 database. Also, the values of the excitation temperatures $T_{ex}^{m,c}$ and the column densities $N_{tot}^{m,c}$ for the different components and molecules are taken from the user defined *molfit* file.

Once the optical depth is calculated, the myXCLASS function generates a synthetic spectrum based on kinetic and background temperatures provided by the user. Then, the program uses the MAGIX optimization routine to adjust the user-input parameters within a defined range to find the optimal fit for the observed spectra through a χ^2 minimization routine. MAGIX provides optimization through one or more algorithms that can be applied together and stops when the maximum iterations or desired χ^2 value are reached. One of the important features of myXCLASS function is the myXCLASSMapFit. This function can perform the above steps pixel

by pixel and generate output maps for each free parameter the user intends to model. The following section will show our use of the `myXCLASSMapFit` function and present the corresponding outcomes.

B

ERROR ESTIMATION FOR CH₃CCH

To exam the temperature variations seen in the small angular scales (see the upper right plot of Fig. 5.2), we performed the error estimation using the Markov chain Monte Carlo (MCMC) algorithm included in XCLASS. The MCMC algorithm estimates the posterior probability distribution and the highest posterior density (HPD) interval for each input free parameter. In this work, we have four free parameters; T_{rot} , N_{tot} , line width ($v_{\text{width}}^{\text{Gauss}} = \text{FWHM}$), and velocity offset from v_{LSR} . First, we ran the LevenbergMarquardt (LM) algorithm to decide the initial parameters for the MCMC error estimation. These initial parameters are used as a start-point in the walking space for MCMC walkers before their random walks. We extracted CH₃CCH spectra from three different pixel positions that have different T_{rot} ; at Position 1 (Fig. B.1), $T_{\text{rot}} = 17\text{K}$, at Position 2 (Fig. B.2), $T_{\text{rot}} = 39\text{K}$, and at Position 3 (Fig. B.3), $T_{\text{rot}} = 98\text{K}$. For the three positions, we used the same MCMC error estimation parameters; the number of walkers is 100, the burn-in iteration finding the best solution (indicated as blue lines in Figs. B.1, B.2, and B.3) for each parameter is 700. The maximum iteration, including the burn-in and determination of uncertainties of the solutions, is 1500. For defining the upper and lower limits of HPD corresponding to upper and lower errors (marked as the most left and most right vertical dashed lines), we set 2σ (or 95.4%) confidence interval for uncertainty. Figures B.1, B.2, and B.3 show the corner plots from the MCMC error estimation, and the corner plots are generated using the *corner* package¹.

¹<https://pypi.org/project/corner/>

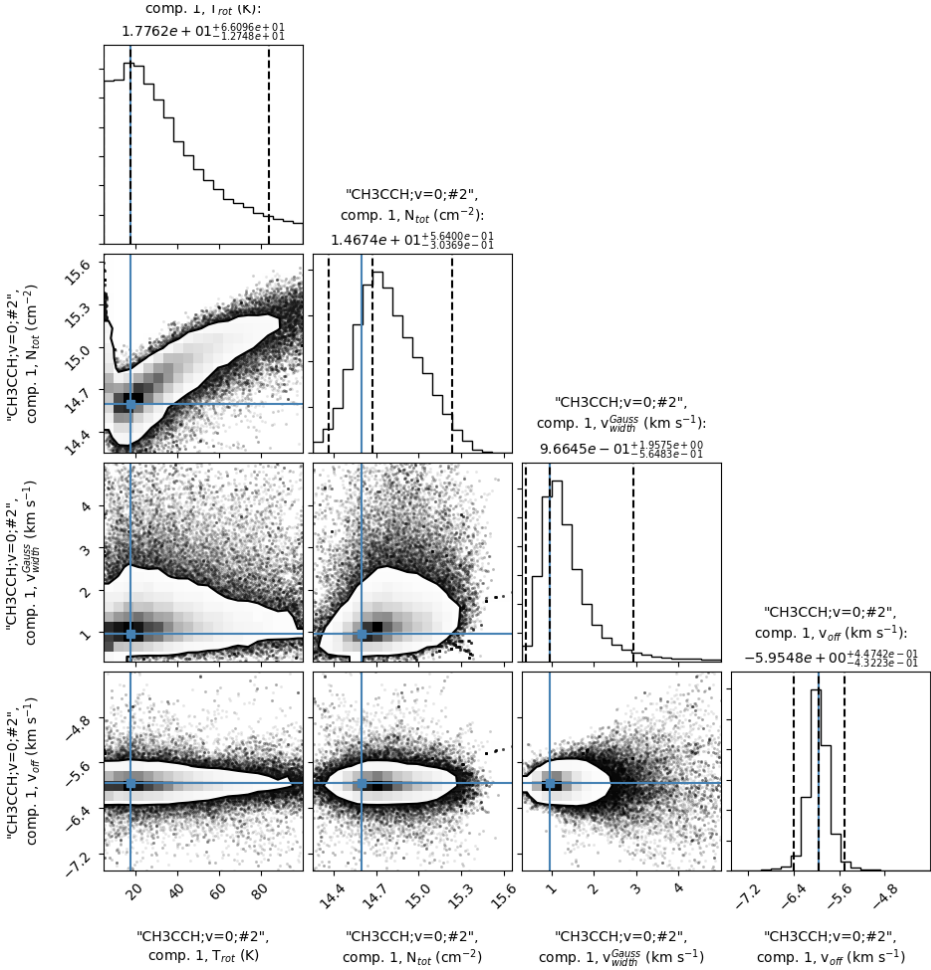


Figure B.1.: Corner plot for T_{rot} , $N(\text{CH}_3\text{CCH})$, $v_{\text{width}}^{\text{Gauss}}$ and v_{LSR} toward Position at R.A. (J200) = 17:19:56.02 and Dec. (J2000) = -35:58:11.86, The temperature at the position from the T_{rot} map in Fig. 5.2 is 17 K.

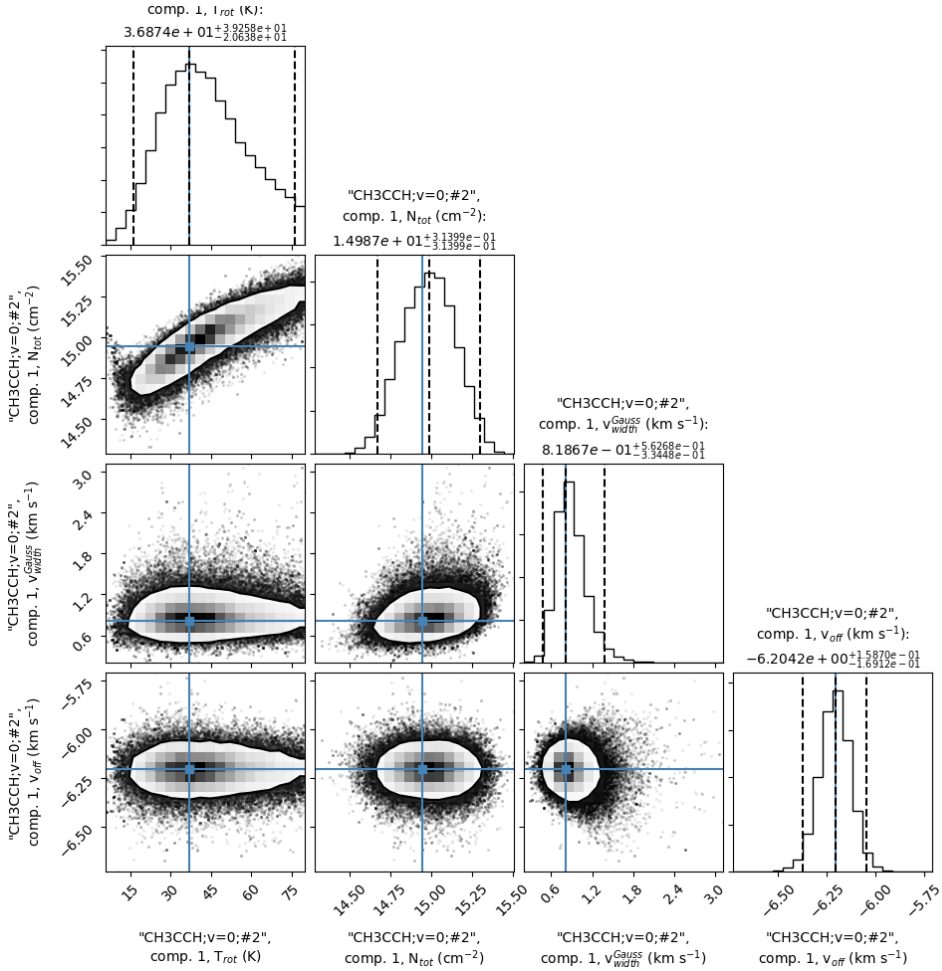


Figure B.2.: Corner plot for T_{rot} , $N(\text{CH}_3\text{CCH})$, $v_{\text{width}}^{\text{Gauss}}$ and v_{LSR} toward Position at R.A. (J2000) = 17:19:55.83 and Dec. (J2000) = -35:58:05.19. The temperature at the position from the T_{rot} map in Fig. 5.2 is 39 K.

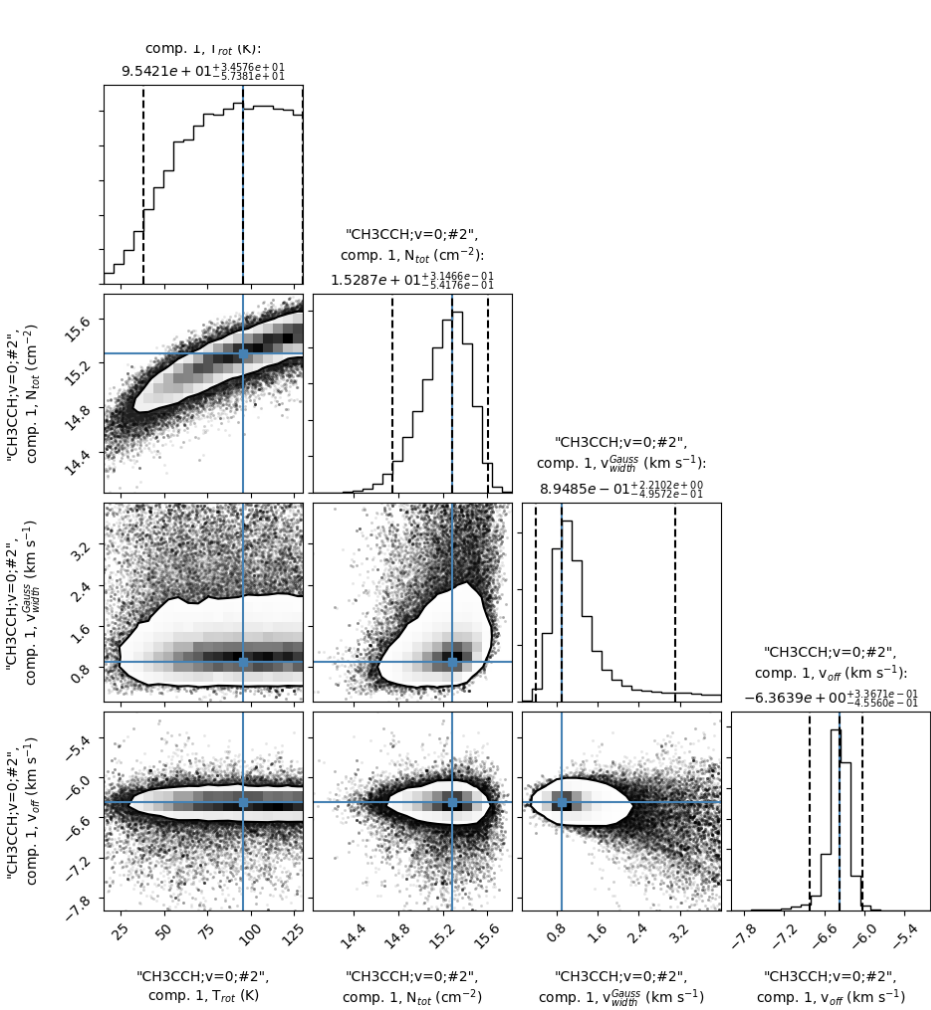


Figure B.3.: Corner plot for T_{rot} , $N(\text{CH}_3\text{CCH})$, v_{width}^{Gauss} , and v_{LSR} toward Position 1 at R.A. (J2000) = 17:19:55.88 and Dec. (J2000) = -35:58:08.02. The temperature at the position from the T_{rot} map in Fig. 5.2 is 98 K.



DISPERSE

Discrete Persistent Structures Extractor (DisPerSE) is a software tool developed to identify filamentary structures or voids in 2D and 3D distributions in a dataset (Sousbie, 2011). The algorithm implemented in DisPerSE focuses on the discrete Morse theory (Forman, 2002) to identify features and persistent theory (Edelsbrunner, Letscher, and Zomorodian, 2000) to remove the topological noise from the Morse complex and to identify structures at optimal resolution.

The Morse theory (Milnor, 1963) considers astrophysical objects as distinct topological functions in their most smooth and simple form. It provides a way to capture the intricate relationship between the geometrical and topological properties of the function. In the study of astronomical features, Morse theory faces limitations due to its requirements for smoothness and differentiability of functions, whereas typical astrophysical data may either result from inherently discrete processes like galaxy distribution or be derived through samplings, such as in numerical simulations or observational data. Forman, 2002 developed the discrete Morse theory to modify the Morse theory to apply to discrete or sampled data, which is more common in astrophysical research.

Within DisPerSE, the discrete MSC is computed for the density function to identify various cosmic structures such as voids, walls, filaments, and clusters based on the ascending 3-, 2-, 1-, and 0-manifolds of the theory. The MSC is a decomposition of the domain based on the gradient flow behavior, and it helps in understanding the topological and geometric properties of the function. In the context of cosmic structures, DisPerSE identifies different features like voids, walls, filaments, and clusters based on the ascending 3-, 2-, 1-, and 0-manifolds of the theory. Fur-

thermore, *DisPerSE* handles sampling and noise by using the persistence theory. By framing persistence criteria in terms of the confidence level concerning noise, *DisPerSE* becomes user-friendly, requiring only a single parameter for identifying structures at optimal resolution.

The main input parameter of the `mse` function is the persistence level, which we define interactively using a persistence diagram where all critical point pairs are plotted. To run *DisPerSE*, start by entering the command below:

```
> mse MolFitsFile.fits -interactive -upSk1 -periodicity 0
```

With the option `-interactive`, *DisPerSE* plots a persistence diagram where all the critical point pairs are plotted, and user can decide by eye where to set the persistence threshold. The function `upSk1` is used to connect maxima to saddle points, and to generate the so-called skeleton file, which contains the information (position and velocity) of the identified filaments. *DisPerSE* also assumes periodic boundaries by default for the dataset which is disabled by setting `-periodicity` to 0. The Figure C.1 is an example of the persistence diagram which is the 2D histogram of the critical point pair distribution based on a column density map. The y-axis shows the persistence, which is the difference between the densities of the critical points in a pair, while the x-axis represents the lowest density value of a pair. A pink dash-dot line is the persistence threshold that can be set by the user manually. This threshold is positioned where most points are within the bulk of the distribution.

The command `mse` generates two files: an `.MSC` file, which stores all the information of the `MSC`, and an `.NDSk1` file, where the information of filaments is stored after applying the persistence threshold.

For the second step, we need the `.NDSk1` file to extract the information on filaments. By executing the `skelconv`, we can modify various parameters to the skeleton and produce the output in a more workable format of `.FITS`, `.ASCII`, or `.vtp` file. This is gained through the second command line as

```
> skelconv skeletonfile.NDsk1 -breakdown -smooth 6
      -trimBelow 0.06 -assemble 70 -toFITS
```

Where the parameters are defined as follows:

- `breakdown` is used to set dummy critical points to prevent arcs from overlapping.
- `smooth <N>` is used to smoothen the filaments by enforcing them to be smooth over 'N' consecutive sampling points.

- `trimBelow <N>` is used to set the value of the detection threshold 'N', which is also shown by the vertical green dashed line in the persistence diagram (Fig. C.1). The detection threshold can be determined through visual inspection of the persistence diagram or configured as the noise level, a known parameter in observational datasets.
- `assemble <angle>` is used to assemble filamentary arcs into elongated filaments with the limitations of `<angle>` (in degrees), which means the assembled arcs must not form an angle greater than the specified angle.
- `toFITS` is used for writing the resulting skeleton to a file in *FITS* format. Alternatively, `–tovtp` or `–toASCII` can be used, depending on the preferred output format.

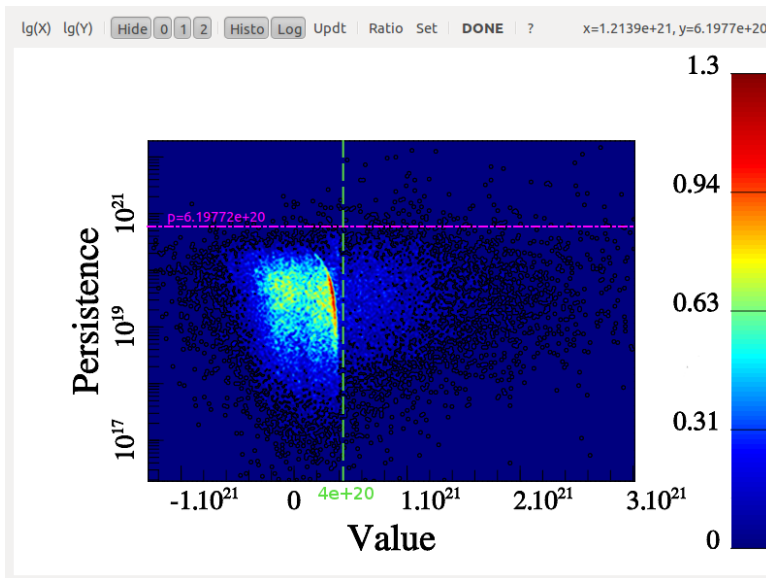


Figure C.1.: An example of a persistence diagram represents the distribution of critical points. The x-axis displays the lower density value from a pair of critical points, and the y-axis shows the difference in densities between the two critical points. A pink line indicates the persistence threshold and a green dashed line marks the detection threshold.

Credit: <https://github.com/thierry-sousbie/DisPerSE/blob/master/manual/web/images>

D

BEHIND THE SPECTRUM (BTS)

Behind The Spectrum (BTS)¹ as explained in Clarke et al., 2018b study, is an automated multi-Gaussian fitting algorithm that can be applied to optically thin spectra. This Python routine has the advantage that the number of Gaussian components in a spectrum does not need to be entered as an input. Instead, the BTS routine uses the first, second, and third derivatives of the spectrum to determine the number and positions of the velocity components. Once the number of components is found, BTS applies a least-squares fitting routine to determine the best-fit parameters.

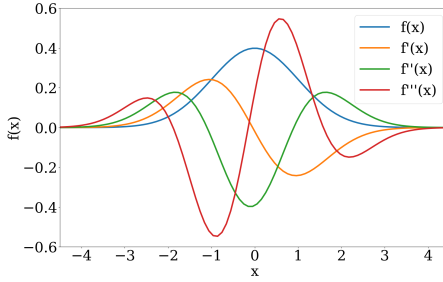
Figure D.1 (a), shows a perfect Gaussian $f(x)$ with a mean of zero and a standard deviation of one, along with its first, second, and third derivatives. The Gaussian maximum position aligns with the $f'(x) = 0$ and decreasing, the $f'''(x) = 0$ and increasing, minimum of second derivative ($f''(x)$), which is used as an indicator of the centroid of the line or velocity component. The first and third derivatives can also be used for additional checks.

Figure D.1 (b) shows the case of overlapping two Gaussian profiles, where the profile centered on $x = 2$ and has the same width, and half amplitude as the first Gaussian profile. In this case $f'(x)$ is not zero and $f'''(x)$ is close to zero, but the $f''(x)$ shows the first minimum at $x = 0$ second minimum at $x = 2.2$ which is better fit the velocity components of two Gaussian profile. In the real observations, the spectra are noisy which highly distorts higher derivatives of the intensity.

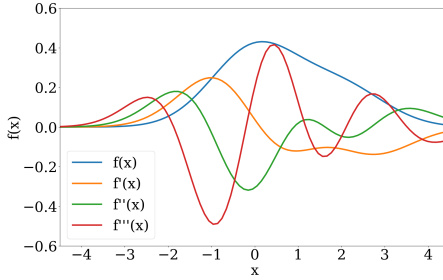
Figure D.1 (c) shows the noisy Gaussian profile of (a), where the second line profile $f''(x)$ is dominated by noise and no pronounced local minimum appears at the location of the peak. In this case the BTS works by smoothing noisy spectra

¹available at <https://github.com/SeamusClarke/BTS>

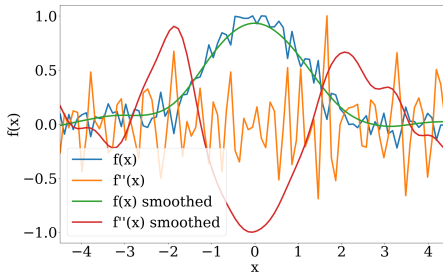
($f(x)$ smoothed) and then determine the derivatives. In order to smooth the spec-



(a) A Gaussian line profile centred on $x = 0$, along with the first three derivatives.



(b) Two Gaussian line profiles centred on $x = 0$ and $x = 2$, along with the first three derivatives.



(c) A noisy Gaussian line profile centred on $x = 0$, along with the second derivative, its smoothed Gaussian, and its second derivative.

Figure D.1.: A comparison of three different Gaussian Line Profiles: single, multiple, and noisy distributions with derivatives.

trum, the spectrum is convolved with a Gaussian kernel with a smoothing length of h . The choice of smoothing length is important since the large value of h over smooths and erases the spectrum, and the small value of h includes a high noise level with too many fake peaks. As seen in D.1 (c), adjusting only the smoothing length parameter is insufficient to remove local minima in the second derivative. To solve this issue, BTS compares the intensity of the spectrum in these velocity channels with a signal-to-noise threshold. Both smoothing length and signal-to-noise threshold are free parameters set by the user.

BTS uses the locations of local minima in the second derivative to determine the number and positions of velocity components. These values also serve as an initial estimate for the number of velocity components C and the velocity centroids \tilde{v}_c ($1 < c < C$) of the components. Also, the intensity and the FWHM width of the spectrum at velocity \tilde{v}_c are used by BTS as an initial estimate for the amplitudes \tilde{I}_c^0 and velocity dispersion $\tilde{\sigma}_c$ of the components, respectively. After determining the number of components C and initial estimation values for \tilde{v}_c , \tilde{I}_c^0 and $\tilde{\sigma}_c$, BTS uses the `curve_fit` routine from the Scipy Python library with the Trust Region Reflective option to set boundaries on the fitting parameters as follows:

$$\begin{aligned} \beta_{\text{BTS}} I_{\text{noise}} &\leq I_c^0 \leq 2I_{\text{max}}; \\ v_{\text{min}} &\leq v_c \leq v_{\text{max}}; \\ 2\Delta v_{\text{channel}} &\leq \sigma_c \leq v_{\text{max}} - v_{\text{min}}; \end{aligned} \tag{D.1}$$

Where β_{BTS} is the signal-to-noise threshold for a velocity component, I_{max} is the maximum observed intensity, v_{min} and v_{max} are the minimum and maximum velocity, and $2\Delta v_{\text{channel}}$ is the spectral resolution.

The fitting process calculates the reduced χ^2 and compares the new value with the user-defined limit χ_{limit}^2 . Depending on the value of reduced χ^2 , if $\chi^2 > \chi_{\text{limit}}^2$, repeat the fitting process with one additional component, and if $\chi^2 < \chi_{\text{limit}}^2$, the fitting could be correct. However, the process will be repeated with one less component to avoid over-fitting. After refitting with one fewer velocity component, the routine recalculates the reduced chi-square, and if it remains below the limit, the result is saved as the new fitting parameters; otherwise, the old parameters are held. Therefore, the algorithm systematically tests adding or removing components based on how well they improve the fit and avoid over-fitting too many velocity components.

BTS routine works based on 23 parameters, including the χ_{limit}^2 , smoothing length, signal to noise ratio, noise level, input, and output FITS files, and the spectrum properties, which users could set within the `.param` file. One example of a parameter file with all values and an explanation of all user-define parameters is shown in the listing D.1.

```

1  ### Important three parameters
2
3  chi_limit           :   1.2           ### The reduced
   chi_squared limit which is compared to to determine the goodness of
   fit.
4  smoothing_length   :   4.0           ### The smoothing
   length used to smooth the spectrum before the determination of the
   number of peaks
5  signal_to_noise_ratio :   4           ### Signal to noise
   ratio to determine if a component is significant enough to fit
6
7  ### Noise level parameters. Not needed for test runs
8
9  lower_integrated_emission_limit :   0.05           ### The integrated
   emission limit which is used to determine if a spectrum is
   significant enough to warrant fitting
10 variable_noise     :   0             ### A flag which
   determines if the noise level is constant for all spectra fitted,
   or if it is estimated from the spectrum
11 noise_level        :   0.001         ### If variable_noise =
   0 then we use a constant noise level for all spectra and this is
   set by noise_level
12 noise_clip         :   50            ### If variable_noise =
   1 then we take the standard deviation of the intensity for the
   first N velocity bins where N is the value of noise_clip
13
14 ### Flags
15
16 check_overlap      :   1             ### A flag to turn on
   the function to check if two components have velocity centroids
   within 1 velocity bin of each other
17 debug              :   0             ### A flag to turn on
   the debug mode, this produces a lot of screen output and so should
   be turned off for normal runs
18
19 ### File names for the input and output of fits files, only used for
   the FitAFits function
20
21 in_file_name       : /direc/SiO_fitsIMG.fits   ### The
   name of the fits file one wishes to fit
22 out_file_base      : SiO_BTS           ### The name base for
   the output fits file, i.e. Amp_tests.fits, Vel_tests.fits
23
24 ### Parameters used when one uses one of the test functions. Not used
   in normal runs.
25

```

```
26 test_number          :    1000      ### Number of test
    spectra generated
27 test_spec_min       :   -89000.0    ### Minimum velocity of
    the spectra
28 test_spec_max       :    69500.0    ### Maximum velocity of
    the spectra
29 test_spec_num       :     300      ### Number of velocity
    channels
30 test_noise          :     0.001    ### The level of noise
    added to the test spectra
31 test_amplitude_min  :     0.003    ### The minimum
    amplitude of the components in the test spectra
32 test_amplitude_max  :     12.0     ### The maximum
    amplitude of the components in the test spectra
33 test_width_min      :    100.0     ### The minimum width
    of the components in the test spectra
34 test_width_max      :   20000.0    ### The maximum width
    of the components in the test spectra
35 test_vel_cen_min    :   -10000.0    ### The minimum
    velocity centroid of the components in the test spectra
36 test_vel_cen_max    :    60000.0    ### The maximum
    velocity centroid of the components in the test spectra
37 test_plot_tag       :     1        ### A flag to turn on
    or off the plotting of the errors and reduced chi_squared in the
    single Gaussian test function
```

Listing D.1: User defined initial parameters within the FitsFileFit.param file.

E

EXAMPLE GRID OF SHOCK MODELS IN PDSM

In this section, I used the PDSM model and calculated a grid of shock models by initializing the following parameters for preshock conditions based on current knowledge of NGC 6334-V.

Preshock density: $n_H = 10^5$ and 10^6 . I derived the column density based on the filament masses computed in section 5.3.4. I assumed a cylinder of the same length as the filaments and determined the column density and volume density within this cylinder. Most values for volume density ranged between 10^5 and 10^6 , with a mean of 9.57×10^5 . Therefore, I included both cases of 10^5 and 10^6 in our calculations.

shock velocity: $v_s = 4, 6, 8, 10, 12, 14, 16, 18 \text{ km s}^{-1}$. The width of the SiO (2-1) line profiles in Region B, derived in Sect. 3.2.2, has an FWHM ranging from approximately 0.5 km s^{-1} to 1.8 km s^{-1} , and in a few pixels, it reaches up to 4 km s^{-1} . Louvet et al., 2016 assumed the shock velocity to be twice the velocity width in case of observing a single shock along the line of sight. PDSM is also a one-dimensional model for shock velocities of 4 km s^{-1} and higher (Bonne et al., 2020), and the shock is assumed to be seen face-on. In actual observation of NGC 6334-V much lower velocities than 4 km s^{-1} were observed. However, based on the source orientation, the shocks could propagate toward the sky plane, resulting in lower or higher shock velocities, respectively. Therefore, running the code on a series of shock velocities is beneficial.

Magnetic field parameter: $b\beta = 1$ The transverse magnetic field, relative to the direction of shock propagation is $B(\mu\text{G}) = b\beta \times \sqrt{n_{\text{H}}(\text{cm}^{-3})}$, where B is the intensity of the magnetic field, and $b\beta$ is a freely adjustable parameter in the code. I set $b\beta=1$ to 1, corresponding to a standard value for molecular clouds in the interstellar medium (e.g., Crutcher, 2012; Louvet et al., 2016).

Radiation field: $G_0 = 0$ In the high cloud volume densities reached within the filament (up to a few 10^6 cm^{-3}), and when the column density reaches a few 10^{21} cm^2 , the intensity of the radiation field becomes negligible $<0.1 G_0$ (Louvet et al., 2016). I adopted the values from Louvet et al., 2016 and computed the model without any irradiation $G_0 = 0$, and run few cases with a standard interstellar radiation field (ISRF) $G_0 = 1$ (Draine, 1978) to prove if they remain constant or not. The results as I expected stay unchanged in filaments with column densities of $\sim 10^{22} \text{ cm}^2$.

E

Apart from the initial condition of the grid, the assumption regarding the presence of free silicon in the gas phase or grain mantles in the preshock model is unknown, and different estimations can affect the results. Figures E.1 and E.3 serve as two examples of shock models with the assumption of a 10% fraction of the solar value of neutral Si in the gas phase and only 1% in grain mantles (scenario -G). Meanwhile, Figure E.2 and E.4 represent cases where 10% of the free silicon is in grain mantles, with the remaining 1% in the gas phase (scenario -M). This modification is done in the species input file (`species_2022_05.in`). Each figure consists of eight panels, where the shock velocities vary from 4 km s^{-1} to 18 km s^{-1} with increments of 2 km s^{-1} for a specific shock density of 10^5 or 10^6 cm^{-3} . The two scenarios (-G) and (-M) were adopted from Louvet et al., 2016.

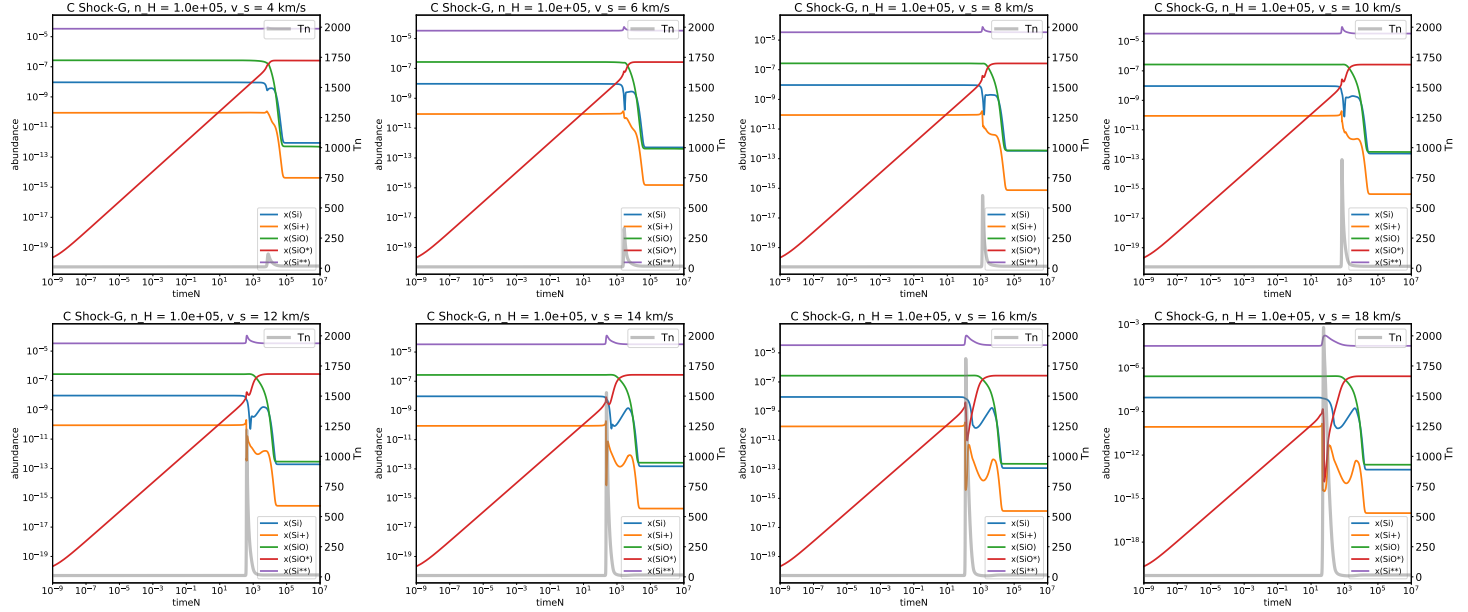


Figure E.1.: The abundance of Si, Si⁺, SiO, and SiO* as functions of time, calculated for $n_H = 10^5 \text{ cm}^{-3}$, where the fraction of preshock silicon in gas phase is 10% (or the (-G) scenario). Each panel corresponds to a shock velocity ranging from 4 km s^{-1} to 18 km s^{-1} with increments of 2 km s^{-1} .

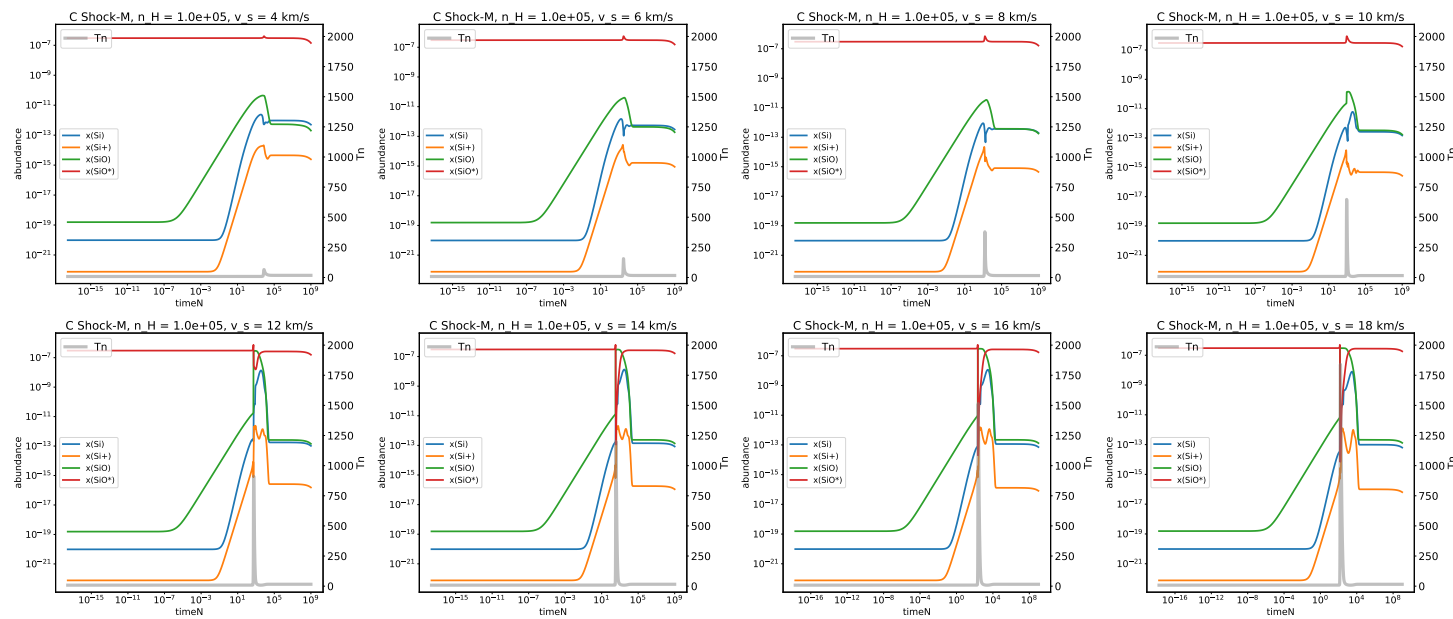


Figure E.2.: The abundance of Si, Si⁺, SiO, and SiO* as functions of time, calculated for $n_H = 10^5 \text{ cm}^{-3}$, where the fraction of preshock silicon in grain mantles is 10% (or the (-M) scenario). Each panel corresponds to a shock velocity ranging from 4 km s^{-1} to 18 km s^{-1} with increments of 2 km s^{-1} .

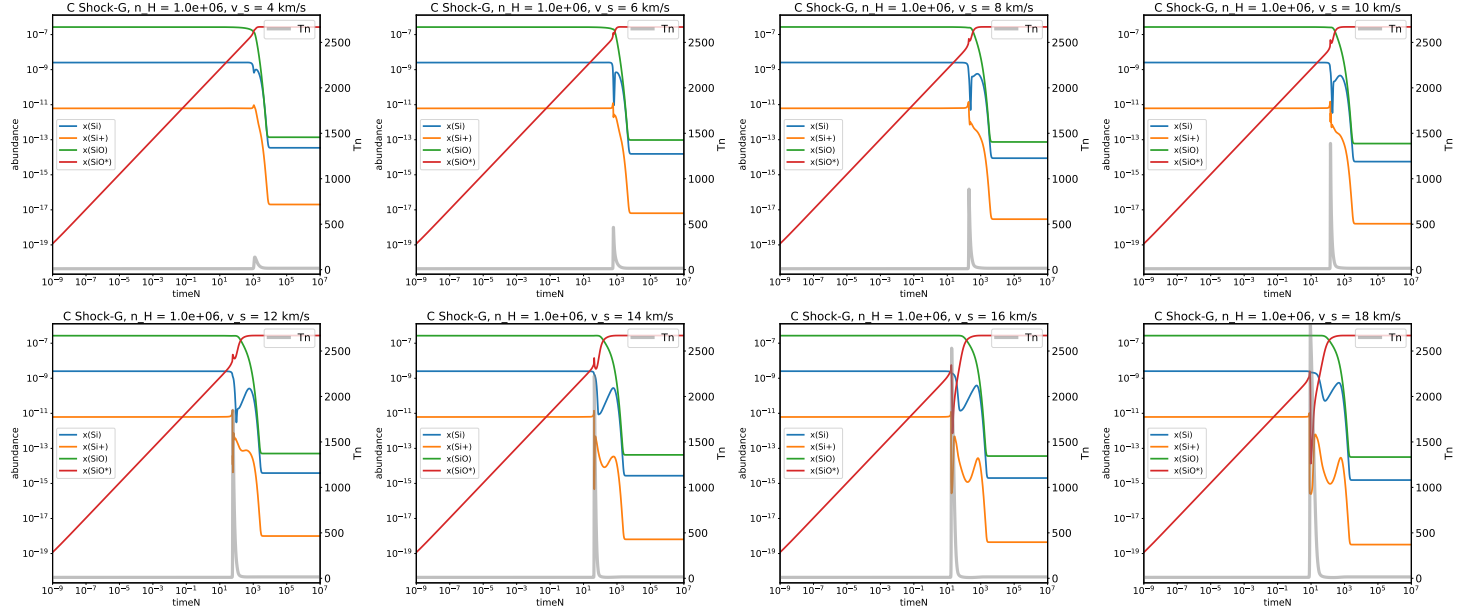


Figure E.3.: The abundance of Si, Si⁺, SiO, and SiO* as functions of time, calculated for $n_H = 10^6 \text{ cm}^{-3}$, where the fraction of preshock silicon in gas phase is 10% (or the (-G) scenario). Each panel corresponds to a shock velocity ranging from 4 km s^{-1} to 18 km s^{-1} with increments of 2 km s^{-1} .

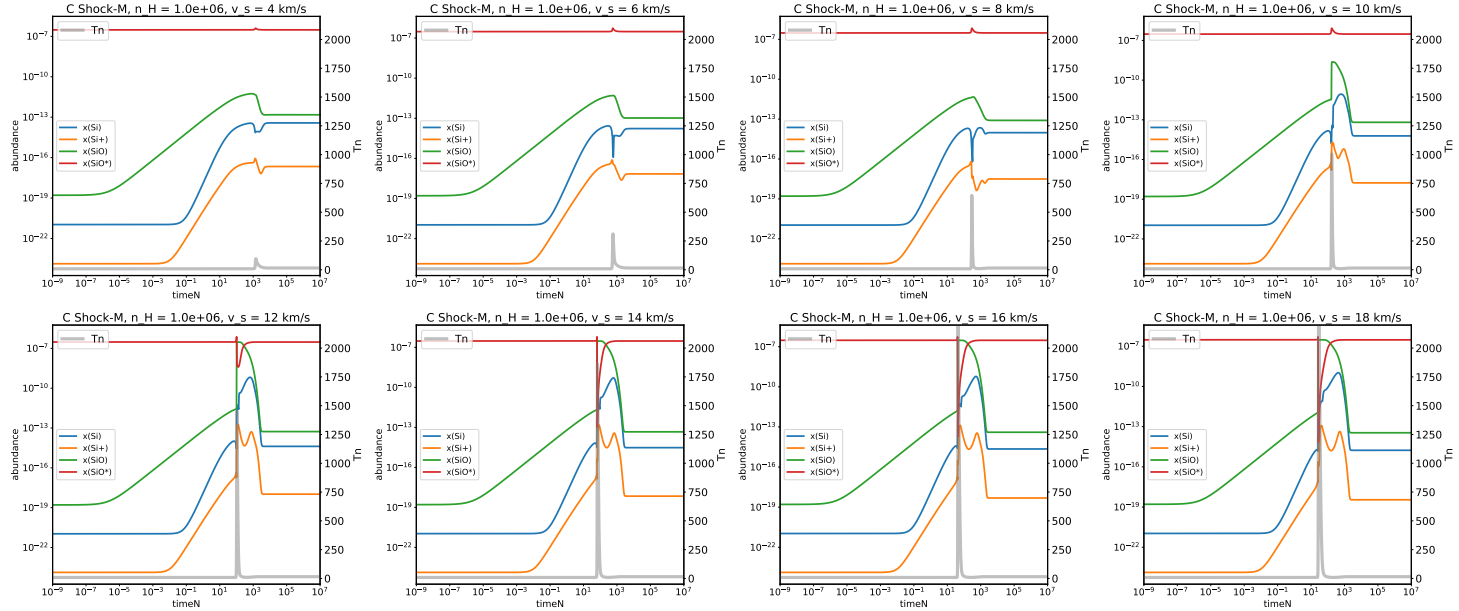


Figure E.4.: The abundances of Si, Si⁺, SiO, and SiO* as functions of time, calculated for $n_H = 10^6 \text{ cm}^{-3}$, where the fraction of preshock silicon in grain mantles is 10% (or the (-M) scenario). Each panel corresponds to a shock velocity ranging from 4 km s^{-1} to 18 km s^{-1} with increments of 2 km s^{-1} .

F

SUPPLEMENTARY FIGURES

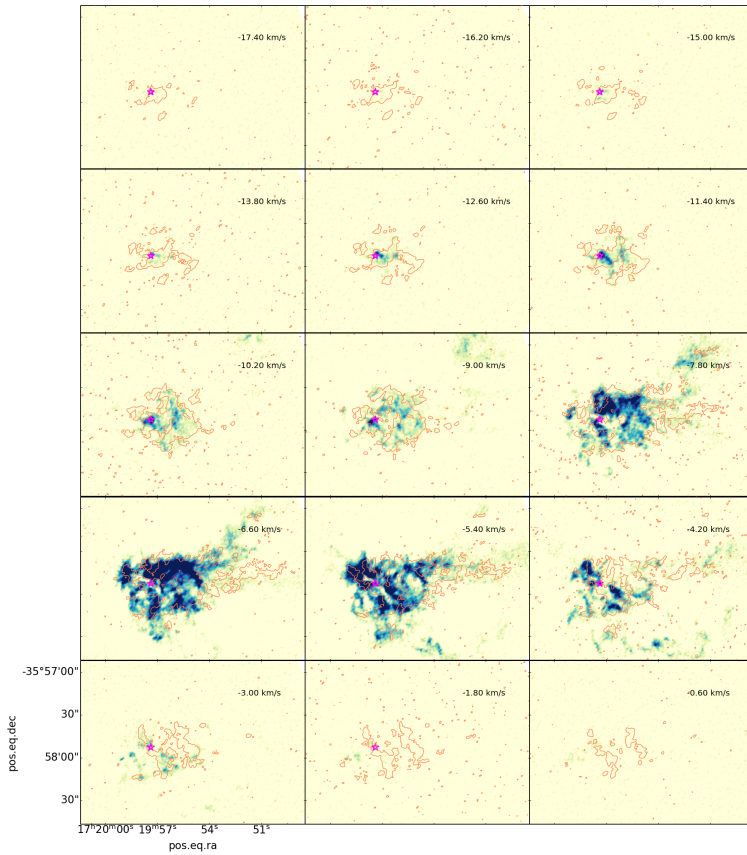
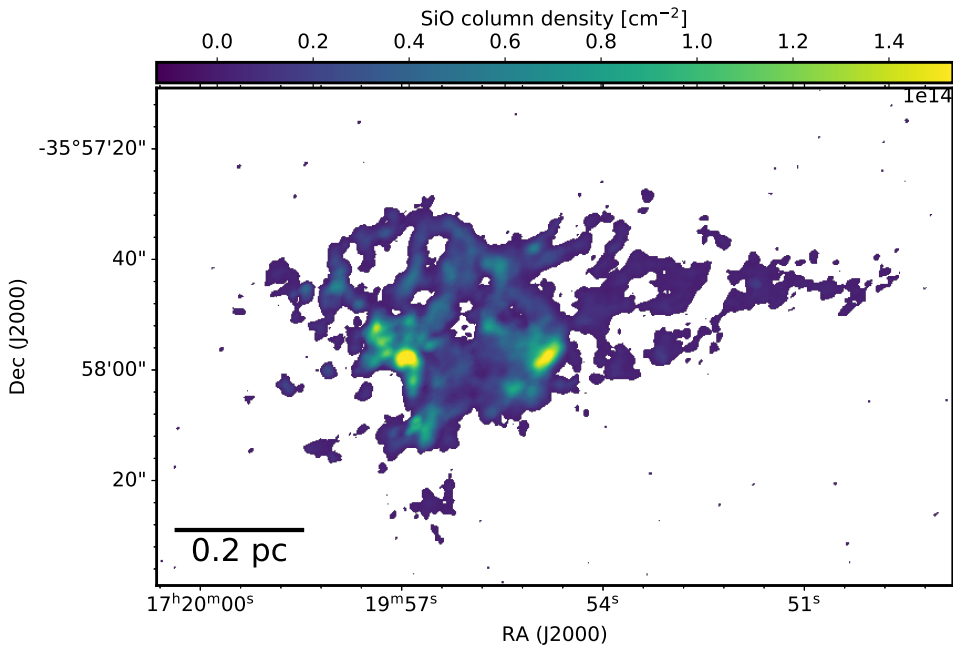
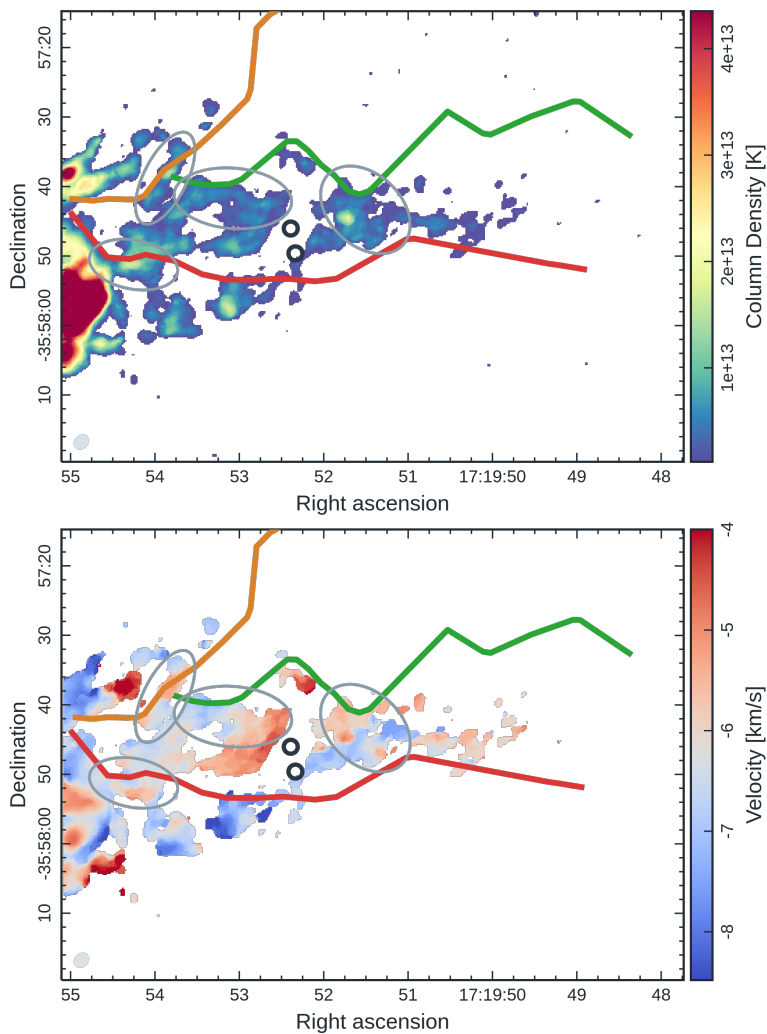


Figure F.1.: SiO velocity channel maps are in colour, and H¹³CO⁺ maps are indicated in orange contours. The purple star symbol marks a location of the hot core which is a source of the main outflow.



F

Figure F.2.: The column density map of SiO is based on the (2–1) transition. The column density is estimated by $N_{tot} = 1.8 \times 10^{12} \int T_{mb} dv [\text{cm}^{-2}]$ (Csengeri et al., 2016), where the constant coefficient is determined based on the excitation temperature, statistical weight, electrical dipole moment, and rest frequency. For detailed calculations, refer to Csengeri et al., 2016.



F

Figure F.3.: The column density map and moment one map of SiO are based on the (2–1) transition in region B. The 2-D KDE plot in figure 6.14 is produced based on the information derived from these two plots. Grey ellipses mark the position of velocity jumps in SiO velocity map and black circles represent the position of continuum cores.

LIST OF ABBREVIATIONS

- ACA** Atacama Compact Array
- ALMA** Atacama Large Millimeter/submillimeter Array
- APEX** Atacama Pathfinder EXperiment
- BTS** Behind The Spectrum
- CASA** Common Astronomical Software Application
- CNM** Cold Neutral Medium
- CMF** Core Mass Function
- DisPerSE** Discrete Persistent Structures Extractor
- EGOs** Extended Green Objects
- FWHM** Full Width at Half-Maximum
- GMCs** Giant Molecular Clouds
- GCs** Global Clusters
- HIM** Hot Ionised Medium
- KDE** Kernel Density Estimation
- ISM** Interstellar Medium
- IRAS** Infrared Astronomical Satellite
- IRDCs** Infrared dark clouds
- IMF** Initial Mass Function
- LTE** Local Thermodynamic Equilibrium

MSC Morse-Smale Complex
MCMC Markov chain Monte Carlo
MST Minimum Spanning Tree
OCs Open Clusters
PDSM ParisDurham shock model
PDRs Photodissociation Regions
SED Spectral Energy Distribution
SExtractor Source Extractors
TE Thermodynamic Equilibrium
WNM Warm Neutral Medium
WIM Warm Ionized Medium
YSOs Young stellar objects
ZAMS Zero Age Main Sequence

BIBLIOGRAPHY

- Allison, Richard J. et al. (Aug. 2009a). “Dynamical Mass Segregation on a Very Short Timescale”. In: *ApJ* 700.2, pp. L99–L103. DOI: 10.1088/0004-637X/700/2/L99. arXiv: 0906.4806 [astro-ph.GA].
- Allison, Richard J. et al. (May 2009b). “Using the minimum spanning tree to trace mass segregation”. In: *MNRAS* 395.3, pp. 1449–1454. DOI: 10.1111/j.1365-2966.2009.14508.x. arXiv: 0901.2047 [astro-ph.GA].
- Alves, J., M. Lombardi, and C. J. Lada (Jan. 2007). “The mass function of dense molecular cores and the origin of the IMF”. In: *A&A* 462.1, pp. L17–L21. DOI: 10.1051/0004-6361:20066389. arXiv: astro-ph/0612126 [astro-ph].
- André, Ph. (Jan. 2002). “The Initial Conditions for Protostellar Collapse: Observational Constraints”. In: *EAS Publications Series*. Ed. by Jerome Bouvier and Jean-Paul Zahn. Vol. 3. EAS Publications Series, pp. 1–38. DOI: 10.1051/eas:2002043.
- André, Ph. et al. (July 2010). “From filamentary clouds to prestellar cores to the stellar IMF: Initial highlights from the Herschel Gould Belt Survey”. In: *A&A* 518, L102, p. L102. DOI: 10.1051/0004-6361/201014666. arXiv: 1005.2618 [astro-ph.GA].
- André, Ph. et al. (July 2016). “Characterizing filaments in regions of high-mass star formation: High-resolution submillimeter imaging of the massive star-forming complex NGC 6334 with ArTéMiS”. In: *A&A* 592, A54, A54. DOI: 10.1051/0004-6361/201628378. arXiv: 1605.07434 [astro-ph.GA].
- Araya, Esteban et al. (Apr. 2005). “CH₃CN Observations toward Southern Massive Star-forming Regions”. In: *ApJS* 157.2, pp. 279–301. DOI: 10.1086/427187.
- Arzoumanian, D. et al. (Jan. 2019). “Characterizing the properties of nearby molecular filaments observed with Herschel”. In: *A&A* 621, A42, A42. DOI: 10.1051/0004-6361/201832725. arXiv: 1810.00721 [astro-ph.GA].
- Arzoumanian, D. et al. (Mar. 2021). “Dust polarized emission observations of NGC 6334. BISTRO reveals the details of the complex but organized magnetic field structure of the high-mass star-forming hub-filament network”. In: *A&A* 647,

- A78, A78. DOI: [10.1051/0004-6361/202038624](https://doi.org/10.1051/0004-6361/202038624). arXiv: 2012.13060 [astro-ph.GA].
- Arzoumanian, Doris et al. (Apr. 2022). "Velocity structure of the 50 pc long NGC 6334 filamentary cloud. Hints of multiple compressions and their impact on the cloud properties". In: *A&A* 660, A56, A56. DOI: [10.1051/0004-6361/202141699](https://doi.org/10.1051/0004-6361/202141699). arXiv: 2201.04267 [astro-ph.GA].
- Askne, J. et al. (Jan. 1984). "Methyl acetylene as a temperature probe in molecular clouds." In: *A&A* 130, pp. 311–318.
- Bally, John (Sept. 2016). "Protostellar Outflows". In: *ARA&A* 54, pp. 491–528. DOI: [10.1146/annurev-astro-081915-023341](https://doi.org/10.1146/annurev-astro-081915-023341).
- Bania, T. M. and J. G. Lyon (July 1980). "OB stars and the structure of the interstellar medium - Cloud formation and effects of different equations of state". In: *ApJ* 239, pp. 173–192. DOI: [10.1086/158099](https://doi.org/10.1086/158099).
- Barnes, A. T. et al. (Sept. 2020). "LEGO - II. A 3 mm molecular line study covering 100 pc of one of the most actively star-forming portions within the Milky Way disc". In: *MNRAS* 497.2, pp. 1972–2001. DOI: [10.1093/mnras/staa1814](https://doi.org/10.1093/mnras/staa1814). arXiv: 2007.11005 [astro-ph.GA].
- Bate, Matthew R., Ian A. Bonnell, and Volker Bromm (Mar. 2003). "The formation of a star cluster: predicting the properties of stars and brown dwarfs". In: *MNRAS* 339.3, pp. 577–599. DOI: [10.1046/j.1365-8711.2003.06210.x](https://doi.org/10.1046/j.1365-8711.2003.06210.x). arXiv: astro-ph/0212380 [astro-ph].
- Bergin, Edwin A. et al. (Aug. 1994). "CH 3C 2H as a Temperature Probe in Dense Giant Molecular Cloud Cores". In: *ApJ* 431, p. 674. DOI: [10.1086/174518](https://doi.org/10.1086/174518).
- Bertin, E. and S. Arnouts (June 1996). "SExtractor: Software for source extraction." In: *A&AS* 117, pp. 393–404. DOI: [10.1051/aas:1996164](https://doi.org/10.1051/aas:1996164).
- Bica, E. et al. (June 2003). "New infrared star clusters in the Northern and Equatorial Milky Way with 2MASS". In: *A&A* 404, pp. 223–232. DOI: [10.1051/0004-6361:20030486](https://doi.org/10.1051/0004-6361:20030486). arXiv: astro-ph/0304379 [astro-ph].
- Blandford, Roger and David Eichler (Oct. 1987). "Particle acceleration at astrophysical shocks: A theory of cosmic ray origin". In: *Phys. Rep.* 154.1, pp. 1–75. DOI: [10.1016/0370-1573\(87\)90134-7](https://doi.org/10.1016/0370-1573(87)90134-7).
- Blitz, L. and F. H. Shu (May 1980). "The origin and lifetime of giant molecular cloud complexes". In: *ApJ* 238, pp. 148–157. DOI: [10.1086/157968](https://doi.org/10.1086/157968).
- Blitz, Leo (Jan. 1993). "Giant Molecular Clouds". In: *Protostars and Planets III*. Ed. by Eugene H. Levy and Jonathan I. Lunine, p. 125.

- Bock, D. C. J., M. I. Large, and Elaine M. Sadler (Mar. 1999). "SUMSS: A Wide-Field Radio Imaging Survey of the Southern Sky. I. Science Goals, Survey Design, and Instrumentation". In: *AJ* 117.3, pp. 1578–1593. DOI: [10.1086/300786](https://doi.org/10.1086/300786). arXiv: [astro-ph/9812083](https://arxiv.org/abs/astro-ph/9812083) [astro-ph].
- Bonne, L. et al. (Sept. 2020). "Dense gas formation in the Musca filament due to the dissipation of a supersonic converging flow". In: *A&A* 641, A17, A17. DOI: [10.1051/0004-6361/201937104](https://doi.org/10.1051/0004-6361/201937104). arXiv: [2009.03083](https://arxiv.org/abs/2009.03083) [astro-ph.GA].
- Bonnell, Ian A. and Matthew R. Bate (July 2006). "Star formation through gravitational collapse and competitive accretion". In: *MNRAS* 370.1, pp. 488–494. DOI: [10.1111/j.1365-2966.2006.10495.x](https://doi.org/10.1111/j.1365-2966.2006.10495.x). arXiv: [astro-ph/0604615](https://arxiv.org/abs/astro-ph/0604615) [astro-ph].
- Bonnell, Ian A., Matthew R. Bate, and Stephen G. Vine (Aug. 2003). "The hierarchical formation of a stellar cluster". In: *MNRAS* 343.2, pp. 413–418. DOI: [10.1046/j.1365-8711.2003.06687.x](https://doi.org/10.1046/j.1365-8711.2003.06687.x). arXiv: [astro-ph/0305082](https://arxiv.org/abs/astro-ph/0305082) [astro-ph].
- Bonnell, Ian A. and Melvyn B. Davies (Apr. 1998a). "Mass segregation in young stellar clusters". In: *MNRAS* 295.3, pp. 691–698. DOI: [10.1046/j.1365-8711.1998.01372.x](https://doi.org/10.1046/j.1365-8711.1998.01372.x).
- (Apr. 1998b). "Mass segregation in young stellar clusters". In: *MNRAS* 295.3, pp. 691–698. DOI: [10.1046/j.1365-8711.1998.01372.x](https://doi.org/10.1046/j.1365-8711.1998.01372.x).
- Brooks, K. J. and J. B. Whiteoak (Feb. 2001). "Ground-state OH observations towards NGC 6334". In: *MNRAS* 320.4, pp. 465–476. DOI: [10.1046/j.1365-8711.2001.03964.x](https://doi.org/10.1046/j.1365-8711.2001.03964.x). arXiv: [astro-ph/0010399](https://arxiv.org/abs/astro-ph/0010399) [astro-ph].
- Burkert, Andreas and Lee Hartmann (Nov. 2004). "Collapse and Fragmentation in Finite Sheets". In: *ApJ* 616.1, pp. 288–300. DOI: [10.1086/424895](https://doi.org/10.1086/424895). arXiv: [astro-ph/0409680](https://arxiv.org/abs/astro-ph/0409680) [astro-ph].
- Busquet, G. et al. (Mar. 2019). "Unveiling a cluster of protostellar disks around the massive protostar GGD 27 MM1". In: *A&A* 623, L8, p. L8. DOI: [10.1051/0004-6361/201833687](https://doi.org/10.1051/0004-6361/201833687). arXiv: [1902.07581](https://arxiv.org/abs/1902.07581) [astro-ph.SR].
- Busquet, Gemma et al. (Feb. 2013). "Unveiling a Network of Parallel Filaments in the Infrared Dark Cloud G14.225-0.506". In: *ApJ* 764.2, L26, p. L26. DOI: [10.1088/2041-8205/764/2/L26](https://doi.org/10.1088/2041-8205/764/2/L26). arXiv: [1212.5917](https://arxiv.org/abs/1212.5917) [astro-ph.GA].
- Cartwright, Annabel and Anthony P. Whitworth (Feb. 2004). "The statistical analysis of star clusters". In: *MNRAS* 348.2, pp. 589–598. DOI: [10.1111/j.1365-2966.2004.07360.x](https://doi.org/10.1111/j.1365-2966.2004.07360.x). arXiv: [astro-ph/0403474](https://arxiv.org/abs/astro-ph/0403474) [astro-ph].
- Casoli, F. and F. Combes (June 1982). "Can giant molecular clouds form in spiral arms". In: *A&A* 110.2, pp. 287–294.

- Causi, A. G. Li et al. (July 2016). “Hi-fidelity multi-scale local processing for visually optimized far-infrared Herschel images”. In: *SPIE* 9904. DOI: [10.1117/12.2233241](https://doi.org/10.1117/12.2233241).
- Chambers, E. T. et al. (Apr. 2009). “Star Formation Activity of Cores within Infrared Dark Clouds”. In: *ApJS* 181.2, pp. 360–390. DOI: [10.1088/0067-0049/181/2/360](https://doi.org/10.1088/0067-0049/181/2/360).
- Chandrasekhar, S. (Dec. 1951). “The Gravitational Instability of an Infinite Homogeneous Turbulent Medium”. In: *Proceedings of the Royal Society of London Series A* 210.1100, pp. 26–29. DOI: [10.1098/rspa.1951.0228](https://doi.org/10.1098/rspa.1951.0228).
- Chandrasekhar, Subrahmanyan (1942). *Principles of stellar dynamics*.
– (1960). *Radiative transfer*.
- Chen, H. et al. (May 1995). “Bolometric Temperature and Young Stars in the Taurus and Ophiuchus Complexes”. In: *ApJ* 445, p. 377. DOI: [10.1086/175703](https://doi.org/10.1086/175703).
- Chen, Xi et al. (May 2013). “Newly Identified Extended Green Objects (EGOs) from the Spitzer GLIMPSE II Survey. I. Catalog”. In: *ApJS* 206.1, 9, p. 9. DOI: [10.1088/0067-0049/206/1/9](https://doi.org/10.1088/0067-0049/206/1/9).
- Cheung, L. et al. (Dec. 1978). “1.0 millimeter continuum map of cool sources in the NGC 6334 complex.” In: *ApJ* 226, pp. L149–L152. DOI: [10.1086/182852](https://doi.org/10.1086/182852).
- Clarke, S. D. et al. (June 2017). “Filamentary fragmentation in a turbulent medium”. In: *MNRAS* 468.2, pp. 2489–2505. DOI: [10.1093/mnras/stx637](https://doi.org/10.1093/mnras/stx637). arXiv: 1703.04473 [astro-ph.GA].
- Clarke, S. D. et al. (Sept. 2018a). “Synthetic C¹⁸O observations of fibrous filaments: the problems of mapping from PPV to PPP”. In: *MNRAS* 479.2, pp. 1722–1746. DOI: [10.1093/mnras/sty1675](https://doi.org/10.1093/mnras/sty1675). arXiv: 1806.08564 [astro-ph.GA].
- (Sept. 2018b). “Synthetic C¹⁸O observations of fibrous filaments: the problems of mapping from PPV to PPP”. In: *MNRAS* 479.2, pp. 1722–1746. DOI: [10.1093/mnras/sty1675](https://doi.org/10.1093/mnras/sty1675). arXiv: 1806.08564 [astro-ph.GA].
- Cortés, Paulo C. et al. (Dec. 2021). “Magnetic Fields in Massive Star-forming Regions (MagMaR). II. Tomography through Dust and Molecular Line Polarization in NGC 6334I(N)”. In: *ApJ* 923.2, 204, p. 204. DOI: [10.3847/1538-4357/ac28a1](https://doi.org/10.3847/1538-4357/ac28a1). arXiv: 2109.09270 [astro-ph.GA].
- Cosentino, G. et al. (Mar. 2018). “Widespread SiO and CH₃OH emission in filamentary infrared dark clouds”. In: *MNRAS* 474.3, pp. 3760–3781. DOI: [10.1093/mnras/stx3013](https://doi.org/10.1093/mnras/stx3013). arXiv: 1711.09679 [astro-ph.GA].
- Crutcher, Richard M. (Sept. 2012). “Magnetic Fields in Molecular Clouds”. In: *ARA&A* 50, pp. 29–63. DOI: [10.1146/annurev-astro-081811-125514](https://doi.org/10.1146/annurev-astro-081811-125514).

- Csengeri, T. et al. (Feb. 2016). "ATLASGAL-selected massive clumps in the inner Galaxy. II. Characterisation of different evolutionary stages and their SiO emission". In: *A&A* 586, A149, A149. DOI: [10.1051/0004-6361/201425404](https://doi.org/10.1051/0004-6361/201425404). arXiv: [1511.05138](https://arxiv.org/abs/1511.05138) [astro-ph.GA].
- Cuadrado, S. et al. (Mar. 2015). "The chemistry and spatial distribution of small hydrocarbons in UV-irradiated molecular clouds: the Orion Bar PDR". In: *A&A* 575, A82, A82. DOI: [10.1051/0004-6361/201424568](https://doi.org/10.1051/0004-6361/201424568). arXiv: [1412.0417](https://arxiv.org/abs/1412.0417) [astro-ph.GA].
- Cyganowski, C. J. et al. (Dec. 2008). "A Catalog of Extended Green Objects in the GLIMPSE Survey: A New Sample of Massive Young Stellar Object Outflow Candidates". In: *AJ* 136.6, pp. 2391–2412. DOI: [10.1088/0004-6256/136/6/2391](https://doi.org/10.1088/0004-6256/136/6/2391). arXiv: [0810.0530](https://arxiv.org/abs/0810.0530) [astro-ph].
- De Buizer, James M. and William D. Vacca (July 2010). "Direct Spectroscopic Identification of the Origin of "Green Fuzzy" Emission in Star-forming Regions". In: *AJ* 140.1, pp. 196–202. DOI: [10.1088/0004-6256/140/1/196](https://doi.org/10.1088/0004-6256/140/1/196). arXiv: [1005.2209](https://arxiv.org/abs/1005.2209) [astro-ph.SR].
- Deharveng, L. et al. (Oct. 2015). "Bipolar H II regions - Morphology and star formation in their vicinity. I. G319.88+00.79 and G010.32-00.15". In: *A&A* 582, A1, A1. DOI: [10.1051/0004-6361/201423835](https://doi.org/10.1051/0004-6361/201423835). arXiv: [1507.00215](https://arxiv.org/abs/1507.00215) [astro-ph.GA].
- Dobbs, C. L. (Dec. 2008). "GMC formation by agglomeration and self gravity". In: *MNRAS* 391.2, pp. 844–858. DOI: [10.1111/j.1365-2966.2008.13939.x](https://doi.org/10.1111/j.1365-2966.2008.13939.x). arXiv: [0809.1942](https://arxiv.org/abs/0809.1942) [astro-ph].
- Dobbs, C. L. et al. (Jan. 2014). "Formation of Molecular Clouds and Global Conditions for Star Formation". In: *Protostars and Planets VI*. Ed. by Henrik Beuther et al., p. 3. DOI: [10.2458/azu_uapress_9780816531240-ch001](https://doi.org/10.2458/azu_uapress_9780816531240-ch001). arXiv: [1312.3223](https://arxiv.org/abs/1312.3223) [astro-ph.GA].
- Dopita, M. A., D. S. Mathewson, and V. L. Ford (May 1977). "Optical emission from shock waves. III. Abundances in supernova remnants." In: *ApJ* 214, pp. 179–188. DOI: [10.1086/155242](https://doi.org/10.1086/155242).
- Draine, B. T. (Apr. 1978). "Photoelectric heating of interstellar gas." In: *ApJS* 36, pp. 595–619. DOI: [10.1086/190513](https://doi.org/10.1086/190513).
- (Jan. 1994). "Dust in Diffuse Interstellar Clouds". In: *The First Symposium on the Infrared Cirrus and Diffuse Interstellar Clouds*. Ed. by Roc M. Cutri and William B. Latter. Vol. 58. Astronomical Society of the Pacific Conference Series, p. 227.
- Draine, Bruce T. (2011). *Physics of the Interstellar and Intergalactic Medium*. Princeton University Press.

- Draine, Bruce T. and Christopher F. McKee (Jan. 1993). “Theory of interstellar shocks.” In: *ARA&A* 31, pp. 373–432. DOI: [10.1146/annurev.aa.31.090193.002105](https://doi.org/10.1146/annurev.aa.31.090193.002105).
- Duarte-Cabral, A. et al. (Oct. 2014). “SiO emission from low- and high-velocity shocks in Cygnus-X massive dense clumps”. In: *A&A* 570, A1, A1. DOI: [10.1051/0004-6361/201423677](https://doi.org/10.1051/0004-6361/201423677). arXiv: 1407.6400 [astro-ph.GA].
- Duarte-Cabral, Ana and C. L. Dobbs (Oct. 2017). “The evolution of giant molecular filaments”. In: *MNRAS* 470.4, pp. 4261–4273. DOI: [10.1093/mnras/stx1524](https://doi.org/10.1093/mnras/stx1524). arXiv: 1706.05421 [astro-ph.GA].
- Edelsbrunner, H., D. Letscher, and A. Zomorodian (2000). “Topological persistence and simplification”. In: *Proceedings 41st Annual Symposium on Foundations of Computer Science*, pp. 454–463. DOI: [10.1109/SFCS.2000.892133](https://doi.org/10.1109/SFCS.2000.892133).
- Federrath, Christoph (Mar. 2016). “On the universality of interstellar filaments: theory meets simulations and observations”. In: *MNRAS* 457.1, pp. 375–388. DOI: [10.1093/mnras/stv2880](https://doi.org/10.1093/mnras/stv2880). arXiv: 1510.05654 [astro-ph.SR].
- Feigelson, Eric D. et al. (July 2009). “Stellar Clusters in the NGC 6334 Star-Forming Complex”. In: *AJ* 138.1, pp. 227–239. DOI: [10.1088/0004-6256/138/1/227](https://doi.org/10.1088/0004-6256/138/1/227). arXiv: 0905.0716 [astro-ph.GA].
- Ferrière, Katia M. (Oct. 2001). “The interstellar environment of our galaxy”. In: *Reviews of Modern Physics* 73.4, pp. 1031–1066. DOI: [10.1103/RevModPhys.73.1031](https://doi.org/10.1103/RevModPhys.73.1031). arXiv: astro-ph/0106359 [astro-ph].
- Field, G. B., D. W. Goldsmith, and H. J. Habing (June 1969). “A Theoretical Model for the Interstellar Medium”. In: *Bulletin of the American Astronomical Society*. Vol. 1, p. 240.
- Fischer, J. et al. (July 1982). “Near-infrared observations of the far-infrared source V region in NGC 6334.” In: *ApJ* 258, pp. 165–169. DOI: [10.1086/160064](https://doi.org/10.1086/160064).
- Flower, D. R. and G. Pineau des Forêts (Aug. 2003). “The influence of grains on the propagation and structure of C-type shock waves in interstellar molecular clouds”. In: *MNRAS* 343.2, pp. 390–400. DOI: [10.1046/j.1365-8711.2003.06716.x](https://doi.org/10.1046/j.1365-8711.2003.06716.x).
- (June 2015). “Interpreting observations of molecular outflow sources: the MHD shock code mhd_vode”. In: *A&A* 578, A63, A63. DOI: [10.1051/0004-6361/201525740](https://doi.org/10.1051/0004-6361/201525740).
- Forman, Robin (2002). “Discrete Morse Theory and the Cohomology Ring”. In: *Transactions of the American Mathematical Society* 354.12, pp. 5063–5085. ISSN: 00029947. URL: <http://www.jstor.org/stable/3072980> (visited on 06/12/2023).

- Forster, J. R. and J. L. Caswell (Apr. 1989). "The spatial relationship of OH and H₂O masers." In: *A&A* 213, pp. 339–350.
- Fukuda, Naoya and Tomoyuki Hanawa (Apr. 2000). "Sequential Star Formation Triggered by Expansion of an H II Region". In: *ApJ* 533.2, pp. 911–923. DOI: 10.1086/308701.
- Gezari, D. Y. (Aug. 1982). "The remarkable 400micron source NGC 6334/I(North)." In: *ApJ* 259, pp. L29–L33. DOI: 10.1086/183842.
- Godard, B. et al. (Feb. 2019). "Models of irradiated molecular shocks". In: *A&A* 622, A100, A100. DOI: 10.1051/0004-6361/201834248. arXiv: 1901.04273 [astro-ph.GA].
- Gómez, Gilberto C. and Enrique Vázquez-Semadeni (Aug. 2014). "Filaments in Simulations of Molecular Cloud Formation". In: *ApJ* 791.2, 124, p. 124. DOI: 10.1088/0004-637X/791/2/124. arXiv: 1308.6298 [astro-ph.GA].
- Gouliermis, Dimitrios A. (July 2018). "Unbound Young Stellar Systems: Star Formation on the Loose". In: *PASP* 130.989, p. 072001. DOI: 10.1088/1538-3873/aac1fd. arXiv: 1806.11541 [astro-ph.GA].
- Guillet, V., G. Pineau Des Forêts, and A. P. Jones (Dec. 2007). "Shocks in dense clouds. I. Dust dynamics". In: *A&A* 476.1, pp. 263–277. DOI: 10.1051/0004-6361:20078094.
- Gusdorf, A. et al. (May 2008). "SiO line emission from C-type shock waves: interstellar jets and outflows". In: *A&A* 482.3, pp. 809–829. DOI: 10.1051/0004-6361:20078900. arXiv: 0803.2791 [astro-ph].
- Gusdorf, A. et al. (Mar. 2015). "Impacts of pure shocks in the BHR71 bipolar outflow". In: *A&A* 575, A98, A98. DOI: 10.1051/0004-6361/201425142. arXiv: 1502.00488 [astro-ph.GA].
- Gusdorf, Antoine (Nov. 2008). "Molecular emission in regions of star formation". PhD thesis. Durham University, UK.
- Hacar, A., M. Tafalla, and J. Alves (Oct. 2017). "Fibers in the NGC 1333 proto-cluster". In: *A&A* 606, A123, A123. DOI: 10.1051/0004-6361/201630348. arXiv: 1703.07029 [astro-ph.GA].
- Hacar, A. et al. (June 2013). "Cores, filaments, and bundles: hierarchical core formation in the L1495/B213 Taurus region". In: *A&A* 554, A55, A55. DOI: 10.1051/0004-6361/201220090. arXiv: 1303.2118 [astro-ph.GA].
- Hacar, A. et al. (Mar. 2022). "Initial Conditions for Star Formation: A Physical Description of the Filamentary ISM". In: *arXiv e-prints*, arXiv: 2203.09562, arXiv: 2203.09562. arXiv: 2203.09562 [astro-ph.GA].

- Haffner, L. M. et al. (July 2009). "The warm ionized medium in spiral galaxies". In: *Reviews of Modern Physics* 81.3, pp. 969–997. DOI: 10.1103/RevModPhys.81.969. arXiv: 0901.0941 [astro-ph.GA].
- Harvey, P. M. and I. Gatley (June 1983). "Infrared observations of OB star formation in NGC 6334." In: *ApJ* 269, pp. 613–624. DOI: 10.1086/161068.
- Harvey, P. M., B. A. Wilking, and M. Joy (Mar. 1984). "Infrared observations of dust cloud structure in young R associations : NGC 1333, S 68 and NGC 7129." In: *ApJ* 278, pp. 156–169. DOI: 10.1086/161777.
- Hashimoto, Jun et al. (Feb. 2007). "Subarcsecond Near-Infrared Images of Massive Star Formation Region NGC 6334V". In: *PASJ* 59, pp. 221–225. DOI: 10.1093/pasj/59.1.221. arXiv: astro-ph/0612522 [astro-ph].
- Hennebelle, Patrick (Aug. 2013). "On the origin of non-self-gravitating filaments in the ISM". In: *A&A* 556, A153, A153. DOI: 10.1051/0004-6361/201321292. arXiv: 1306.5452 [astro-ph.GA].
- Hildebrand, R. H. (Sept. 1983). "The determination of cloud masses and dust characteristics from submillimetre thermal emission." In: *QJRAS* 24, pp. 267–282.
- Hillenbrand, Lynne A. and Lee W. Hartmann (Jan. 1998). "A Preliminary Study of the Orion Nebula Cluster Structure and Dynamics". In: *ApJ* 492.2, pp. 540–553. DOI: 10.1086/305076.
- Inoue, Tsuyoshi and Yasuo Fukui (Sept. 2013). "Formation of Massive Molecular Cloud Cores by Cloud-Cloud Collision". In: *ApJ* 774.2, L31, p. L31. DOI: 10.1088/2041-8205/774/2/L31. arXiv: 1305.4655 [astro-ph.GA].
- Jiménez-Serra, I. et al. (Mar. 2004). "Tracing the Shock Precursors in the L1448-mm/IRS 3 Outflows". In: *ApJ* 603.1, pp. L49–L52. DOI: 10.1086/382784. arXiv: astro-ph/0401390 [astro-ph].
- Jiménez-Serra, I. et al. (July 2010). "Parsec-scale SiO emission in an infrared dark cloud". In: *mnras* 406, pp. 187–196. DOI: 10.1111/j.1365-2966.2010.16698.x. arXiv: 1003.3463.
- Juárez, C. et al. (July 2017a). "Magnetized Converging Flows toward the Hot Core in the Intermediate/High-mass Star-forming Region NGC 6334 V". In: *apj* 844, 44, p. 44. DOI: 10.3847/1538-4357/aa78a6. arXiv: 1706.03534 [astro-ph.SR].
- Juárez, Carmen et al. (July 2017b). "Magnetized Converging Flows toward the Hot Core in the Intermediate/High-mass Star-forming Region NGC 6334 V". In: *ApJ* 844.1, 44, p. 44. DOI: 10.3847/1538-4357/aa78a6. arXiv: 1706.03534 [astro-ph.SR].

- Kahn, F. D. (Dec. 1974). "Cocoons around early-type stars." In: *A&A* 37, pp. 149–162.
- Keto, Eric (Sept. 2007). "The Formation of Massive Stars: Accretion, Disks, and the Development of Hypercompact H II Regions". In: *ApJ* 666.2, pp. 976–981. DOI: [10.1086/520320](https://doi.org/10.1086/520320). arXiv: [astro-ph/0603856](https://arxiv.org/abs/astro-ph/0603856) [astro-ph].
- Kim, W. J. et al. (Dec. 2020). "ATLASGAL-selected massive clumps in the inner Galaxy. VIII. Chemistry of photodissociation regions". In: *A&A* 644, A160, A160. DOI: [10.1051/0004-6361/202039059](https://doi.org/10.1051/0004-6361/202039059). arXiv: [2009.14238](https://arxiv.org/abs/2009.14238) [astro-ph.GA].
- Kim, Woong-Tae (Jan. 2002). "Structure formation in disk galaxies via gravitational instability". PhD thesis. University of Maryland, College Park.
- Kirk, Helen et al. (Apr. 2013). "Filamentary Accretion Flows in the Embedded Serpens South Protocluster". In: *ApJ* 766.2, 115, p. 115. DOI: [10.1088/0004-637X/766/2/115](https://doi.org/10.1088/0004-637X/766/2/115). arXiv: [1301.6792](https://arxiv.org/abs/1301.6792) [astro-ph.GA].
- Klessen, Ralf S., Andreas Burkert, and Matthew R. Bate (July 1998). "Fragmentation of Molecular Clouds: The Initial Phase of a Stellar Cluster". In: *ApJ* 501.2, pp. L205–L208. DOI: [10.1086/311471](https://doi.org/10.1086/311471). arXiv: [astro-ph/9805125](https://arxiv.org/abs/astro-ph/9805125) [astro-ph].
- Klessen, Ralf S. and Simon C. O. Glover (Jan. 2016). "Physical Processes in the Interstellar Medium". In: *Saas-Fee Advanced Course* 43, p. 85. DOI: [10.1007/978-3-662-47890-5_2](https://doi.org/10.1007/978-3-662-47890-5_2). arXiv: [1412.5182](https://arxiv.org/abs/1412.5182) [astro-ph.GA].
- Könyves, V. et al. (Dec. 2015). "A census of dense cores in the Aquila cloud complex: SPIRE/PACS observations from the Herschel Gould Belt survey". In: *A&A* 584, A91, A91. DOI: [10.1051/0004-6361/201525861](https://doi.org/10.1051/0004-6361/201525861). arXiv: [1507.05926](https://arxiv.org/abs/1507.05926) [astro-ph.GA].
- Kraemer, Kathleen E. and James M. Jackson (Jan. 1995). "Shock-excited NH₃ (3,3) Masers in the NGC 6334 Star-forming Region". In: *ApJ* 439, p. L9. DOI: [10.1086/187732](https://doi.org/10.1086/187732).
- Kraemer, Kathleen E. et al. (May 1999). "The Mid-Infrared Properties of Three Star-forming Sites in NGC 6334". In: *ApJ* 516.2, pp. 817–833. DOI: [10.1086/307149](https://doi.org/10.1086/307149).
- Krause, Martin G. H. et al. (June 2020). "The Physics of Star Cluster Formation and Evolution". In: *Space Sci. Rev.* 216.4, 64, p. 64. DOI: [10.1007/s11214-020-00689-4](https://doi.org/10.1007/s11214-020-00689-4). arXiv: [2005.00801](https://arxiv.org/abs/2005.00801) [astro-ph.GA].
- Kroupa, P. (Jan. 2001). "The Local Stellar Initial Mass Function". In: *Dynamics of Star Clusters and the Milky Way*. Ed. by S. Deiters et al. Vol. 228. Astronomical Society of the Pacific Conference Series, p. 187. DOI: [10.48550/arXiv.astro-ph/0011328](https://doi.org/10.48550/arXiv.astro-ph/0011328). arXiv: [astro-ph/0011328](https://arxiv.org/abs/astro-ph/0011328) [astro-ph].

- Krumholz, Mark R. (Nov. 2015). "Notes on Star Formation". In: *arXiv e-prints*, arXiv: 1511.03457, arXiv: 1511.03457. arXiv: 1511.03457 [astro-ph.GA].
- Kruskal Jr., Joseph B. (1956). "On the shortest spanning subtree of a graph and the traveling salesman problem". In: *Proc. Amer. Math. Soc.* 7, pp. 48–50. ISSN: 0002-9939. DOI: 10.2307/2033241. URL: <https://doi.org/10.2307/2033241>.
- Kumar, M. S. N. et al. (Oct. 2020). "Unifying low- and high-mass star formation through density-amplified hubs of filaments. The highest mass stars ($>100 M_{\odot}$) form only in hubs". In: *A&A* 642, A87, A87. DOI: 10.1051/0004-6361/202038232. arXiv: 2008.00295 [astro-ph.GA].
- Lada, Charles J. and Elizabeth A. Lada (Jan. 2003). "Embedded Clusters in Molecular Clouds". In: *ARA&A* 41, pp. 57–115. DOI: 10.1146/annurev.astro.41.011802.094844. arXiv: astro-ph/0301540 [astro-ph].
- Langer, William D. and A. E. Glassgold (Mar. 1990). "Silicon Chemistry in Interstellar Clouds". In: *ApJ* 352, p. 123. DOI: 10.1086/168519.
- Larson, R. B. (Jan. 1984). "Gravitational torques and star formation". In: *MNRAS* 206, pp. 197–207. DOI: 10.1093/mnras/206.1.197.
- Larson, R. B. and S. Starrfield (July 1971). "On the formation of massive stars and the upper limit of stellar masses." In: *A&A* 13, p. 190.
- Lee, Yueh-Ning and Patrick Hennebelle (Apr. 2018). "Stellar mass spectrum within massive collapsing clumps. II. Thermodynamics and tidal forces of the first Larson core. A robust mechanism for the peak of the IMF". In: *A&A* 611, A89, A89. DOI: 10.1051/0004-6361/201731523. arXiv: 1711.00319 [astro-ph.GA].
- Lefloch, B. et al. (Sept. 1998). "Widespread SiO Emission in NGC 1333". In: *ApJ* 504.2, pp. L109–L112. DOI: 10.1086/311581.
- Lesaffre, P. et al. (Feb. 2013). "Low-velocity shocks: signatures of turbulent dissipation in diffuse irradiated gas". In: *A&A* 550, A106, A106. DOI: 10.1051/0004-6361/201219928. arXiv: 1301.7598 [astro-ph.GA].
- Li, Hua-Bai et al. (Apr. 2015). "Self-similar fragmentation regulated by magnetic fields in a region forming massive stars". In: *Nature* 520.7548, pp. 518–521. DOI: 10.1038/nature14291. arXiv: 1510.07094 [astro-ph.GA].
- Lin, C. C., L. Mestel, and F. H. Shu (Nov. 1965). "The Gravitational Collapse of a Uniform Spheroid." In: *ApJ* 142, p. 1431. DOI: 10.1086/148428.
- Lis, D. C. et al. (May 1998). "Submillimeter Continuum Imaging of the Orion A Molecular Cloud with SHARC". In: *American Astronomical Society Meeting Abstracts #192*. Vol. 192. American Astronomical Society Meeting Abstracts, 10.11, p. 10.11.

- Liu, Hauyu Baobab et al. (May 2015). "ALMA Resolves the Spiraling Accretion Flow in the Luminous OB Cluster-forming Region G33.92+0.11". In: *ApJ* 804.1, 37, p. 37. DOI: [10.1088/0004-637X/804/1/37](https://doi.org/10.1088/0004-637X/804/1/37). arXiv: [1505.04255](https://arxiv.org/abs/1505.04255) [astro-ph.SR].
- Liu, Junhao et al. (Oct. 2022). "Multi-scale physical properties of NGC 6334 as revealed by local relative orientations between magnetic fields, density gradients, velocity gradients, and gravity". In: *arXiv e-prints*, arXiv:2211.00152, arXiv:2211.00152. DOI: [10.48550/arXiv.2211.00152](https://doi.org/10.48550/arXiv.2211.00152). arXiv: [2211.00152](https://arxiv.org/abs/2211.00152) [astro-ph.GA].
- Liu, Junhao et al. (May 2023). "Deviation from a Continuous and Universal Turbulence Cascade in NGC 6334 due to Massive Star Formation Activity". In: *ApJ* 949.1, 30, p. 30. DOI: [10.3847/1538-4357/acc4c0](https://doi.org/10.3847/1538-4357/acc4c0). arXiv: [2303.08170](https://arxiv.org/abs/2303.08170) [astro-ph.GA].
- Louvet, F. et al. (Nov. 2016). "Tracing extended low-velocity shocks through SiO emission. Case study of the W43-MM1 ridge". In: *A&A* 595, A122, A122. DOI: [10.1051/0004-6361/201629077](https://doi.org/10.1051/0004-6361/201629077). arXiv: [1607.08668](https://arxiv.org/abs/1607.08668) [astro-ph.GA].
- Mac Low, Mordecai-Mark (Oct. 1999). "The Energy Dissipation Rate of Supersonic, Magnetohydrodynamic Turbulence in Molecular Clouds". In: *ApJ* 524.1, pp. 169–178. DOI: [10.1086/307784](https://doi.org/10.1086/307784). arXiv: [astro-ph/9809177](https://arxiv.org/abs/astro-ph/9809177) [astro-ph].
- Marr, J.M., R.L. Snell, and S.E. Kurtz (2015). *Fundamentals of Radio Astronomy: Observational Methods*. Series in Astronomy and Astrophysics. CRC Press. ISBN: 9781498770194. URL: <https://books.google.de/books?id=T54oCwAAQBAJ>.
- Marsh, K. A. et al. (June 2016). "A census of dense cores in the Taurus L1495 cloud from the Herschel". In: *MNRAS* 459.1, pp. 342–356. DOI: [10.1093/mnras/stw301](https://doi.org/10.1093/mnras/stw301). arXiv: [1602.03143](https://arxiv.org/abs/1602.03143) [astro-ph.GA].
- Martin-Pintado, J., R. Bachiller, and A. Fuente (Feb. 1992). "SiO emission as a tracer of shocked gas in molecular outflows." In: *A&A* 254, pp. 315–326.
- McBreen, B. et al. (Sept. 1979). "Evidence for a variable far-infrared source in NGC 6334." In: *ApJ* 232, pp. L183–L187. DOI: [10.1086/183061](https://doi.org/10.1086/183061).
- McCray, Richard and Minas Kafatos (June 1987). "Supershells and Propagating Star Formation". In: *ApJ* 317, p. 190. DOI: [10.1086/165267](https://doi.org/10.1086/165267).
- McKee, C. F. and J. P. Ostriker (Nov. 1977). "A theory of the interstellar medium: three components regulated by supernova explosions in an inhomogeneous substrate." In: *ApJ* 218, pp. 148–169. DOI: [10.1086/155667](https://doi.org/10.1086/155667).
- McKee, Christopher F. and Eve C. Ostriker (Sept. 2007). "Theory of Star Formation". In: *ARA&A* 45.1, pp. 565–687. DOI: [10.1146/annurev.astro.45.051806.110602](https://doi.org/10.1146/annurev.astro.45.051806.110602). arXiv: [0707.3514](https://arxiv.org/abs/0707.3514) [astro-ph].

- McKee, Christopher F. and Jonathan C. Tan (Mar. 2002). “Massive star formation in 100,000 years from turbulent and pressurized molecular clouds”. In: *Nature* 416.6876, pp. 59–61. DOI: 10.1038/416059a. arXiv: astro-ph/0203071 [astro-ph].
- Meier, David S. and Jean L. Turner (Jan. 2005). “Spatially Resolved Chemistry in Nearby Galaxies. I. The Center of IC 342”. In: *ApJ* 618.1, pp. 259–280. DOI: 10.1086/426499. arXiv: astro-ph/0410039 [astro-ph].
- Meyer, J. P. (Aug. 1985). “Galactic cosmic ray composition”. In: *19th International Cosmic Ray Conference (ICRC19), Volume 9*. Vol. 9. International Cosmic Ray Conference, p. 141.
- Milnor, John (1963). *Morse Theory. (AM-51), Volume 51*. Princeton: Princeton University Press. ISBN: 9781400881802. DOI: doi:10.1515/9781400881802. URL: <https://doi.org/10.1515/9781400881802>.
- Miyama, S. M., S. Narita, and C. Hayashi (Dec. 1987). “Fragmentation of Isothermal Sheet-Like Clouds. II —Full Nonlinear Numerical Simulations—”. In: *Progress of Theoretical Physics* 78.6, pp. 1273–1287. DOI: 10.1143/PTP.78.1273.
- Moeckel, Nickolas and Ian A. Bonnell (July 2009). “Limits on initial mass segregation in young clusters”. In: *MNRAS* 396.4, pp. 1864–1874. DOI: 10.1111/j.1365-2966.2009.14813.x. arXiv: 0903.3893 [astro-ph.SR].
- Möller, T., C. Endres, and P. Schilke (Feb. 2017). “eXtended CASA Line Analysis Software Suite (XCLASS)”. In: *A&A* 598, A7, A7. DOI: 10.1051/0004-6361/201527203. arXiv: 1508.04114 [astro-ph.IM].
- Möller, T. et al. (Jan. 2013). “Modeling and Analysis Generic Interface for eXternal numerical codes (MAGIX)”. In: *A&A* 549, A21, A21. DOI: 10.1051/0004-6361/201220063. arXiv: 1210.6466 [astro-ph.IM].
- Motte, F. et al. (July 2010a). “Initial highlights of the HOBYS key program, the Herschel imaging survey of OB young stellar objects”. In: *A&A* 518, L77, p. L77. DOI: 10.1051/0004-6361/201014690.
- (July 2010b). “Initial highlights of the HOBYS key program, the Herschel imaging survey of OB young stellar objects”. In: *A&A* 518, L77, p. L77. DOI: 10.1051/0004-6361/201014690.
- Motte, Frédérique, Sylvain Bontemps, and Fabien Louvet (Sept. 2018). “High-Mass Star and Massive Cluster Formation in the Milky Way”. In: *ARA&A* 56, pp. 41–82. DOI: 10.1146/annurev-astro-091916-055235. arXiv: 1706.00118 [astro-ph.GA].

- Murray, Stephen D. and Douglas N. C. Lin (Aug. 1996). "Coalescence, Star Formation, and the Cluster Initial Mass Function". In: *ApJ* 467, p. 728. DOI: [10.1086/177648](https://doi.org/10.1086/177648).
- Neckel, T. (Sept. 1978). "UBV, VRI and Hbeta observations of stars in the H II regions NGC 6334 and NGC 6357." In: *A&A* 69, pp. 51–56.
- Nguyen-Luong, Q. et al. (Oct. 2013). "Low-velocity Shocks Traced by Extended SiO Emission along the W43 Ridges: Witnessing the Formation of Young Massive Clusters". In: *ApJ* 775.2, 88, p. 88. DOI: [10.1088/0004-637X/775/2/88](https://doi.org/10.1088/0004-637X/775/2/88). arXiv: [1306.0547](https://arxiv.org/abs/1306.0547) [astro-ph.GA].
- Nielbock, M. et al. (Feb. 2007). "The Morphology of M17-UC1: A Disk Candidate Surrounding a Hypercompact H II Region". In: *ApJ* 656.2, pp. L81–L84. DOI: [10.1086/512972](https://doi.org/10.1086/512972). arXiv: [astro-ph/0610559](https://arxiv.org/abs/astro-ph/0610559) [astro-ph].
- Ntormousi, Evangelia et al. (Apr. 2011). "Formation of Cold Filamentary Structure from Wind-blown Superbubbles". In: *ApJ* 731.1, 13, p. 13. DOI: [10.1088/0004-637X/731/1/13](https://doi.org/10.1088/0004-637X/731/1/13). arXiv: [1011.5751](https://arxiv.org/abs/1011.5751) [astro-ph.GA].
- Ossenkopf, V. and Th. Henning (Nov. 1994). "Dust opacities for protostellar cores." In: *A&A* 291, pp. 943–959.
- Ostriker, J. (Nov. 1964). "On the Oscillations and the Stability of a Homogeneous Compressible Cylinder." In: *ApJ* 140, p. 1529. DOI: [10.1086/148057](https://doi.org/10.1086/148057).
- Palau, Aina et al. (Nov. 2015). "Gravity or turbulence? - III. Evidence of pure thermal Jeans fragmentation at 0.1 pc scale". In: *MNRAS* 453.4, pp. 3785–3797. DOI: [10.1093/mnras/stv1834](https://doi.org/10.1093/mnras/stv1834). arXiv: [1504.07644](https://arxiv.org/abs/1504.07644) [astro-ph.GA].
- Palau, Aina et al. (May 2021). "Does the Magnetic Field Suppress Fragmentation in Massive Dense Cores?" In: *ApJ* 912.2, 159, p. 159. DOI: [10.3847/1538-4357/abee1e](https://doi.org/10.3847/1538-4357/abee1e). arXiv: [2010.12099](https://arxiv.org/abs/2010.12099) [astro-ph.GA].
- Palmeirim, P. et al. (Feb. 2013). "Herschel view of the Taurus B211/3 filament and striations: evidence of filamentary growth?" In: *A&A* 550, A38, A38. DOI: [10.1051/0004-6361/201220500](https://doi.org/10.1051/0004-6361/201220500). arXiv: [1211.6360](https://arxiv.org/abs/1211.6360) [astro-ph.SR].
- Parker, Quentin A. et al. (Sept. 2005). "The AAO/UKST SuperCOSMOS H α survey". In: *MNRAS* 362.2, pp. 689–710. DOI: [10.1111/j.1365-2966.2005.09350.x](https://doi.org/10.1111/j.1365-2966.2005.09350.x). arXiv: [astro-ph/0506599](https://arxiv.org/abs/astro-ph/0506599) [astro-ph].
- Pelkonen, V. M. et al. (June 2021). "From the CMF to the IMF: beyond the core-collapse model". In: *MNRAS* 504.1, pp. 1219–1236. DOI: [10.1093/mnras/stab844](https://doi.org/10.1093/mnras/stab844). arXiv: [2008.02192](https://arxiv.org/abs/2008.02192) [astro-ph.SR].

- Peretto, N. et al. (May 2012). "The Pipe Nebula as seen with Herschel: formation of filamentary structures by large-scale compression?" In: *A&A* 541, A63, A63. DOI: [10.1051/0004-6361/201118663](https://doi.org/10.1051/0004-6361/201118663). arXiv: 1203.3403 [astro-ph.GA].
- Peretto, N. et al. (July 2013). "Global collapse of molecular clouds as a formation mechanism for the most massive stars". In: *A&A* 555, A112, A112. DOI: [10.1051/0004-6361/201321318](https://doi.org/10.1051/0004-6361/201321318). arXiv: 1307.2590 [astro-ph.GA].
- Peretto, N. et al. (Jan. 2014). "SDC13 infrared dark clouds: Longitudinally collapsing filaments?" In: *A&A* 561, A83, A83. DOI: [10.1051/0004-6361/201322172](https://doi.org/10.1051/0004-6361/201322172). arXiv: 1311.0203 [astro-ph.GA].
- Persi, P. and M. Tapia (2008). "Star Formation in NGC 6334". In: *Handbook of Star Forming Regions, Volume II*. Ed. by B. Reipurth. Vol. 5. ASP, p. 456.
- Plunkett, Adele L. et al. (July 2018). "Distribution of Serpens South protostars revealed with ALMA". In: *A&A* 615, A9, A9. DOI: [10.1051/0004-6361/201732372](https://doi.org/10.1051/0004-6361/201732372). arXiv: 1804.02405 [astro-ph.SR].
- Pokhrel, Riway et al. (Jan. 2018). "Hierarchical Fragmentation in the Perseus Molecular Cloud: From the Cloud Scale to Protostellar Objects". In: *ApJ* 853.1, 5, p. 5. DOI: [10.3847/1538-4357/aaa240](https://doi.org/10.3847/1538-4357/aaa240). arXiv: 1712.04960 [astro-ph.GA].
- Raimond, Ernst and Baldur Eliasson (Mar. 1969). "Positions and Stokes Parameters of Seven Oh-Emission Sources". In: *ApJ* 155, pp. 817–830. DOI: [10.1086/149912](https://doi.org/10.1086/149912).
- Rengarajan, T. N. and P. T. P. Ho (July 1996). "Search for Optically Thick H II Regions and Ionized Stellar Wind from Luminous Embedded Infrared Sources". In: *ApJ* 465, p. 363. DOI: [10.1086/177425](https://doi.org/10.1086/177425).
- Roberts, W. W. (Oct. 1969). "Large-Scale Shock Formation in Spiral Galaxies and its Implications on Star Formation". In: *ApJ* 158, p. 123. DOI: [10.1086/150177](https://doi.org/10.1086/150177).
- Rodriguez, L. F., J. Canto, and J. M. Moran (Apr. 1982). "Radio sources in NGC 6334." In: *ApJ* 255, pp. 103–110. DOI: [10.1086/159808](https://doi.org/10.1086/159808).
- Russeil, D. et al. (June 2010). "The earliest phases of high-mass star formation: the NGC 6334-NGC 6357 complex". In: *A&A* 515, A55, A55. DOI: [10.1051/0004-6361/200913632](https://doi.org/10.1051/0004-6361/200913632).
- Russeil, D. et al. (June 2013). "The Herschel view of the massive star-forming region NGC 6334". In: *A&A* 554, A42, A42. DOI: [10.1051/0004-6361/201219971](https://doi.org/10.1051/0004-6361/201219971).
- Russeil, D. et al. (Mar. 2016). "NGC 6334 and NGC 6357: H α kinematics and the nature of the H II regions". In: *A&A* 587, A135, A135. DOI: [10.1051/0004-6361/201424484](https://doi.org/10.1051/0004-6361/201424484).

- Russeil, D. et al. (May 2019). "Herschel-HOBYS study of the earliest phases of high-mass star formation in NGC 6357". In: *A&A* 625, A134, A134. DOI: [10.1051/0004-6361/201833870](https://doi.org/10.1051/0004-6361/201833870).
- Russeil, D. et al. (Oct. 2020). "OB stars and YSO populations in the region of NGC 6334-NGC 6357 as seen with Gaia DR2". In: *A&A* 642, A21, A21. DOI: [10.1051/0004-6361/202037674](https://doi.org/10.1051/0004-6361/202037674).
- Sadaghiani, M. et al. (Mar. 2020). "Physical properties of the star-forming clusters in NGC 6334. A study of the continuum dust emission with ALMA". In: *A&A* 635, A2, A2. DOI: [10.1051/0004-6361/201935699](https://doi.org/10.1051/0004-6361/201935699). arXiv: [1911.06579](https://arxiv.org/abs/1911.06579) [astro-ph.SR].
- Sadaghiani, Mahya (2021). "Unveiling the properties of the clusters in the NGC6334 filamentary cloud including the physics of shocked gas and accretion". PhD thesis. Universität zu Köln. URL: <https://kups.ub.uni-koeln.de/53084/>.
- Sánchez-Monge, Á. et al. (May 2015). "Mass accretion flows in the high-mass star forming complex NGC 6334". In: *EAS Publications Series*. Vol. 75-76. EAS Publications Series, pp. 269–272. DOI: [10.1051/eas/1575053](https://doi.org/10.1051/eas/1575053).
- Sánchez-Monge, Á. et al. (July 2017). "The physical and chemical structure of Sagittarius B2. II. Continuum millimeter emission of Sgr B2(M) and Sgr B2(N) with ALMA". In: *A&A* 604, A6, A6. DOI: [10.1051/0004-6361/201730426](https://doi.org/10.1051/0004-6361/201730426). arXiv: [1704.01805](https://arxiv.org/abs/1704.01805) [astro-ph.GA].
- Schilke, P. et al. (May 1997). "SiO production in interstellar shocks." In: *aap* 321, pp. 293–304.
- Schisano, Eugenio et al. (Mar. 2020). "The Hi-GAL catalogue of dusty filamentary structures in the Galactic plane". In: *MNRAS* 492.4, pp. 5420–5456. DOI: [10.1093/mnras/stz3466](https://doi.org/10.1093/mnras/stz3466). arXiv: [1912.04020](https://arxiv.org/abs/1912.04020) [astro-ph.GA].
- Schneider, S. and B. G. Elmegreen (Sept. 1979). "A catalog of dark globular filaments." In: *ApJS* 41, pp. 87–95. DOI: [10.1086/190609](https://doi.org/10.1086/190609).
- Schwörer, A. et al. (Aug. 2019). "The physical and chemical structure of Sagittarius B2. IV. Converging filaments in the high-mass cluster forming region Sgr B2(N)". In: *A&A* 628, A6, A6. DOI: [10.1051/0004-6361/201935200](https://doi.org/10.1051/0004-6361/201935200). arXiv: [1906.10979](https://arxiv.org/abs/1906.10979) [astro-ph.GA].
- Seifried, D. and S. Walch (Sept. 2015). "The impact of turbulence and magnetic field orientation on star-forming filaments". In: *MNRAS* 452.3, pp. 2410–2422. DOI: [10.1093/mnras/stv1458](https://doi.org/10.1093/mnras/stv1458). arXiv: [1503.01659](https://arxiv.org/abs/1503.01659) [astro-ph.GA].

- Shu, Frank H., Fred C. Adams, and Susana Lizano (Jan. 1987). "Star formation in molecular clouds: observation and theory." In: *ARA&A* 25, pp. 23–81. DOI: [10.1146/annurev.aa.25.090187.000323](https://doi.org/10.1146/annurev.aa.25.090187.000323).
- Simon, T. et al. (Jan. 1985). "The morphology of NGC 6334 IRS V-1." In: *MNRAS* 212, 21P–25. DOI: [10.1093/mnras/212.1.21P](https://doi.org/10.1093/mnras/212.1.21P).
- Simpson, J. A. (Jan. 1983). "Elemental and Isotopic Composition of the Galactic Cosmic Rays". In: *Annual Review of Nuclear and Particle Science* 33, pp. 323–382. DOI: [10.1146/annurev.ns.33.120183.001543](https://doi.org/10.1146/annurev.ns.33.120183.001543).
- Simpson, Janet P. et al. (Aug. 2009). "Hubble Space Telescope NICMOS Polarization Observations of Three Edge-on Massive Young Stellar Objects". In: *ApJ* 700.2, pp. 1488–1501. DOI: [10.1088/0004-637X/700/2/1488](https://doi.org/10.1088/0004-637X/700/2/1488). arXiv: 0906.0940 [astro-ph.GA].
- Soler, J. D. and P. Hennebelle (Oct. 2017). "What are we learning from the relative orientation between density structures and the magnetic field in molecular clouds?" In: *A&A* 607, A2, A2. DOI: [10.1051/0004-6361/201731049](https://doi.org/10.1051/0004-6361/201731049). arXiv: 1705.00477 [astro-ph.GA].
- Sousbie, T. (June 2011). "The persistent cosmic web and its filamentary structure - I. Theory and implementation". In: *MNRAS* 414.1, pp. 350–383. DOI: [10.1111/j.1365-2966.2011.18394.x](https://doi.org/10.1111/j.1365-2966.2011.18394.x). arXiv: 1009.4015 [astro-ph.CO].
- Spitzer Lyman, Jr. (Dec. 1969). "Equipartition and the Formation of Compact Nuclei in Spherical Stellar Systems". In: *ApJ* 158, p. L139. DOI: [10.1086/180451](https://doi.org/10.1086/180451).
- Springel, Volker et al. (June 2005). "Simulations of the formation, evolution and clustering of galaxies and quasars". In: *Nature* 435.7042, pp. 629–636. DOI: [10.1038/nature03597](https://doi.org/10.1038/nature03597). arXiv: astro-ph/0504097 [astro-ph].
- Stahler, S. W. (Nov. 1983). "The birthline for low-mass stars." In: *ApJ* 274, pp. 822–829. DOI: [10.1086/161495](https://doi.org/10.1086/161495).
- Stahler, Steven W. and Francesco Palla (2004). *The Formation of Stars*.
- Suri, Sümeyye et al. (Mar. 2019). "The CARMA-NRO Orion Survey. Filamentary structure as seen in C¹⁸O emission". In: *A&A* 623, A142, A142. DOI: [10.1051/0004-6361/201834049](https://doi.org/10.1051/0004-6361/201834049). arXiv: 1901.00176 [astro-ph.GA].
- Tafalla, M. and A. Hacar (Feb. 2015). "Chains of dense cores in the Taurus L1495/B213 complex". In: *A&A* 574, A104, A104. DOI: [10.1051/0004-6361/201424576](https://doi.org/10.1051/0004-6361/201424576). arXiv: 1412.1083 [astro-ph.GA].
- Tahani, Mehrnoosh et al. (Dec. 2022). "JCMT BISTRO Observations: Magnetic Field Morphology of Bubbles Associated with NGC 6334". In: *arXiv e-prints*, arXiv:

- 2212.10884, arXiv: 2212.10884. DOI: 10.48550/arXiv.2212.10884. arXiv: 2212.10884 [astro-ph.GA].
- Tielens, A. G. G. M. (2005). *The Physics and Chemistry of the Interstellar Medium*.
- Tigé, J. et al. (June 2017). “The earliest phases of high-mass star formation, as seen in NGC 6334 by Herschel-HOBYS”. In: *A&A* 602, A77, A77. DOI: 10.1051/0004-6361/201628989. arXiv: 1703.09839 [astro-ph.GA].
- Tiwari, M. et al. (June 2019). “Observational study of hydrocarbons in the bright photodissociation region of Messier 8”. In: *A&A* 626, A28, A28. DOI: 10.1051/0004-6361/201834567. arXiv: 1903.10444 [astro-ph.GA].
- Tokuda, Kazuki et al. (Nov. 2019). “An ALMA View of Molecular Filaments in the Large Magellanic Cloud. II. An Early Stage of High-mass Star Formation Embedded at Colliding Clouds in N159W-South”. In: *ApJ* 886.1, 15, p. 15. DOI: 10.3847/1538-4357/ab48ff. arXiv: 1811.04400 [astro-ph.GA].
- Townes, C. H. and A. L. Schawlow (1975). *Microwave spectroscopy*.
- Treviño-Morales, S. P. et al. (Sept. 2019). “Dynamics of cluster-forming hub-filament systems. The case of the high-mass star-forming complex Monoceros R2”. In: *A&A* 629, A81, A81. DOI: 10.1051/0004-6361/201935260. arXiv: 1907.03524 [astro-ph.GA].
- Vazquez-Semadeni, Enrique, Thierry Passot, and Annick Pouquet (Mar. 1995). “A Turbulent Model for the Interstellar Medium. I. Threshold Star Formation and Self-Gravity”. In: *ApJ* 441, p. 702. DOI: 10.1086/175393.
- Wada, Keiichi, Gerhardt Meurer, and Colin A. Norman (Sept. 2002). “Gravity-driven Turbulence in Galactic Disks”. In: *ApJ* 577.1, pp. 197–205. DOI: 10.1086/342151. arXiv: astro-ph/0207641 [astro-ph].
- Wang, Ke et al. (July 2011). “Hierarchical Fragmentation and Jet-like Outflows in IRDC G28.34+0.06: A Growing Massive Protostar Cluster”. In: *ApJ* 735.1, 64, p. 64. DOI: 10.1088/0004-637X/735/1/64. arXiv: 1105.4559 [astro-ph.GA].
- Wang, Ke et al. (Apr. 2014). “Hierarchical fragmentation and differential star formation in the Galactic ‘Snake’: infrared dark cloud G11.11-0.12”. In: *MNRAS* 439.4, pp. 3275–3293. DOI: 10.1093/mnras/stu127. arXiv: 1401.4157 [astro-ph.GA].
- Ward-Thompson, Derek and Anthony P. Whitworth (2011). *An Introduction to Star Formation*.
- (2015). *An Introduction to Star Formation*. Cambridge University Press.
- Weingartner, Joseph C. and B. T. Draine (Feb. 2001). “Dust Grain-Size Distributions and Extinction in the Milky Way, Large Magellanic Cloud, and Small Magellanic

- Cloud". In: *ApJ* 548.1, pp. 296–309. DOI: [10.1086/318651](https://doi.org/10.1086/318651). arXiv: [astro-ph/0008146](https://arxiv.org/abs/astro-ph/0008146) [[astro-ph](#)].
- Whittet, D. C. B. (1993). "Observations of Molecular Ices". In: *Dust and Chemistry in Astronomy*. Ed. by T. J. Millar and D. A. Williams, p. 9.
- Willis, S. et al. (Dec. 2013). "A Wide-field near- and Mid-infrared Census of Young Stars in NGC 6334". In: *ApJ* 778.2, 96, p. 96. DOI: [10.1088/0004-637X/778/2/96](https://doi.org/10.1088/0004-637X/778/2/96). arXiv: [1310.0821](https://arxiv.org/abs/1310.0821) [[astro-ph.SR](#)].
- Wootten, A. et al. (Aug. 1980). "Detection of C₂H in cold dark clouds". In: *ApJ* 239, pp. 844–854. DOI: [10.1086/158168](https://doi.org/10.1086/158168).
- Yorke, Harold W. and Cordula Sonnhalter (Apr. 2002). "On the Formation of Massive Stars". In: *ApJ* 569.2, pp. 846–862. DOI: [10.1086/339264](https://doi.org/10.1086/339264). arXiv: [astro-ph/0201041](https://arxiv.org/abs/astro-ph/0201041) [[astro-ph](#)].
- Zernickel, A. (May 2015). "Submm Observations of Massive Star Formation in the Giant Molecular Cloud NGC 6334 : Gas Kinematics with Radiative Transfer Models". PhD thesis. University of Cologne, Institute for Physics.
- Zernickel, A., P. Schilke, and R. J. Smith (June 2013). "The global velocity field of the filament in NGC 6334". In: *A&A* 554, L2, p. L2. DOI: [10.1051/0004-6361/201321425](https://doi.org/10.1051/0004-6361/201321425).
- Zhang, Qizhou et al. (Sept. 2014). "Magnetic Fields and Massive Star Formation". In: *ApJ* 792.2, 116, p. 116. DOI: [10.1088/0004-637X/792/2/116](https://doi.org/10.1088/0004-637X/792/2/116). arXiv: [1407.3984](https://arxiv.org/abs/1407.3984) [[astro-ph.GA](#)].
- Zhang, Qizhou et al. (May 2015). "Fragmentation of Molecular Clumps and Formation of a Protocluster". In: *ApJ* 804.2, 141, p. 141. DOI: [10.1088/0004-637X/804/2/141](https://doi.org/10.1088/0004-637X/804/2/141). arXiv: [1503.03017](https://arxiv.org/abs/1503.03017) [[astro-ph.SR](#)].
- Zinnecker, Hans, Mark J. McCaughrean, and Bruce A. Wilking (Jan. 1993). "The Initial Stellar Population". In: *Protostars and Planets III*. Ed. by Eugene H. Levy and Jonathan I. Lunine, p. 429.
- Zinnecker, Hans and Harold W. Yorke (Sept. 2007). "Toward Understanding Massive Star Formation". In: *ARA&A* 45.1, pp. 481–563. DOI: [10.1146/annurev.astro.44.051905.092549](https://doi.org/10.1146/annurev.astro.44.051905.092549). arXiv: [0707.1279](https://arxiv.org/abs/0707.1279) [[astro-ph](#)].

ACKNOWLEDGEMENTS

THIS research is conducted as part of the Collaborative Research Centre 956 (sub-project "A6: Evolution of High-Mass Stars"), supported and funded by the Deutsche Forschungsgemeinschaft (DFG).

As I reach the closing chapter of my academic journey, I am deeply grateful to the many individuals who helped and supported me throughout this monumental journey in my academic life.

Dear Peter, I would like to thank you for your trust and the opportunity you gave me to discover the magical world of radio astronomy. Thank you for being so patient and letting me experience more and open up the horizons of my creativity without feeling stressed.

Dear Alvaro, It is difficult for me to imagine finishing my doctorate without your unwavering support and guidance. I have learned a lot from you. You taught me how to have a scientifically organized mind, and your spectacular discipline in solving problems is a unique skill that keeps me moving after every failure.

Regardless of all the ups and downs, the weekly meeting remains the strongest motivation for consistent progress in my scientific life. I want to express my gratitude to Gary, Wonju, Veena, and my former colleagues Alvaro and Mahya for our weekly topical meetings, where we shared our work and discussed science. Your insightful comments, constructive criticisms, and collaborative spirit played an invaluable role in shaping my research direction.

I would also like to convey my thanks to Wonju for being patient in answering my endless questions, which significantly improved the quality and clarity of my work. Also, thanks to Thomas for assisting me in resolving issues with XCLASS and providing invaluable support in executing XCLASS jobs.

My heartfelt appreciation also extends to Alvaro, Daniel, Beth, Mahya, Shashwata, Wonju, and Veena; your diligent review and constructive feedback have greatly enriched the depth and quality of this thesis in its present form. I am sincerely grateful to Prof. Gary Fuller for serving on my thesis committee and providing invaluable advice for this thesis. I also extend my gratitude to Prof. Andreas Zilges for accepting the role of defense chair.

This work was undertaken amidst a global pandemic and an ongoing revolution in my homeland. The only reason I could overcome all these challenges and persist with my research was the immense help and emotional support from my family and friends.

I want to highlight my gratitude towards my dearest friend and former colleague, Mahya. From the first day I joined the group and met you through our scientific chats, our travels, and shared experiences in street photography to this moment as I write these words, you have been a constant source of support and joy.

A special shout-out goes to my friends and colleagues in the group, Flavia, Beth, Tianwei, and Philip, for all the pleasant moments and activities we have shared, and also to my fellow Iranian girls at the institute, Nafiseh, Elahe, Roya, and Nasim, for our cherished tea times. I will always remember you

and eagerly anticipate seeing where life takes each of you.

I also want to warmly mention my beloved friends Atena, Anna, Bitra, Theresa, Katarina, and Fatima for keeping me company all these years, and making my time in Germany feel like home.

I want to take a moment to remember my TMU gang from my bachelor days. To my best friends Anna, Mahsa, Eli, Elmira, Elham, and Ronak: our days back in TMU and the memories we made during my yearly visits to Tehran have been unforgettable. A special nod also goes to Anna, Amir, Ahad, and Nagmeh, who now live closer, and I am excited for many future adventures together.

Last but certainly not least, I want to express my deepest gratitude to my parents and brother for sending their support and love from another continent. Even when vast distances separated us, I always felt your presence close to my heart. Your unwavering faith in my abilities, even when I doubted myself, has been the anchor that kept me grounded.

Finally, I cannot conclude without acknowledging Mehdi, who has had the most profound impact on my life, from our bachelor's days to our time living in Germany. Through every high and low, Mehdi, you were there, holding my hand in just the right way. Your unwavering encouragement and simple acts of kindness made the challenging moments more bearable.

Erklärung zur Dissertation
gemäß der Promotionsordnung vom 12. März 2020

***Diese Erklärung muss in der Dissertation enthalten sein.
(This version must be included in the doctoral thesis)***

„Hiermit versichere ich an Eides statt, dass ich die vorliegende Dissertation selbstständig und ohne die Benutzung anderer als der angegebenen Hilfsmittel und Literatur angefertigt habe. Alle Stellen, die wörtlich oder sinngemäß aus veröffentlichten und nicht veröffentlichten Werken dem Wortlaut oder dem Sinn nach entnommen wurden, sind als solche kenntlich gemacht. Ich versichere an Eides statt, dass diese Dissertation noch keiner anderen Fakultät oder Universität zur Prüfung vorgelegen hat; dass sie - abgesehen von unten angegebenen Teilpublikationen und eingebundenen Artikeln und Manuskripten - noch nicht veröffentlicht worden ist sowie, dass ich eine Veröffentlichung der Dissertation vor Abschluss der Promotion nicht ohne Genehmigung des Promotionsausschusses vornehmen werde. Die Bestimmungen dieser Ordnung sind mir bekannt. Darüber hinaus erkläre ich hiermit, dass ich die Ordnung zur Sicherung guter wissenschaftlicher Praxis und zum Umgang mit wissenschaftlichem Fehlverhalten der Universität zu Köln gelesen und sie bei der Durchführung der Dissertation zugrundeliegenden Arbeiten und der schriftlich verfassten Dissertation beachtet habe und verpflichte mich hiermit, die dort genannten Vorgaben bei allen wissenschaftlichen Tätigkeiten zu beachten und umzusetzen. Ich versichere, dass die eingereichte elektronische Fassung der eingereichten Druckfassung vollständig entspricht.“

Teilpublikationen:

*Dynamics of hub-filament cluster NGC 6334-V:
I. Detection of SiO shocked gas along accreting filaments
(Aghababaei et al., in prep., 2023)*

Datum, Name und Unterschrift

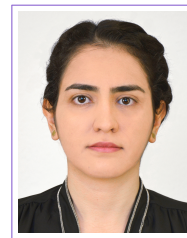
*Köln, den 05.07.2023
Atefeh Aghababaei*


Atefeh Aghababaei

CURRICULUM VITÆ

Atefeh–Mitra Aghababaei

Curriculum vitae



Paul-Schallück-Straße 21
50939 Köln

+49(0)177 49 220 42

✉ atefeh.aghababaei90@gmail.com

Educations

- 2018 –present **PhD Candidate, Astrophysics**, *University of Cologne*, Germany.
- 2016 – 2018 **Masters of Science (M.Sc.), Physics**, *University of Cologne*, Germany.
- 2008 – 2013 **Bachelor of Science (B.Sc.), Physics**, *Kharazmi University of Tehran*, Iran.

Scientific Activities

- 2018 –present **Doctoral Thesis**, *Kinematics and Structure of Massive Star Formation in NGC6334 V*, under the Supervision of Prof. Dr. Peter Schilke, Dr. Alvaro Sánchez Monge, I. Physikalisches Institut - University of Cologne.
- 2017 – 2018 **Master thesis**, *Characterizing the High Mass Protocluster NGC6334 V via High-Resolution ALMA Observations*, under the Supervision of Prof. Dr. Peter Schilke, Dr. Alvaro Sánchez Monge, I. Physikalisches Institut - University of Cologne.
- 2015 – 2016 **Trainee at VLBI Group Research**, *The Comparison of Different Calibration of Data Sets for Different Radio Telescopes*, Under the Supervision of Dr. Helge Rottmann, Max Planck Institute for Radio Astronomy (MPIFR).
- 2014 – 2015 **Trainee at VLBI Group Research**, *Evaluation Phasing of ALMA Regression Test Data Sets*, Under the Supervision of Dr. Helge Rottmann, Max Planck Institute for Radio Astronomy (MPIFR).
- 2012 – 2013 **Bachelor thesis**, *Determination of Moon's and Sun's Dimensions as well as their Distance from Earth via Investigating the Moon's Phases and Eclipses*, Under the Supervision of Prof. Farzan Momeni, Kharazmi University of Tehran.
- 2011 – 2013 **Research Fellow in Robotics Lab**, *Leader of mechanics group for Small Size Robots in Iran Open Competition 2012 SSL and Robocup 2012 (Mexico)*, Under the Supervision of Dr. Mohammad Laali, Kharazmi University of Tehran.

Publications

- 2023 **Dynamics of the Hub-Filament System NGC 6334 V: I. Detection of SiO Shocked Gas along Accreting Filaments**, *Aghababaei et al., in prep., 2023*.
- 2023 **First Detection of SiO Shocked Gas along Accreting Filaments in the Hub-Filament System NGC 6334 V**, *Aghababaei, A.; Sánchez-Monge, á.; Kim, W. -J. ; Schilke, P. .*
- 2019 **The Role of Accretion and Extended SiO Emission in Forming High Mass Protocluster NGC 6334-V**, *Aghababaei, A., ALMA2019: Science Results and Cross-Facility Synergies, held 14-18 October 2019 in Cagliari, Italy.*

Honors and awards

- 2019 **Best Poster in ALMA2019 Conference : Science Results and Cross-Facility Synergies**, Cagliari - Italy.
- 2012 **Qualified in Robocup 2012 World Cup, Soccer Small Size League, as KAVAK Team**, Mexico City, Mexico.
- 2012 **5th Place in the Tournament of Iran Open Robotics Competition (Small Size)**, Tehran, Iran.

Conferences, Workshops, and Schools

- 2022 **The 7th Chile-Cologne-Bonn-Symposium: Physics and Chemistry of Star Formation**, *Puerto Varas, Chile*.
Conference - Contributed Talk
- 2022 **Les Houches Session on Interstellar Shocks**, *Les Houches, France*.
Summer school - Participation
- 2022 **European Astronomical Society Annual Meeting**, *Valencia, Spain*.
Conference - Contributed talk
- 2022 **Multi-line Diagnostics of the Interstellar Medium**, *Nice, France*.
Conference - Poster presentation
- 2019 **ALMA 2019: Science Results and Cross-Facility Synergies**, *Cagliari, Italy*.
Conference - Poster presentation
- 2019 **The Links between Massive Star and Star Cluster Formation**, *York, UK*.
Conference - Poster presentation
- 2019 **Improving Image Fidelity on Astronomical Data**, *Leiden, Niederlande*.
Summer school - Participation
- 2018 **30th General Assembly of the International Astronomical Union (IAU)**, *Vienna, Austria*.
Volunteer organizing committee
- 2015 **Dissecting the Universe Workshop on Results from High-Resolution VLBI**, *Bonn, Germany*.
Workshop - Participation
- 2015 **6th European Radio Interferometry School (ERIS)**, *Munich, Germany*.
Summer school - Participation

Teaching experiences

- WS2020 – **Course Tutor**, *Astrophysik*, Lecturer: Prof. Schilke, P; Möller, T.
- 2021 University of Cologne
- WS2019 – **Course Tutor**, *Experimentalphysik III (Atomphysik)*, Lecturer: Prof. Schilke, P; Möller, T.
- 2020 University of Cologne
- SS2019 **Course Tutor**, *Star and Planet Formation*, Lecturer: Prof. Schilke, Dr. Sánchez Monge, A.
University of Cologne
- WS2012 – **Course Tutor**, *The Analytical Mechanics Course*, Lecturer: Prof. Momeni, F.
- 2013 Kharazmi University of Tehran
- 2011 – 2012 **Teacher**, *Basic Astronomy for Kids*.
Shahran Center for scientific public outreach in Tehran

Memberships, Other activities

- 2019 – 2021 **First Speaker and Main Member of SFB students Council**, , *University of Cologne*.
- 2009 – 2013 **Founder and Main Member of Astronomy Group**, , *Kharazmi University of Tehran*.
- 2008 – 2013 **Main Member of Physics Association**, , *Kharazmi University of Tehran*.
- 2011 – 2013 **Member of Robotics Association**, , *Kharazmi University of Tehran*.

Skills

- Languages Persian (Native), English (C2), German (B2), Arabic (A2)
- Programming Python, Bash, LATEX

Köln, der August 2, 2023



Atefeh Aghababaei